Computational modelling of stent deployment and mechanical performance inside human atherosclerotic arteries

Computational Modelling of Stent Deployment and Mechanical Performance Inside Human Atherosclerotic Arteries

By

Alessandro Schiavone

A Doctoral Thesis

Submitted in partial fulfilment of the requirements for the award of Doctor of Philosophy of Loughborough University

Abstract

Atherosclerosis is the obstruction of blood stream caused by the formation of fatty plaques (stenosis) within human blood vessels. It is one of the most common cardiovascular conditions and the primary cause of death in developed countries. Nowadays stenting is a standard treatment for this disease and has been undergoing a rapid technological development. The aim of this PhD is to simulate the deployment of stents within atherosclerotic arteries in order to understand the mechanical performance of these devices. To this purpose, specific objectives were identified to study: (i) the effects of stent design, material and coating on stent deployment; (ii) the influence of balloon type, arterial constraints and vessel constitutive models in stenting simulation; (iii) the importance of plaque thickness, stenosis asymmetry and vessel curvature during the process of stent deployment; (iv) the necessity of considering vessel anisotropy and post-deployment stresses to assess stents' mechanical behaviour; (v) the performance of biodegradable polymeric stents in comparison with metallic stents.

Finite element (FE) analyses were employed to model the deployment of balloon-expandable stents. The balloon-stent-artery system was generated and meshed using finite element package Abaqus. Individual arterial layer and stenosis were modelled using hyperelastic Ogden model, while elastic-plastic behaviour with nonlinear hardening was used to describe the material behaviour of stents. The expansion of the stent was obtained by application of pressure inside the balloon, with hard contacts defined between stent, balloon and artery. The FE model was evaluated by mesh sensitivity study and further validated by comparison with published work.

Comparative study between different commercially available stents (i.e. Palmaz-Schatz, Cypher, Xience and Endeavor stents) showed that open-cell design tends to have easier expansion and higher recoiling than closed-cell design, with lower stress level on the plaque after deployment. Also, stents made of materials with lower yield stress and weaker strain hardening experience higher deformation and recoiling, but less post-deployment stresses. Folded balloon produces sustained stent expansion under a lower pressure when compared to rubber balloon, with also increased stress level on the stent and artery. Simulations with different arterial constraints showed that stress on the plaque-artery system is higher for a free artery as a result of more severe stretch. Study of arterial constitutive models showed that saturation of expansion could not be noticed for models that neglect the second stretch invariant in the strain energy potential.

Stent expansion is highly affected by plaque thickness, and stresses and recoiling increased considerably with the increasing level of stenosis. Asymmetry of the plaque causes non-uniform stent expansion and high levels of vessel wall stresses are developed in the regions covered by thin layer of plaque. Also, a reduction in stent expansion is observed with the increase of artery curvature, accompanied by an elevation of stresses in the plaque and arterial layers. Vessel anisotropic behaviour reduces the system expansion at peak pressure, and also lowers recoiling effect significantly. The post-deployment stresses caused by stent expansion increase the system flexibility during in-plane bending and radial compression. Comparative study of a PLLA stent (Elixir) and a Co-Cr alloy stent (Xience) showed that polymeric stent has a lower expansion rate and a reduction in final expansion than metallic stent.

Acknowledgements

It's not worth doing something unless someone, somewhere, would much rather you weren't doing it.

Terry Pratchett

It is my personal ritual to dedicate every single of my achievements to the people of my past who consistently wanted me to fail in life. Their mockery has always been the fuel of my passion, I will always carry it with me as a reminder that in life there is only one direction worth going and that is the future.

Between all the different versions of me that I imagined when I was a child, none was remotely close to the person I have become. I know as a fact that this work of research will always be one of my greatest achievements in life, which I would have never accomplished without the help and the guidance of those who are close to me. Thinking of gratitude, the first that comes to my mind is my supervisor Dr. Liguo Zhao. He believed in me for all these years, guiding me through all the struggles I had to face with extreme patience and confidence. I will always be grateful of being under his supervision, because his mentoring was the most valuable of my resources and in all the time I have worked with him I felt genuinely valorised and supported. Also, I would like to thank the head of the Mechanics of Advanced Materials research group Prof. Vadim Silberschmidt, all the other members of my research group and all the technical staff that helped me through my research.

The person I was, when I arrived in UK with two bags and a backpack, could have never imagined what life had prepared for him. For this journey and all the fortune that will bring to me, I will always have to thank my parents. My mother, as her understanding of life never failed me, and my father, who thought me that in life there can be no end for perseverance. In my family nobody is

closer to me than my brother, whose sarcasm is the only thing I trust more than the man himself, for all good decisions of my life should always pass the exam of his honesty.

Since I remember, friendship was always the biggest of my treasures, as the most precious ones are those who reveal themselves to be authentic. My thanks go to my best friend Umberto, for no matter how much time pass and how much we change we will always be there for a new adventure, and to Francesco, for always finding the time to share a laugh no matter how far away life brings us. Also to Ana, for joining me into this journey as a true partner in life and gifting me every day with her courage and passion.

A journey wouldn't be complete without all the people I met, that supported me every day and had to deal with me whether I was mad, sad or happy. My thanks go to Chris, Matt, Troy, Laurence, Javad, Felix, Andrea, Gayan, Emrah, Tianyang, Alkaios, Lorenzo, Andreas, Hanifeh, Farukh, Vahid, Qifei, Maryam and all the people that shared a laugh with me during these years, for showing me that happiness looks the same from every part of the world. Unfortunately it is impossible for me to mention everyone, so I shall thank also all my friends who despite the distance never forget me and never stop to support me.

List of Publications

Journal Papers

Alessandro Schiavone, Liguo Zhao (2015) A Study of Balloon Type, System Constraint and Artery Constitutive Model Used in Finite Element Simulation of Stent Deployment. Mechanics of Advanced Materials and Modern Processes 1

Alessandro Schiavone, Liguo Zhao and Adel A. Abdel-Wahab (2014) Effects of material, coating, design and plaque composition on stent deployment inside a stenotic artery—Finite element simulation. Materials Science and Engineering C 42, 479–488.

DOI: *10.1016/j.msec.2014.05.057*

Conference Papers

Alessandro Schiavone, Liguo Zhao and Adel A. Abdel-Wahab (2013) Dynamic Simulation of Stent Deployment - Effects of Design, Material and Coating. Journal of Physics: Conference Series 451, 012032

DOI: *10.1088/1742-6596/451/1/012032*

Conference Abstracts

Alessandro Schiavone, Liguo Zhao and Adel A. Abdel-Wahab (2013) Dynamic Simulation of Stent Deployment - Effects of Design, Material and Coating. International Symposium on Dynamic Deformation and Fracture of Advanced Materials (D2FAM). Loughborough, U.K.

Alessandro Schiavone, Liguo Zhao and Adel A. Abdel-Wahab (2014) Finite Element Simulation of Stent Deployment Inside a Stenotic Artery. 11th World Congress on Computational Mechanics (WCCM XI). Barcelona, Spain.

Alessandro Schiavone, Liguo Zhao (2015) Modelling of Stent Deployment and Deformation in Diseased Arteries by Considering Vessel Anisotropic Property. Advanced Problems in Mechanics (APM). St. Petersburg, Russia.

Alessandro Schiavone, Liguo Zhao (2015) A Computational Study of Stent Deployment Inside a Diseased Artery with Variable Degrees of Stenosis, Asymmetry and Curvature. 25th Congress of the International Society of Biomechanics (ISB). Glasgow, U.K.

Table of Contents

List of Figures

List of Tables

Chapter 1 – Introduction

1.1. The Atherosclerosis

Atherosclerosis is a progressive inflammatory condition of blood vessels that develops since childhood (Kalanuria *et al.*, 2012). The early lesion begins with the accumulation of cholesterol on the inner surface of the artery (i.e. the endothelium) of large vessels, such as aorta, coronary arteries and cerebral arteries. The inflammation can be aggravated by numerous factors, such as the presence of abnormal amount of fat and cholesterol in the blood stream (dyslipidemia), lack of antioxidants (oxidative stress), blood hypercoagulability, endothelial dysfunction and infection (Mallika *et al.*, 2007).

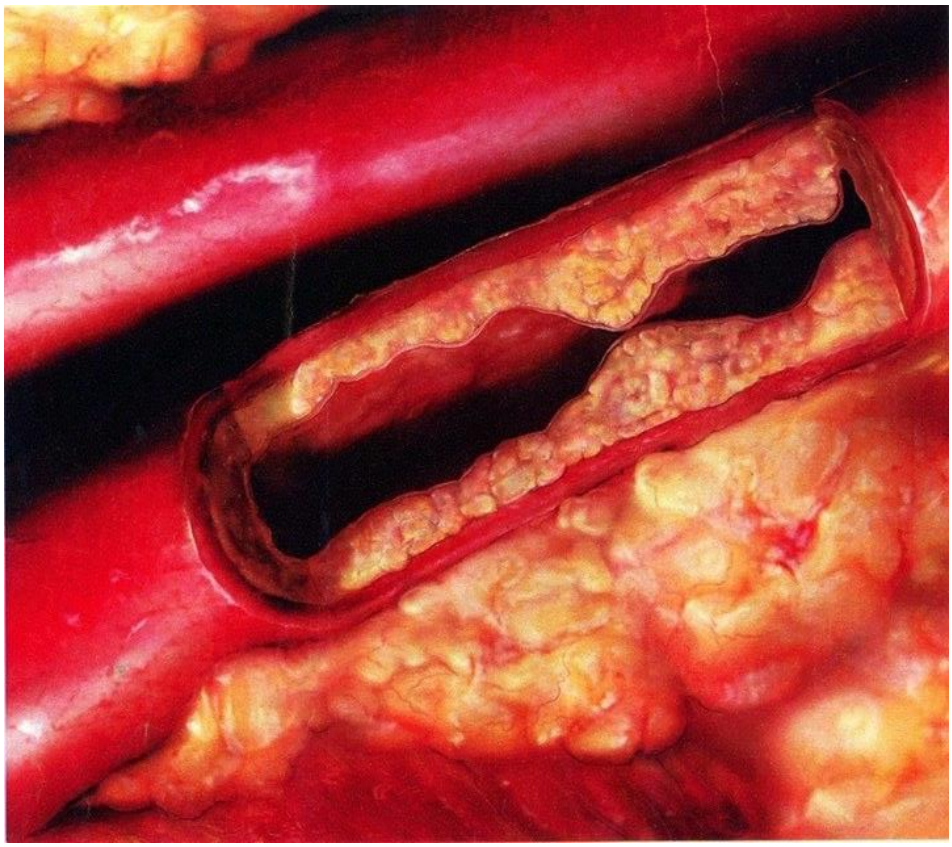

Figure 1.1. Illustration of a human artery with stenosis.

(*Source: Brains and Bodies* – *http://www.brainsandbodies.com*)

The process of development of this disease was given in detail in a review by Lusis (2000). The aggregation of lipoprotein particles on the intima layer is caused by high cholesterol and high fat diet. After the fatty layer is formed on the surface of the endothelium, monocytes (which are the largest among the blood cells) tend to adhere to this layer. Damage of the endothelium allows these cells to migrate within the intima layer, where they proliferate to form foam cells along with the lipoproteins. After the death of the foam cells, the plaque develops and increases in size, and a lipid pool forms inside the lesion and a fibrous cap develops around it. Figure 1.1 shows an illustration of arterial branch with stenosis. The lesion continues to grow as new cells from the blood stream adhere to the plaque, it develops within the blood vessel causing an increasing obstruction. After the full development of the plaque, several complications may occur such as the development of plaque calcification and thrombus or plaque rupture that may lead to heart attack.

Several statistical studies prove that atherosclerosis is one of the principal causes of death in industrialised world. A summary from the American Heart Association (AHA) by Go *et al.* (2013) showed that in the United States alone, more than 600,000 people die of coronary attack each year. The report also estimated that a coronary event is triggered every 34 seconds in USA and approximately one death occurs every minute. The office of national statistic (ONS) in England and Wales reported all the deaths occurred in 2010, divided by cause (ONS, 2011). There were almost 500,000 deaths, with causes summarised by The Guardian in the form of infographic (Figure 1.2). The statistics clearly shows that the circulatory disease is the second most prominent cause of death in England and Wales, with 139,000 casualties during the year. Based on data collected by the World Health Organization, the graphic producer Simran Khosla (Khosla, 2014) also created a map, showing the dominant death-related diseases across the world and published on GlobalPost (Figure 1.3). Data clearly illustrate that the heart disease is one of the major causes of death in industrialised nations.

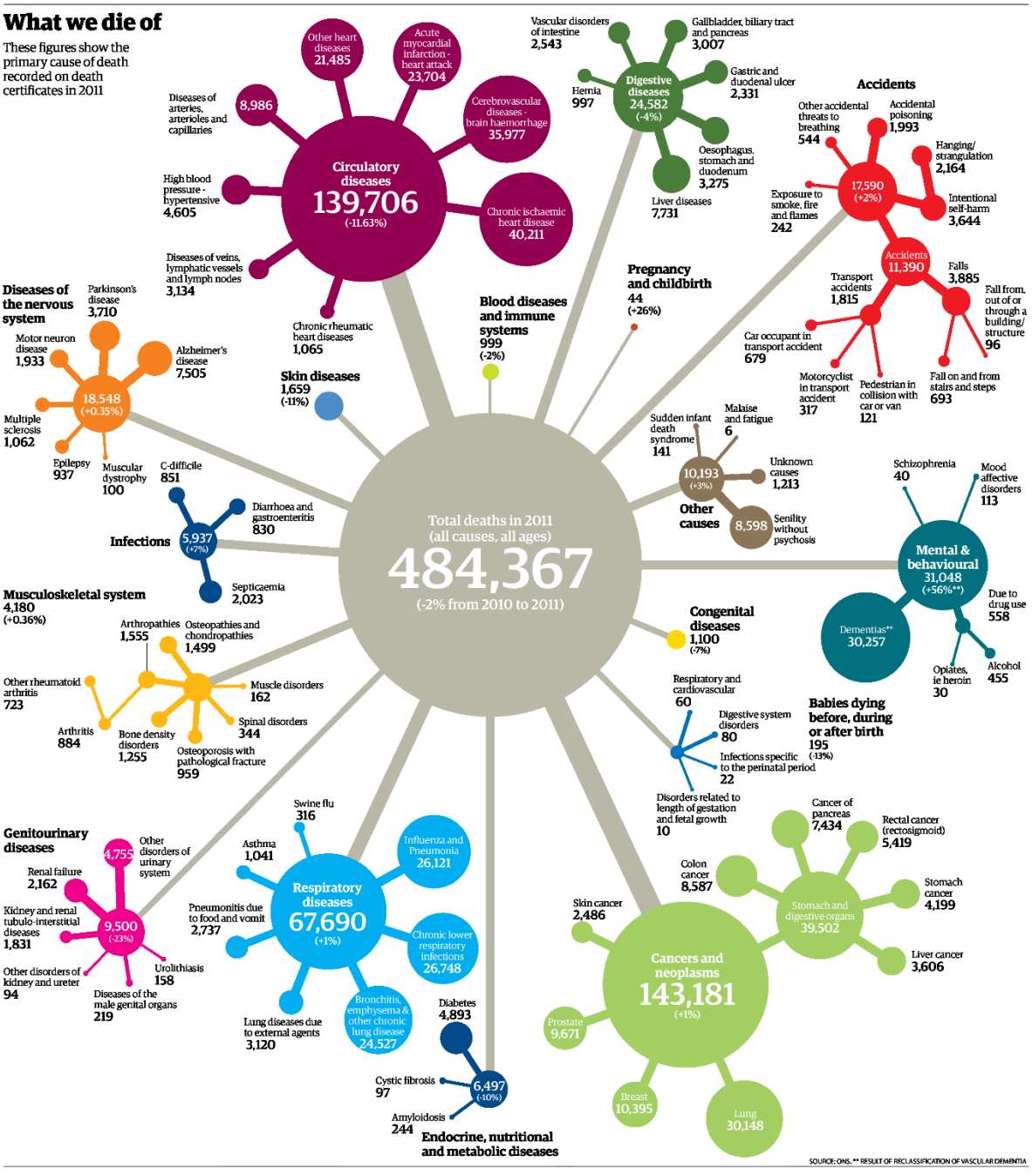

Figure 1.2. Infographic showing deaths occurred in England and Wales in 2010 (ONS, 2011).

(*Source: The Guardian – Mortality statistics: every cause of death in England and Wales*)

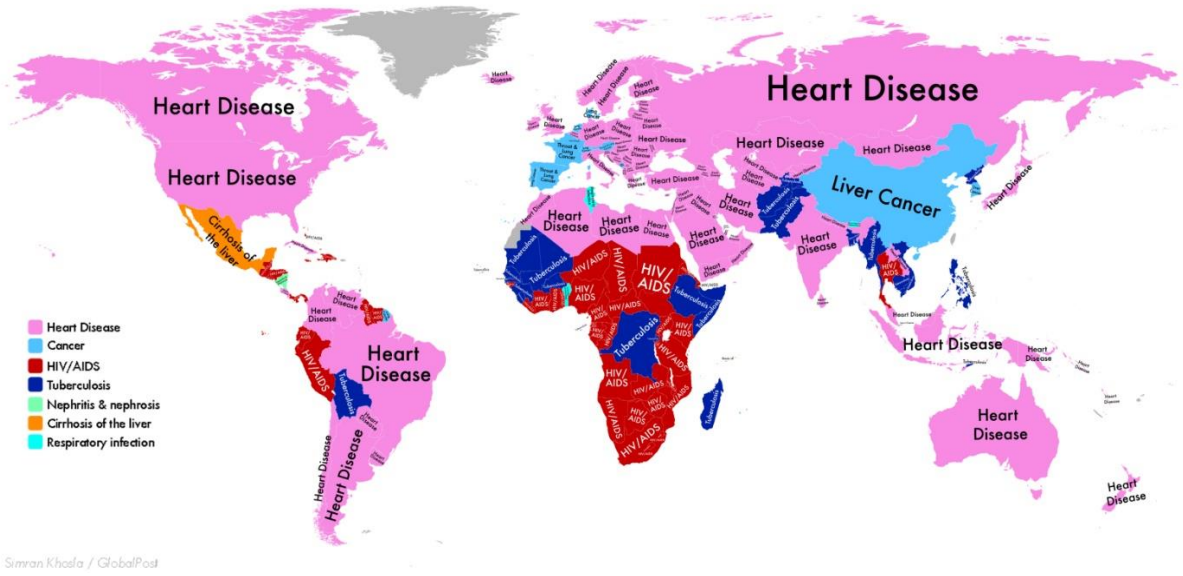

Figure 1.3. Map illustrating the principal causes of death in different nations according to data published by the World Health Organization (2014).

(*Source: GlobalPost – This map shows which disease is most likely to kill you depending on where you live*)

The possible treatments of atherosclerosis can be pharmacological and surgical. Pharmacological treatments are used only in case of asymptomatic stenosis, with the use of antihypertensive agents and satin medications. In case of symptomatic stenosis, surgical treatments must be used, which are either the surgical removal of the plaque, i.e. endarterectomy (EA), or the expansion of the vessel by means of carotid angioplasty and stenting (AS). A review by Lanzino *et al.* (2009) shows that EA is currently considered safe, effective and durable in preventing ipsilateral strokes. However, the treatment is highly invasive and cannot be performed if the patient has severe cardiopulmonary disease or recent cerebral infarctions. The treatment is usually accompanied by an aggressive pharmacological treatment to avoid recurrent strokes after the revascularization of the vessel. However, AS has been proposed as an alternative treatment, which is minimally invasive and requires only mild sedation and no incision. This treatment has been shown to be consistently effective within 30 days following the procedure. Also, the same review reports that, whilst the

risk of stroke within 30 days of AS was slightly higher compared to EA, the effectiveness after 2-3 years was close for the two different treatments. Despite the promising outcomes, the debate between the advantages of AS over EA is still open, in particular it has been shown that there is an age-associated increase of complications when treated with AS, but not for EA.

1.2 The Stent Technology

Since the first stent was developed about three decades ago, many different designs, have been created by the medical device industries, which allowed to extend the use of this device to the treatment of majority human vessels' obstructions, from the very common case of an atherosclerotic artery to aneurysms and obstructions of tracheas and bile vessels. The device consists of a cylindrical scaffold that, once deployed inside the body, expands to open the blocked vessels and allow the body fluid to flow normally. At the present, stenting has become a standard treatment for atherosclerosis and aneurysms. As reported by Riley *et al.* (2011), only in the USA have been performed around 425.000 percutaneous coronary interventions (PCI) per year between 2001 and 2009, of which about 382.000 involved the deployment of stents. An ideal process of stent deployment requires an expansion which is sufficient to clear vessel obstructions and also induces minimal damage to the vessel walls (Farooq *et al.*, 2011), as in-stent restenosis can be triggered by unsuccessful treatments including vessel over-stretch and injury, incomplete expansion of the stent and fracture of the stent struts.

A variety of designs have been produced by medical device companies which extended the use of stent to the treatment of majority human vessels' obstructions (e.g., stenotic arteries, brain aneurysms and obstructions of tracheas and bile vessels). Between these designs, two exemplar stents for the treatment of atherosclerosis are shown in Figure 1.4: the MultiLink and the Absorb by Abbott Vascular (USA). Despite the different applications of stent technology, Sangiorgi *et al.*

(2006) suggested that all stents must be flexible, trackable, radio-opaque, thromboresistant, biocompatible and reliably expandable. They also need to have high radial strength, low unconstrained profile, high circumferential coverage, low surface area and hydrodynamic compatibility. Stents can be distinguished from each other according to the mechanisms of expansion, materials, geometries and manufacturing techniques, which can affect their mechanical properties and biocompatibility.

1.2.1 Expansion Mechanisms

Stents can be classified as self-expanding or balloon expandable. Self-expanding stents are made of shape memory alloys, such as Nitinol. Shape memory stents can be plastically deformed if cooled below a certain temperature (namely critical temperature), but restore their original as-manufactured shape when heated above the critical temperature. Balloon-expandable stents, on the other hand, rely on the plasticity of metallic materials. They are manufactured in expanded shape and then crimped onto an angioplasty balloon. The deployment of the stent is obtained by inflating pressure inside the balloon, which plastically deform the stent to its expanded diameter.

Figure 1.4. Example of as-manufactured commercially available stents – (a) MultiLink and (b) Absorb (Abbott Vascular, Abbott Laboratories, Illinois, USA).

1.2.2 Stent Materials

All materials must exhibit excellent corrosion resistance and biocompatibility as well as radio opacity. They also must create minimal artefacts during Magnetic Resonance Imaging (MRI). According to Hanawa (2009), stainless steel is the most common material for balloon-expandable stents, but being gradually replaced by Co-Cr alloys and Tantalum alloys. On the other hand, Nitinol is the most common choice for self-expanding stents due to its shape memory feature. Most recently, Poly-L-Lactid Acid (PLLA) or Magnesium alloys are explored to manufacture the first generation of bioresorbable stents (Muramatsu *et al.,* 2013).

1.2.3 Stent Geometries

Generally, stents are formed by sinusoidal or Z-shaped rings joined together by connector elements. The majority of commercially available stents can be divided into two major groups, i.e. closed-cell and open cell design, with different types of connection such as peak to peak or valley to valley. Closed-cell designs have connector elements on each strut of the sinusoidal ring. The slotted tube design is also considered as closed-cell, and is obtained by cutting slots on the surface of a hollow metal cylinder. For open-cell designs, the sinusoidal rings are only selectively joined by connector struts. Other geometries include coil stents (the most common in non-vascular applications), helical spiral stents (generally promoted for their flexibility) and woven shape stents (a variety of designs manufactured from one more strands of wire).

1.2.4 Manufacturing Methods

The manufacturing methods used for stents are highly dependent on the forms of raw material used. Kathuria (2005) reviewed the different fabrication techniques for stents including etching, micro-EDM, electrodeforming, die casting and laser beam cut. Also, the paper identify different

dross adherence and removal processes, such as pickling soft etching, annealing and electropolishing. Typically, Balloon-expanding stents are cut by laser or water jet and require polishing. This is associated with surface finish problems during laser processing, such as dross, identified by Kathiuria (2005) due to temperature gradient, beam divergence and cutting depth increase. Possible cleaning processes were investigated, such as pickling and soft etching, but the best results were obtained by electrochemical etching. On the other hand, self-expandable stents are mainly formed by wires using the conventional wire-forming techniques such as coiling, braiding and knitting.

1.2.5 Drug Eluting Coating

Besides the scaffold structure, stents tend to have drug elution coatings. These coatings are made of porous polymers (e.g. polyurethane), which are wet with drugs (such as sirolimus and everolimus) that are released onto the surface of the artery upon contact between the stent and the vessel. The purpose of drug eluting coating is to reduce the risk of restenosis after deployment of the stent. A trial study conducted on patients with diabetes (Sabaté *et al.,* 2005) showed that after 9 months of the treatment with drug eluting stents (DES), the restenosis rate was reduced by 5% when compared with bare metal stents (BMS). Also, the major adverse cardiac events were reduced by 4% with DES. These results are also supported by the trial study of Hayes *et al.* (2010), who analysed a total of 1147 BMSs and 1246 DESs in 3-year follow-up. In their study, the risk of restenosis was found to be reduced by 4.7% for patients treated with DESs.

1.3. Clinical Studies

1.3.1 Case Reports

The complications associated with stent angioplasty are highlighted by case reports. These reports mostly address cases of stent failure and the associated complications for the patients, which can be chest pain, restenosis and thrombosis. The occurrence of these complications can also vary from few days after the deployment to months later. A case reported by Kang *et al.* (2007) revealed a very early stent fracture that occurred two days after surgery on a 76 years old male with history of hypertension, smoking and diabetes, who underwent the deployment of two drug eluting Cypher stents (Cordis, Europe, Netherlands) at 10 atm and 14 atm, respectively. Park *et al.* (2009) showed a complete stent fracture on a 44 years old male after twenty two months of stent implantation that caused a myocardial infarction. The stent deployed was a Cypher (Cordis, Miami Lakes, FL, USA). Park *et al.* (2009) also presented a zerotalimus eluting stent fractured after five months of deployment in an angulated right coronary artery associated with restenosis, highlighting the vessel tortuosity as the cause of stent fracture (Figure 1.5).

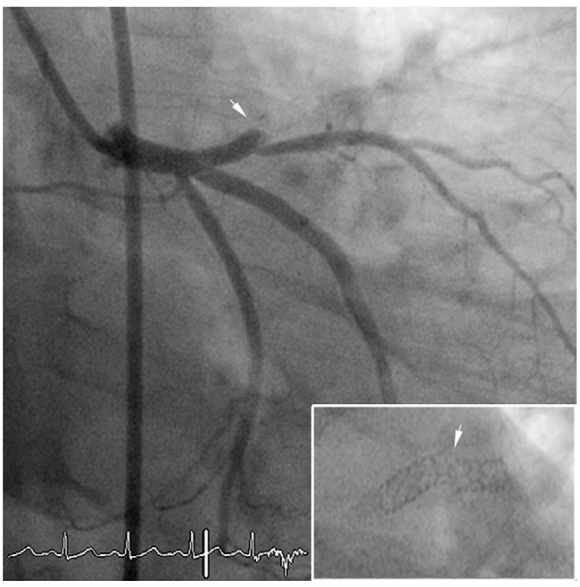

Figure 1.5. Coronary angiogram showing the left anterior coronary artery treated with Cypher stent (with diameter of 3.5 mm and length of 23 mm) with fracture (Park *et al.*, 2009).

Okamura *et al.* (2008) reported late failures of two stents, a Cypher (Johnson & Johnson, Miami, FL, USA) sirolimus stent and a bare metal Multi-Link (Guidant Corp., USA) stent, after eight months of deployment in a 73 years old woman with history of hypertension, diabetes mellitus and hypercholesterolemia. Identified failures are associated with a 90% restenosis for the Cypher stent and a large eccentric saccular coronary aneurysm for the Multi-Link stent. Failure was identified as fracture of the stent at the location of maximum bending and tension of the artery. Choe *et al.* (2009) showed the case of a late Cypher (Cordis, Miami Lakes, FL, USA) stent fracture in a 72 years old woman after fifteen months of surgery, which might be the cause of a thrombosis. Kamura *et al.* (2008) presented a case of migration associated with stent fracture that occurred in six months after implantation in an 80 years old man with coronary risk factors, such as hypertention and diabetes mellitus, due to 90% of calcified restenosis. The stent implanted was a sirolimus eluting Cypher stent (Cordis, Miami Lakes, FL, USA) deployed at 22 atm. During follow-up check, it was observed that the stent migrated away from the site of calcification and only five struts were visible. Leong *et al.* (2008) reported a case of very late stent fracture that occurred three and half years after the surgery. Valibhoy *et al.* (2007) showed a 83 years old man who experienced a stroke due to a stenosis and was treated with a Xact (Abbott Laboratories, Abbott Park, Ill), a self-expandable Nitinol stent dilated to 5 mm. After three months of stent implantation, follow-up study reported a 60% restenosis, and after four months a 50% narrowing on the stent was confirmed due to 80% of restenosis. Furthermore a complete fracture was found through the waist of the stent. Adlakha *et al.* (2010) showed the case of a 56 years old man with ischemic cardiomyopathy status post bypass grafting, who was found with a 60-70% stenosis and treated with a serolimus eluting stent deployed at 18 atm for 18 s. Five months later, he was readmitted with unstable angina, and intravascular ultrasound showed a stent fracture without signs of restenosis.

These reports seem to suggest that the occurrence of stent failure is generally within the first 6 months of implantation. In one case (Kang *et al.*, 2007), stent failure happened even within days after the implantation. The fracture of stents can be attributed to defects developed during the manufacturing process or facilitated by the accumulation of high stresses on the stent struts during the expansion. For example, over expansion of the stent or overlapping of two or more devices, are some of the scenarios that can introduce high residual stresses on the struts of the device, which can affect its integrity and reduce the fatigue strength of the material. Furthermore, it is clear that the consequences of stent fracture can lead restenosis, thrombosis and angina according to case reports.

1.3.2 Statistics on Stent Treatment

Many clinical reports also offered statistical studies about stent failure. These studies provided percentage or frequency of occurrence of stent failure, based on the gathered clinical data. Kim *et al.* (2009) carried out a study involving 415 patients and showed a fracture frequency of 1.7% which includes cases of minor, moderate and severe fracture (according to the guidelines of American College of Cardiology-American Heart Association). Stent failure (Figure 1.6) ranging from 1% to 2% was also reported by Kandzari *et al.* (2009) and Lee *et al.* (2007). The former study involved 199 patients treated with serolimus eluting stents, and 2 patients (1%) were found with thrombosis due to stent fracture after 6-months of follow-up. The latter was based on a collection of 868 patients, and among those, after (14±9) months of deployment 366 patients underwent follow-up coronary angiography. From the follow up, 26 lesions were found, of which 10 also presented stent fracture (2.7%). Umeda *et al.* (2009) published a further stent fracture study that involved a total number of 422 patients, and 33 patients showed a stent fracture (7.7%) of which 4.2% were recognised as a complete fracture.

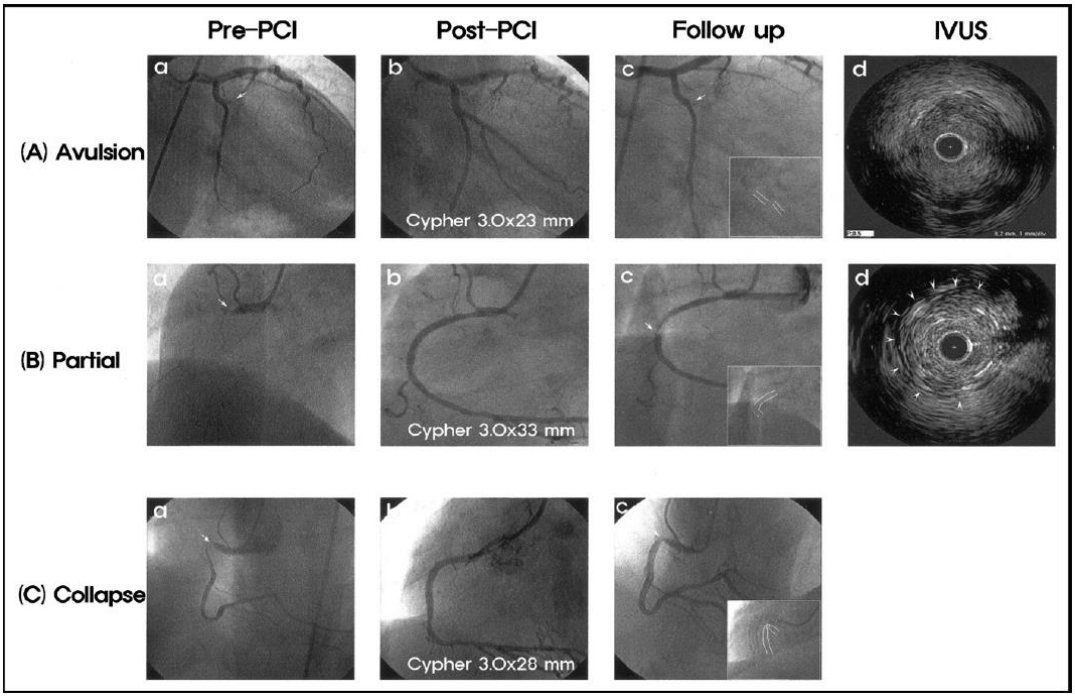

Figure 1.6. Examples of three different stent failures showed by Lee *et al.* (2007): (A) Avulsion, complete separation of the stent in two or more parts; (B) Partial, fracture of the scaffold without complete separation; (C) Collapse, narrowing of the stent diameter.

Peng *et al.* (2006) collected data from patients who underwent placement of bare metal stents in a pulmonary outflow conduit between 1990 and 2004. 270 stents were deployed in 241 conduits (214 Palmaz, 25 Genesis and 31 non pre-mounted Genesis), with multiple overlapping or serial stents placed in 28 conduits, and with one conduit stented three times. One stent deployment was unsuccessful due to entrapment of the front loaded stent in the tricuspid valve during advancement through the right ventricle. The length of the stents varied between 10 mm and 30 mm and their expanded diameter was between 5.5 mm and 26 mm. The echocardiographic data showed that 29 of 221 (13%) patients had moderate-severe Right Ventricle (RV) dysfunction, 18 (8%) had moderate-severe Tricuspid Regurgitation (TR) and 162 of 210 (77%) had moderate-severe Pulmonary Regurgitation (PR). During stenting procedure, there were no deaths, strokes,

myocardial infarction, cardiac perforations or damage to the conduit that required surgery. But 1% of the patients required a stent removal surgery due to stent malposition, whilst in 2.1% patients malposition of the stent was found which required an additional stent for the treatment. Also, in 6 patients crack and tear of the conduit was found due to the stent placement, which did not require surgery. However, within the follow-up period there were 9 deaths and 3 heart transplantation, in a mean of 1.6 years after conduit stenting. The hemodynamic study showed moderate RV dysfunction for 29 patients, moderate-severe TR for 18 patients and less-moderate PR for 48 patients. Among all the patients, 87 underwent repeat balloon dilation (100 cycles) of the stented conduit, whilst 41 had additional conduit stents placed. A total of 146 patients underwent surgical reintervention on the RV-PA conduit. Stent was replaced in 108 patients and augmented with a patch in the rest 38 ones. Stent fracture occurred in 56 patients, these included 54 (out of 126) who underwent repeat catheterization during follow up and 2 (out of 63) patients who underwent conduit surgery without preceding follow up catheterization. Also, 50 stent fractures occurred immediately behind the sternum or chest wall, due to the compression between the chest wall and heart.

Qureshi *et al.* (2007) provided a review of a large series of stenting procedures for the treatment of aortic carctation. The database relating to their cardiovascular programme was gathered from queries of patients who underwent implantation of an aortic stent between December 1989 and July 2005. A total of 153 patients had been subjected to the study and 16 of them presented multiple stents. This database included the implantation of 123 Palmaz large or XL stents (Cordis, Warren, NJ, USA) and 41 Palmaz Genesis XD stents (Cordis Endovascular Miami, FL, USA). Their results showed the haemodynamics and diameters of the coarctation prior to and after dilation. After stenting, a residual obstruction was found in 7 patients (5%) at a pressure gradient of at least 20 mmHg, while 16 patients (10%) were found with a residual obstruction at a pressure of 15 mmHg. Diffuse or complex obstruction of the transverse aortic arch were found in 7 patients

(out of 16), while 29 (out of 139) patients showed other types of obstruction. Angiography demonstrated pre-existing aneurysms in 19 patients (12%), 16 of whom underwent prior interventions to the aortic arch. In 13 patients (8.5%), complete jailed artery was identified, while 11 (7.2%) patients had partial jailing in subclavian arteries or common carotid arteries. In addition, separate jailing of the vertebral artery was found in another patient. Therefore, jailing occurred in 24 patients (16%), and in 10 cases stents were modified after implantation. Acute adverse events occurred in 3 patients (1.9%) and 2 patients (1.3%) died from complications of pre-existing cardiac disease.

Recently, stent angioplasty has been also associated with the increase of artery perforation (Al-Mukhaini *et al.*, 2011), which can be caused by the guidewires, the angioplasty balloons or the stent itself. Artery perforation is a life-threatening condition that can be classified into three types: Grade I, extraluminar crater, Grade II, myocardial or pericardial blushing, and Grade III, contrast streaming or cavity spilling. A study involving 72 artery perforations caused by stent PCI (Javaid *et al.*, 2006) showed that Grade I perforations are mostly caused by the angioplasty catheter, whilst angioplasty balloon and stents are connected mainly to Grade II and Grade III lesions. Yıldız *et al.* (2013) showed that out of 7452 patients that underwent PCI, 17 (0.2%) exhibited artery perforation which was caused by the stenting procedure. Consistently with previous reports, Grade I perforations were caused by the guidewire and grade II and III by the balloon and stent. In total, the incidence of Grade I perforations caused by stent PCIs is 16.7% for Javaid *et al.* (2006) and 23.5% according to Yıldız *et al.* (2013), for Grade II perforations it was 54.2% and 47.1% respectively for the two studies, and for Grade III the incidence was 29.1% and 29.4%.

The main complications caused by stenting includes stent fracture, stent collapse and arterial damage. Partial fracture of stents had an occurrence of up to 8% and can potentially happen on the stent struts during the deployment procedure, leading to complete fracture later after the procedure. On the other hand, arterial perforation can also be a major complication caused by

stent treatment. Most severe cases of perforation were attributed to the stents themselves, suggesting that damage to the arterial tissue can develop during the stent deployment. For a better understanding of these problems, it is important to study the mechanical deformation involved in the stent deployment which has a direct connection with stent failure, stent collapse and tissue damage.

1.3.3 Post-deployment studies

Clinical studies were also performed to assess the effectiveness of stent treatment, including stent design, failure and restenosis. Serruys *et al.* (1991) assessed the early morphologic changes in stenosis geometry, including the recoil, by quantitative angiography. They also calculated the blood pressure drop across the stenosis. Fifty patients were studied before and immediately after implantation. Stent implantation resulted in an additional increment in the minimal luminal cross-sectional area and minimal luminal diameter, without changing the curvature of the stenosis. Recoil of 0.1±0.36 mm was observed after stent implantation. Celik *et al.* (2009) identified some of the relationship between stent geometries and the occurrence of fracture. Open cell designs, with varied size and shape along the stent, provide flexibility to avoid fracture, although the individual cell may open excessively on the outer side when implanted in a curved segment. While closed cell designs, typically with repeating unicellular element, provides more uniform wall coverage with lower tendency to prolapse, but they also tend to straighten the vessel with an increased chance of stent fracture.

Rosenfield *et al.* (1997) studied the occurrence of restenosis in vascular segments subjected to unfavourable extrinsic (external compression) or intrinsic (elastic recoil) mechanical forces. Intravascular ultrasound examination measured the lumen dimension (both minor and major), cross sectional area and uniformity index, defined as the ratio between the minor and major lumen

diameter, for each lesion site. The uniformity index immediately after initial stent deployment was 0.89±0.25, indicating nearly concentric geometry and uniform expansion. In contrast, the ratio of minor to major lumen dimension felt to 0.37±0.35 during the initial episode of restenosis, indicating eccentric stent compression. Fluoroscopic and angiographic of dialysis conduits showed that the percentage of stenosis was 75±5% before intervention and after initial stent deployment, the lumen diameter was typically greater than that of the reference site. During the first episode of restenosis, lumen narrowing increased 48±5%, but improved to 14±4% after repeat dilation. During the second episode of restenosis, lumen diameter narrowing was 87±4% and four vessels were re-dilated with the residual narrowing of 4±5%.

The deployment of stents within human vessels significantly modify the morphology of the arterial branch, along with the hemodynamic and blood pressure. The geometrical features of the device also influence the uniformity of the stent expansion. In particular, open cell stents tend to adapt to the arterial branch, reducing the likeliness of stent fracture. Also, post-stenting restenosis can be treated by a second expansion of the stent, however this does not prevent subsequent episodes of arterial narrowing due to the persistent restenosis. In fact, from these studies it appears that a second event of restenosis after the first re-dilation are also consistently more aggravated, suggesting that the treatment by re-dilation can be considered only as a temporary solution.

The prevention of restenosis is a major aspect of stent research. In fact, restenosis is a complication that can be influenced by stent design, which can change the stresses developed on the plaque during implantation. This is directly linked to one of the main objectives of this thesis, i.e. to study how the stresses developed on the stenosis are affected by different stent designs and materials (Section 1.3).

1.4. Experimental Work

1.4.1 Stent Deformation

A large body of experimental work has been carried out to study deformation, fatigue and biomechanical behaviour of stents. Some of the experiments have been carried out in a simulated body environment, such as Nam *et al.* (2009) who studied stent deformation using SS316L specimens with and without Si-incorporated diamond-like carbon (Si-DLC) coating. Slow strain rate and constant load tests were carried out in simulated body environment, with the entire gauge length of the specimen immersed in saline solution (0.89 wt.%) at 37°C Results showed that the coated steel is more ductile and less susceptible to fracture than the uncoated one. Zhou and Dong (2005) studied the dynamic deformation of stents, where a microscopic series of photos were used to obtain the deformation of the sample. In addition, they also studied the recoiling of the artery after expansion by 11 metal stents. Results showed the radius-thickness ratio is a major and important factor for the initial imperfections, which tend to reduce the buckling strength of stents. A multi buckling phenomena was found to depend on both material and geometrical features. So if the structure is designed and constructed with sudden change of local stiffness, multi buckling phenomena is more likely to appear.

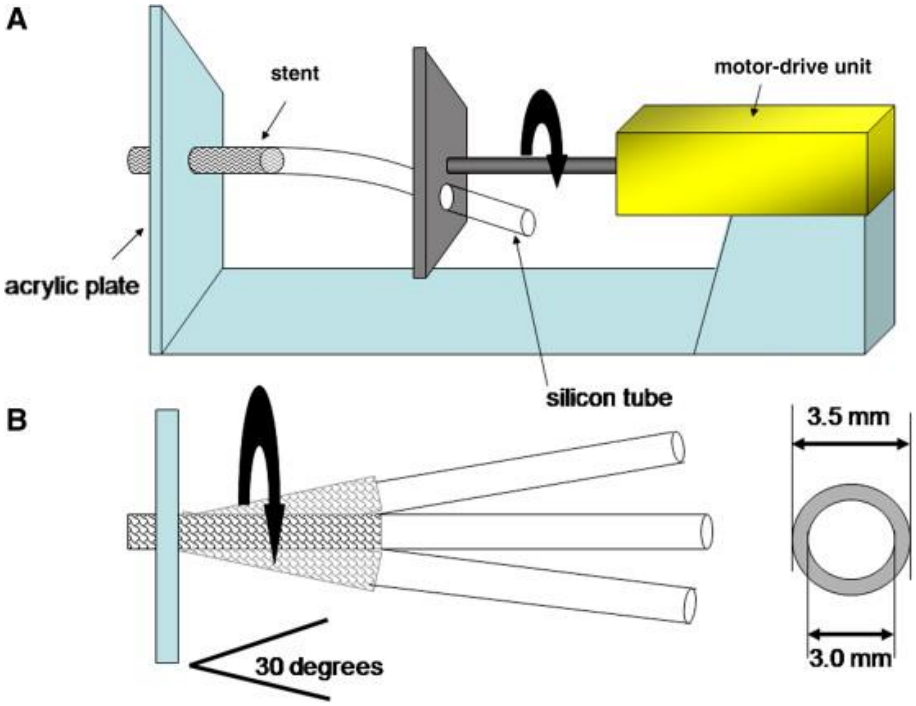

Figure 1.7. Illustration of the experimental coronary ostium setup used in Tsunoda *et al.* (2009).

Tsunoda *et al.* (2009) constructed an experimental coronary ostium setup which used an acrylic plate as aortic wall and a silicon tube as coronary artery. The proximal end of the tube was attached to the acrylic plate with clips, and the distal end was connected to a motor drive unit that continuously rotated the end of the artificial artery as shown in Figure 1.7. Using the setup, the study investigated the deformation of three kinds of coronary stents, the Cypher (John- son & Johnson, Miami Lakes, FL, USA), Express^2 (Boston scientific, Mountain View, CA, USA) and Tsunami (Terumo, Japan). Statistical study of the results was performed using analysis of variance (ANOVA) and post hoc Scheffe's test, a statistical method used for multiple comparisons in which the sample sizes are unequal. Results showed that Tsunami was the stent with the largest cross sectional area (>8 mm^2), compared to Cypher (7-7.5 mm^2) and Express^2 (7-8 mm^2). Recoiling was observed for the Cypher and Express^2 after the deployment and under external deformation, whilst

only a minimal decrease of the area was observed for the Tsunami. Also, one of the Cypher stents fractured after 3 minutes of exposure to external load.

The deformation of stents after implantation in coronary bifurcation was studied by Vassilev and Giv (2008). The experimental setup consisted of an elastic wall model in which the main branch had a diameter of 3.5 mm and the side branches had a diameter of 3.5 mm and 2.75 mm, respectively. Deployment of Chopin 2 (Balton, Warsaw, Poland) stents was performed inside the artificial vessels, followed by balloon redilation and kissing balloon (with two overlapping balloons) inflations. Results of the stent deployment showed that the general cross-sectional shape of the proximal portion was elliptical, while in the distal portion the shape was circular. Generally, balloon redilation led to lateral displacement and opening of stent cell, in both the proximal and distal portions. However, there was always a distance between stent struts and the adjacent wall of the vessel branches. This strut-wall distance was considerably reduced by using kissing balloon inflation. Another mechanism of stent deformation after deployment was studied by Pitney *et al.* (2011), by analysing the deformation and fracture of stents caused by post-dilation balloon catching. The phenomenon was observed when using non-compliant balloon for post stenting redilation. Basically, one or more stent struts were "catched" and deformed by the balloon during redilation (Figure 1.8). For this study, both clinical and bench tests were performed. In the clinical study, a number of 775 stents were considered with the attempt of post-dilation, whilst in the bench test, 7 crown stents were deployed within a clear vinyl tube (with pressures 12, 16 or 20 atm). Results showed that 14 out of 775 stents exhibited separation after post-stenting redilation, which was caused by balloon catching. On the other hand, during the bench test 50% of the cases showed balloon catch when provocative manoeuvres were used (such as using stiffer wires for the balloon and bending or change in aspect ratio of the stent), this incidence reduced to 20% when provocative manoeuvres were not applied.

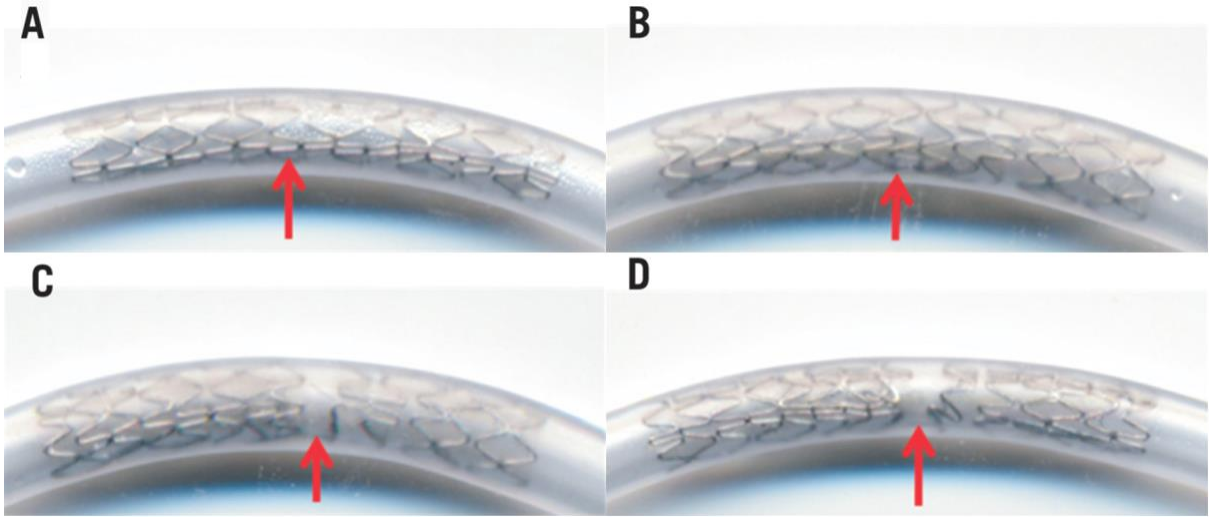

Figure 1.8. Stages of stent deformation (A and B) and fracture (C and D) caused by post-dilation balloon catch.

1.4.2 Fatigue and Failure Studies

An important feature of stent devices is the resistance to fatigue damage and fracture, which is also suggested by the clinical studies (Section 2.2). An experimental study made by Bourauel *et al.* (2008) investigated the number of cycles required to induce fracture of NiTi archwires (Figure 1.9). The specimens were tested using a setup that can simulate cyclic deflections up to 5 mm. Their results showed that the specimens of the as-received round wires, with cross-sectional diameter of 0.30 mm and 0.35 mm, survived 2×10^6 loading cycles under a deflection of 2.0 mm. The 0.40 mm-diameter wires fractured after 150,000 loading cycles, even at a low deflection of 1.5 mm. Ring *et al.* (2006) studied the fatigue properties of four different commercial available stents using two different in vitro setups which could simulate loading conditions involving bending and pulsating mechanical strain, respectively. After the bending fatigue test, grain boundaries were outlined and slip lines were found on the surface of the stent struts, along with increased roughness and the

formation of pits. For Co-Cr alloy stents, the slip lines and roughness were reduced when compared to Stainless Steel. Stent expansion in the vessel model was found as the main contributor to the formation of slip lines and metamorphosis of the microstructure. While, the fatigue tests under pulsating mechanical strain did not introduce more roughness and slip lines on the material.

Gorman *et al.* (1997) ran both in-vitro and ex-vivo tests to investigate the mechanical performance of polyurethane ureteral stents. The ex-vivo study was carried out for stents retrieved from 17 selected patients, while the in-vitro tensile test was performed on stents immersed in poled healthy human or artificial urine. Their results indicated that the polyurethane stents did not show any greater tendency to fracture compared to the Stainless Steel 316L counterparts. Grewe *et al.* (2000) studied the morphological changes for a Palmaz-Schatz stent caused by high inflation pressures using three different methods, with the pressure varied between 5 atm and 20 atm. Results showed that the expansion was negatively influenced by calcifications of the vessel wall at all pressures. Also the stents implanted with pressure in the range 10-20 atm had a significantly higher cross sectional areas, when compared to stents expanded at 5 atm of pressure. However, no significant difference was found between expansions at pressures of 15 atm and 20 atm. Failure analysis was performed by Shih *et al.* (2005) through studying explanted stainless steel sternal wires, which are used as standard procedure for closure of sternotomy incisions. The work showed possibilities of surgical mistakes that cause the wires to be over twisted during closure of median sternotomy. Moreover, a majority of cases showed corrosion pits and transgranular cracks, which extended from the surface to the middle of the wires' cross sections. Also, crack branching was observed inside the twisted areas. Möller *et al.* (2001) studied the residual stress introduced during dilatation in order to gain a reliable fail-safe criteria for stent design. Results showed that the inhomogeneity of the plastic deformation increases with the degree of dilation, which is also the case for the residual micro stress presented at microstructure level (e.g. grain level).

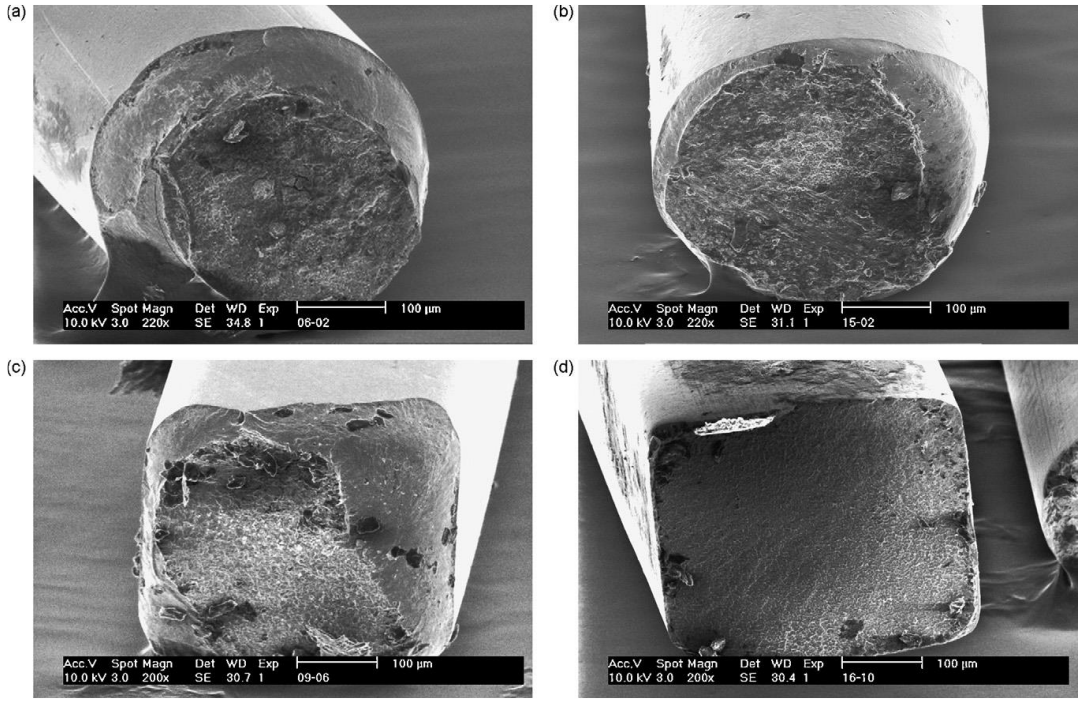

Figure 1.9. Scanning electron micrographs of the fracture surfaces of Nitinol stents (Bourauel *et al.*, 2008).

These studies show that fatigue fracture of stents can be associated with both design factors, such as the strut thickness, and environmental factors, such as the plaque composition and the deployment process. While increasing the strut thickness of the stent improves the fatigue strength of the device, excessive dilation of the stent during the expansion can lead to the formation of high residual micro-stresses, which facilitate the stent fracture. Also, the calcification of the tissues negatively affects the expansion and the strength of the stent.

1.4.3 Comparative Studies of Stent Performance

Experimental studies have also been carried out to compare the performance between commercially available stents in terms of radial stiffness and flexibility. Smouse *et al.* (2005)

evaluated the change of biomechanical behaviour of stented vessel system during limb movements like walking, running and sitting using seven human cadavers (a total of fourteen limbs). Their results showed that stenting affected the stiffness of the artery by increasing its rigidity and also made the blood vessels become shorter. A comparative study between stent designs was performed by Schmitz *et al.* (1999) for five different commercially available coronary stents. They analysed the longitudinal flexibility, the radial stiffness, the foreshortening and the elastic recoil. The experiments showed that the slotted tube stents have a higher bending stiffness than the single wire coil. The NIR Primo stent showed a considerably higher stiffness than all others, with a value of 165 Nmm^2. The RX Multilink has the second highest stiffness with a value of 21.50 Nmm^2 while the Wiktor has the lowest stiffness with a value of 0.73 Nmm^2. The collapse pressure, related to the radial stiffness, was also considerably high for the NIR Primo, which has a value greater than 1.5 bar. The RX Multilink has the second highest collapse pressure with a value of 0.8 bar while the Tenax Complete has the lowest collapse pressure with a value of 0.5 bar. The Wiktor has the highest recoil effect (6.04%), followed by the Freedom Force (4.05%). NIR Primo has the lowest recoil effect (2.83%).

An in-vitro study of the flexibility and deformation was performed by Flueckiger *et al.* (1994) for stents subjected to distributed loads, point loads and loads applied on circular surfaces. They monitored the resistance of the stents to deformation under the increasing load. In this case, the Palmaz-Schatz, Cragg and Gianturco stents had no change of their resistance to deformation when coated in foil, while the Wallstent and the Strecker showed significantly higher resistance to deformation when coated. Lossef *et al.* (1994) studied the mechanical deformation of Palmaz-Schatz, Wallstent and Strecker stents using an in-vitro setup to simulate forces exerted by eccentric lesion. A modified version of the Wallstent was also included in the study, which is obtained by a reduction of the braiding angle from 140° to 104° in order to achieve less shortening and more

flexibility upon stent expansion. The results showed that there is a 21-fold difference in the elastic modulus among the Wallstent, Palmaz-Schatz and Streker stents. The Palmaz-Schatz was the only device showing permanent plastic deformation, and the 10 mm stent underwent 15% focal eccentric narrowing at 0.75 atm pressure. The standard braid and modified braid 10 mm-Wallstents underwent narrowing at a pressure of 0.55 atm and 0.25 atm, respectively, while the 10mm-Strecker stent narrowed at 0.08 atm pressure. Overlapping of stent doubles the stiffness of the Wallstent and the Strecker stent and the yield stress of the Palmaz-Schatz stent. The 4-9 mm version of Palmaz-Schatz stent was 30% more resistant than the 8-12mm version when expanded to an identical diameter of 8 mm.

Stent longitudinal strength was studied by Ormiston (2011) for 7 different stents, i.e. Cypher Select (Cordis), Liberte (Boston Scientific), Vision (Abbott Vascular), MultiLink 8 (Abbott Vascular), Driver (Medtronic), Integrity (Medtronic) and Omega (Boston Scientific). An Instron universal testing machine was used to test the force required to compress or elongate the stents more than 5 mm. Results showed that for the Omega and Driver stents compression of 5 mm was achieved by forces of 0.4 N and 0.7 N respectively. For all other stents, the force applied varied between a magnitude of 1.08 N and 1.12 N. For elongation of 5 mm, Driver stent required a force of only 0.4 N, while the Omega required 0.7 N. Liberte and Integrity required 0.8 N to elongate 5 mm, Vision and MultiLink stents achieved the elongation with respectively 1.32 N and 1.34 N. The Cypher Select was found to be the stiffest, requiring a force of 5.7 N to reach the desired elongation. In a more recent study, Ormiston *et al.* (2013) studied the longitudinal strength after deployment of stents in a silicone phantom vessel, using point compression. In this case, the stents studied were the Vision (Abbott Vascular), the MultiLink 8 (Abbott Vascular), the Biomatrix Flex (Biosensors), the Integrity (Medtronic), the Element (Boston Scientific) and the Promeus Premier (Boston Scientific). Stents were deployed in a silicone phantom vessel and a probe was used to compress the stent in the longitudinal direction by applying a displacement of 4 mm to one end

of the stents. Results showed that Element stent was the weakest, requiring only 0.4 N to reach a compression of 4 mm. Vision stent reached the desired compression with application of 0.6 N, whilst MultiLink and Premier required a force of around 0.7 N. The stiffest stents were the Integrity and Biomatrix Fles, showing compression of 4 mm under a force of 0.8 N and 0.9 N, respectively.

These experimental studies compared the mechanical behaviour of different stent designs, aiming to especially longitudinal and radial flexibility, and established a connection between the biomechanical behaviour of the devices and their geometries. In is also demonstrated that a small modification of stent design can improve the flexibility of the device in both longitudinal and radial directions.

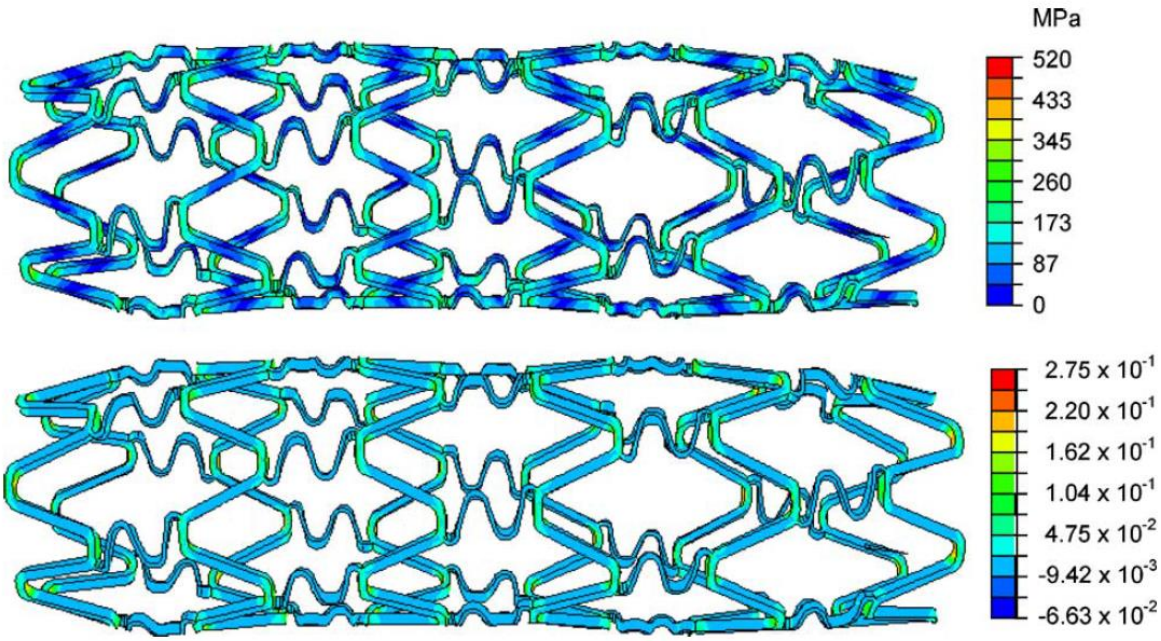

Figure 1.10. Stress distribution (top) and equivalent plastic deformation (bottom) on a Cypher stent after expansion according to Migliavacca *et al.* (2005).

1.5. Computational Analyses

1.5.1 Free Expansion of Stents

Computational analyses has been widely employed to study the mechanical behaviour of stents, aiming to investigate the deformation of a stent during the deployment, particularly the recoiling and dogboning effects. These are the major effects that occur during stent deployment, which determine the efficacy of a stent in terms of diameter of expansion and coverage. Recoiling refers to a reduction of the stent diameter due to the resistance of the arterial wall, and it happens during the balloon deflation following the stent expansion. Dogboning, on the other hand, occur during the expansion and refers to the unequal expansion for stent ends and the middle section. Dogboning and recoiling effects are defined by Migliavacca *et al.* (2005), by means of the following equations:

$$Dogboning\% = \frac{(d_e - d_m)}{d_m} \times 100\% \qquad (1.1)$$

where d_e is the mean diameter at the ends of the stent and d_m the diameter in the middle of the stent after deflation.

$$Recoiling\% = \frac{(d_0 - d_1)}{d_0} \times 100\% \qquad (2.2)$$

where d_0 is the diameter in the middle of the stent at maximum pressure and d_1 is the diameter in the middle of the stent after deflation.

In the worst case, dogboning can cause high levels of stress on the vessel walls, resulting in damage of the tissue. Migliavacca *et al.* (2005) used finite element (FE) analysis to study the expansion of coronary stent Cordis BX Velocity in order to examine the distal and central radial recoil, the longitudinal recoil, the forshortening and the dogboning effects. The simulation was compared with experimental measurement of stent expansion using an optical extensometer. The inflating

pressure was 1.2 MPa, equal for both experiment and simulation. Results showed that similar stent expansion, with a diameter of 3.5 mm, were obtained at a pressure of 0.5 MPa for simulation and experiment. For the simulation, the stent continued to expand until it reached a diameter of 5.5 mm at 1.2 MPa. On the other hand, the experimental expansion rate decreased after 0.5 MPa and showed a diameter of 4 mm at 1.2 MPa. This difference was due to the neglecting of balloon in the simulation. Elastic recoil was calculated for the middle position of the stent after expansion at a pressure of 0.5 MPa. The experimentally determined recoil was 1.1%, while the simulated recoil was 1.2%. Also, in their work, both experiment and simulation show high plastic deformation at the U-bends of the sinusoidal struts (Figure 1.10).

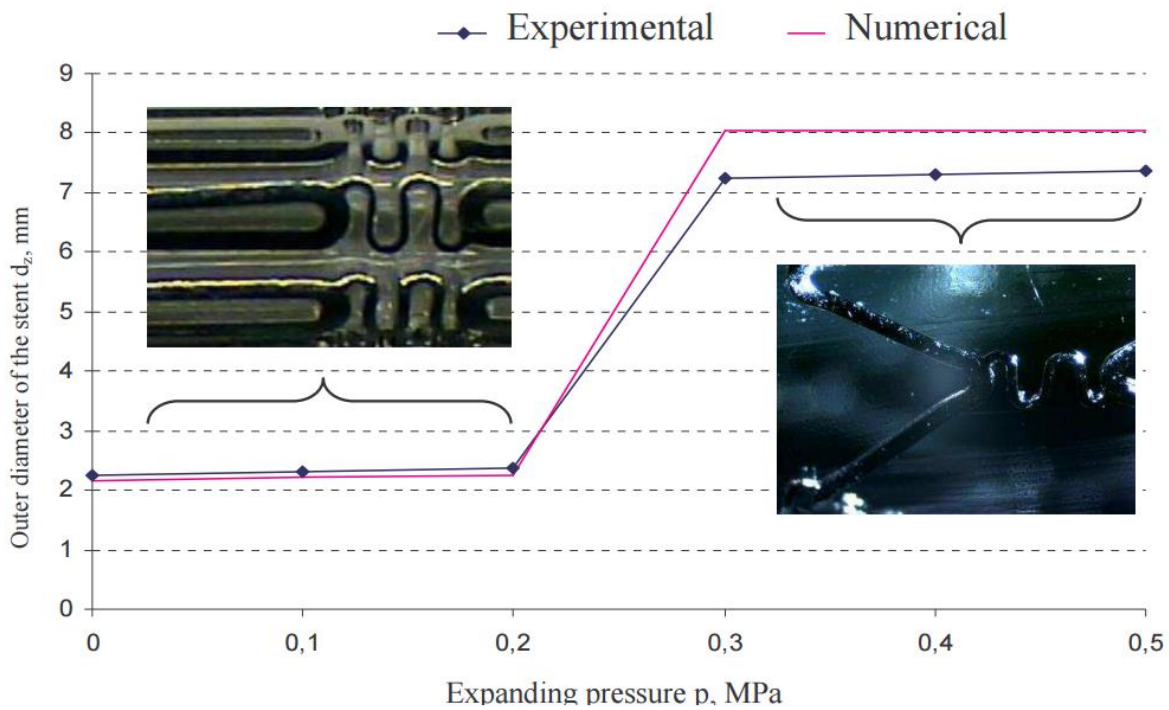

Figure 1.11. Expansion of Genesis stent studied by Walke *et al.* (2005), comparison between the experimental results (with images) and numerical expansion.

A study of a Genesis stent made of stainless steel was performed by Walke *et al.* (2005) using both experimental and computational methods, aiming to determine the diameter as a function of the pressure. The experimental results showed that the process of the stent enlargement is not proportional to the pressure inside the balloon (Figure 1.11). A sudden increase of the stent diameter was observed after exceeding a critical value of the balloon pressure. FE analysis showed a very good agreement with the experimental data and the increment used for numerical analyses (0.002MPa) was small enough to determine the pressure responsible for the sudden increase of the diameter. McGarry *et al.* (2004) used crystal plasticity theory to study the mechanical performances of a cardiovascular stent made of stainless steel. Additional models based on J_2 flow theory of plasticity were also considered, which accounted for the non-uniform deformation of polycrystalline metals. Results of the study showed that stent recoiling obtained from crystal plasticity model with different sets of random grain orientations were consistently lower than that for the J_2 flow model, with a value of 1.27% for the former and 2.92% for the latter. The crystal plasticity model in this case gave more realistic results, although still considerably higher than that quoted for the NIR stent by Richter *et al.* (2000) which was less than 1.00%. These work shows that FE analyses can be applied to predict stent expansion, however for a good correlation between experiment and computational simulation, the angioplasty balloon needs to be included in the simulation and also the material behaviour needs to be modelled properly.

Along this line, Chua *et al.* (2003) carried out FE analysis of a Palmaz-Schatz stent expansion with a rubber balloon. The stent had a slotted tube design and due to its symmetry only one quarter was modelled, with a cylindrical hyperelastic balloon placed within the stent and inflated with pressure. The diameter was measured by monitoring the radial displacements of the nodes, located in the midsection of the stent. At the beginning of the expansion, slipping movements between stent and balloon were observed due to the increased friction and interaction. At about 0.25 ms, the stress began to stabilize after passing the yield point of the material. During the process of

stent expansion, some parts of the stent were highly stressed beyond the yielding point, such as the four inner corners of each slot, the bridging struts and the middle portion of the slot. To study the stent-balloon interaction, Ju *et al.* (2008) used three different FE models to simulate expansion of a Palmaz-Schatz stent: the panel model, the repeated unit cell (RUC) model and the repeated unit cell with a free end (RUC+) model. The results showed that the RUC model gave similar expansion (4.8 mm in diameter) and von Mises stress (286 MPa) compared to those (diameter of 4.6 mm and von Mises stress of 286 MPa) in Chua *et al.* (2003). It was also noted that RUC gave very good prediction of deformation for the middle section of the stent but failed in predicting the deformation for the stent ends, while the RUC+ method can provide good predictions for both inner and distal segments.

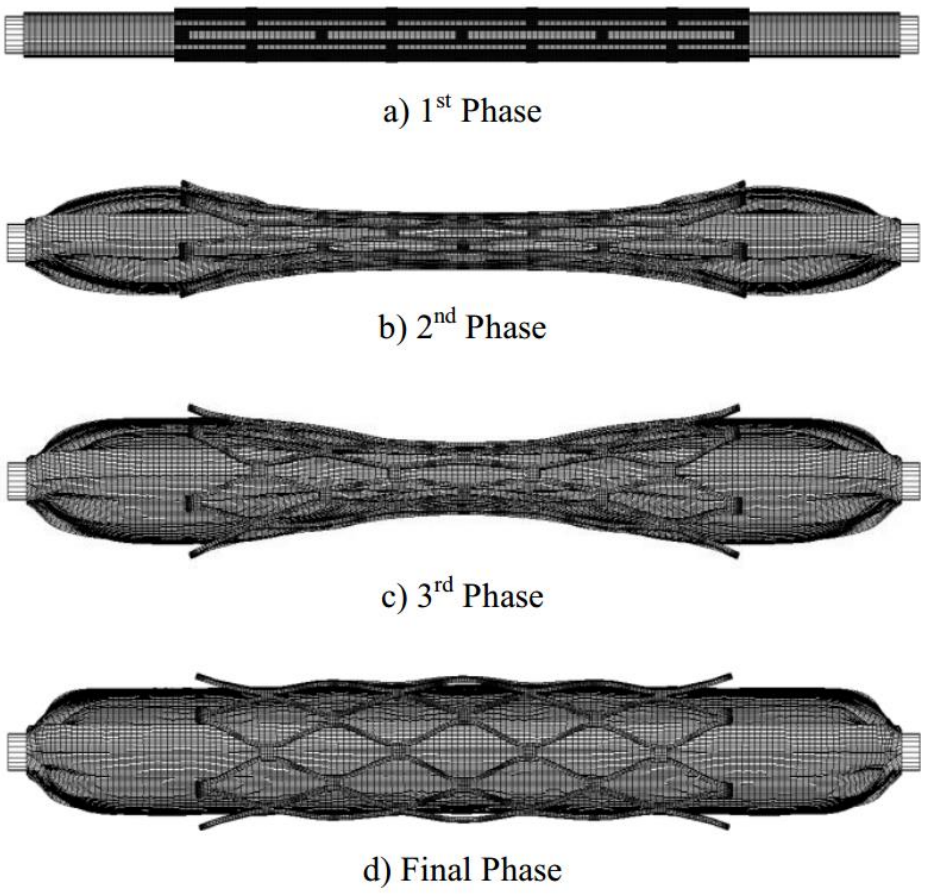

Figure 1.12. Expansion of a Palmaz-Schatz stent by balloon inflation (Park *et al.*, 2008).

Tan *et al.* (2001) simulated the expansion of a Freedom Stent design and a Palmaz-Schatz stent. The freedom design consisted of a series of paraboloidal loops arranged into a helical form, while the Palmaz-Schatz is a slotted tube design. Simulated results showed a limited radial expansion for the Freedom geometry, but with an increased flexibility compared to the Palmaz-Schatz. Park *et al.* (2008) carried out further studies of the expansion of 7 stents, i.e. Palmaz-Schatz, Tenax, Coroflex, MAC Standard, MAC Q23, MAC Plus and RX Ultra, Multi-Link. The simulation of the expansion was carried out using a realistic polypropylene balloon modelled by hydrostatic fluid element. The balloon-stent expansion was simulated by controlling the features of the hydrostatic fluid elements. A pneumatic flow at 1 atm and surgical room temperature was used for the stent, with an amplitude option that allowed arbitrary time variations of the amount of fluid mass (flow rate) to be supplied throughout the simulation. A fluid flux option was used to specify changes in the fluid mass of the fluid-filled cavity modelled by the hydrostatic fluid elements, and the balloon-stent expansion was controlled by a change in the amount of fluid mass. The simulated process of expansion is shown in Figure 1.12. The simulation calculated the bending stiffness, radial stiffness, longitudinal recoil, foreshortening, radial recoil, dogboning, coverage area and target life. The results showed that almost all the stents had similar expansion patterns, except for the Palmaz-Schatz PS153. The Tenax was excellent in flexibility and coverage area, while the MAC standard was excellent in radial stiffness, foreshortening and both longitudinal and radial recoil. The Palmaz-Schatz was excellent in fatigue durability but with improper flexibility. From these simulations, it is clear that FE analysis can be used as an effective tool to compare the biomechanical behaviour of different stent designs during expansion. The stress analyses of Palmaz-Schatz stent showed that the stress is not equally distributed through the longitudinal direction due to dogboning. Results also confirmed that increased radial stiffness also led to higher fatigue strength. Although slotted tube designs (i.e. Palmaz-Schatz) have high strength and radial stiffness, they considerably lack longitudinal flexibility.

Two stent designs were studied by Etave *et al.* (2001), a Palmaz-Schatz PS154 model, which is a tubular stent, and a Freedom model, which is a coil stent. Each stent was modelled with two different lengths in order to investigate the effect of these dimensions on the stent's mechanical properties. The results showed that the pressure required for the deployment of coil stent was significantly lower (0.71 atm) than that of the tubular stent (2.10 atm). The tubular stent with longer length showed an interesting phenomenon, such as when the deployment diameter exceeded 4.5 mm, the pressure suddenly began to increase and reached 8 atm at a diameter of 5 mm. The elastic recoil for the tubular stents varied between 5.4% and 7% for the first design (shorter one) and between 3.7% and 4.1% for the second design (longer one). While for the coil stents, the recoil was in the range from 2.6% to 6.3% for the first type of design and from 6.3% to 12.8% for the second type of design. This difference is due to the fact that the height of the first coil stent design's sinusoids is one-half of that for the second design. The stent's resistance to compressive pressure is dependent on the deployment diameter. The tubular stent could be deformed by 10% at pressures between 0.7 atm and 1.3 atm for the first type of design, and between 8.5 atm and 20 atm for the second type of design. Lower deployment pressures were required for the coil stents, about 0.7 atm for the first design and 0.2 atm for the second one. The shortening was up to 8% (second design) or 11% (first design) for the tubular designs, while the coil stents had a shortening up to 8% (second design) or 27% (first design). The contact area of the tubular stents was 24% for the first design and 48% for the second design, while for the coil stents, the contact area was 8.75% for the first design and 17.5% for the second design. FE Methods have also been used to study stent flexibility, which is one of the major requirements for optimal stent performance. Wu *et al.* (2007a) analysed a Nirflex design longitudinal flexibility. The simulation included two models. The first model considered the bending of a single unit whilst the second one subjected the whole stent to two equal and opposite moments at each end (resulted in an S-shaped stent after deformation). Results showed that during the bending of a single unit, the deformation is localised

in just one of the two struts. For the whole stent, the middle part of the S-shaped stent experienced less deformation, which was expected as the load was applied only at the ends of the stent. These results confirmed the correlation between stent design and biomechanical behaviour, including the effect of stent length.

1.5.2 Simulations of Stented Vessel Systems

One of the most challenging issues in finite element modelling of stent is the description of human tissue behaviour. The simulations performed so far used simplified constitutive models for the material properties of the human blood vessels, as well as more sophisticated ones. The blood vessel is often described using hyperelastic strain energy potentials, and its geometry is often assumed as cylindrical or obtained from a digital image. As the thickness, shape and composition of an artery, for both healthy and diseased ones, are variable and human specific, the results will inevitably have limitations even if realistic artery geometry is considered in the model.

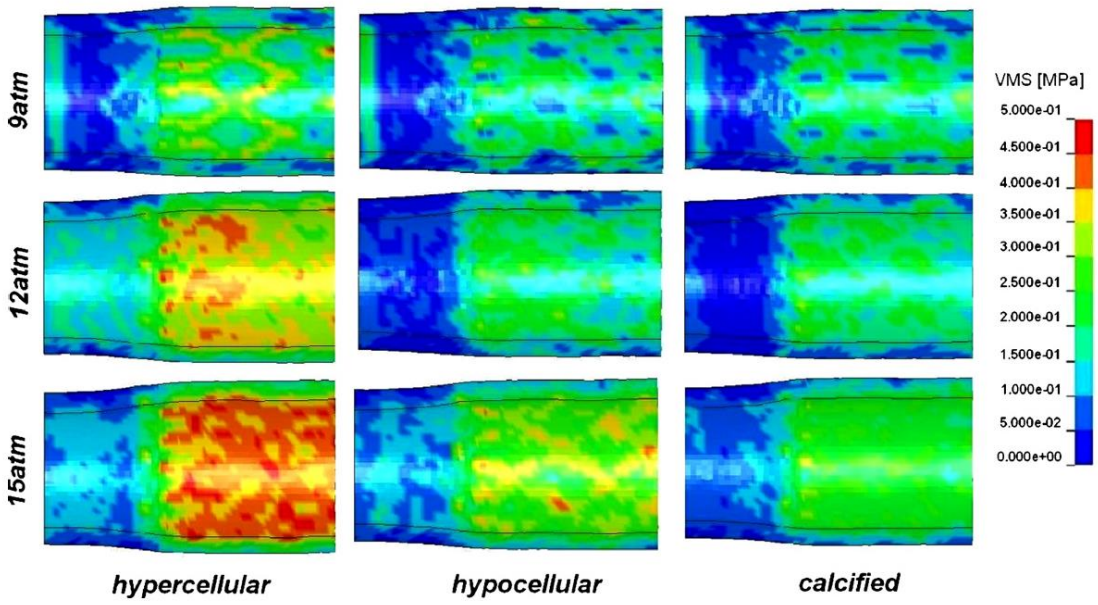

Figure 1.13. Stress contour plot in arteries with different plaque compositions for three different inflating pressures as presented in Pericevic *et al.* (2009).

Pericevic *et al.* (2009) investigated the influence of plaque composition on stent deployment by considering three different plaques, i.e., cellular plaque, hypocellular and calcified plaque. The work modelled the process of stent deployment in an artery with different plaque composition models. Results showed that the level of maximum stress depends on the type of plaque. The hypercellular plaque had higher stress level while the calcified had reduced stress level (Figure 1.13). Hamid *et al.* (1985) evaluated the influence of stent flexibility on the magnitude and distribution of stress on the closed leaflets of a porcine bioprosthetic valve using large deformation FE analysis. The leaflets were assumed symmetrical and equal in size, with uniform thickness and isotropic and homogeneous material behaviour. Results showed that flexible stents caused much lower magnitude of stress for most parts of the leaflet. A simulation of the expansion of a Palmaz-Schatz stent within a diseased artery was performed by Chua *et al.* (2004a). The artery was modelled as a simple cylindrical tube with symmetric plaque. Both artery and plaque are treated as elastic materials with different properties. Results showed that the most prominent deformation occurred at the ends of the stent, and the maximum stress was located at the inner corners of struts (which is typical for this design) as well as in the middle part of the slots. Pujari and Udupi (2009) simulated the expansion of a balloon-dilated stent and its interaction with the blood vessel and the plaque using Ansys. In this case, the vessel and the plaque were characterized by linear isotropic and nearly incompressible materials. In this simulation, the maximum stress was found to be located at the corners of the struts and the minimum stress in the middle of the struts, which is not affected by the inclusion of the vessel and plaque. In the stented vessel, a maximum stress occurred near the edge of the plaque, where also the plaque fracture tended to happen. The stenting caused an increase of the stress level by 5.4% and 5.1% on the inner and outer surfaces of the artery-plaque system, respectively. The effect of stent strut thickness on the deployment process of stent was shown by Zahedmanesh *et al.* (2009). ACS MultiLink RX and ACS MultiLink RX Duet stents were modelled and expanded within an artery with stenosis by direct application of pressure on the

inner surface of the stents. The strut thicknesses of the stents were 50 μm and 140 μm, respectively for the MultiLink RX and MultiLink RX Duet. Results showed that thinner stent strut thickness induce lower stress levels over the atherosclerotic blood vessel. The high residual stresses induced in the vessel after unloading may act as a chronic stimulus for cell proliferation, caused by the regeneration and thickening of the arterial tissue. These studies show that stent designs and arterial tissues are equally important in the study of stent performance. The stress distribution on the artery is affected by both plaque calcification and the stent stiffness. Previous studies (Sections 2.4.1 and 2.3.2) showed that the strut thickness increase the fatigue resistance of the stent, but they also induce higher stresses on the stenosis.

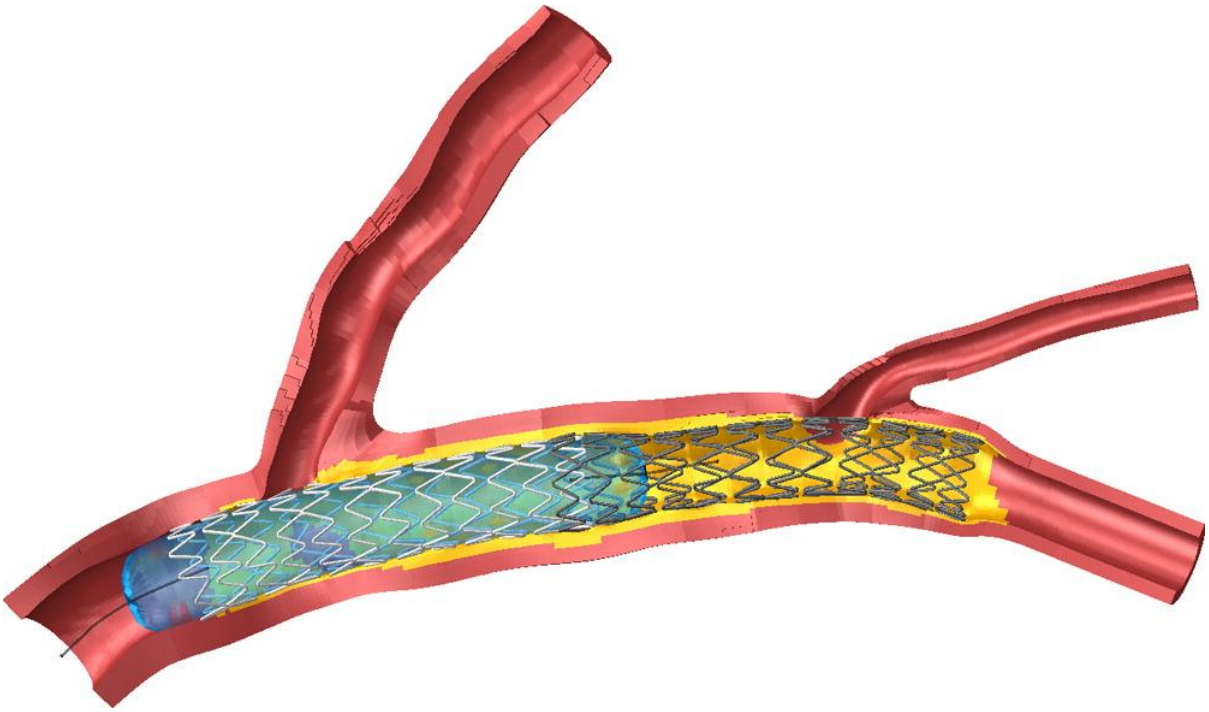

Figure 1.14. Resulted geometry of a patient specific stent expansion in arterial bifurcation with stent overlapping (Morlacchi *et al.*, 2013).

Computational methods can be used effectively to compare the deployment behaviour of different stent designs. Lally *et al.* (2005) analysed the expansion of two different stents, the S7 and the NIR. Both the blood vessel and the stenosis were modelled as idealized cylindrical and axisymmetric tube with hyperelastic behaviour. Results showed the maximum tissue prolapse between the stent struts was 0.056 mm for the S7 and 0.124 mm for the NIR. The contact area was 11.3 mm^2 and 13.9 mm^2 for S7 and NIR, respectively. It was also found that high tensile stress (>4MPa) occurred in 21% of the artery when stented with the NIR, compared to 4% for S7. The radial retraction was found to be greater for S7, and the final lumen diameter corresponded to a final stenosis of 23% for S7, compared to 14% for the NIR. This comparative study shows clearly that stents with higher radial stiffness also induce more severe stresses on the vessel walls.

The geometry of the artery also represented an important factor in stent deployment. Wu *et al.* (2007b) briefly compared stent expansion in curved and straight arteries, and showed that artery curvature tended to increase the stress levels on both the plaque and the arterial layers. Gu *et al.* (2012) studied the arterial wall mechanics during stent deployment by considering an asymmetric plaque layer with an edge ratio of 2:1 and an overall stenosis of 50%. The results showed that, in addition to stent design, plaque composition and the local thickness, due to the asymmetry, significantly affect the stresses in the artery induced by stent deployment. An increase in plaque thickness or an increase in plaque stiffness (e.g. plaque calcification) tended to reduce the stress concentration in the arterial layers. In addition, the tortuosity of arterial branches and the eccentricity of stenosis are also important factors that influence the deployment of stent.

In some of the recent work, analyses were also carried out for patient specific modelling of stent deployment, evaluation of restenosis rate and prediction of stent fatigue life. For instance, by digital reconstruction of arteries with Computer Tomography Angiography (CTA), Morlacchi *et al.* (2013) were able to produce two models of patient specific arterial bifurcation and model the deployment of two stents (Figure 1.14). The study showed that high stresses can be found in the areas of stent

overlapping for both the stents and the arteries, leading to potential stent and arterial failure. Simulation of stent expansion was performed by Imani *et al.* (2014) to study the effects of stent designs on arterial wall stresses and restenosis rate. For the three designs studied (i.e., Palmaz-Schatz, MultiLink and NIR stents), their results showed that Palmaz-Schatz stent generated the highest level of stress on the artery, specifically 15.6% more than MultiLink stent and 7.6% more than NIR stent. In clinical trials, Palmaz-Schatz stent showed the highest rate of restenosis, suggesting a strong correlation between wall stresses and restenosis rate. Morlacchi *et al.* (2014) also studied the fatigue life of a stent and the influence of plaque calcification and cardiac wall movements on its failure. The model simulated the expansion of the stent inside the artery (with and without calcification) and post-deployment deformation subjected to cyclic blood pressure and wall movement. Results showed that plaque calcification can be associated with an increased risk of stent fracture due to the increased stress on the stent mainly caused by the heterogeneity of the partially calcified atherosclerotic plaque. Kamenskiy *et al.* (2013) analysed the connections between plaque calcification, adverse vessel geometry, hemodynamic variation, mechanical change and stent deployment. The study involved 15 patients undergoing stent angioplasty, and computer tomography angiography (CTA) images were gathered and used to digitally reconstruct the arterial section. Tortuosity and arterial elongation were measured in all the arteries, as well as the hemodynamic of the artery. Their results showed that highly calcified plaques limit the ability of the stent to deform the abnormal portion of the artery, transferring the deformation to the healthy tissue. Hemodynamic of the artery improved after the stent deployment by decreasing the area of low shear, which was located on the point of maximum stenosis. Straightening of the carotid bifurcation was also observed, along with stent-induced elongation of the diseased region.

Another interesting aspect that involved finite element analysis is the effect of the stenting on the local hemodynamics of blood flow in the vessel (Balossino *et al.*, 2008). The influence of stent designs on blood hemodynamics was studied by considering four different designs: Cordis BX

Velocity, Jostent Flex, Sorin Carbostent and Palmaz-Schatz. In this case, the artery and plaque were modelled as simple coaxial hollow cylinders. Results showed that the Jostent Flex generally had the largest area with low wall shear stress during the cardiac cycle, while artery stented with the BX Velocity had the highest value of shear stress. Gay *et al.* (2006) analysed the interaction of balloon-expandable stent with the surrounding fluid using immersed finite element method. Results showed that during deployment the diameter of the stent increased from 1.64 mm to 2.82 mm, and the stress distribution was uniform longitudinally. Stress was increasing with the expansion and reached the highest level at the end of the expansion. The highest values of the von Mises stress followed a linear variation during the entire simulation. Berry *et al.* (2002) carried out a finite element analysis to assess the mechanical behaviour of the compliance matching stent (CMS) in a stent-artery hybrid structure. This stent was developed to provide a smooth compliance mismatch between the stent and the host vessel. Both in vivo hemodynamics and change of wall mechanical properties caused by the stent were investigated using a swine model by direct measurements of flow, pressure, diameter and histology in the stented segment after 7 days. Results showed that the compliance of the artery, was reduced by stenting (approximately 60% for the CMS and nearly 90% for the Palmaz-Schatz stent). In vivo analysis showed that there were no significant changes in either pressure or flow characteristics based on both upstream and downstream measurements in the stented superficial femoral arteries.

1.5.3 Effect of Balloon Modelling

Another factor that has important influence in the simulation of stent expansion is the type of balloon used in the modelling. Rubber balloons, inflated by internal pressure, were generally used to simulate expansion of early generation stents (e.g. Palmaz-Schatz). Modelling of a rubber balloon is relatively easy, and produces reliable results including both stent expansion and stresses in the stent-artery system (Chua *et al.*, 2003; Ju *et al.*, 2008). While De Beule *et al.* (2008) assessed

the importance of balloon folding in the expansion behaviour of a Cypher stent and proved that the folded balloon was the only model that produced results consistent with the data provided by the manufacturer, in terms of diameter change as a function of pressure. This is particularly the case for the recent generation of stents (e.g. Cypher, Cordis) which are designed to be expended by folded balloons.

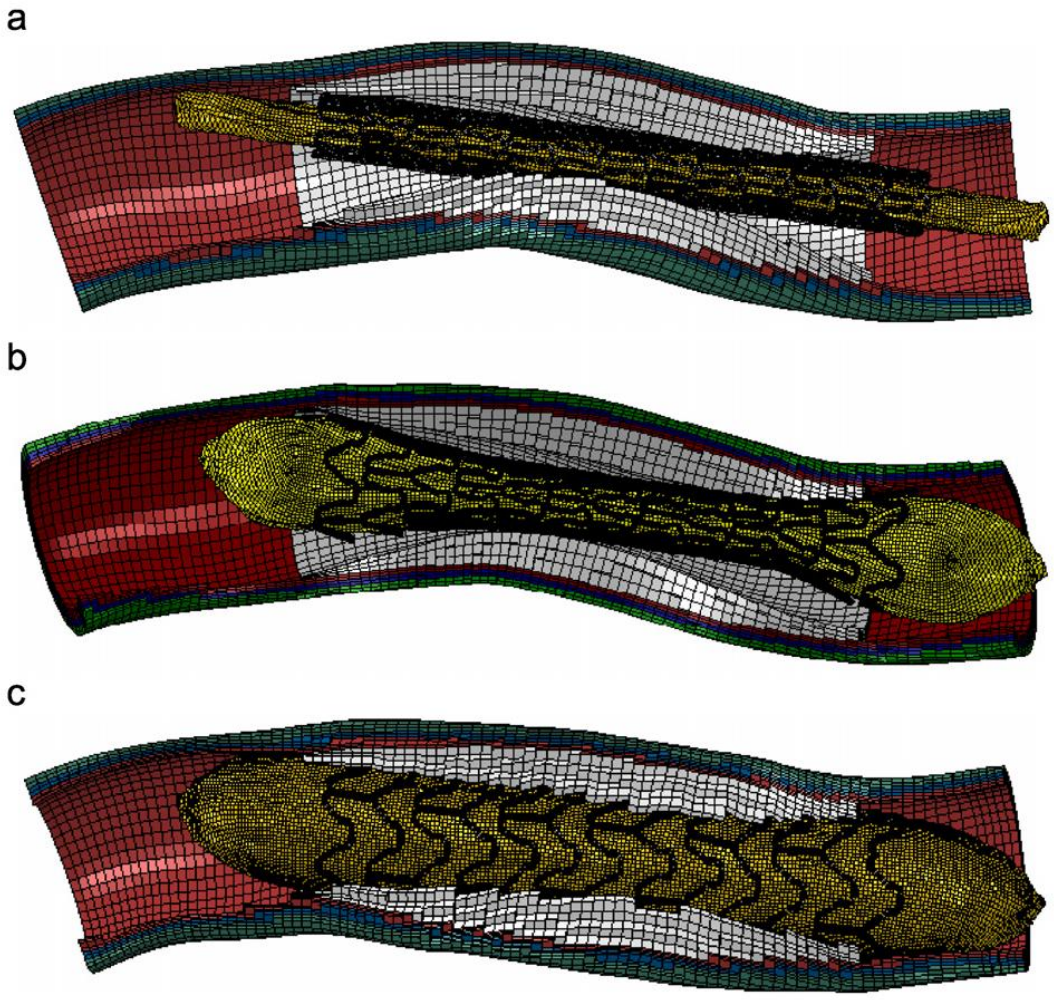

Figure 1.15. Expansion of an artery with stenosis by means of folded balloon inflation (Zahedmanesh *et al.*, 2010): (a) the crimped state of stent and balloon, (b) the dogboning effect at the beginning of the expansion and (c) the configuration at maximum pressure.

The effect of balloon folding on the symmetry of stent deployment was studied by Narracott *et al.* (2007), using experimental and computational methods. In the work, they compared the expansion obtained by means of two different types of folded angioplasty balloons: the dual lobe folded balloon, which shows an S-shaped profile through its cross-section, and the single lobe folded balloon, characterised by a C-shaped profile. According to their findings, deployment of stent by means of balloon with dual lobe folding pattern produced a more uniform expansion, compared to the balloon with single lobe folding pattern. The difference between the two expansion behaviour was recorded at an early stage of the expansion, with no significant difference in the overall pressure-radius response between the two balloons.

A study by Gervaso *et al.* (2008) compared three different methods in modelling stent expansion, i.e., no balloon (pressure applied on the stent inner surface), free rubber cylinder inside the stent and folded balloon. The work showed that the folded balloon gave the expansion behaviour of Cordis BX-Velocity stent closer to the company data. On the other hand, Zahedmanesh *et al.* (2010) simulated a balloon expansion of stent in a coronary artery (Figure 1.15) using three different approaches. In the first one, the expansion of the stent was obtained by the application of pressure directly over the inner surface of the stent struts. The second approach considered the application of pressure on the inner surface of the stent, but with the addition of a partial constraint on the artery, which was obtained by means of spring elements (with stiffness 1kN/m) connected to the nodes at the ends of the artery. The third approach was to apply pressure within a folded balloon which is the most realistic. Results showed that stent expanded by folded balloon achieved the target diameter of 3.5 mm with an applied pressure of 15 atm, whilst simulations with a direct application of pressure on the stent inner surface showed a stent expansion of only 3 mm at 15 atm (irrespective of the use of arterial constrains). However, the simulation with arterial constraints managed to achieve the desired expansion of 3.5 mm at a peak pressure of 30 atm. After recoiling, stent expansion achieved by direct application of inner pressure (with arterial constrains) was

found to be around 3.3 mm in diameter, which is similar to that achieved by the folded balloon. The von Mises stress on the artery were also similar at the peak pressure and after recoiling for both cases. More recently, Martin and Boyle (2013) showed that considering the tri-folded balloon led to a simulated expansion of Cordis BX-Velocity stent which is closer to the manufacturer data. These studies are consistent with the literature review presented in Section 2.4.1, indicating that realistic balloon modelling is necessary to obtain a good correlation between experimental and computational results.

One further example is the study of the stress distribution on the balloon by numerical simulations of the expansion of a catheter balloon on bladder (Shuib *et al.*, 2007). At an inflating pressure of 92.5 kPa, the maximum stress was found to be 0.0925 MPa, 0.271 MPa and 0.155 MPa for Natural Rubber, Silicone and Polyurethane balloons, respectively. Also the simulated expansion reached a maximum diameter of 24.43 mm, 19.55 mm, and 17.48 mm for balloons made of Natural Rubber, Silicone and Polyurethane, respectively. However, experimental measurements of the achieved maximum diameter were found to be 26 mm for the Natural Rubber balloon and 25 mm for both Silicone and Polyurethane balloons, which are consistently higher than those obtained by the simulations.

1.5.4 Arterial and Plaque Modelling

One of the most important key aspects of modelling stent biomechanics is the constitutive material behaviour of the arterial walls and stenosis. A review by Holzapfel and Ogden (2010) shows that the main constituents of the artery are collagen fibres, elastin and smooth muscle (Figure 1.16), making the arterial tissue exhibit highly non-linear, anisotropic and incompressible behaviour.

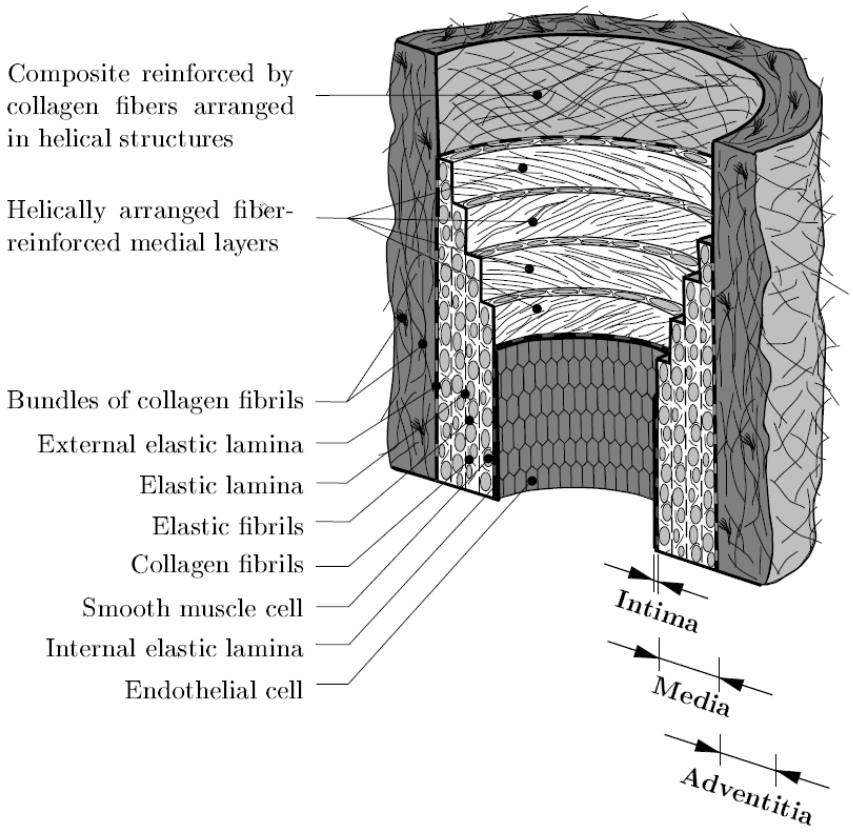

Figure 1.16. Illustration of the main layers composing a human blood vessel wall (Holzapfel *et al.*, 2000).

In most cases arterial layers can be assumed as purely elastic and therefore characterised by hyperelastic strain energy potentials, but the fibre orientation and its interaction with the other constituents can be considered to refine the constitutive model. Also, the biomechanical behaviour of arterial layers is affected by age and disease, which results in a reduction of elasticity due to the degradation of the elastin. It was also pointed out that the understanding of arterial material behaviour is a key aspect in FE modelling of cardiovascular systems, such as the stent-artery system. Refinement in the constitutive modelling of the arterial layers will increase the potential of FE analyses in predicting physiological functional interactions. Holzapfel *et al.* (2005) measured the stress-strain behaviour of individual arterial layer (i.e. intima, media and adventitia) gathered

from 13 diseased cadavers. Their results showed that the elasticity of the material in tension is highly heterogeneous among the patients and all the specimens exhibited hysteresis and strong anisotropic non-linear behaviour. A constitutive model, which was developed originally by Holzapfel *et al.* (2000), was used in their study to model the experimental stress-strain behaviour. The model consists of a strain energy potential, that is given by the equation:

$$W = C_{10}(I_1 - 3) + \frac{k_1}{2k_2}\left[\exp\left(k_2\langle E\rangle^2\right) - 1\right] + \frac{1}{D}\left(\frac{(J)^2 - 1}{2} - \ln J\right), \qquad (1.2)$$
$$E = \kappa(I_1 - 3) + (1 - 3\kappa)\left[I_4 - 1\right]$$

where C_{10}, D, k_1, k_2 and κ are material parameters, I_4 is the invariant of Cauchy-Green deformation tensor and E represents the deformation of the fibre families. The Macauley bracket is indicated by the operator <>.

Results demonstrated that the Holzapfel-Gasser-Ogden (HGO) model was able to describe the stress-strain responses of all the layers. Holzapfel and Gasser (2007) analyzed the stress and deformation of a Left Anterior Descending (LAD) coronary artery, modelled as a double layered (consisting of media and adventitia), thick walled, anisotropic and inelastic circular tube. Results showed that the media was the layer that carried most of the stress (75% of the pressure load), while the adventitia took the load-carrying role at supraphysiological loading. Due to its high stiffness, the adventitia provided a support to soft artery layers during radial compression. From these work, it is clear that the mechanical properties of arterial tissues are heterogeneous, anisotropic and inelastic. As reviewed in Section 2.4.2, the arterial layers play an equally important role in the stent expansion. It is therefore important to understand to what extent arterial factors (i.e. anisotropy, inelasticity and layers' stiffness) can affect the process of stent deployment.

For this purpose, modelling of the arterial and plaque inelasticity was carried out by Maher *et al.* (2011 and 2012) in two published papers. In the first paper, the inelasticity of the atherosclerotic

plaque was tested experimentally under uniaxial compressive loading and a constitutive model was developed to account for the permanent deformation and stress softening of the plaque. From the experimental results, the inelastic behaviour of the plaque (i.e. plastic deformation and stress softening) could be observed and independent of the plaque composition. A material model was then developed to account for the stress softening, by introducing a continuum damage approach, and the plastic deformation, by means of an additive split of the stress tensor. FE results showed that the novel constitutive model produced a consistent quality fit of the experimental loading-unloading curves. In the second paper, Maher *et al.* (2012) presented an anisotropic inelastic model for the arterial tissue, using the same constitutive model developed in their first paper. Numerical simulations of the aorta and carotid arterial tissue were performed to simulate uniaxial tensile testing in both longitudinal and circumferential directions. Results were compared with their own experimental data, showing consistency between the model prediction and the experimental curves during uniaxial loading and unloading of the specimens in both directions. It was discussed that neglecting the inelasticity of the arterial tissues and stenosis would lead to an underestimation of stent expansion. It should be noted that the plaque and arterial plasticity is not included in the material formulation used in this thesis due to the level of complexity, but worth investigation in future studies.

Other interesting aspects that are relevant to stent simulations are the mechanisms of plaque rupture and arterial perforation, which have been the subjects of FE studies. As shown by the clinical studies (Section 2.2.2), stent deployment has been associated with arterial perforation and plaque rupture. The mechanisms of rupture of human soft tissues, such as the arterial layers and the stenotic plaque, have been capturing the interest of researchers for decades. Cheng *et al.* (1993) analysed the circumferential stress distribution in 24 plaques in order to understand the mechanisms of plaque rupture. Their findings showed that circumferential stress plays an important role in the plaque rupture, along with local variations in the plaque properties. Stress

analysis of the atherosclerotic plaque has also been studied through imaging techniques, i.e. Magnetic Resonance Imaging (MRI), combined with FE Analysis by Li *et al.* (2006) (Figure 1.17). Their findings showed that plaques which underwent rupture exhibited considerably higher stresses (0.683MPa) compared to those not ruptured (i.e. 0.227MPa). Also the relative stiffness of fribrous cap to lipid pool can lead to high stress levels within the cap and should be considered as a predicting factor for the vulnerability of the plaque. A further investigation by Li *et al.* (2009) compared two possible mechanisms for plaque rupture, i.e. the shear stress and the pressure gradient. The shear stress plays a major role on the damage on the endothelium and fissure plaque, but according to these studies the pressure gradient is likely to be one of the main mechanical trigger for the plaque rupture.

Arterial failure was recently investigated by Khamdaengyodtai *et al.* (2012), who, in particular, analysed the effect of pressure on the failure prediction of arterial layers. The model included a 5-layered arterial wall which were affected by internal pressure, and results showed that the rupture occurs in the circumferential direction, starting from the inner part of the media layer and propagating towards the outside. Another numerical study on the fracture of human arteries was made by Ferrara *et al.* (2008), adopting a digitally reconstructed geometry of a damaged human artery. Results showed that stress concentrations are critically dependent on the geometry of the fibrous cap and the lipid pool, while the percentage of occlusion caused by the stenosis was not a remarkable factor. Furthermore, all ruptures originated from the internal intima and developed in longitudinal direction. Arterial dissection caused by angioplasty was also studied by Badel *et al.* (2014) using cohesive interface surfaces on a simplified arterial FE model. The analysis revealed several damage processes, i.e. detachment of the stenotic plaque and overt media dissection, which may lead to proliferation of restenosis. These studies prove that the stress concentration on the plaque obtained by FE analyses can be used as a predictor for plaque rupture and arterial damage. However, none of the studies modelled the actual failure process of the stenosis or the arterial

layers, which may be considered as a challenge. In this thesis, the failure of the arterial layers and plaque was not modelled, but the stress distributions on the artery-plaque system were used to discuss the effect of stenting on the potential damage of blood vessels.

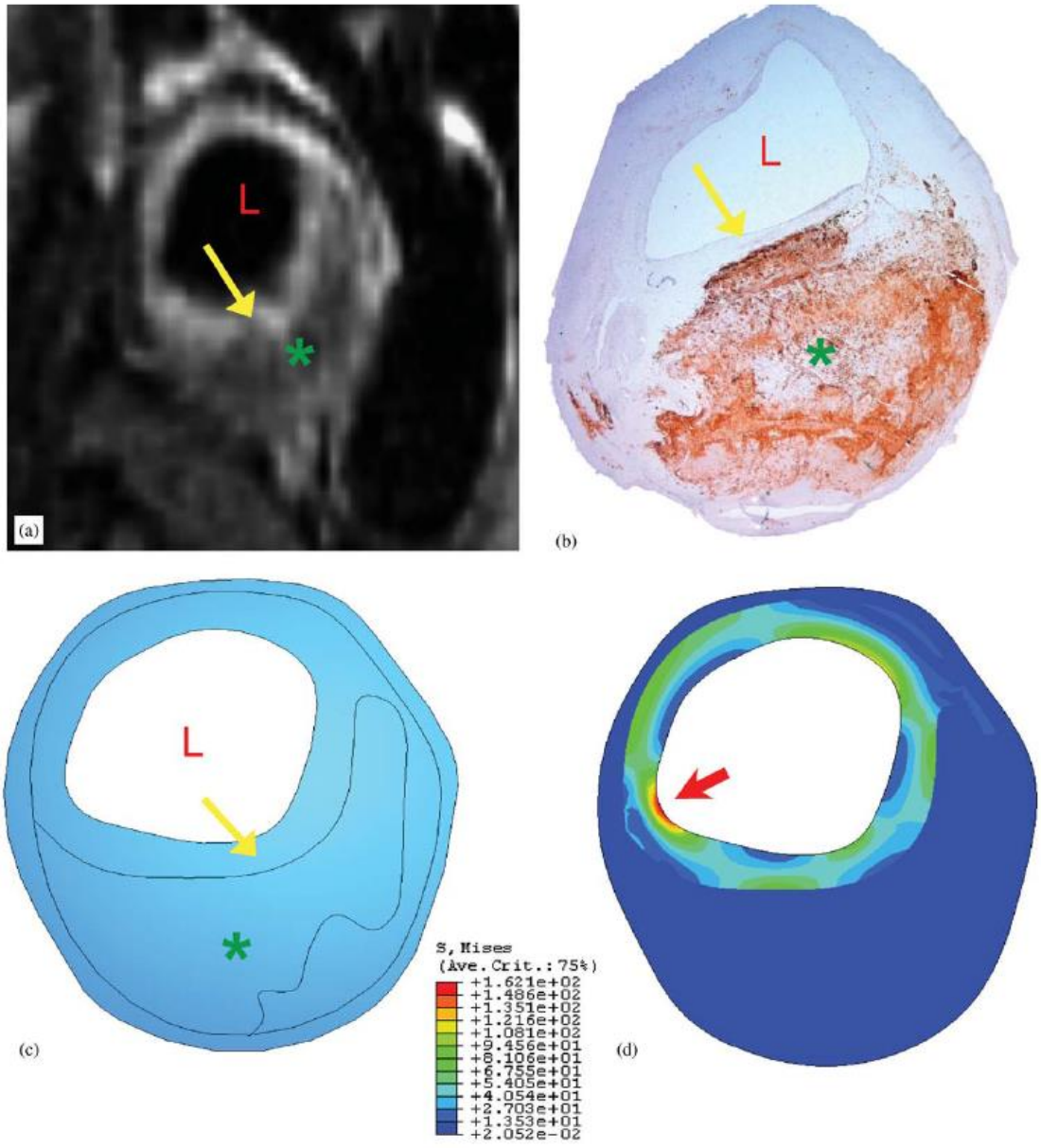

Figure 1.17. Stress contour of a carotid plaque (70% stenosis):, showing (a) the MRI image of the plaque, (b) the histology for co-registration of plaque characterization, (c) the FEA model of the plaque and (d) the von Mises stress contour (Li *et al.*, 2006).

1.5.5 Optimisation of Stent Geometries

According to the experimental studies discussed in Section 2.3.3, geometrical optimization of the device can lead to significant improvement in stent performance. For this purpose, computational studies have been carried out to investigate the effects of stent geometry on the mechanical behaviour of stents. This also includes comparative studies of different stent designs or performing an optimization process to work out the best geometrical parameters for a stent design. Regarding the Palmaz-Schatz, Chua *et al.* (2004b) made a shape optimization study by varying the slotted tube geometry. The slotted tube geometry was manufactured by cutting slots around the surface of a metallic tube, and the dimensions of the slots determined the flexibility of the design. In this study, a total of five designs were produced. The first design was the same as that used for the expansion simulation in their previous work (Chua *et al.*, 2003). The other three designs were obtained with an alteration of 10% for the width and length of the slot (both increase and decrease). The last design has a 50% increase in the number of the slots. The analysis showed that the design with wider slots and narrower struts had lower stress magnitude, but similar distribution, compared to the original design. The residual stress was almost the same as the first one, but with less deployment pressure. The design with wider slots and narrower struts was shown to be the strongest in terms of radial stiffness. Increase of the length showed the same stress distribution and no major differences were found. By increasing the number of struts, the minimum stress location shifted from the end to the middle of the stent, and the stent experienced more severe bending with highly localised stress concentration. The design with increased number of slots also had the greatest expansion, almost 2 mm more than the rest, but also accompanied by the maximum shrinkage (about 19.70%) and foreshortening effects. The design with wider struts was shown to have less foreshortening. From this study, it proved that optimisation of stent geometry can enhance its flexibility and lead to more uniform distribution of stresses along the struts, which can increase the life-span of the stent.

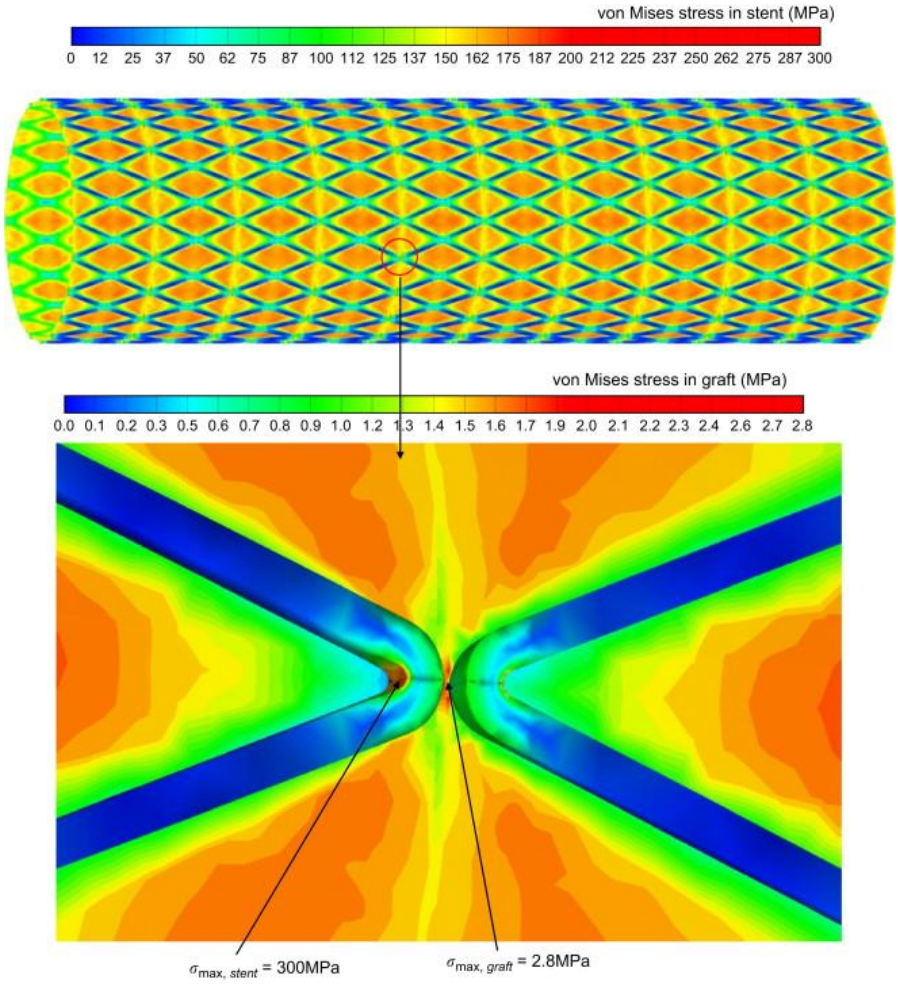

Figure 1.18. Stress distributions in the main body a Nitinol stent graft (Kleinstreuer *et al.*, 2008).

In addition, Migliavacca *et al.* (2002) modelled a common diamond shaped stent Palmaz-Schatz with a parametric analysis through varying the metal-artery ratio, the strut thickness and the slot length. Results showed that increasing the metal-artery ratio decreased the radial and longitudinal recoil but increased the foreshortening, dogboning, expansion pressure and plastic strain. Reduction in strut thickness decreased the expansion pressure but increased forshortening, dogboning and recoiling effects. Increase in the slot length increased the radial recoil, but without causing significant influence on the other quantities. Li *et al.* (2009a) performed a shape

optimization study of coronary artery stent. The geometry of the stent has been parameterized and the stent was then expanded with different values of those parameters, in order to find a collection of values that gave the minimum dogboning effect. It was shown that the optimal design reduced the dogboning from 9.06% to 0.40%. A virtual optimization of self-expandable braided wire stents was also been performed by De Beule *et al.* (2008). The work aimed to establish the correlation of the radial and axial stiffness, the foreshortening and the wire surface ratio with the geometric parameters. The introduced optimization tool was able to combine analytical and computational models, so the stiffness was obtained from numerical simulations whereas the foreshortening and the ratio of wire were analytically calculated. A Monte Carlo approach was used to extract a random combination of possible design variables in order to calculate the axial force. Results were in close agreement with the experimental data and the proposed analytical approximation. Over the whole range of loading conditions, the simulation differed from the analytical and experimental data by less than 3%. Generally, the foreshortening effect was over-predicted and the longitudinal stiffness was found to increase with the stent length, a behaviour in line with expectations. However, the study demonstrated the feasibility and efficacy of braided stent shape optimization. In fact, the optimization process reduced the foreshortening by 20% whilst maintaining the radial stiffness of the original design. The optimized design was achieved by increasing the wire diameter from 0.22 mm to 0.25 mm, the number of wires from 24 to 34 and the pitch angle from 30.85° to 37.40°. From these studies, it is clear that geometrical optimization can be used to improve the stent design significantly by reducing the adverse effects caused by excessive deformation of the device.

On the other hand, shape optimization was also used to improve the fatigue life of the stent. Kleinstreuer *et al.* (2008) studied fatigue behaviour of nitinol stent grafts, considering the crimping and compressing process of the stent as well as the stent contact with the arterial wall and the stent graft. They used two different Nitinol models, called NITI-1 and NITI-2, with two different stent grafts, i.e. polytetrafluoroethylene (ePTFE) and polyethylene terephthalate (PET). Results showed

that NITI-1 stents have a better crimping performance than NITI-2, and under representative cyclic pressure loading, the two stents are both located in the safe zone of the fatigue-life diagram. For the major section of the stent (Figure 1.18), NITI-1 showed good fatigue resistance with both ePTFE and PET grafts, while NITI-2 exhibited good performances only with PET grafts. Another study was carried out by considering fluid-structure interaction with a stochastic optimization process in order to define the optimal stent design (Blouza *et al.*, 2008). The simulation considered three particular geometric parameters: the strut spacing, the strut height and the strut width. From the results, a rule of thumb has been established. Specifically, the characteristic ratio "strut spacing over strut height" shall be above the critical value of 5.7 to ensure a sufficiently high wall shear stress while maintaining a low level of flow swirl. Non-uniform rational basis spline parameterization was used by Clune *et al.* (2014) to perform a shape optimization study of stents, aiming to optimize the fatigue resistance and radial flexibility of the device by FE modelling. Results showed that there is a trade-off between flexibility and fatigue resistance, and fatigue-resistant designs increase the potential of restenosis due to the excessive stiffness. Whilst the deformation of the stent can be easily improved by geometrical optimization, the fatigue strength represent more challenge. Specifically the studies show that fatigue failure can be reduced by introducing designs that would compromise the stent flexibility. Maintaining certain level of flexibility is critical to reduce the risk of stent fracture (Celik *et al.,* 2009) and also lower the stresses on the arterial walls and associated restenosis rate (Zahedmanesh *et al*, 2009; Lally *et al.*, 2005).

1.5.6 Effect of Coating and Simulation of Drug Elution

FE simulations are also widely used to study the effects of various designs and drug eluting coating on the mechanical behaviour of stents. Gu *et al.* (2005) studied the influence of coating on expansion of Palmaz-Schatz stent. An ultra-thin silicone coating was applied to the stent before

deployment. The coated stent was then placed into an artery with a long fusiform aneurysm. The analysis was also validated against an in vitro experiment of stent expansion. The inflating pressure was increased in very small steps in order to compare the experimental diameter-pressure curve with the one obtained from the simulation. Results showed that the coated stent needs approximately 30% higher pressure to expand the artery to the same diameter, due to the change of flexibility of the device. This could also lead to increased stress levels on the plaque-artery system. Hopkins *et al.* (2010) investigated the coating delamination during stent deployment. The simulations considered the expansion of a stent strut coated with three different polymeric coatings, i.e. polyurethane, poly-styrene-b-isobutyl-b-styrene (SIBS) and polyurethane-glyco-phosphorylcholine (PU-GPC). Results showed that the normal interface strength increased linearly with the coating thickness for all three coating materials. Also, the PU-GPC was the type of coating that showed the highest interface strength. Furthermore, the paper modelled coating delamination for stent struts, in good comparison with experimental observations.

Most of the stents currently on the market are coated with drug eluting polymer layers to prevent restenosis of blood vessels. A simulation of the drug elution process for coronary stents was performed by Zunino *et al.* (2008), focusing on the effect of interplay between the mechanical force, exerted on the vessel wall by the stent, and the blood flow. The drug release simulations featured just one chemical species, namely heparin, which was governed by standard advection-diffusion equations. The heparin was a relatively small molecule with negligible diffusive properties, so a mass transfer model was sued to simulate drug release into the lumen and the arterial walls. The advective phenomenon of drug transport into the arterial walls was neglected. The analysis showed that the interaction between the stent and the blood stream generated very complex flow patterns. The fluid remained trapped for some time, and after that the flow may re-joined the high speed flow. Almost all the drugs were released within 1 hour after the implantation. The direct contact between the stent and the walls allowed 15% of the total amount of drug to be

released into the walls, but more than half of this portion was transferred into the lumen due to the negative concentration gradient between the lumen and the walls.

1.6. New Materials for Stent Application

The latest advancements in stent designing focus mainly on the development of novel materials, especially bioadegradable polymers and metals, such as Poly-L-Lactic Acid (PLLA) and Magnesium alloys. A paper by Ormiston *et al.* (2009) reviewed the bioadsorbable stents currently on the market, compared to permanent metal stents. Bioadsorbable stents made from PLLA are typically adsorbed within 2 years, and the strut thickness varied between 0.17 mm to 0.20 mm. On the other hand, Magnesium alloy stents have an absorption time of less than 4 months, with a strut thickness of 0.17 mm. This doubles the strut thickness for permanent metal stents, such as Xience stent with a strut thickness of 0.08 mm. Demir *et al.* (2013) showed a possible procedure for designing and manufacturing an Mg-alloy (type AZ31) bioadsorbable stent. The novel design was obtained by means of 2D shape-optimization procedure with a morphing procedure. This was used to maximize the scaffolding capability of the stent without inducing excessive local large deformations. Manufacture of the stent prototype was done by laser cutting and chemical etching. Results confirmed the feasibility of the applied approach, but also showed that the corrosion rate of the Mg-alloy must be decelerated for stent application.

A collapse pressure study was also performed by Venkatraman *et al.* (2003) for biodegradable stents made of three different kinds of biodegradable poly-l-lactide (PLLA) polymers with intrinsic viscosities of 2.4, 4.3 and 8.4 (called PLLA 2.4, PLLA 4.3 and PLLA 8.4, respectively). The molecular weight measured for each kind were 3.22×10^5 g/mole, 7.075×10^5 g/mole and 1.06×10^6 g/mole, respectively, showing a correlation between the viscosity and the molecular weight. The results showed that the mechanical properties were not significantly affected by the molecular

weight of the polymers, however the mode of failure is significantly different. PLLA 2.4 showed brittle failure whereas PLLA 4.3 and 8.4 exhibited ductile failures. There was no obvious decrease in both the ultimate tensile strength and Young's modulus after immersion in buffer (37°C for 2 to 3 months), as these properties remained almost constant throughout the time period studied. Bünger *et al.* (2007) studied the in-vivo performance of stents made of biodegradable PLLA and stainless steel. They monitored the stents at one and six weeks after the implantation in living pig's carotid arteries. Initial technical success was achieved in all PLLA stents and metal stents, and no significant differences existed in the vessel areas for unloaded and sirolimus (SIR) loaded PLLA stents after 6 weeks. Drug-unloaded PLLA stents showed significantly decreased residual lumen area and increased neointimal area after 1 and 6 weeks as compared to 316L stainless steel stents. In contrast, SIR eluting PLLA stents demonstrated neointimal area after 6 weeks, which is comparable to stainless steel stents. The intimal thickness measured over the struts of unloaded PLLA stents increased significantly from 0.06±0.02 mm to 0.17±0.05 mm, while for metal stents the intimal thickness increased from 0.04±0.01 mm to 0.13±0.04 mm. SIR loaded PLLA stents demonstrated lowest intimal thickness at 6 weeks 0.07±0.02 mm, which is comparable to the neointimal response of pure PLLA at 1 week. PLLA has been proven a good candidate for biodegradable stent applications, as it has a better pace of degradation compared to other bioresobable materials. However, PLLA is considerably softer compared to stainless steel and Co-Cr alloys, which certainly affects the overall radial stiffness of the stent.

1.7 Research Gaps

From the studies reviewed in this chapter, it is possible to identify some of the gaps in stent research. Previous research showed that the difference between stent designs can affect the deployment process. Also, FE analyses can be used to perform comparative studies between

different stents, by predicting the process of stent deployment. However, the effects of stent geometries and materials, along with the thickness of the drug eluting coating, on stent deployment have not been fully studied yet through the use of FE method. Understanding the roles played by these factors are of high importance to the development of future stents.

According to the studies reviewed in this survey, different balloon types were used in the simulations of stent deployment, such as rubber and folded balloons. Also, different arterial constraints were shown to influence the simulations of stent expansion. For the artery and plaque, a different hyperelastic models were often employed to describe the tissue constitutive behaviour. There is a lack of proper study of the effects of balloon type, arterial constraint and tissue constitutive model on the simulation of stent deployment.

Stent deployment can also be influenced by vessel factors, such as vessel curvature and plaque eccentricity. When considering stent deployment, the effects generated by the abnormal geometries of the vessel and stenosis must be taken into account. However, according to this review, studies on the impact of vessel factors in stent deployment are scarce. Also, anisotropic behaviour of the vessel layers was also neglected by most of FE analyses and there is an urgent need to investigate the effect of arterial anisotropy.

Expansion of stents has been shown to generate significant post-deployment stresses on the stent struts and the vessel. Almost no studies were carried out to clarify the roles played by these post-deployment stresses when considering the deformation of stented arteries under biomechanical forces (i.e. bending and radial compression). Furthermore, considerable stresses were also generated by the crimping of the stent onto the balloon prior to the deployment, and their effects on the process of stent deployment have not been well studied yet according to this literature survey.

Finally, bioresorbable polymeric stents are the latest generation of stents currently available on the market. However, there is very limited work devoted to modelling the deployment of bioresorbable polymeric stents, especially comparative studies against metallic stents, which is important to evaluate the performance of these new-generation devices.

1.8. Aim and Objectives

The aim of this Ph.D. project is to investigate the mechanical performance of stents during deployment inside atherosclerotic human arteries, by means of computational mechanics, focusing on the effects of stent designs and blood vessel factors. To achieve this aim, the following objectives have been specifically identified and addressed in five Chapters:

- To determine the effects of stent designs, materials, polymeric coating and plaque calcification on stent deployment (Chapter 3);
- To investigate the influence of balloon type, arterial constraints and tissue constitutive models in finite element simulation of stent expansion (Chapter 4)
- To study the importance of blood vessel factors, such as vessel curvature, plaque thickness and eccentricity, in the process of stent treatment (Chapter 5)
- To simulate stent deployment and deformation in diseased arteries by considering vessel anisotropy (Chapter 6)
- To model the process of stent crimping and the effect of generated post-deployment stresses on subsequent stent deployment (Chapter 7)
- To compare the performances of commercial polymeric bioresorbable stent with those of metallic stents (Chapter 7)

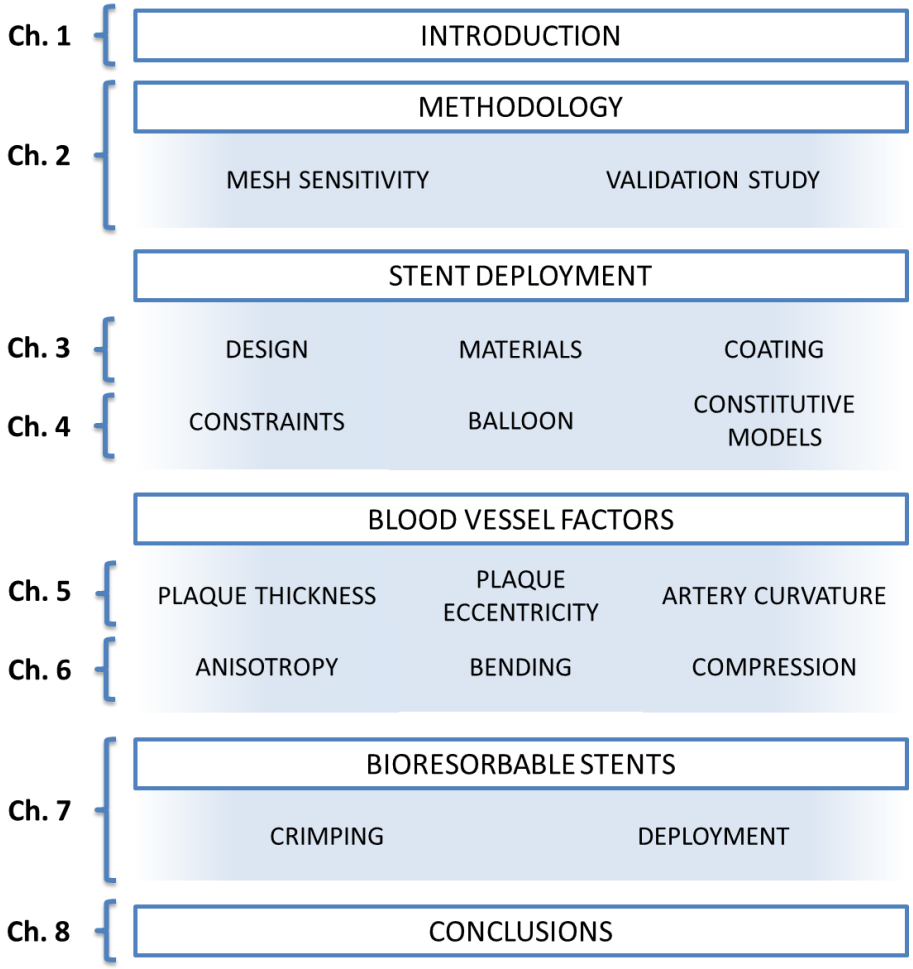

Figure 1.19. Illustration of the thesis structure, sorted by topics, objectives and chapters.

An overall structure of the thesis is illustrated in Figure 1.19. Chapter 2 contains detailed description of the methodologies used in this research, along with mesh sensitivity and model validation studies. Effects of designs, materials and coating on stent deployment were studied in Chapter 3 by means of finite element (FE) analyses. This was followed by Chapter 4 which investigated artery constraints, balloon type and tissue constitutive models used in stent deployment simulations. Chapter 5 provides an investigation of the effects of blood vessel factors, such as plaque thickness, stenosis eccentricity and vessel curvature, on the deployment of stent in atherosclerotic arteries. The influence of anisotropy of arterial layers in stent deployment and

system deformation under bending and radial compression is presented in Chapter 6. Chapter 7 modelled the deployment of bioresorbable polymeric stents, including the effects of post-crimping stresses generated prior to the implantation (by crimping). The conclusions of this thesis are given in Chapter 8, along with brief recommendations regarding clinical and design aspects of stent treatments based on the findings of this project.

1.9. Conclusions

In this chapter, a review of literature has been presented, regarding the current status of research in stent. Clinical studies confirmed that stent failure can happen at any time after stent angioplasty. Post-stenting complications to the patient were identified as chest pain, restenosis and thrombosis. On the other hand, statistical studies showed that stent failure can occur up to 7.7% if non-complete fracture was accounted for. Also, stent deployment has been associated with arterial damage and perforation that can be caused by both the angioplasty balloon and stent.

In the second section, experimental studies have been reviewed, especially the study of stent flexibility using in-vivo, in-vitro and ex-vivo experimental setups. A large body of work also focused on comparison between commercially available stent designs, in terms of flexibility and fatigue strength. However, experimental studies are still very limited due to the small size of the devices and complexity of human body environment.

Computational approaches (i.e. FE analyses) have been considerably used to study the mechanical behaviour of stents, such as the stress concentration, dogboning, foreshortening and recoiling effects. Also, shape optimization techniques were employed to improve the stent performances by reducing the recoiling and dogboning effects as well as increasing the fatigue strength of the stent.

In addition, simulations have also been carried out to study drug elution process, delamination of drug eluting coating and the effect of coating on the stents' radial stiffness.

Computational methods have also been used to predict the stresses on plaque and blood vessels caused by stent deployment, which is linked to the risk of restenosis and tissue damage. Furthermore, MRI and FE methods can be combined to carry out patient specific simulations to gain more insightful understanding of stent deployment and its impact on patients. Other studies included how plaque calcification, vessel tortuosity and stent designs can affect the stent performances during stent deployment, and how stents can affect the hemodynamics of the human artery. Furthermore, simulations have also been carried out to study the mechanisms of plaque rupture and arterial damage, which can be predicted by the stress distributions in the vessel tissue layers.

In the last section of the chapter, research regarding the latest materials used for stents is reviewed, focusing on biodegradable alloys and polymers, such as PLLA and magnesium alloys. Bioabsorbable materials can dissolve in the blood stream after the deployment and reduce the risk of restenosis and long-term clinical complications. However, there are limitations for these materials. For instance, while the feasibility of designing and manufacturing magnesium alloy stents has been proven, it was also shown that the degradation of Mg-alloys was too fast for this kind of application. PLLA exhibits improved degradation rate, but lacks ductility and strength. Bioabsorbable stents are still under development and require significant research effort.

The literature review also led to the identification of major gaps in stent research which have been addressed in the following chapters.

Chapter 2 – Finite Element Model and Material Constitutive Behaviour

2.1. Introduction

There are many stent designs which can be very different from each other, but as suggested by Sangiorgi *et al.* (2006), ideal stents should be flexible, trackable, radio-opaque, thromboresistant, biocompatible and reliably expandable. They also need to have high radial strength, high circumferential coverage, low surface area and hydrodynamic compatibility. Stents fall into different categories based on expansion mechanism, manufacturing material, geometrical design and surface coating.

2.1.1 Mechanism of expansion

The mechanisms of expansion can be self-expandable or balloon-expandable. Self-expandable stents are made of materials, such as Nitinol, that exhibit shape memory behaviour (Stoeckel *et al.*, 2003). Materials like Nitinol are characterised by a critical temperature, also called transformation temperature, which is dependent on the alloy composition and processing. Below this temperature, the alloy changes its crystalline structure and can be deformed plastically. When the material is above the critical temperature, it exhibits super-elasticity and revert to its original shape. Stents made of Nitinol are manufactured in their expanded shape, whose diameter is slightly larger than the target vessel size. The stents are then cooled down below the critical temperature (i.e. between 20°C and 30°C in the case of stent applications), compressed to their crimped diameter and attached to the catheter by means of a sliding tube. During the deployment process, the stent is positioned at the diseased site of the blood vessel and warmed up to the human body temperature of about 37° which allow itself to expand radially to restore its former shape.

Balloon expandable stents are generally made of ductile materials, such as stainless steel and Co-Cr alloy, and delivered by means of an angioplasty balloon. Either rubber or folded balloon can be used. The balloon is generally attached to one end of a catheter. The balloon can be expanded by being inflated with pressure pumped from the other end of the catheter. The stent needs to be crimped over the angioplasty balloon, and then positioned into the site with stenosis disease. When the balloon is loaded with internal pressure, it expands together with the stent to a maximum diameter. The pressure is then decreased to zero, and the balloon deflates completely, leaving the stent inside the blood vessel.

2.1.2 Materials

The stent materials must exhibit excellent corrosion resistance and biocompatibility as well as radio opacity. The corrosion resistance and biocompatibility are mandatory features that ensure the stent is suitable to be placed inside the human body without being a cause for poisoning or rejection. The radio opacity is necessary so that the deployment procedure can be performed with accuracy. They also must create minimal artefacts during Magnetic Resonance Imaging (MRI), which is used to monitor the conditions of the stent and the artery following the deployment surgery.

Typically, materials for self-expandable stents must exhibit shape memory behaviour, whilst materials for balloon expandable stents must have high strength and ductility. According to Hanawa (2009), stainless steel is the most common material used for balloon-expandable stents, but gradually replaced by high-strength alloys such as Tantalum and Co-Cr alloys. Nitinol is the dominant metallic material used for shape memory stents. New generations of stents intend to use bioabsorbable materials such as Mg alloys and Poly-l-lactid acid (PLLA).

2.1.3 Geometry

Stents can be produced into different geometries according to their application. Coil is the most common design in non-vascular applications, such as tracheal stents. Helical and spiral designs are generally promoted for their flexibility, which makes them suitable for vessels that undergo large bending. Woven shape includes a variety of designs manufactured from one more strands of wire. Sequential ring geometry is the most common for vascular application and includes stents comprised of a series of individual sinusoidal ring struts joined together by connecting elements.

The majority of commercially available stents can be generally divided into two groups, i.e. closed cell and open cell design, with different types of connection such as peak to peak or valley to valley. In a closed cell design, the individual rings are fully connected together by connective struts as illustrated in Figure 2.1a. While in an open cell design, the individual rings are only connected at selective points via connective struts as shown in Figure 2.1b. In this example, the connective elements form a spiral over the stent. Other examples of open cell designs include the use of connective elements at only two peaks/valleys, or at every other peak/valley, of the sinusoidal ring.

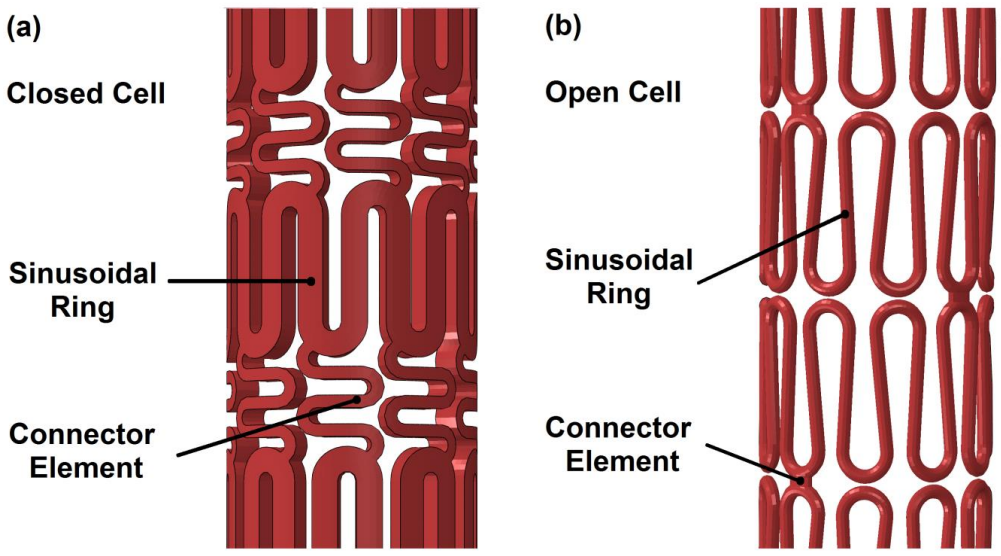

Figure 2.1. Illustration of (a) closed cell and (b) open cell stent designs.

2.1.4 Surface Coating

Stents with metal only platform are called bare-metal stents. Stents can also be produced by the addition of drug eluting coating, called drug eluting stents. In this case, stent platform is covered by a thin layer of polymer, such as Phosphorylcholine (PC) and poly(butyl methacrylate) (PBMA), which all exhibit a porous microstructure filled with drugs to battle restenosis. The drugs used include Sirolimus, Everolimus, Paclitaxel and Zotarolimus, which are released slowly from the stent coating to prevent the re-narrowing of arteries, i.e. restenosis, following stent deployment.

2.2. 3D Stent Model and Material Constitutive Model

2.2.1 Creation of 3D Stent Model

The stent geometries used for this research are produced with Abaqus CAE (Simulia, Dassault Systèmes). The stent models are created according to the design features of stents available in the market, such as Xience (Abbott Vascular), Palmaz-Schatz (Johnson & Johnson), Cypher (Cordis) and Endeavor (Medtronic). The geometrical shape and the thickness of the stent struts were reproduced for each stent, according to specifications reported in various open resources. The overall stent diameter (in its crimped state) was determined by the number of struts in the ring, whilst the length of the stent was determined by the number of rings selected.

The procedure of creating the stent geometries consisted of three stages: (i) creation of the flat version of stent; (ii) partitioning and meshing of the flat stent; (iii) wrapping of the meshed stent. In the first stage, a sketch is produced for a key cell following the centreline of the strut, as shown in Figure 2.2a. Once the centreline is defined, using a sweep tool we can obtain the 3D flat model of the key cell (Figure 2.2b). The crimped diameter of the stent is defined by the following equation:

$$d = \frac{n \cdot x}{\pi} \tag{2.1}$$

where n is the number of cells contained in one ring and x is the width of a single cell. Once n is defined, we can use a pattern tool to create the flat model of a single ring, as illustrated in Figure 2.2c. The length of the stent is also defined by a simple equation:

$$L = i \cdot y \tag{2.2}$$

where i is the number of rings for the stent and y is the height of one ring in the longitudinal direction. Once i is defined we can create the flat model of the full stent geometry by using a pattern tool (Figure 2.2d).

The second stage consists of the generation of the finite mesh of the stent. The mesh for the stents is generated by using 8-node hexahedral elements. For stent, we used full-integration incompatible elements formulation (type C3D8I) to accommodate large bending deformation analyses. This is also strongly recommended by Abaqus for stent deformation simulation. The mesh density is controlled by the number of elements through the width and the thickness of the stent struts. For example, a 2×4 mesh means that there are two elements through the width and four elements through the thickness of the stent struts. In order to obtain a quality mesh, the stent struts are first partitioned by considering also the presence of the connective elements.

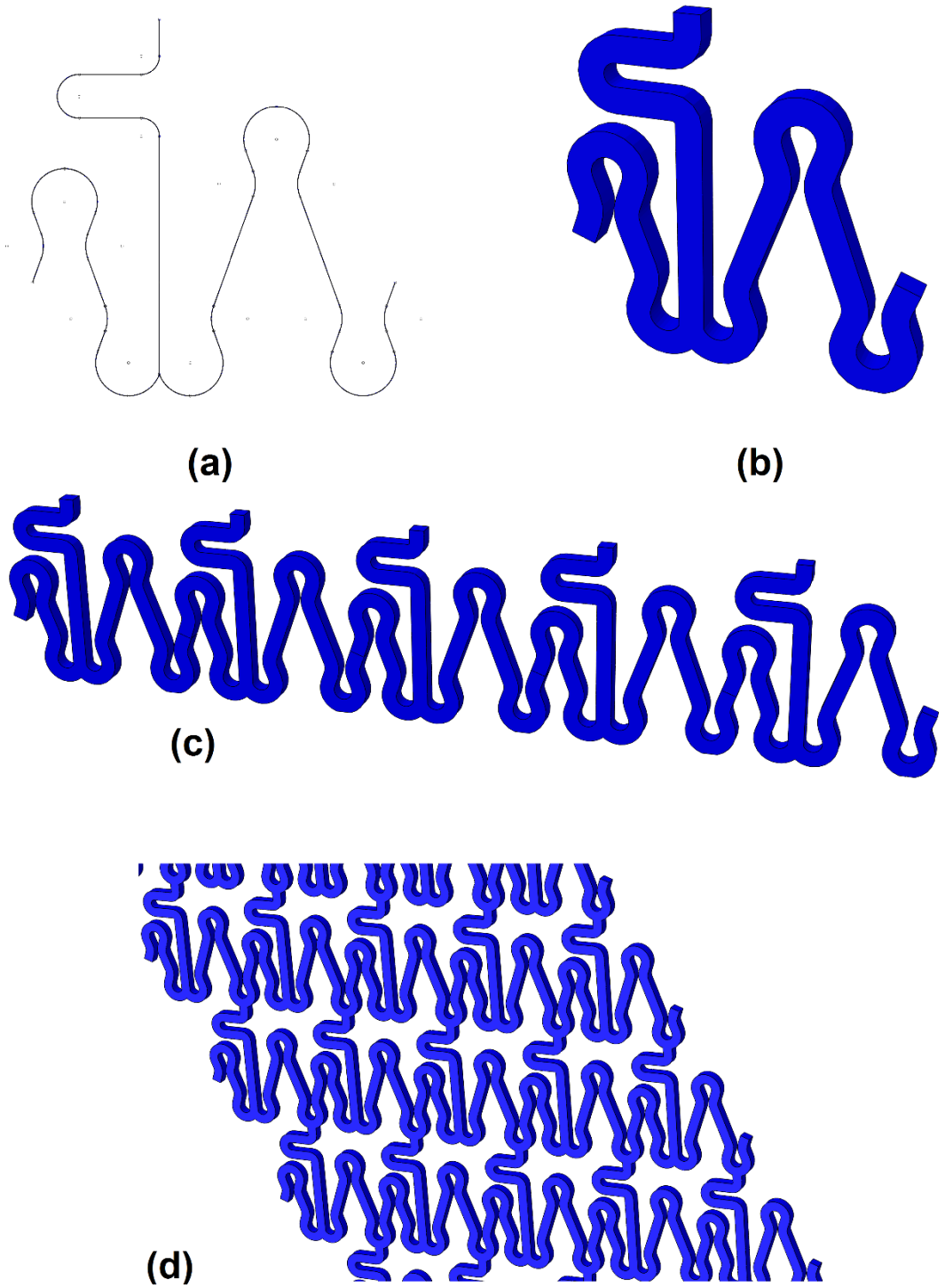

Figure 2.2. Four stages of creating the flat stent model: (a) sketching of the centreline of the key cell; (b) sweeping to produce the key cell; (c) creating one stent ring via pattern tool; (d) creation of the flat model of full stent via pattern tool.

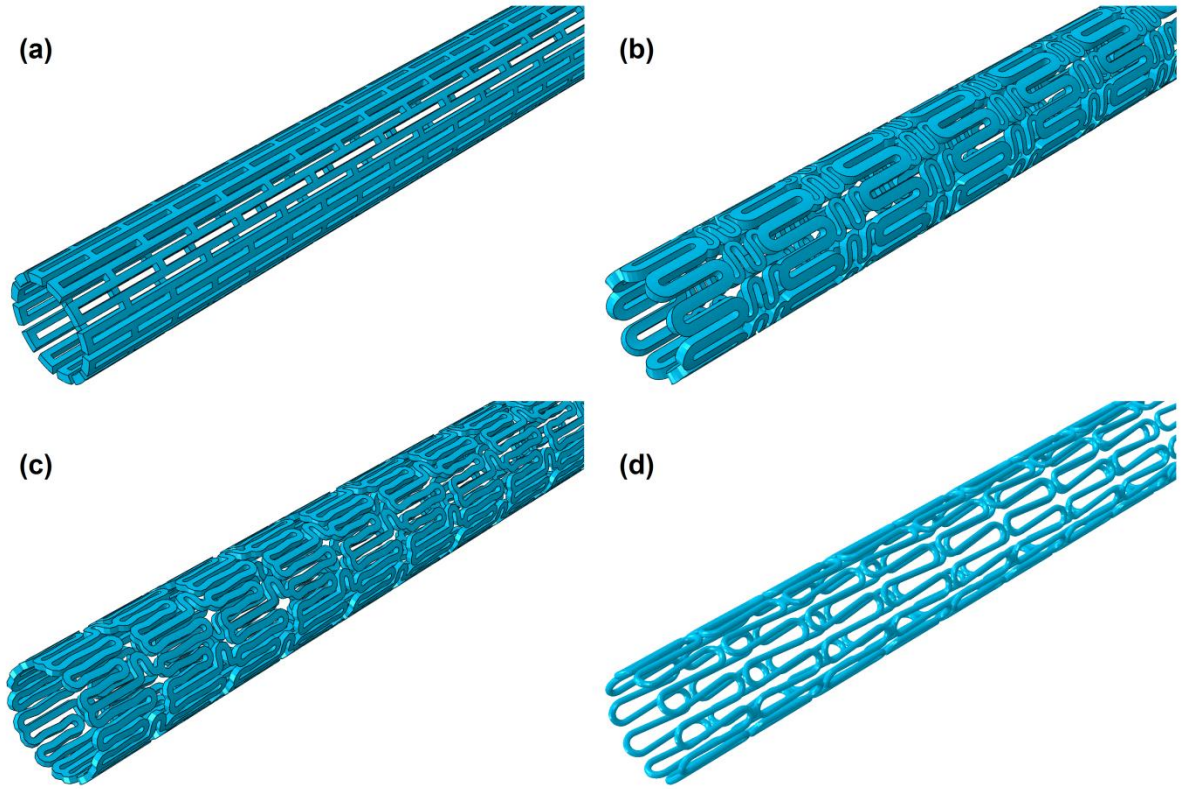

Figure 2.3. Final 3D stent geometry of (a) Palmaz-Schatz, (b) Cypher, (c) Xience and (d) Endeavor stent designs after wrapping of the flat model.

In the third stage, a wrap-up tool is used to revolve the flat model around its longitudinal axis to achieve the final tube shape of the stent. The complete 3D models for Palmaz-Schatz, Cypher, Xience and Endeavor stents are shown in Figure 2.3.

2.2.2 Constitutive Behaviour of Stent Materials

Balloon expandable stents are made of materials that exhibit highly elastic modulus and ductility. The stent deforms plastically during the inflation process and retain its deformation after the deflation of the balloon. In order to open the blocked artery effectively, the stent needs to undergo large plastic deformation, which requires the material to possess a high degree of ductility.

Table 2.1. Properties for the SS316L, Co-Cr L605 and Mg AZ31 stent materials (Medtronic Technical Bulletin, 2003; Poncin *et al.*, 2003; Wu *et al.*, 2010).

Material	ρ (kg/mm^3)	E (GPa)	ν	σ_y (MPa)
SS316L	$7.8 \cdot 10^{-6}$	190	0.30	195
Co-Cr L605	$9.1 \cdot 10^{-6}$	243	0.30	476
Mg AZ31	$1.7 \cdot 10^{-6}$	43	0.35	164

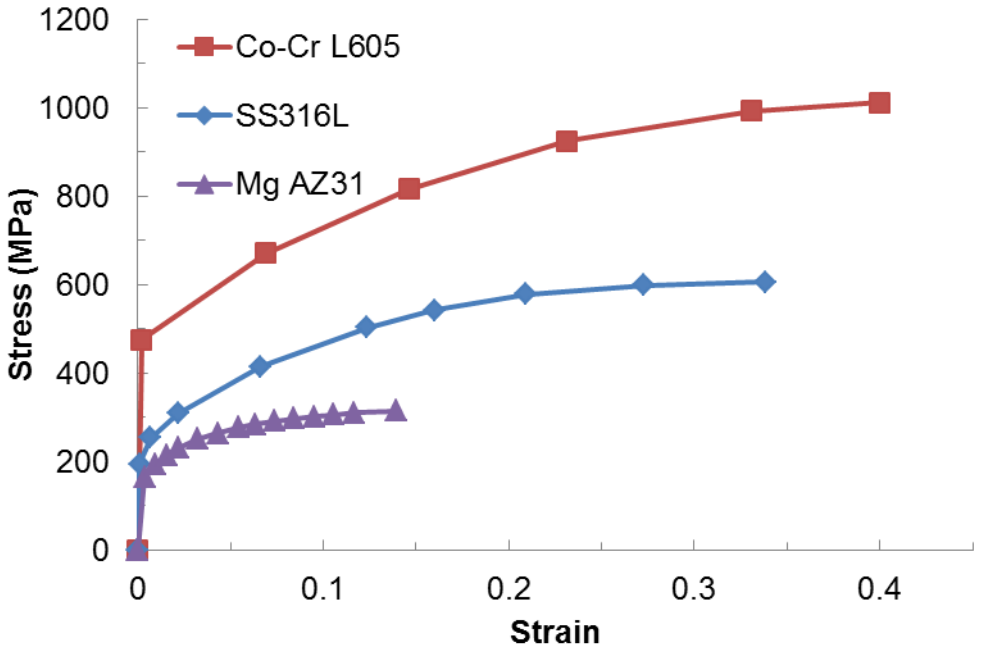

Figure 2.4. Tensile behaviour for the SS316L, Co-Cr L605 and Mg alloy (Medtronic Technical Bulletin, 2003; Poncin *et al.*, 2003; Wu *et al.*, 2010).

The stents considered in this work are made of stainless steel (SS) 316L and Co-Cr alloys (type L605 and F562). The mechanical properties for SS316L, Co-Cr L605 and Mg AZ31 are found in literature (Medtronic Technical Bulletin, 2003; Poncin *et al.*, 2003; Wu *et al.*, 2010). Table 2.1 gives the mechanical properties of the three alloys, whilst Figure 2.4 shows the stress-strain response used in our simulations. The material hardening behaviour during plastic deformation was implemented in Abaqus by considering the increase of yield stress as function of the plastic strain (Abaqus, 2013).

Co-Cr alloy is the material that shows the highest strength and ductility, it is used in the latest generations of balloon expandable stents, such as the Xience and Endeavor stents. Stainless steel is the most common material used for earlier generations of stents, such as the Palmaz-Schatz and Cypher. Magnesium alloys such as Mg AZ31, are used for development of bioresorbable metallic stents. With bioabsorbable stents, there is no need for stent removal surgeries in case of failure, as the stent will be absorbed in the bloodstream after a period of time. The shortcoming of these materials is the mechanical behaviour of such materials, which exhibits reduced ductility and strength compared to stainless steel and Co-Cr alloys. Also the biodegradation of magnesium alloys is too fast to provide a satisfactory mechanical support within the required period.

2.2.3 Constitutive Models of the Artery and Plaque

The artery consists of intima, media and adventitia layers which all consist of anisotropic fibre reinforced materials (Holzapfel *et al.*, 2005). In a first instance the layers are all assumed isotropic materials and described by the third-order Ogden hyperelastic model (Zahedmanesh and Lally, 2009). The third-order Ogden hyperelastic strain energy potential is given by the following equation:

$$W = \sum_{i=1}^{3} \frac{2\mu_i}{\alpha_i^2}\left(\lambda_1^{\alpha_i} + \lambda_2^{\alpha_i} + \lambda_3^{\alpha_i} - 3\right) + \sum_{i=1}^{3} \frac{1}{D_i}(J-1)^{2i} \tag{2.3}$$

where λ_i (i =1, 2, 3) are the stretches in the three principal directions, and μ_i (MPa), α_i and D_i are model parameters. In this model, μ_i and α_i are associated with the shear modulus which can be calculated using the equation $\mu = \frac{1}{2}\sum_{i=1}^{3} \mu_i \alpha_i$, and D_i represents the compressibility. In this work, the artery and the plaque are assumed to be nearly incompressible. This assumption was realised by specifying a Poisson's ratio of 0.49 for the material and infinitesimal values for D_1 ($D_2 = D_3 = 0$). Values of model parameters are given in Table 2.2 for the three layered blood vessel (Zahedmanesh and Lally, 2009). The material behaviour of the three layers are fitted against experimental data by Holzapfel *et al.* (2005).

The same Ogden hyperelastic model, but with i = 1 (i.e., the first order), was also used to describe the constitutive behaviour of the hypocellular and calcified plaques with parameter values given in Table 2.3 (Loree *et al.*, 1994; Zahedmanesh and Lally, 2009). The stress-strain behaviour, predicted from the Ogden model, was plotted in Figure 2.5a for the artery. It can be seen that the intima layer is stiffer than the media and adventitia layers. The stress-strain behaviour for the calcified plaque and the hypocellular plaque is compared in Figure 2.5b, indicating that the calcified plaque is more resistant to stretch or deformation than the hypocellular plaque.

It should be clarified that the strain energy potential given in equation 2.3 is the third-order Ogden model and not a generic Ogden model. The Ogden model formulation used in this paper is exactly the same as that in Abaqus. Also, the parameter values taken from Zahedmanesh and Lally (2009) were fitted for the same model (i.e. the third-order Ogden model). This is slightly different from the standard (generic) form of Ogden model, which requires particular attention when fitting parameters are taken from published papers that refer to the standard Ogden formulation.

Table 2.2. Values of the Ogden model parameters for the three vessel wall layers (Holzapfel, 2005; Zahedmanesh and Lally, 2009).

Material	ρ (kg/mm^3)	μ_1	μ_2	μ_3	α_1	α_2	α_3	D_1
Intima	$1.07 \cdot 10^{-6}$	-7.04	4.23	2.85	24.48	25.00	23.54	8.95E-7
Media	$1.07 \cdot 10^{-6}$	-1.23	0.88	0.45	16.59	16.65	16.50	5.31E-6
Adventitia	$1.07 \cdot 10^{-6}$	-1.28	0.85	0.44	24.63	25.00	23.74	4.67E-6

Table 2.3. Values of the Ogden model parameters for hypocellular and calcified plaques (Loree *et al.*, 1994; Zahedmanesh and Lally, 2009).

Material	ρ (kg/mm^3)	μ_1	α_1	D_1
Hypocellular Plaque	$1.45 \cdot 10^{-6}$	0.093	8.17	4.30E-7
Calcified Plaque	$1.45 \cdot 10^{-6}$	0.084	20.82	2.70E-7

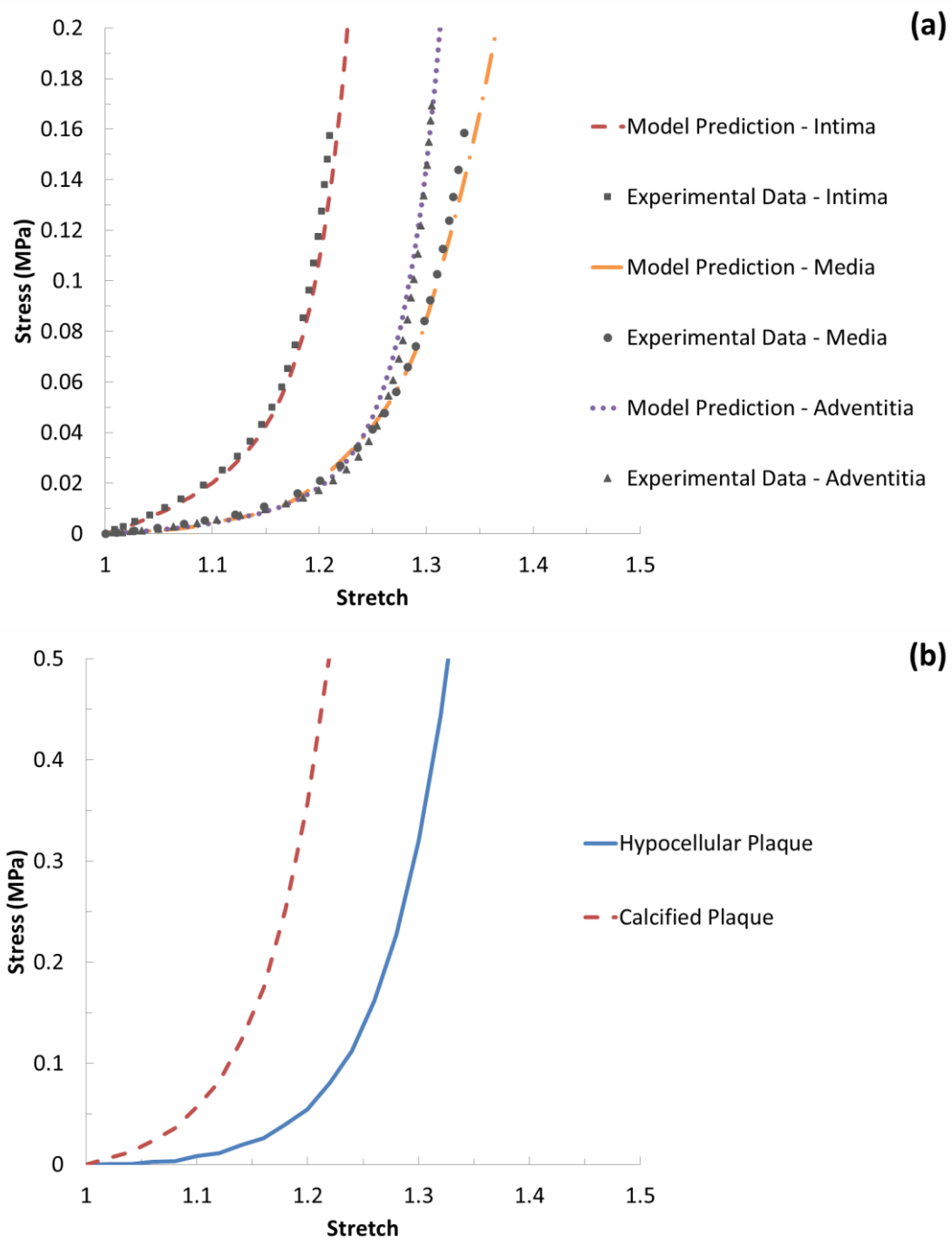

Figure 2.5. Stress-stretch curve for (a) intima, media and adventitia vessel layers (Holzapfel, 2005; Zahedmanesh and Lally, 2009) and (b) hypocellular plaque and calcified plaque predicted by the Ogden model (Loree *et al.*, 1994; Zahedmanesh and Lally, 2009).

Subsequently, the anisotropic behaviour of the three arterial layers is introduced, by using the Holzapfel-Gasser-Ogden model (HGO) formulation, with strain energy potential described by Equation 1.3. In this model, two families of fibres were considered and γ is the angle between the mean directions of the two families of fibres. The HGO model for the three arterial layers was calibrated against the average stress-strain behaviour measured for 13 patients in Holzapfel *et al.* (2005). The calibrated parameters for the HGO model are shown in Table 2.4. Figure 2.6 plots the circumferential and longitudinal stress-stretch responses of the HGO model for the intima, media and adventitia layers, which are in very good agreement with the experimental data (Holzapfel *et al.*, 2005). The radial stress-strain responses were also given in Figure 2.6, further confirming the anisotropic behaviour of the vessel layers.

Table 2.4. Parameter values of the anisotropic HGO model for the arterial layers (Holzapfel *et al.*, 2005).

Material	ρ(kg/mm^3)	C_{10}	D	k_1	k_2	κ	γ
Intima	1.066E-6	0.03	8.95E-7	4.0	1300.0	0.303	13.1°
Media	1.066E-6	0.005	5.31E-6	0.18	90.0	0.313	24.9°
Adventitia	1.066E-6	8.32E-3	4.67E-6	1.0	800.0	0.298	75.3°

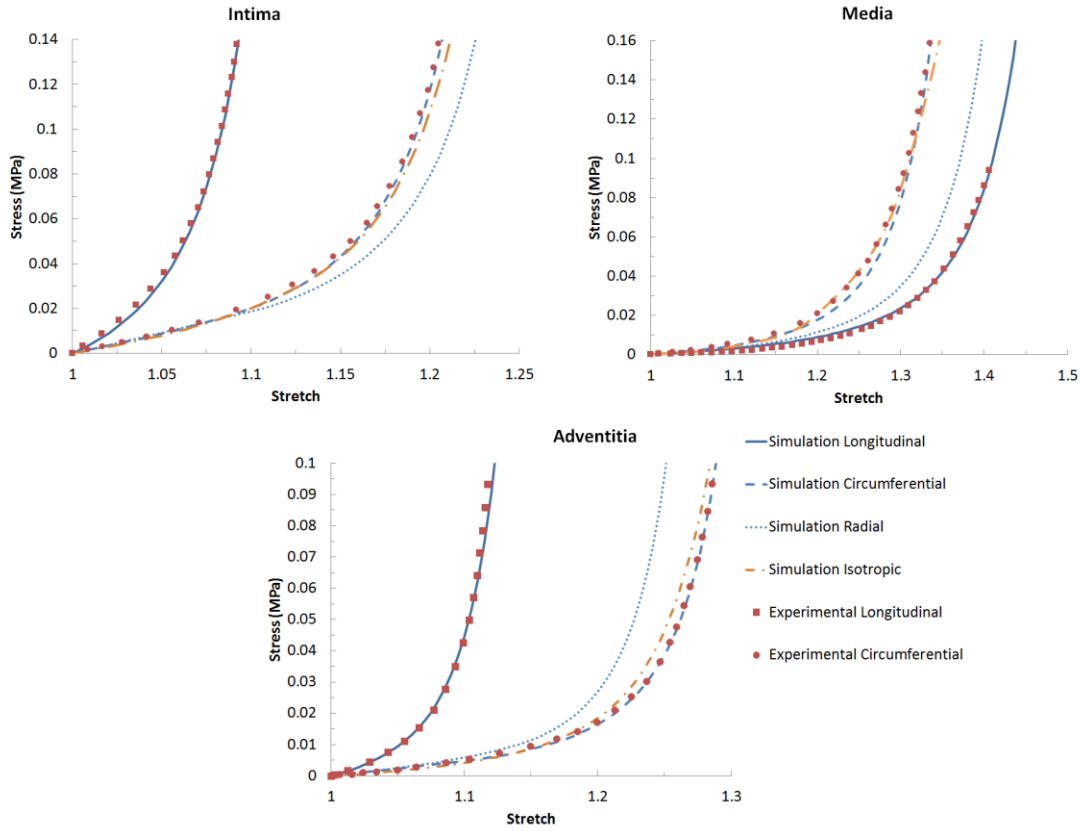

Figure 2.6. Stress-stretch response simulated using the HGO model, in comparison with experimental results given in Holzapfel *et al.* (2005).

2.2.4 Constitutive Material Behaviours of the Angioplasty Balloon

The rubber balloon was modelled using a Mooney-Rivlin hyperelastic strain energy potential W:

$$W = C_{10}(I_1 - 3) + C_{01}(I_2 - 3) + \frac{1}{D_1}(J - 3)$$
$$I_1 = \lambda_1^2 + \lambda_2^2 + \lambda_3^2 \qquad (2.4)$$
$$I_2 = \lambda_1^2\lambda_2^2 + \lambda_2^2\lambda_3^2 + \lambda_1^2\lambda_3^2$$

where λ_i (i=1, 2, 3) are the stretches in the three principal directions, J is the volumetric stretch, C_{10} (MPa), C_{01} (MPa) and D_1 are model coefficients. Physically, C_{10} is associated with the

stiffness of the material in the stretch mode, C_{01} refers to the stiffness in the shear mode and D_1 represents the compressibility of the material. Table 2.5 lists the values of the corresponding parameters (Chua *et al.*, 2004a). The stress-strain curve obtained with these parameters is shown in Figure 2.7

Table 2.5. Coefficients of the Mooney-Rivlin model used to describe the behaviour of the polyurethane balloon (Chua *et al.*, 2004a).

Material	ρ (kg/mm^3)	C_{10}	C_{01}	D_1
Polyurethane	$1.07 \bullet 10^{-6}$	1.03176	3.69266	0

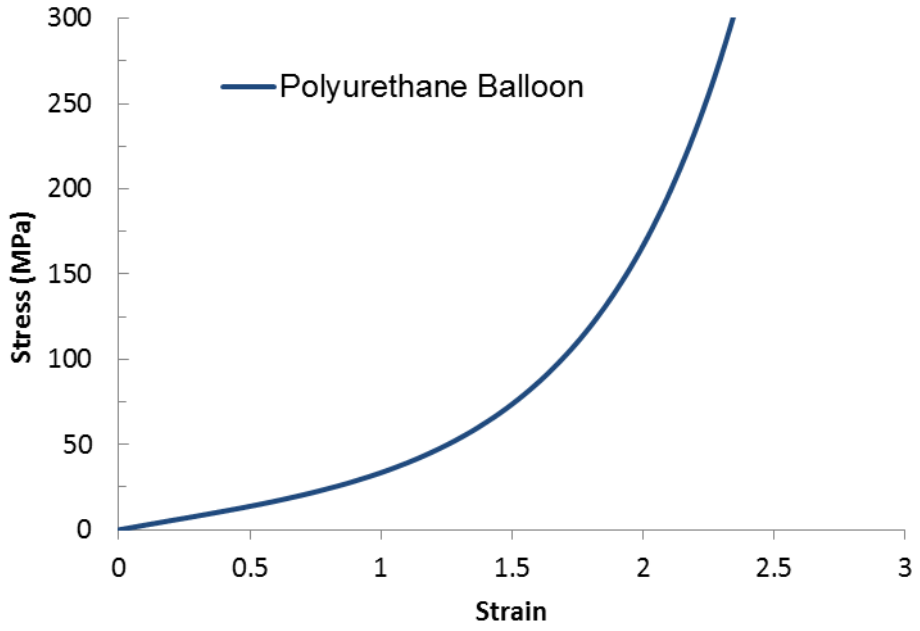

Figure 2.7. Stress-strain curve for the polyurethane Mooney-Rivlin balloon model (Chua *et al.,* 2004a).

23. Finite Element Simulation

2.3.1 Description of the Model

The simulations were carried out using Abaqus explicit solver (Abaqus, 2013), which was formed of two steps, corresponding to the inflation and deflation of the balloon. The step time was chosen to be 0.1 s for each step. The time increment was on the order of 10^{-8}s throughout the analysis. The internal and kinetic energies have been monitored during the analyses, and the kinetic energy for whole the system was always less than 5% of the internal energy, which confirmed the validity of our quasi-static analyses. Also, Abaqus used enhanced hourglass control approach for the hyperelastic materials (i.e. artery, plaque and balloon), which provides resistance to hour glassing. For the stent, since full integration elements were used, hour glassing was not encountered.

The balloon was modelled as a cylinder with a diameter that matched the inner diameter of the stent. The balloon was always 2 mm longer than the stent (i.e. one millimetre longer at each end). The blood vessel was modelled as a cylinder with axisymmetric stenotic plaque. The artery had an overall wall thickness of 1 mm and a diameter of 4 mm. The length of the artery varied between 20 mm and 40 mm depending on the different simulations. The artery was considered to consist of three tissue layers, i.e., intima, media and adventitia, with a thickness of 0.27 mm, 0.35 mm and 0.38 mm, respectively. The stenotic plaque was modelled with a length of 10 mm in all cases and thickness depending on the level of stenosis. The percentage of stenosis is related to the thickness of the plaque by the following relation:

$$\tau = \frac{1}{2}\left(\frac{\eta \cdot D}{100}\right) \tag{2.5}$$

where τ is the thickness of the plaque, η is the percentage of stenosis and D is the diameter of the healthy artery. For example, if the diameter of the healthy artery is 4 mm and the percentage of stenosis is 50%, the maximum thickness of the plaque is 1 mm. The interfaces between different

vessel layers were assumed to be coherent, and treated as perfectly bonded, which is also the case for the interface between the artery wall and the stenotic plaque.

2.3.2 Loading and Constraints

A uniform and linearly increasing pressure was applied over a time of 0.1 s to the inner surface of the balloon to simulate the inflation process, followed by deflation (pressure decreased to zero linearly). The applied pressure is between 1.4 MPa and 1.6 MPa, depending on the radial stiffness of the stents as well as the deformability of the stent-artery systems. Specifically, 1.4 MPa was used for Xience and Endeavor stents while 1.5 MPa and 1.6 MPa were used for Cypher and Palmaz-Schatz stents, respectively. In all simulations, the ends of the balloon were fully constrained as is in the real situation (fixed onto catheter), and the ends of the blood vessel were also fixed to reflect the constraint from the human body environment unless specified otherwise (Figure 2.8). Interactions between the balloon, the stent and the blood vessel were modelled as surface to surface hard contacts, with a frictional coefficient of 0.25 (Ju *et al.*, 2008). All contacts were defined prior to the inflation step. At the beginning of the simulation, there is no direct contact between any surfaces of the model. When pressure initially increased within the balloon, contact between the balloon and the stent was first established. During inflation, contacts between the stent and the artery, as well as between the artery and balloon, were also established. At the end of deflation, contacts between the balloon and all other parts were removed, whilst contact between the stent and the artery were retained which allowed t the system to recoil to equilibrium.

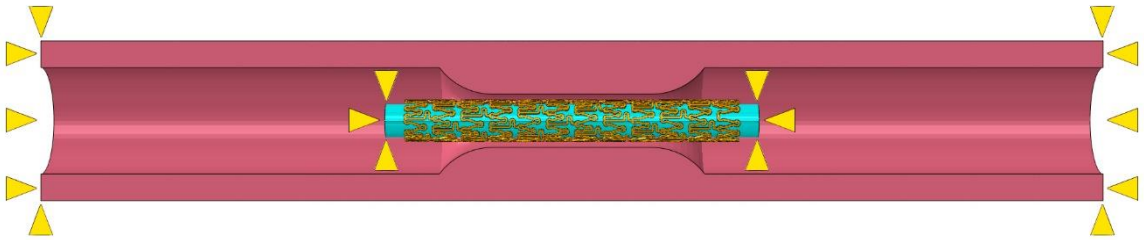

Figure 2.8. Schematics showing the boundary conditions applied to the model.

2.3.3 Post-Processing of Results

The diameter change against pressure was monitored for the stent in all simulations. Also, the coordinates of three nodes on the stent (i.e., one in the middle and two at the ends) were particularly tracked and used to determine the dogboning and recoiling effects (equations 1.1 and 1.2). The computational cost was also monitored. The simulations of full deployment were carried out using 14 cores with a frequency of 2.3 GHz each. The average CPU time of a full deployment simulation was around 4 days.

Stent indicators, such as the volume average stress (VAS), are often used to quantify the change in the stress environment induced by the deployment procedure. In this study, the stresses on the artery are caused only by the stent deployment, as the residual arterial stress is neglected throughout the simulation. Also, indicators such as the total average curvature (TAC) and torsion (TAT), are not significant due to the cylindrical symmetry of the vessel, the stent and balloon. In this study, the stress contour plot was obtained for the artery-plaque system and the stents at the end of the deflation step. Averaged stress indicators were not necessary in the case of this study, hence only the maximum values of stress on the stent and the artery were compared.

2.4. Mesh Sensitivity Study

2.4.1 Model Geometry, Materials and Meshing

Mesh sensitivity study has been carried out using a simplified stent model for which only two rings were considered. Figure 2.9 shows the finite element geometry used for this study. The stent has a length of 2 mm and an initial diameter of 1.42 mm, and the strut thickness was taken as 80 μm. The artery-plaque system was modelled as a perfect cylinder, with a length of 2 mm. The plaque had a thickness of 0.75 mm, resulting in a 40% stenossis (2.5 mm inner diameter for the artery-plaque system). The cylindrical balloon had a length of 2mm, an outer diameter of 1.25 mm and a wall thickness of 0.05 mm.

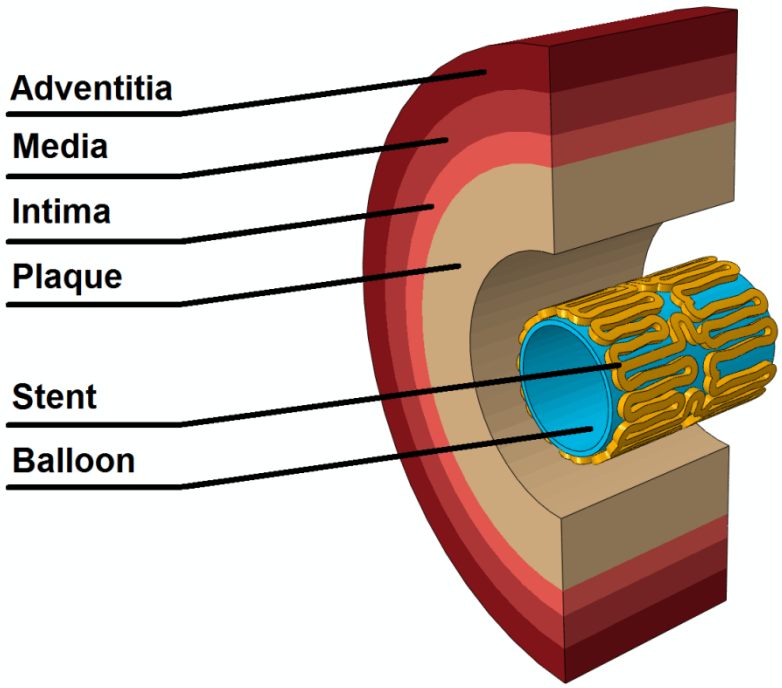

Figure 2.9. Illustration of the model used for the mesh sensitivity study.

The material model used for the Xience stent was Co-Cr alloy as detailed in Section 2.2.2 of this Chapter. For the arterial layers and stenotic plaque, Ogden model with hypocellular plaque composition has been used (Section 2.2.3) with parameters given in Tables 2.2 and 2.3 of this Chapter.

For the stent, four different finite element meshes were compared with densities 2×2, 2×4, 4×4 and 6×6 layers of elements, in the same way as already described in Section 2.2.1. Figure 2.10 shows the 2-ring Xience stent model with four different mesh densities. The mesh used was refined in correspondence of the U-bends of the struts, where higher stress levels are expected during the process of expansion.

The arterial layers were meshed using 8-node hexahedral elements with reduced integration (type C3D8R). The mesh density of the artery was studied by varying the number of layers of elements through the thickness of each arterial layer (i.e. intima, media and adventitia). Figure 2.11 shows the diseased artery with four different mesh densities, namely, 1 layer, 2 layers, 4 layers and 6 layers of elements. In all cases, the stenotic plaque was meshed using twice the layers of elements used for the arterial wall. For example, if there are 2 layers of elements through the thickness of the intima, media and adventitia layers, 4 layers of elements will be used through the thickness of the stenotic plaque.

Due to the simplification of the model, only the axial direction was fixed at the ends of the artery-plaque system and the balloon. This ensured that the artery was able to expand in the radial direction and at the same time prevented the system from rigid body movements.

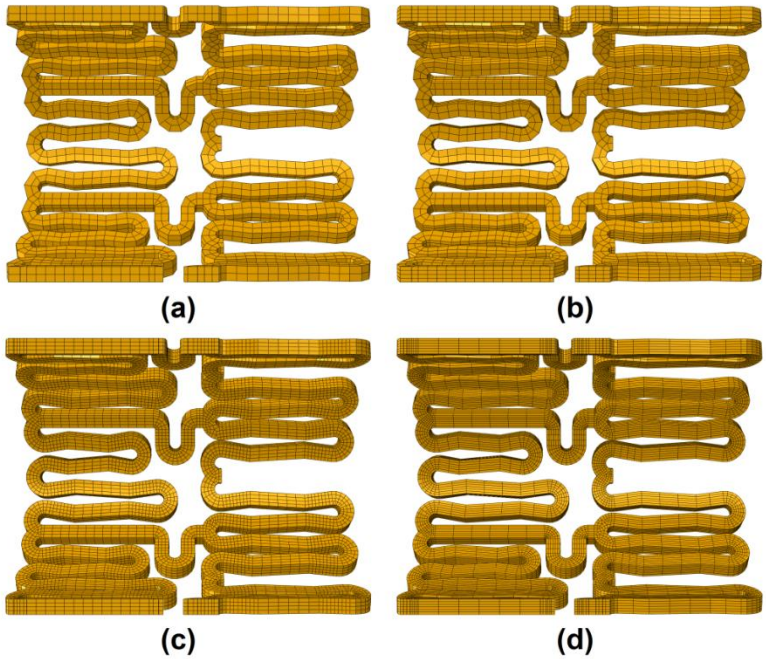

Figure 2.10. Different mesh densities used for the 2-ring Xience stent, namely, (a) 2×2, (b) 2×4, (c) 4×4 and (d) 6×6 layers of elements.

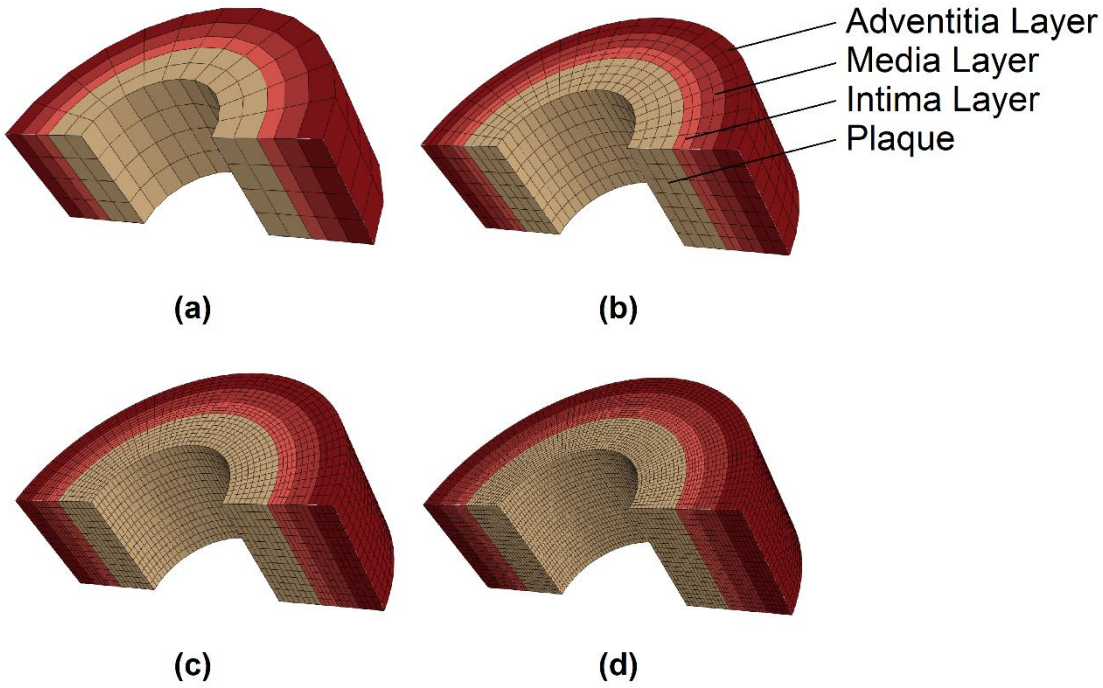

Figure 2.11. Different mesh densities for the Artery-Plaque system, namely (a) 1 layer, (b) 2 layers, (c) 4 layers and (d) 6 layers meshes.

2.4.2 Stent Mesh Sensitivity

The expansion and recoiling of the stent was similar for different meshes. As shown in Figure 2.12, the diameter was 4.5mm at the maximum pressure, and reduced to 4.0mm following recoiling, suggesting that the overall expansion and recoiling of the stent are mesh insensitive.

The stress distribution for four different meshes is shown in Figure 2.13. The maximum stress is located at the inner corner of the U-bend for all meshes. For finer mesh (4×4 and 6×6), the maximum stress becomes more localised in the central part of the strut compared to that for coarser mesh (2×2 and 2×4).

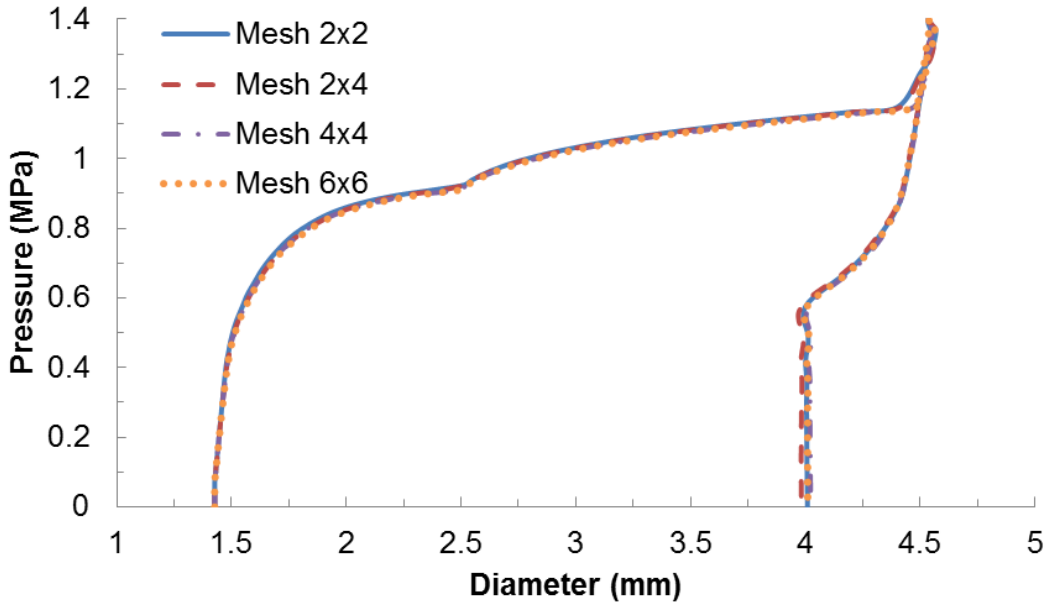

Figure 2.12. Diameter change against pressure for the stent with different mesh densities.

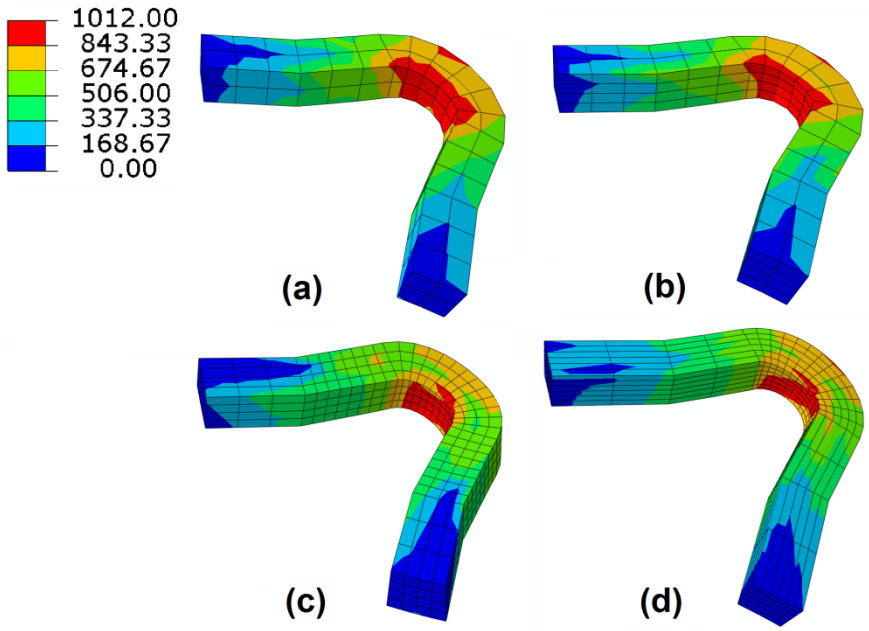

Figure 2.13. Von Mises stress (MPa) distribution on a U-bend strut meshed with (a) 2×2, (b) 2×4, (c) 4×4 and (d) 6×6 layers of elements.

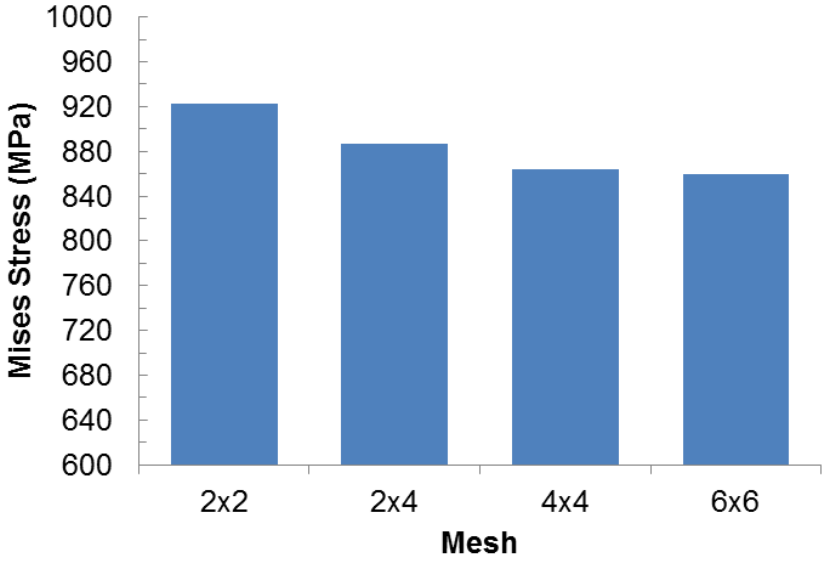

Figure 2.14. Maximum von Mises stress on a stent strut for four different meshes.

In all cases, the maximum von Mises stress was located at the centre of the U-bend, and the corresponding stress magnitude was compared in Figure 2.14 for the four meshes. The stress magnitude was found 920 MPa for 2×2 layers of mesh, which was 7% higher than the converged value of 860 MPa found for the 4×4 and 6×6 layers of meshes. The mesh with 2×4 layers of elements exhibited a value of 880 MPa, which was only 2% higher than the converged value. Consequently, convergence was considered to be achieved for the 2×4 layers of mesh.

2.4.3 Artery Mesh Sensitivity

Again, the stent expansion and recoiling were not sensitive to the mesh of the artery-plaque system, showing the similar levels of expansion at the ends of both inflation and deflation steps in all cases (Figure 2.15). In fact, only the mesh with 1 layer of elements exhibited a different expansion curve, while the stent still achieved the same maximum diameter and final diameter after recoiling as the stent with finer mesh.

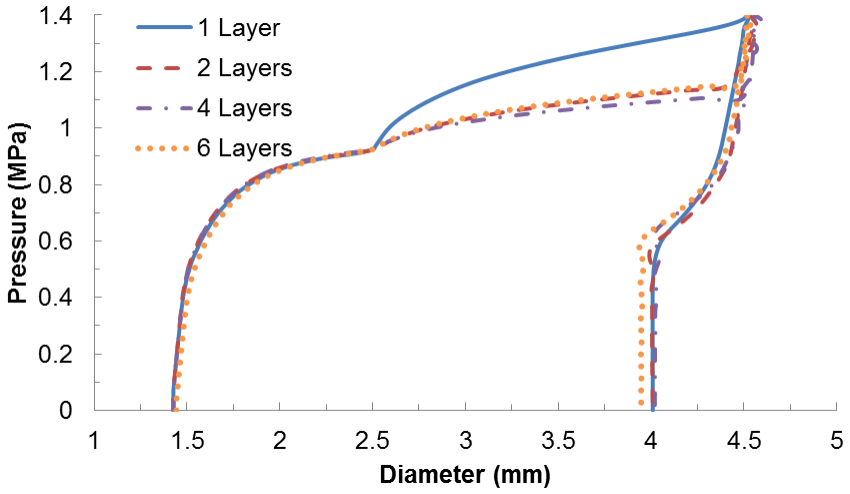

Figure 2.15. Diameter change against pressure modelled using four different meshes for the artery-plaque system.

Figure 2.15 shows the stress distribution computed using the four different meshes. The mesh with 1 layer of elements clearly does not correctly predict the distribution on the artery-plaque system. Stress appeared to be almost uniformly distributed along the plaque inner surface. Also, the magnitudes were considerably lower than what is expected. The stress distributions were consistent for the other three cases, with the highest stresses located on the left end of the vessel that is in contact with the first ring of the stent, which is also the stiffest due to the presence of the connector strut (Figure 2.9). The average stress magnitude around the middle ring of the plaque surface for different meshes is compared in Figure 2.16. The magnitude of the stress was calculated to be 0.54 MPa, 0.73 MPa, 0.79 MPa and 0.82 MPa for meshes with 1, 2, 4 and 6 layers of elements respectively. Due to the high computational costs of the analyses, a discrepancy of 10% was initially considered acceptable, therefore a mesh with two layers of elements was used. However, the mesh was later increased to 4-layer of elements (with discrepancy of 3%) for most of the simulations in this thesis.

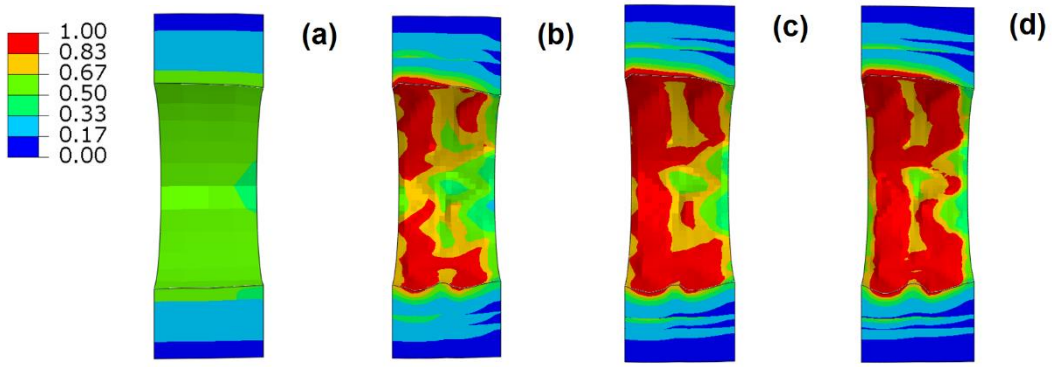

Figure 2.16. Von Mises stress (MPa) distribution after stent deployment on the artery-plaque system meshed with (a) 1 layer, (b) 2 layers, (c) 4 layers and (d) 6 layers of elements for each arterial layer.

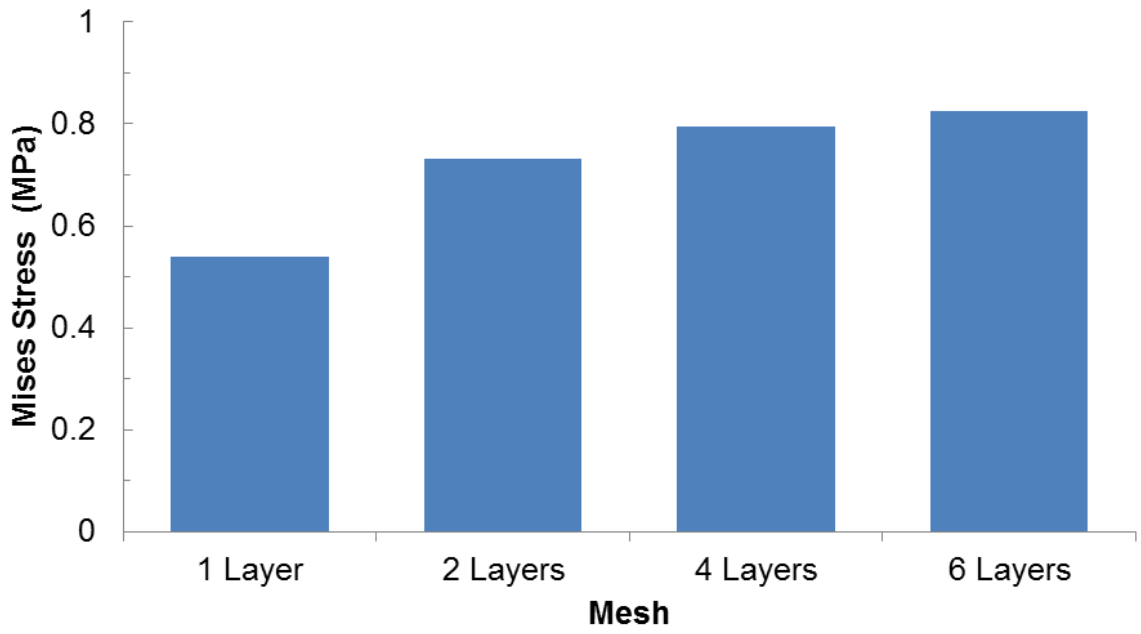

Figure 2.17. Average stress magnitude along the centreline of the plaque surface for different meshes.

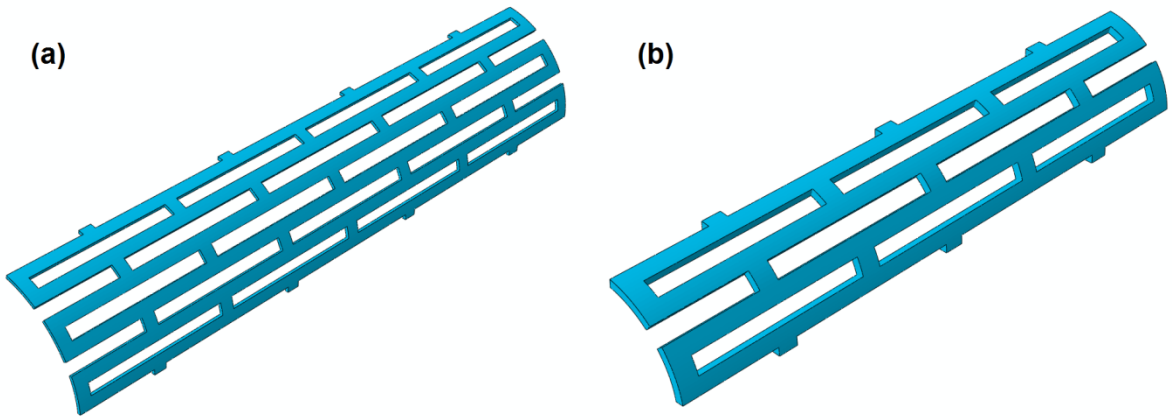

Figure 2.18. Geometries of Palmaz-Schatz stent (with length of 10 mm) as shown in (a) Chua *et al.* (2003) and (b) Chua *et al.* (2004a).

2.5 Model Validation

Due to the reduced dimensions of the device, which precludes us to monitor its expansion behaviour accurately in an artery-plaque environment, it was impossible to validate the deployment simulations with experimental in-vitro expansions. Therefore, validation of the modelling approach was carried out by comparing simulations of Palmaz-Schatz stent expansion, including both free expansion and deployment in a stenotic artery, against those in Chua *et al.* (2003; 2004a). The same approach was also used by Ju *et al.* (2008) for the validation of the Repeated Unit Cell (RUC) balloon model for stent expansion. Results from both Chua *et al.* (2003; 2004a) and Ju *et al.* (2008) were compared with the results obtained in my simulations.

Two slightly different geometries were re-produced for Palmaz-Schatz stent according to the work of Chua *et al.* (2003; 2004a). The first one (Figure 2.18a) was used for balloon-stent interaction simulation while the second one (Figure 2.18b) was used to simulate the stent expansion inside an artery with stenosis. The strut thickness and the outer diameter were 0.1 mm and 3.0 mm for the first geometry and 0.12 mm and 2.54 mm for the second one. The stents were meshed with four elements through the thickness and the width of the struts, with element type according to Section 3.2.1.

The artery with plaque was included according to the geometry in Chua *et al.* (2004a). The blood vessel was modelled as a cylinder with symmetric plaque on its inner surface. The artery has a length of 20 mm and a wall thickness of 0.4 mm while the plaque has a length of 5 mm and a thickness of 0.58 mm. The outer diameter was 4.6mm for the artery and 4.2mm for the plaque. The arterial wall was modelled as a single homogeneous hyperelastic layer. The strain energy potential used is the Ogden model (Figure 2.19), with parameters given in Table 2.6 (Prendergast *et al.*, 2003).

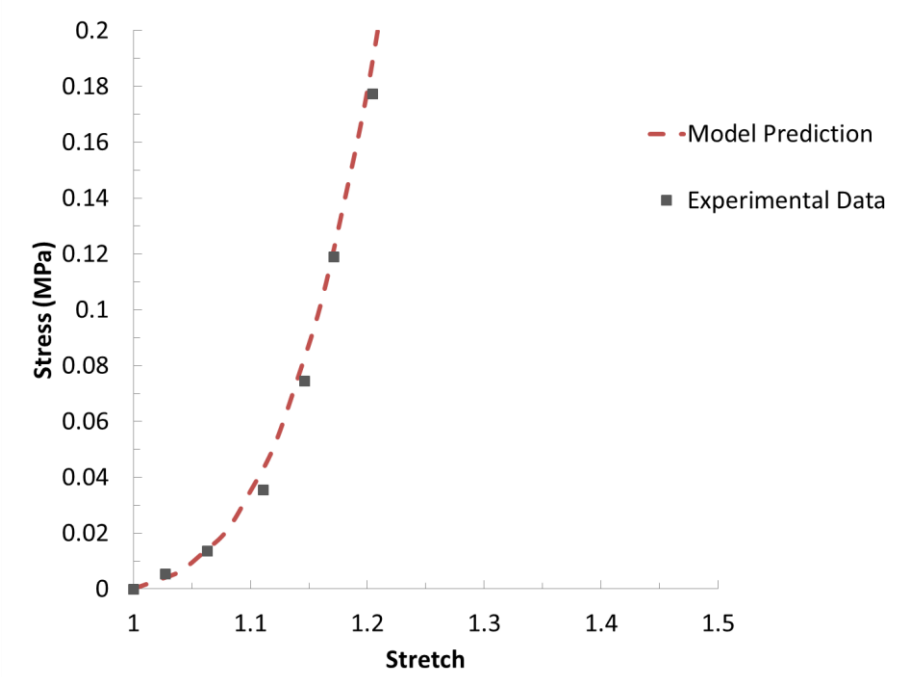

Figure 2.19. Stress-stretch curve for a homogeneous artery predicted by the Ogden model (Prendergast *et al.*, 2003).

Table 2.6. Values of the Ogden model parameters for the homogeneous artery (Prendergast *et al.*, 2003).

Material	ρ (kg/mm^3)	μ_1	μ_2	μ_3	α_1	α_2	α_3	D_1
Artery	$1.07 \cdot 10^{-6}$	-4.73	1.70	3.09	-0.39	4.41	-3.25	3.63E-6

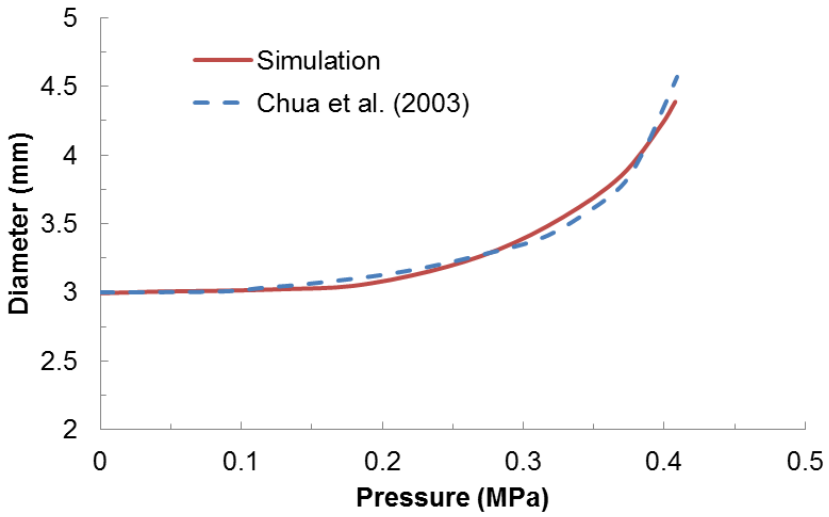

Figure 2.20. Comparison of current simulation with that in Chua *et al.* (2003) in terms of diameter change against inflation pressure during free expansion.

Good agreements were obtained for stent expansion and stress distributions, which confirmed the validity of the general method used in the present paper. Figure 2.20 shows the simulated diameter change against the applied pressure, in a comparison with that in Chua *et al.* (2003). The two curves almost follow the same path. The stent diameter started to increase once the pressure reached a value of 0.2 MPa. At the maximum pressure, the diameter of the stent increased to 4.3 mm which was slightly below that (4.5 mm) reported in Chua *et al.* (2003).

For the simulation of stent expansion in diseased artery, the diameter increased to a peak value of 4.7 mm during inflation, then reduced to a stabilized value of 3.8 mm during the deflation period due to the recoiling effect (14.9%). The achieved diameter was very close to that of the healthy artery (4.0 mm), indicating a successful deployment. The highest stress on the stent was located again at the inner corners of the struts as shown in Figure 2.21a. The magnitudes are 383 MPa at the ends of the inflation. For the inner surface of the plaque, the highest stress is mainly located

at the middle part of the plaque which is the narrowest region of the vessel (Figure 2.21b). It is also noted, especially at the end of inflation, that there are two regions with relatively high stresses which correspond to the ends of the stent. This is caused by the dogboning effect, and might introduce tissue damage to the artery. The maximum stress was found to be 1.74 MPa at the end of the inflation.

These results are comparable with those by Chua *et al.* (2004a), who simulated the same process but with a simple elastic artery model. In their results, the maximum stress was also found at the inner corners of the stent struts, with magnitudes in the range between 374 MPa and 420 MPa at the maximum pressure, which is in line with the current results. For the plaque, the stress distribution in Chua *et al.* (2004a) has the similar pattern to the current study. However, the maximum stress in their case was between 1.23 MPa and 1.38 MPa at the peak pressure, which are lower than the current results, due to the different constitutive models used for the plaque/artery systems.

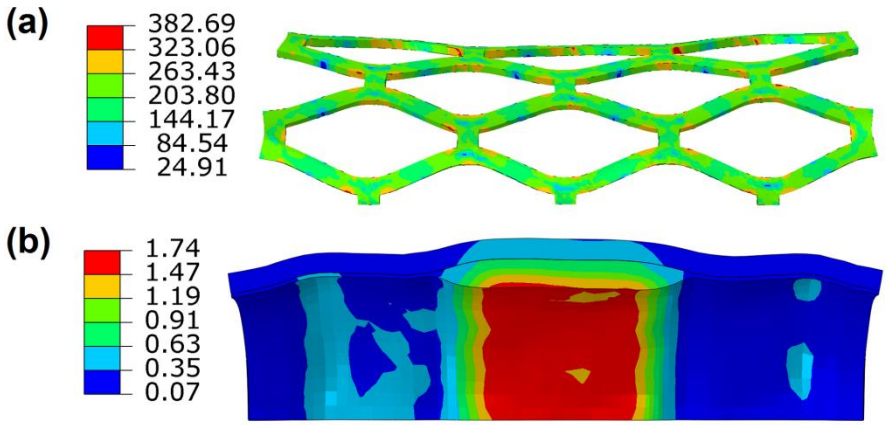

Figure 2.21. Stress distribution at the maximum inflation pressure for (a) the stent and (b) the artery-plaque system.

2.6. Conclusions

In this chapter, details about the creating the models for different stent designs are given, along with the description of the mechanical properties for each stent material. Also, the constitutive models for the arterial layers, stenotic plaque and balloon are described by giving the equations of the hyperelastic strain energy potentials and the respective model parameters.

The mesh sensitivity study showed that the expansion behaviour, i.e., diameter change of stent, is not particularly mesh sensitive. For the stent, good convergence, in terms of both the magnitude and distribution of stresses, was achieved for the mesh with 2 layers of elements through the width and 4 layers of elements through the thickness of the struts. For the artery-plaque system, good convergence was achieved for mesh with 2 layers of elements through the thickness of each tissue layer.

Validation study showed good agreement between my simulations and results published in Chua *et al.* (2003; 2004a). Specifically, the diameter against pressure was very well predicted in simulations of free expansion. The stent deployment was also successfully simulated, with achieved diameter consistent with that of a healthy artery. The stress distributions on both the artery and stent were consistent with the work of Chua *et al.* (2004a).

In conclusions, future simulations of stent expansion will be carried out using at least 4 layers of elements through the thickness and 2 layers of elements through the width of the stent struts. For simulations in which the stent is expected to undergo bending across the axial direction, a mesh with 4 elements through both the thickness and the width will be employed, since more complex deformations of the stent are expected. The mesh on the artery chosen for this study will have at least 2 layers of elements through the thickness of each blood vessel layer for simulations of stent expansion only. Simulations in which complex deformation of the artery are expected, such as

longitudinal bending, will employ a finer mesh with 4 layers of elements for the intima, media and adventitia and 8 layers of elements for the plaque.

In the following chapter, deployment of Xience stent inside a diseased artery will be studied in details by monitoring the system expansion behaviour, the stress distribution on the plaque and the stent, and the dogboning and recoiling effects of the stent. A comparison of stent performance will be presented to show how stent designs, materials, coating and plaque compositions affect the expansion of stent inside stenotic arteries.

Chapter 3 – Effects of Material, Coating, Design and Plaque Composition on Stent Deployment

3.1. Introduction

A number of recent medical case reports showed that stent implants may lead to restenosis (Okamura *et al.*, 2008), myocardial infarction (Park *et al.*, 2009), thrombosis (Choe *et al.*, 2009) and unstable angina (Adlakhna *et al.*, 2009). It was also frequently reported that stent failure might happen at any time, which can cause thrombosis, restenosis, pain and other clinical complications in patients (Kim *et al.*, 2009; Umeda *et al.*, 2009; Celik *et al.*, 2009). If diagnosed with stent failure, patients will need to undergo further surgery to remove the failed stent and implant a new one to solve the problem. To reduce the risk of complications associated with stenting, it is important to implant the most suitable stent for the patient, for which it is necessary to have a thorough understanding of the biomechanical behaviour of stents with different designs, materials and coatings. In addition, stent deployment can be affected by the plaque composition, such as calcified and hypocellular plaques, due to their very different mechanical behaviour (Loree *et al.*, 1994). A study of such effect will help cardiologists to choose the most suitable stent type to control the plaque rupture during and after stenting.

In this Chapter, finite element analyses have been carried out to simulate the deployment of Xience stent (Abbott Laboratories, USA), one of the latest commercial stents, inside a stenotic artery. The essential performances (e.g. expansion, dogboning and recoiling) of the stent were evaluated first, especially the effects of material choice and stent coating. Effect of stent designs on the behaviour is studied through comparison with three other typical stents, Palmaz–Schatz (Palmaz Scientific, USA), Cypher (Cordis Corporation, USA) and Endeavor (Medtronic, USA), representing the stents of three generations. Furthermore, this Chapter also investigated the stresses on the artery-

plaque system, which has a close connection with in-stent restenosis, and the effect of plaque composition on stent deployment.

3.2. Description of the Model

Models of four balloon expandable stents Xience, Palmaz-Schatz, Cypher and Endeavor, were produced according to the methodology in Section 3.1. The length of all stents was chosen to be 10 mm and the diameter at the crimped state was fixed at 1.5 mm. The strut thickness is 120 μm, 140 μm, 80 μm and 90 μm for Palmaz-Schatz, Cypher, Xience and Endeavor, respectively. Xience stent was chosen to investigate the effects of three typical materials, i.e. stainless steel, cobalt-chromium alloy and magnesium alloy, on stent expansion inside a diseased artery. To study the coating effect, a thin layer of polymer (with thickness 8 μm and 12 μm) was applied to Xience stent and assumed to be perfectly bonded at the interface.

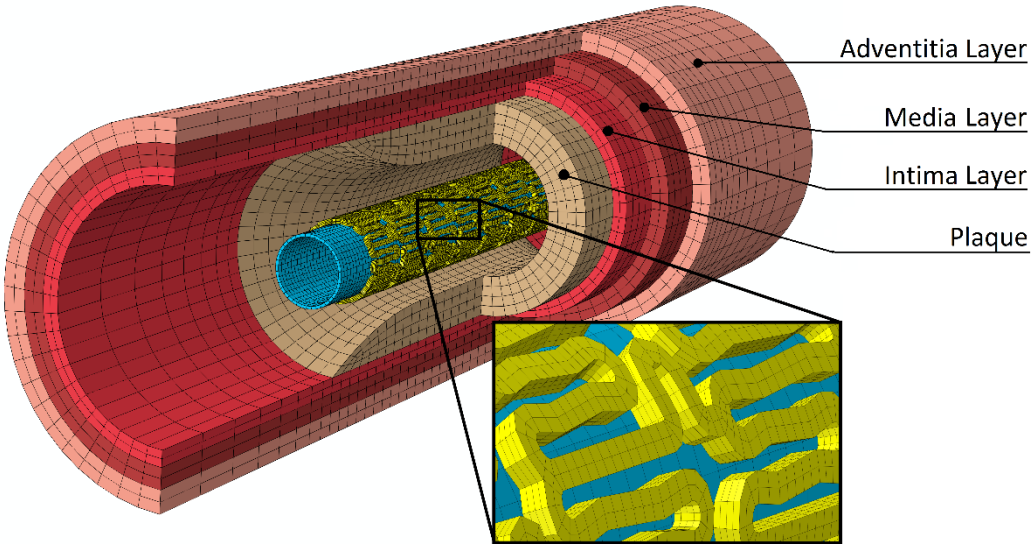

Figure 3.1. Finite element mesh for Xience stent and stenotic artery (with balloon).

Table 3.1. Bilinear properties for the phosphorylcholine (PC) polymer coating (Hopkins *et al.*, 2010).

Material	ρ (kg/mm^3)	E (MPa)	ν	σ_y (MPa)	E_t (MPa)
PC polymer	$1.2 \bullet 10^{-6}$	240	0.5	16	7.7

All the mesh densities used were in accordance with our mesh sensitivity study in Chapter 2 (Sections 2.4 and 2.5). The stents were meshed with 2 layers of elements through the width and 4 layers of elements through the thickness of the struts. The artery was meshed with 2 layers of elements through the thickness of each arterial layer and 4 layers of elements through the thickness of the stenotic plaque. The finite element mesh and geometry for the case of Xience stent is shown in Figure 3.1.

Stainless steel (type 316L) is the material used to manufacture the Palmaz-Schatz and Cypher stents, while Co-Cr alloys (type L605) are used for Xience and Endeavor stents. In addition, Magnesium alloy AZ31 was also considered to study the effect of materials on stent deployment. The three materials were all modelled using the elastic–plastic stress–strain relationship with nonlinear hardening behaviour as given in Figure 2.4 in Chapter 2. The stress-strain curves in Figure 2.4 are the tensile test data for stent materials. The stent coating was made of Phosphorylcholine (PC) polymer with bilinear behaviour and the parameter values are given in Table 3.1 (Hopkins *et al.*, 2010).

Both the blood vessel and stenotic plaque were described by Ogden hyperelastic strain energy potential given by Equation 2.3, with coefficients listed in Tables 2.2 and 2.3, in Chapter 2. The

arterial layers and the plaque were assumed to be nearly incompressible. The corresponding stress-strain curves were plotted in Figure 2.5 (Chapter 2) for these tissues. The balloon was modelled using the Mooney-Rivlin hyperelastic model, described by Equation 2.4, with parameters listed in Table 2.5 (Chapter 2).

3.4. Results and Discussion

3.4.1 Expansion Behaviour of Xience Stent

Figure 3.2a shows the change of diameter against the pressure, applied inside the balloon, for Xience stent and the artery during the process of deployment inside a diseased artery. Expansion was shown to have three stages. At the initial stage (up to 0.8 MPa), stent deforms elastically and has a lower rate of expansion. Beyond 0.8 MPa pressure, plastic deformation occurs and stent seems to expand steadily, together with the artery, at a fairly constant rate (9 mm/MPa). At a pressure of 1.1 MPa, the rate of stent expansion starts to decrease drastically, indicating that the deformation of the stent-artery system seems to reach a saturation stage, i.e., further increase of pressure only results in very limited expansion. This is mainly due to the intrinsic deformation behaviour of the artery which reached a saturation stage of stretch at a pressure of 1.1 MPa, especially the intima layer (see Figure 2.5a). Overall, stent expanded from 1.5mm to 4.8mm at the maximum pressure (1.4 MPa), with an increase in diameter by more than three fold. During deflation, recovered elastic deformation and radial pressure from the viscoelastic artery system lead to the recoil of the stent, but stabilised at 3.7 mm which is close to the diameter of a healthy artery. The achieved expansion was calculated to be 52% for the diseased artery.

Recoiling and dogboning effects were monitored during the whole deflation process, as shown in Figure 3.2b. In this case, the deflation time started when the inflation pressure reached the

maximum value of 1.4 MPa and ended when the pressure was equal to 0. After deflation the recoiling and dogboning were found to be 22% and 17%, respectively (see Figure 3.2b and Figure 3.3b for Co-Cr L605 stent). The development of both dogboning and recoiling effects is plotted in Figure 3.2b during the deflation process. It is noted that dogboning has a "negative" value at the end of inflation, which is due to the more severe expansion at the middle section of the stent. This also led to much more severe stretch for middle part of the artery-plaque system. As a result, during deflation the severely stretched artery at the middle part has a stronger tendency to recover its hyperelastic deformation, which forced the stent to recoil more at the middle section, leading to the "dogboning" effect at the end of deflation process. The development of recoiling is a continuous process due to the elastic recovery of stretched artery-plaque systems (Figure 3.2b).

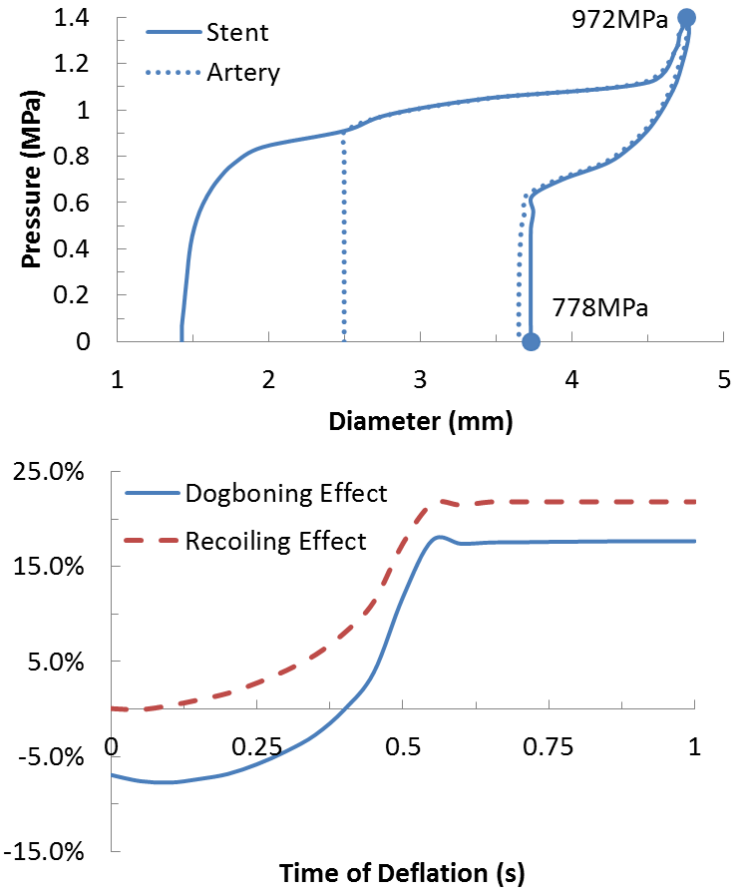

Figure 3.2. (a) Diameter change for both stent and artery during stent deployment; (b) Evolution of dogboning and recoiling during deflation.

3.4.2 Effect of Stent Materials

Three materials, Co-Cr L605, SS316L and Mg alloy AZ31, which are mainly used for stent fabrication, were considered to study the effect of materials on stent expansion. Results showed that the material choice has an influence on the behaviour of expansion (Figure 3.3a). Stents made of Mg alloy AZ31 and SS316L tend to experience higher deformation, compared to Co-Cr L605 stent, exhibiting less radial stiffness. Also, the dogboning and recoiling effects appear to be higher for stent made of stainless steel and Mg alloy (Figure 3.3b).

Figure 3.3 compares the von Mises stress distribution on the stent for the three materials following stent deployment. The stent has severe stress concentrations at the U-bends of the cell struts due to highly localised stretch. These are post-deployment stresses which were developed due to the sustained plastic deformation. From the computed results, it appears that the material choice has an impact on the magnitudes of the maximum von Mises stress on the stent. Stent made of Mg alloy has a significantly lower value (~425 MPa) than those made of Co-Cr L605 and SS316L (>700 MPa). These results are in line with the stress-strain behaviour of the three materials, i.e. higher Young's modulus and stronger strain hardening for Co-Cr L605 alloy and SS316L (Figure 2.4). For Co-Cr L605 stent, the magnitude of post-deployment stress was shown to be around 778 MPa (see Figure 3.4), which is very significant and implies the potential risk of failure during stent employment. Consequently, optimal design of cell strut U-bends appears to be important for modern stents, which can lead to stress reduction and failure resistance. However, it should be noted that in reality, the stresses on the stents might not reach such high magnitude if the stresses developed during stent crimping (Möller *et al.*, 2001; Kleinstreuer *et al.*, 2008; Shankaran *et al.*, 2012) are considered which shall mitigate the stresses developed during stent expansion.

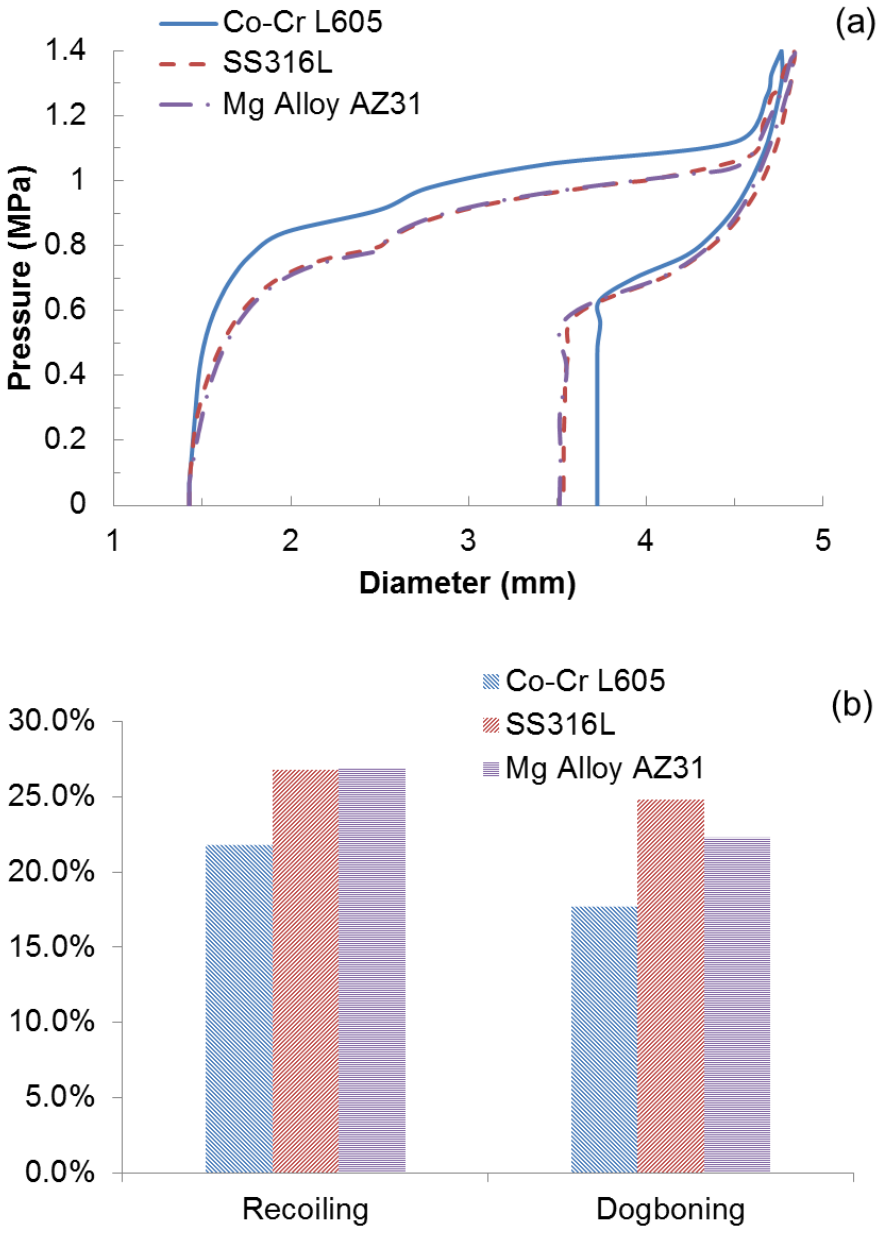

Figure 3.3. Effect of material choice on (a) stent expansion and (b) stent recoiling and dogboning.

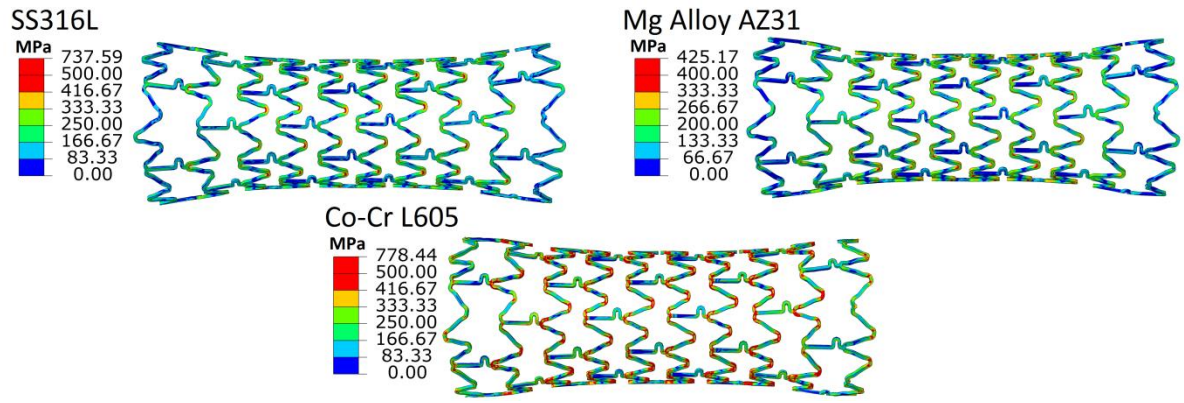

Figure 3.4. The von Mises stresses on the stents, made of different materials, after deployment.

From our simulation, at the peak inflation pressure, the maximum von Mises stresses on the plaque-artery system were located in the intima layer of the artery with a magnitude of 6.3~11.5 MPa, due to the stiffer mechanical properties of the intima layer (Figure 2.5a) as well as the severe constraint on the intima layer imposed by surrounding tissues (Figure 3.1). After deflation, the maximum stress shifted to the plaque, especially at locations where the stent and the plaque are in full contact. Contour plots of the von Mises stresses on the plaque/artery after deflation are shown in Figures 4.5. The magnitude is around 0.58 MPa for arteries expanded by Co-Cr Xience stent, and reduced to 0.36 MPa (by ~40%) and 0.29 MPa (by ~50%) respectively, when the stent material is changed to stainless steel and Mg alloy, indicating a considerable influence of stent materials. This reduction is also associated with the higher recoiling effect for stainless steel and Mg alloy stents, which further relaxed the stresses on the plaque.

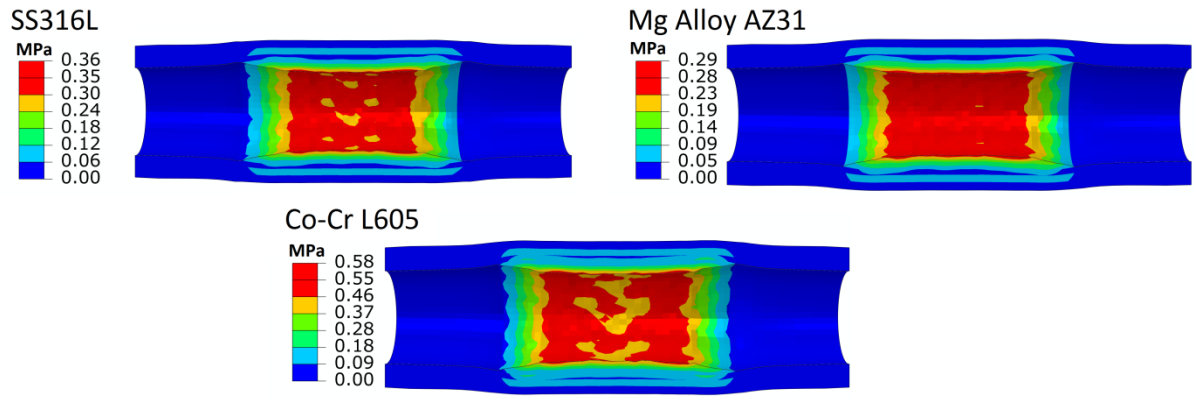

Figure 3.5. The von Mises stresses on the stenotic blood vessel following the deployment of stents made of Stainless Steel, Magnesium alloy and Co-Cr alloy after deflation.

These findings indicate that stents made of stainless steel and magnesium alloy tend to expand more than cobalt-chromium stent, but also with stronger dogboning/recoiling effects. This shows less radial stiffness for stents made of metallic materials with lower yield stress and strain hardening, which is also associated with low level of post-deployment stresses on the stents and stenotic plaque.

3.4.3 Effect of Stent Coating

Fully coated Xience stent was simulated to study the influence of stent coating on stent expansion inside a stenotic artery. Figure 3.6a shows the diameter change during expansion process, in a comparison with that for uncoated one. The maximum diameter reached 4.8mm in both simulations, but the coated stent recoiled less (18.3% for 12μm coating and 20.6% for 8μm coating, against 21.8% for the bare metal stent) due to the coating constraint (Figure 3.6b). The dogboning is also lower for coated stents (16.2% with 12μm coating and 16.8% with 8μm coating) compared to bare metal one (17.7%), as shown in Figure 3.6b. Results suggest that drug eluting

coatings has little effect on stent expansion (i.e. radial stiffness), but reduces recoil effect and increase dogboning effect slightly. For all cases the maximum von Mises stress was located at the U-bends of the cell struts, as shown in Figure 3.7. The coated stent had a higher post-deployment stress level (931.4 MPa and 793.6 MPa, respectively for 12 μm and 8 μm coatings) compared to the bare metal stent (778.4 MPa). The increase of stress level on the coated stent is due to property mismatch between the stent and the coating, which generally leads to delamination as observed in experiments, particularly in the U-bend regions (Hopkins *et al.*, 2010).

The work of Gu *et al.* (2005) showed that the required deployment pressure increases almost linearly with the thickness of coating. For a 0.1 mm thick coating, the coated stent needed an appreciatively 30% higher pressure to expand the artery to the same extent as its bare metal version. But it should be noted that, in their simulations, the coating thickness (varying between 0.08 mm~0.15 mm) is comparable to, and even larger than, the thickness of strut (only 0.1 mm). In our work, the coating thicknesses (12 μm and 8 μm) are only 15% and 10% of the strut thickness (80 μm) for the commercial Xience stent. Consequently, the coating with 8 μm thickness had no significant effect observed on the stent expansion in our computational simulations, due to the relatively thin coating layer. On the other hand, for coating with 12 μm thickness, significant reduction of the dogboning and recoiling effects were found, along with an increase in the von Mises stresses on the stent struts and the blood vessel surface.

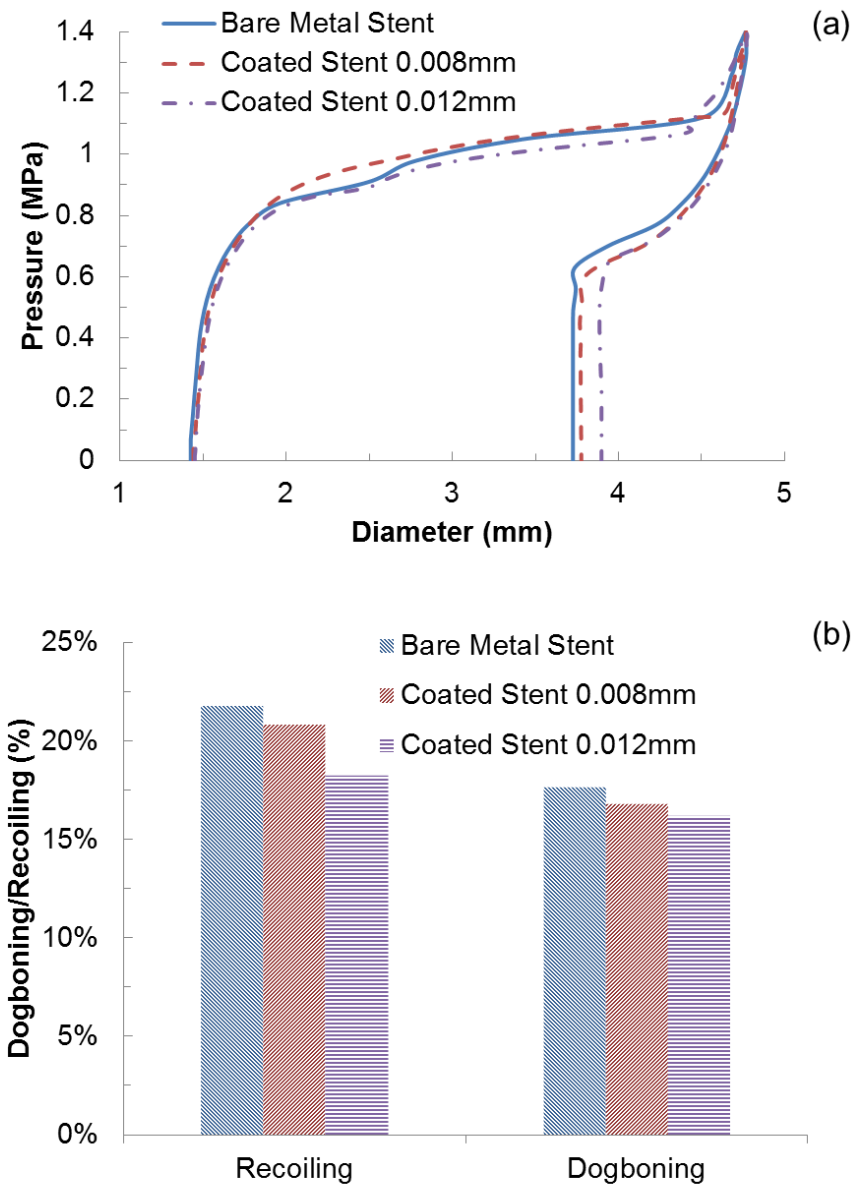

Figure 3.6. Effect of drug eluting coating on (a) stent expansion and (b) stent recoiling and dogboning.

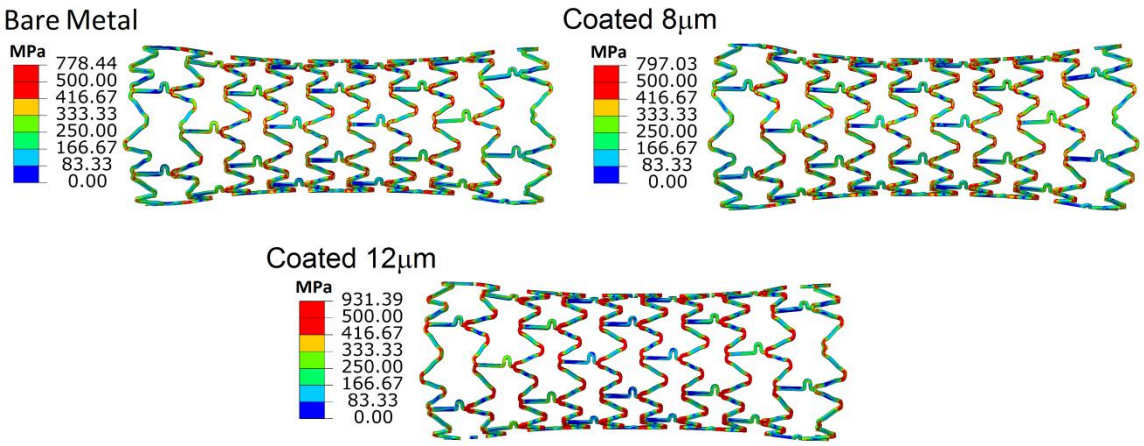

Figure 3.7. The von Mises stresses on bare metal Xience stent and coated Xience stent after stent deployment.

Figure 3.8 shows the stress magnitude and distribution on the stenosis after the expansion of stents with different coating thicknesses. The coating layer seems to increase the stress on the plaque slightly (Figure 3.8), with magnitudes of 0.60 MPa (by ~3%) and 0.68 MPa (by ~17%) respectively for 8μm and 12μm coatings.

Drug eluting coatings have little effect on stent radial stiffness as reflected by comparable expansion behaviour. However the presence of the coating decreased the recoiling/dogboning effects and increased the post-deployment stresses on the stent and plaque, suggesting a higher risk of stent failure and restenosis.

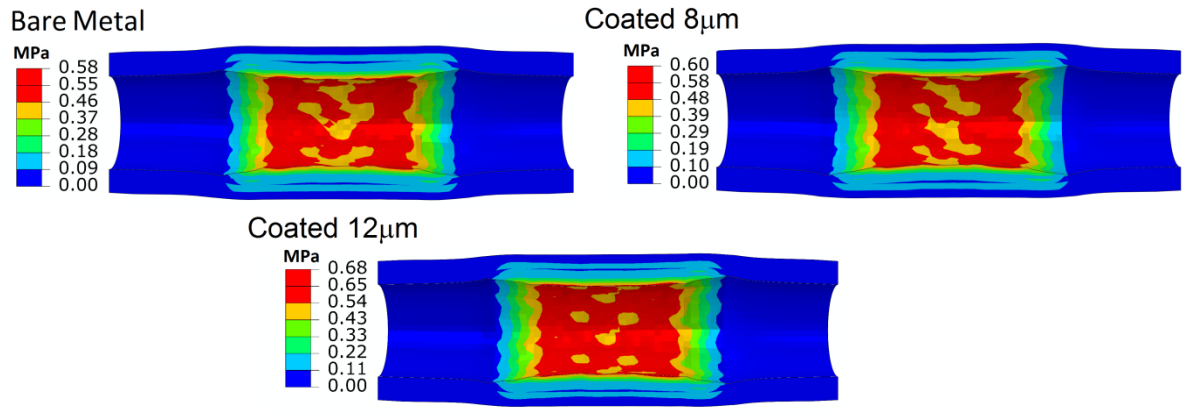

Figure 3.8. Effect of coating on the von Mises stresses on stenotic blood vessel following stent deployment for different coating thicknesses.

3.4.4 Comparative Study of Four Stent Designs

Figure 3.9a shows the change of diameter against the pressure, applied inside the balloon, for four stents, e.g. Palmaz-Schatz, Cypher, Xience and Endeavour, during expansion inside a diseased artery. Xience and Endeavor stents had similar expansion behaviour with a maximum diameter of 4.8 mm achieved at 1.4 MPa pressure. They were also easier to expand due to the open cell designs. While Palmaz-Schatz and Cypher stents, which have closed cell design, required higher pressure to expand to the same extent as Xience and Endeavor. For instance, the pressure required to reach the target diameter of 4 mm expansion is 1.2, 1.3, 1.4 and 1.6 MPa for Endeavor, Xience, Cypher and Palmaz-Schatz, respectively. This suggests that the diameter change is mainly controlled by the radial stiffness of the stent which is closely associated with the stent design.

The diameter change during balloon deflation (Figure 3.9a) appeared to be distinctly different for the four stents. This is also clearly reflected in the recoiling and dogboning effects as shown in Figure 3.9b. Palmaz-Schatz has the least percentage of recoiling (1.6%), followed by Cypher (5%), Xience (21.8%) and Endeavor (31.1%). For dogboning, Endeavor showed the most severe effect (36.8%) due to the high level of recoiling. Palmatz-Schatz also has a high level of dogboning

(22.4%) which is mostly developed during the inflation process as the recoiling effect is very little. Cypher and Xience exhibit less dogboning effect (10.4% and 17.7%, respectively), with mechanisms similar to those for Palmatz-Schatz and Endeavor.

At the end of the deployment process, the finally achieved expansion were considerably different for the four designs. The achieved diameter was found to be 3.3 mm 3.7mm, 4.1mm and 4.4 mm for Endeavor, Xience, Palmaz-Schatz and Cypher stents respectively. Xience and Palmaz-Schatz expanded to a diameter close to the target value of 4.0 mm which corresponds to the diameter of the healthy artery. On the other hand, Cypher produced an excessive expansion of the artery excessively and Endeavor produced insufficient expansion of the artery.

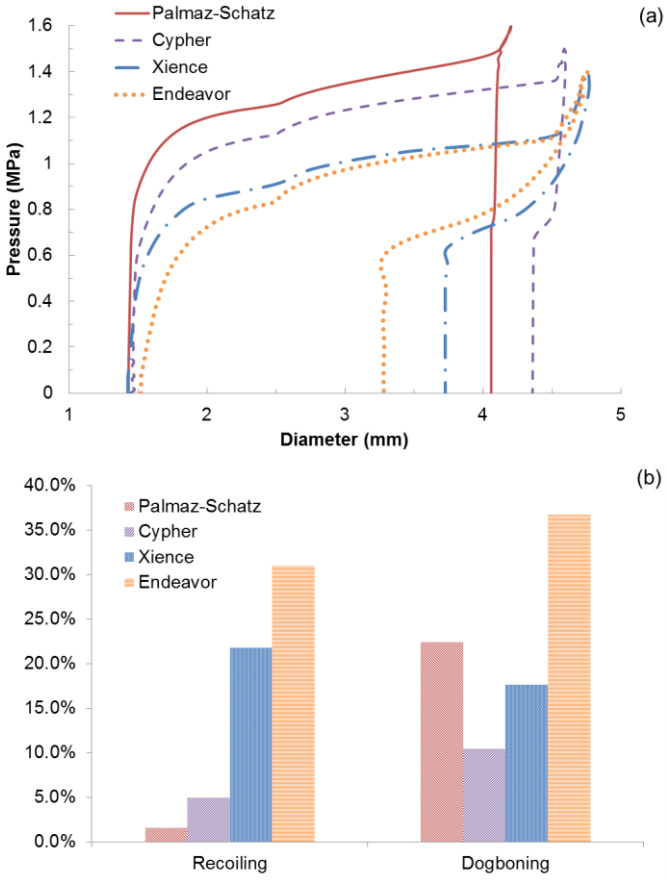

Figure 3.9. Comparison of (a) stent expansion and (b) recoiling and dogboning effects for four types of stents with distinctly different designs.

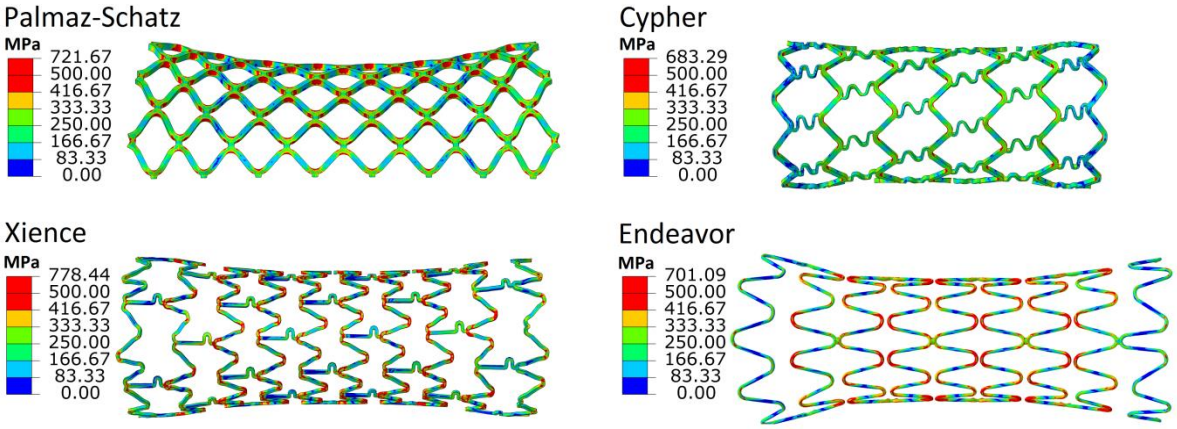

Figure 3.10. The von Mises stresses on the Palmaz-Schatz, Cypher, Xience and Endeavor stents after deployment.

Figure 3.10 gives the von Mises stress distribution after deflation. Again, all four stents showed severe stress concentrations at the corners or bends of struts. These are also the post-deployment stresses developed during the expansion process. The peak stress level seems to be close to or even higher than the ultimate tensile strength (UTS) of the materials. Consider that the UTS is ~1012 MPa for Co-Cr alloys and ~606 MPa for stainless steel, Xience and Endeavor stents, with stresses less than UTS, seem to have a lower risk of fracture during the expansion whilst the Palmaz-Schatz and Cypher exhibit a higher risk of failure as the stress magnitudes exceeded their respective UTS values. As mentioned in Section 3.2, our simulation did not consider the stress developed during stent crimping, which might be the rational for the unrealistically high stress levels obtained in our work.

Comparative study of Palmaz-Schatz, Cypher, Xience and Endeavor stents confirmed that stent expansion is mainly controlled by the radial stiffness of the stent which is closely linked with the stent design. In particular, open-cell design (e.g. Endeavor) tends to have easier expansion than closed-cell design (e.g. Cypher), but with higher recoil effect. Dogboning effect can be reduced

significantly for designs strengthened with longitudinal connective struts (e.g. Xience and Cypher). For all simulations, the maximum von Mises stresses appear to locate consistently at the bends of stent struts and their magnitudes depend on the materials and severity of plastic deformation.

Stresses on the artery-plaque inflated by the four types of stent were compared against each other in Figure 3.11, which showed distinctly different behaviour in terms of both distribution and magnitude. The latest generation of stents (e.g. Xience and Endeavor) tend to cause less stresses on the plaque-artery than the earlier generation of stents (e.g. Palmaz-Schatz and Cypher), even if they are made of stiffer Co-Cr alloys. This indicates the importance of stent designs in reducing the stresses on the artery-plaque system caused by stenting.

For artery-plaque system, the stresses appear to be largely influenced by the stent materials and designs, in terms of both distribution and magnitude. In most cases, the stress concentration tends to occur on the plaque due to the direct contact of the plaque with the expanded stent. For the artery under severe stretch (e.g. Palmaz-Schatz stent), a significant amount of stress was carried by the intima layer of the artery due to its high stiffness and strong constraints imposed by surrounding tissues as well as unrecovered deformation. This was also observed at the peak of balloon inflating pressure when the artery-plaque system experienced the most amount of stretch.

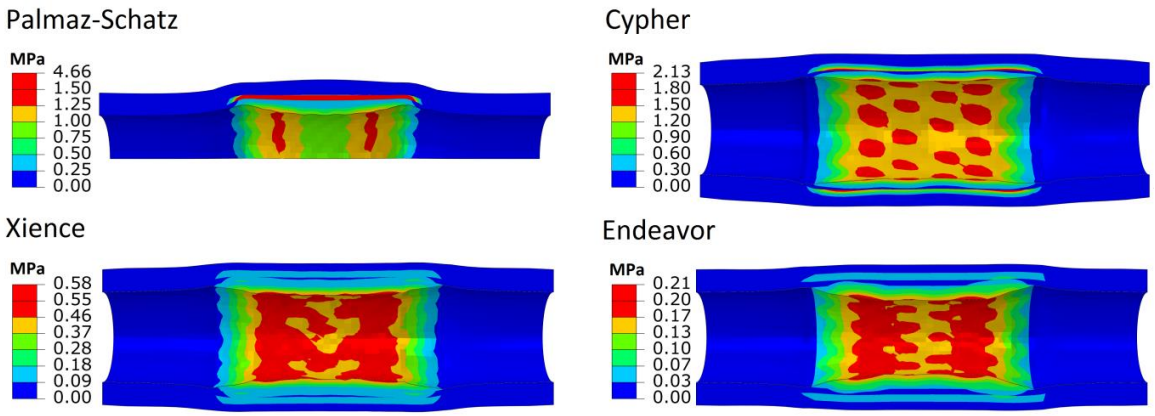

Figure 3.11. The von Mises stresses on stenotic blood vessel expanded with Palmaz-Schatz, Cypher, Xience and Endeavor stents, respectively.

3.4.5 Effect of Plaque Composition

The stenotic plaque can be modelled as hypocellular, cellular or calcified plaque depending on its composition. To study the effect of plaque composition, simulations have also been carried out for calcified plaque (cellular plaque is expected to have the behaviour in between hypocellular and calcified plaques). The calcified plaque was modelled using the Ogden model, consistent with that used for the hypocellular plaque. The model parameters given in Table 2.3 were fitted against the test data in Loree *et al.* (1994) and Pericevic *et al.* (2009). The stress-strain behaviour for calcified and hypocellular plaques is compared in Figure 2.5b, showing that calcified plaque is more resistant to stretch than hypocellular plaque. The simulations were carried out for all four stent designs using exactly the same loading and boundary conditions given in Section 4.2.

As shown in Figure 3.12, the calcified plaque affects the deployment by reducing the stent expansion considerably for all stent designs, with a final diameter between 3.0 mm and 3.3 mm only which is significantly lower than that for hypocellular plaque (Figure 3.2a). The reason is that the calcified plaque is much stiffer than the hypocellular plaque (Figure 2.5b), which prohibited the effective expansion of the stent-artery system. The von Mises stresses on the stents were found to be similar in all cases, in terms of both distribution and magnitude. However, the maximum von Mises stress on the calcified plaque is always higher than that on the hypocellular plaque as compared in Figure 3.13, with stress concentration observed towards the ends of the calcified plaque where the stent and the plaque are in strong contact caused by the dogboning effect.

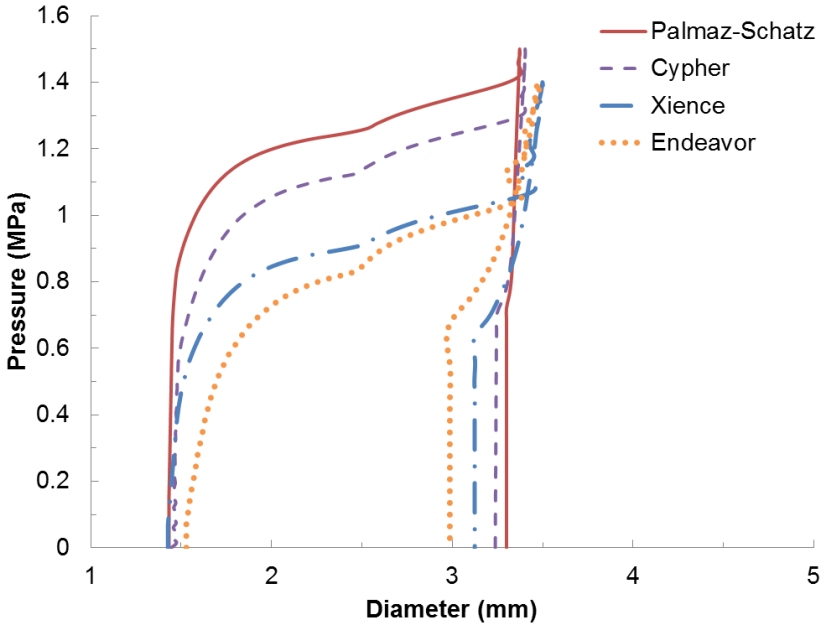

Figure 3.12. Simulated stent expansion for four types of stents using the calcified plaque model.

These results indicate that stent deployment also strongly depends on the composition of the stenotic plaque. Stent expansion simulated using a calcified plaque model tends to reach a saturation stage far earlier than that using a hypocellular plaque model (Figure 3.9a). The finally achieved expansion for calcified plaque model is significantly lower than that for hypocellular plaque model, which is true for all four stent designs. However, the stresses in the artery-plaque system suggest that Xience and Endeavor stents with open cell design are less likely to cause plaque rupture, regardless of the plaque composition, due to the lower stress levels on the plaque when compared to Cypher and Palmaz-Schatz stents with closed cell design.

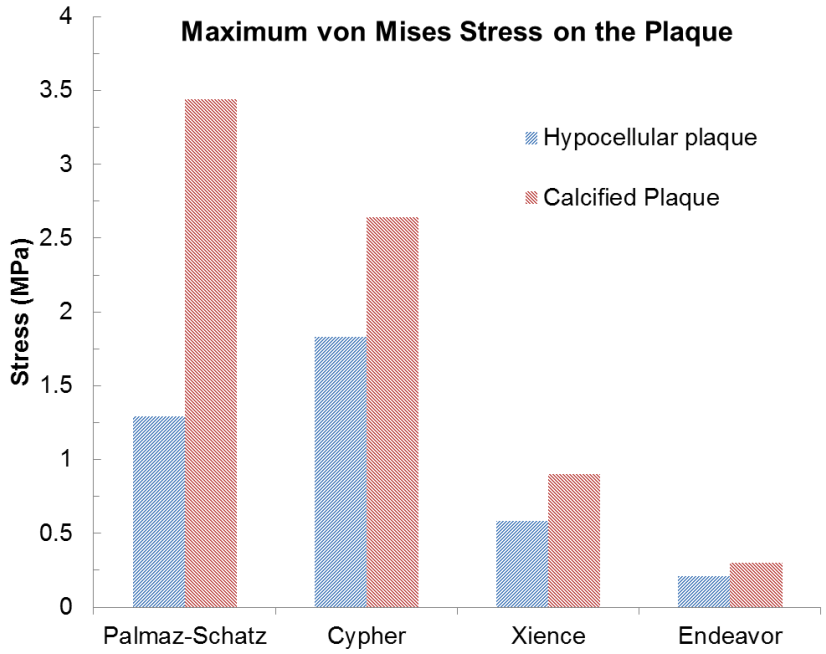

Figure 3.13. Comparison of the maximum von Mises stresses on the calcified and hypocellular plaques for the four stent designs following deployment.

3.5. Conclusions

Effects of material choice and drug eluting coating on the expansion behaviour of stents have been studied based on finite element simulations of the full process of stent deployment inside a stenotic artery. At a given deployment pressure, more severe deformation, stronger dogboning-recoiling effects and considerably reduced post-deployment stresses were observed for stents made of metallic materials with lower yield stress and weaker strain hardening. Drug eluting coatings have limited effect on stent expansion at maximum pressure, but reduced the recoiling and dogboning effects, as reflected by the diameter change against pressure. This also resulted in increased post-deployment stresses on the stent struts and the stenotic plaque.

Comparative study of Palmaz-Schatz, Cypher, Xience and Endeavor stents confirmed that stent design is one of the major factors that control stent expansion. In particular, open-cell design (e.g.

Endeavor) tends to expand more easily than closed-cell design (e.g. Cypher), but with higher recoiling effect. Dogboning effect can be reduced considerably for designs strengthened with longitudinal connective struts (e.g. Xience and Cypher). For all four stents, the maximum von Mises stresses appear to locate consistently at the U-bends of stent cell struts, with magnitudes depending on the materials and severity of plastic deformation.

Stent deployment also strongly depends on the composition of the stenotic plaque. The finally achieved expansion for calcified plaque is considerably lower than that for hypocellular plaque, which is the case for all four types of stent designs. In addition, the stresses in the plaque-artery system imply that stents with open cell design are less likely to cause plaque rupture, regardless of the plaque composition, due to the lower stress level on the plaque when compared to stents with closed cell design.

The distribution and magnitude of stresses on the artery-plaque system appear to be largely influenced by the stent materials and designs. Closed-cell designs increase the radial stiffness of stents, and hence introduce strong interaction between stent and artery during stent deployment, leading to higher stress levels on the artery. While stents made of materials with low yield stress and weak strain hardening soothed the mechanical interaction between stent and artery, leading to stress reduction on the plaque.

Overall, Xience stent was the one which performed better in the case of hypocellular plaque, leading to an expanded vessel close to the healthy arterial diameter of 4 mm and low levels of stress on the plaque-artery system. Findings also showed that Endeavor stent can be a preferred choice with the increasing plaque calcification, in order to avoid damage to the plaque and reduce the risk of restenosis.

In the following Chapter, simulations were carried out to study the effects of balloon type, artery constraints and constitutive models on the deployment of a Xience stent in a stenotic artery.

Chapter 4 – A Study of Balloon Type, Artery Constraint and Constitutive Model Used in Stent Deployment Simulation

4.1. Introduction

Finite element is an effective tool to simulate the process of stent expansion inside stenotic arteries, which helps to understand the insight of the biomechanical behaviour of the whole stent-artery system during the procedure. In stent deployment simulation, different boundary conditions have been proposed to constrain the rigid body motion of the artery. For instance, Gijsen *et al.* (2008) performed a simulation of stent deployment in a realistic coronary artery, which was obtained by three-dimensional reconstruction of a mildly stenosed coronary artery. In this simulation, the artery was fully constrained at the ends to avoid translations and rotations. Results showed the arterial walls were successfully enlarged by the stent, with peak stress values observed on the thinner portions of the artery wall. Zahedmanesh *et al.* (2010) simulated the stent expansion in a realistic artery using folded-balloon geometry. The artery was constrained at its ends using connector elements with a stiffness of 1kN/m. Expansion of stent inside the artery was simulated by either inflating the balloon or applying internal pressure directly on the stent. Application of direct pressure to the inner stent surface was found to be incapable of accurately predicting stress-strain field and the deformed configuration of both the stent and artery. However, application of pressure with restraining elements, which prevent expansion of the stent beyond the desired diameter, may be used as a computationally efficient method to accurately predict the stress-strain field in the vessel wall following full stent expansion and recoil.

One factor that has important influence in the simulation of stent expansion is the type of balloon used in the modelling. Rubber balloons, inflated by internal pressure, were generally used to simulate expansion of early generation stents (e.g. Palmaz-Schatz). Modelling of a rubber balloon

is relatively easy, and produces reliable results including both stent expansion and stresses in the stent-artery system (Chua *et al.*, 2003; Ju *et al.*, 2008). While De Beule *et al.* (2008) assessed the importance of balloon folding in the expansion behaviour of a Cypher stent and proved that the folded balloon was the only model that produced results consistent with the data provided by the manufacturer, in terms of diameter change as a function of pressure. This is particularly the case for the recent generation of stents (e.g. Cypher, Cordis) which are designed to be expanded by folded balloons. Gervaso *et al.* (2008) compared three different methods in modelling stent expansion, i.e., no balloon (pressure applied on the stent inner surface), free rubber cylinder inside the stent and folded balloon. The work showed that the folded balloon gave the expansion behaviour of Cordis BX-Velocity stent closer to the company data. Martin and Boyle (2013) also showed that considering the tri-folded shape of the balloon led to an expansion curve of Cordis BX-Velocity stent closer to the manufacturer data.

The artery constitutive model is another important factor that needs to be carefully thought about for simulation of stent deployment. Holzapfel and Ogden (2010) reviewed the mathematical modelling of the mechanical behaviour of the human artery wall. This review showed the state of the art of development of constitutive models in the last ten years to describe the mechanical behaviour of artery tissue. It highlighted the highly nonlinear and anisotropic behaviour of the blood vessel tissue (see Chapter 6). This work also suggested that in many cases the artery behaves purely elastically and can be characterized by hyperelastic strain energy functions, including the layer specific constitutive models used to describe mechanical behaviour of arteries. Holzapfel *et al.* (2005) published an extensive experimental work to determine the layer-specific mechanical properties of the human coronary arteries. Their results showed that the intima is the stiffest layer over the whole deformation domain whereas the media in the longitudinal direction is the softest. They also proposed a strain energy function to model human coronary arteries as a composite structure composed of three solid mechanically relevant layers with different mechanical

properties. Although strain energy potentials have been dominantly employed to describe the constitutive behaviour of blood vessels, the influence of different hyperelastic potentials in simulation of stent expansion has not been studied yet.

In this Chapter, computational analyses have been carried out with Xience stent to evaluate the effect of different modelling practices used in the simulation of stent expansion inside a diseased artery. The simulations using folded balloon and polyurethane rubber balloon were compared against each other in terms of diameter change, recoiling, dogboning and stresses for the whole stent-artery system. The effects of boundary conditions were assessed by comparing the stent expansion in fully constrained, partially constrained and unconstrained arteries. Simulation of stent expansion was also studied by considering different strain energy potentials used to describe the constitutive behaviour of blood vessel and stenosis. This work is of help and guidance for reliable finite element analyses of stent deployment in-vivo.

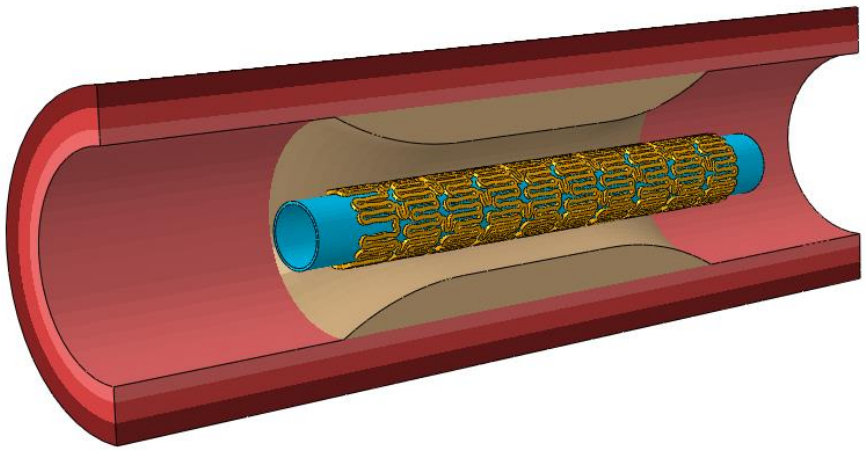

Figure 4.1. Finite element model and geometry of the stent, balloon and stenotic artery.

4.2. Description of the Model

4.2.1 Finite Element Model

In all simulations, Xience stent was employed. The finite element model, mesh, geometry and constitutive models for the stent, balloon, artery and hypocellular stenotic plaque were equivalent to those described in Chapters 2 and 3 of this thesis. Figure 4.1 shows the finite element model used, with Xience stent, rubber balloon and diseased stenotic artery.

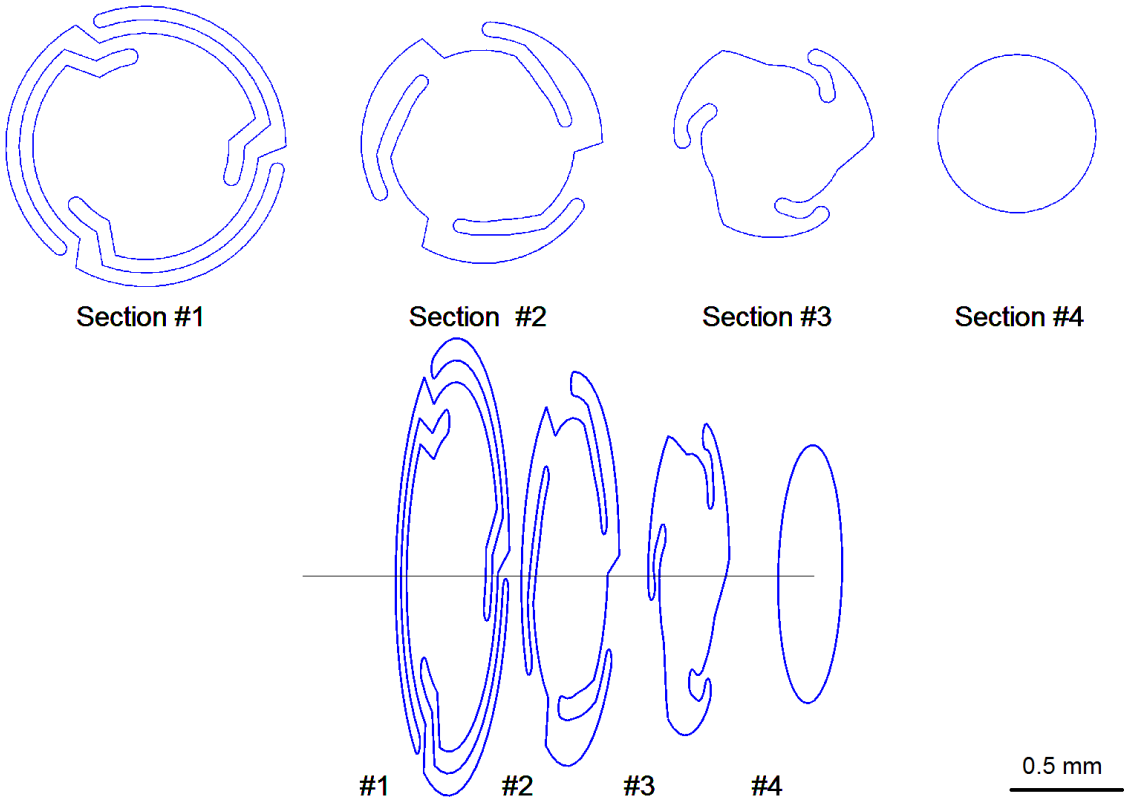

Figure 4.2. Cross sectional sketches of the folded balloon, from fully folded shape (#1) to a simple circular shape (#4).

4.2.2 Modelling of Folded Balloon

The geometry of the balloon was modelled using NX (Siemens PLM Software, UK) as a fully folded shell surface with an overall length of 12 mm. The folded shape of the balloon was firstly sketched as shown in Figure 4.2 (#1), with a diameter of 1.25 mm when fully folded and a diameter of 3.7 mm when fully unfolded. The sketched section was then extruded to the prescribed length of the balloon, which was 10mm in this case. Both ends of the angioplasty balloon are attached to a catheter and fully contrained in our simulations. The geometry of the ends of the balloon was reproduced using the sweep tool in NX. Specifically, a series of cross-sectional sketches were drawn first, gradually transiting into a simple circle with a diameter of 0.75 mm, as shown in Figure 4.2 (from #2 to #4). The sketches were positioned with an even distance across a length of 1mm at each end of the balloon, and subsequently the surface was produced by sweeping through the cross sectional sketches to obtain the desired geometry. The final model of the fully folded balloon is shown in Figure 4.3, showing the cross sectional and side views.

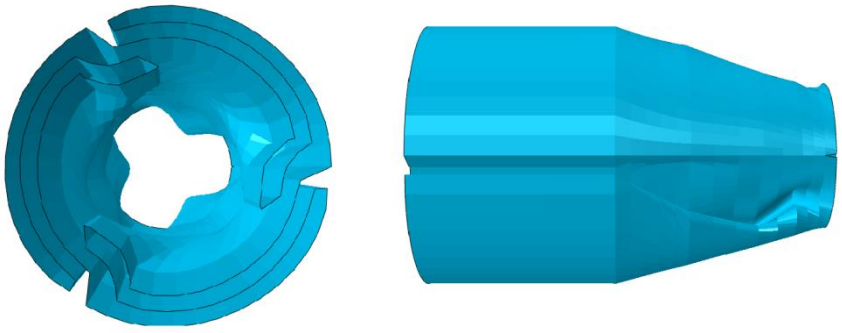

Figure 4.3. Cross sectional and side view of the folded balloon.

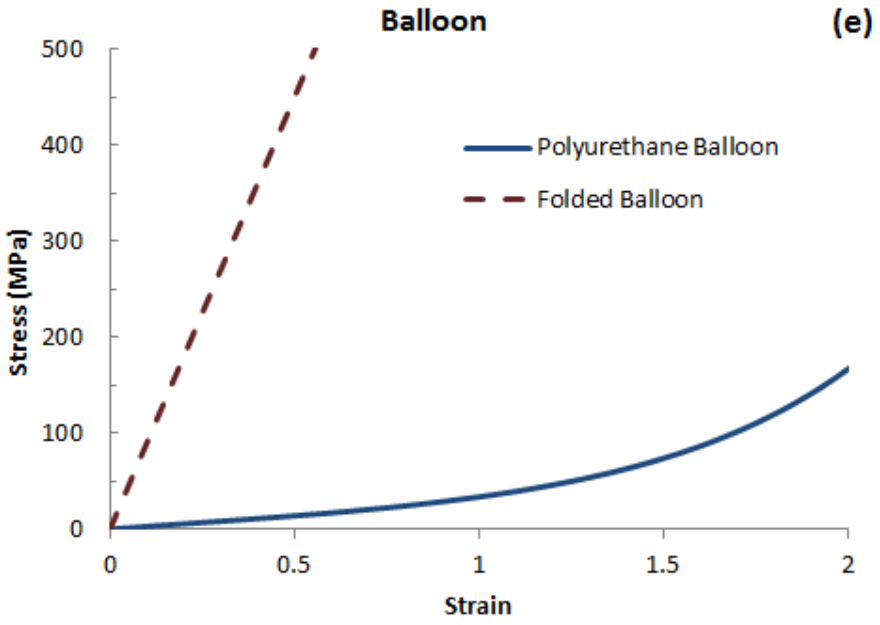

Figure 4.4. Stress-strain curve for polyurethane balloon model (Chua *et al.,* 2004a) and folded balloon (Gervaso *et al.*, 2008).

The folded balloon was meshed using 4-node shell elements with reduced integration (S4R), which were found suitable to simulate the balloon unfolding process. The choice of membrane formulation, characterised by the absence of bending stiffness, was also considered in literature to save computational effort. However, membrane elements were not employed in this thesis as they were less efficient in modelling the contacts of the balloon with the stent and the artery when compared to shell elements. The balloon material modelled as a linear elastic material with Young's modulus of 900 MPa and Poisson ratio of 0.3 (Gervaso *et al.*, 2008). The stress-strain response of the folded balloon is compared with that of a rubber balloon in Figure 4.4. At a given strain, the folded balloon has a high stress level due to its linear elastic behaviour and higher modulus.

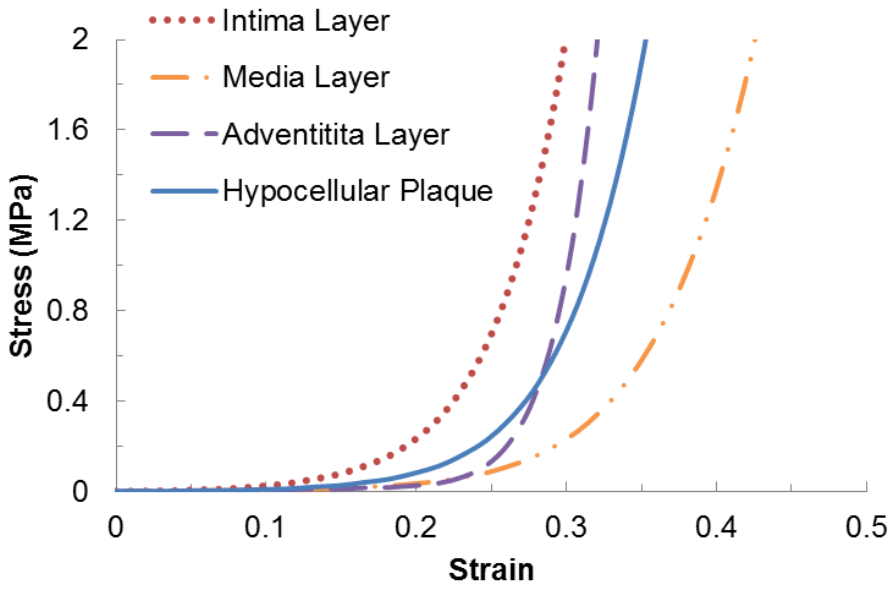

Figure 4.5. Stress-strain curve for three vessel layers (intima, media, adventitia) and hypocellular predicted from the polynomial model (Holzapfel *et al.*, 2005; Prendergast *et al.*, 2003; Gastaldi *et al.*, 2010).

4.2.3 The Polynomial Model for the Arterial Layers

To study the effect of different constitutive models, the incompressible polynomial strain energy potential is considered for both the artery and the hypocellular plaque based on the work of Gastaldi *et al.* (2010). The incompressible polynomial strain energy potential is given as:

$$W = C_{10}(I_1 - 3) + C_{20}(I_1 - 3)^2 + C_{30}(I_1 - 3)^3 + C_{40}(I_1 - 3)^4 + \\ + C_{50}(I_1 - 3)^5 + C_{60}(I_1 - 3)^6 \quad (4.1)$$

where C_{i0} (i=1-6) are model parameters. The artery was modelled as a 3-layered structure and the corresponding values for all parameters are given in Table 4.1 (Gastaldi *et al.*, 2010). Model parameter values for hypocellular plaque are also given in Table 4.1 (Loree *et al.*, 1994). Figure 4.5 shows the stress-strain behaviour, predicted from the incompressible polynomial strain energy

potential, for the artery and the hypocellular plaque, which is similar to those predicted from Ogden model (Figure 2.5 in Chapter 2).Unlike the Ogden model given in Equation 2.3 in Chapter 2, the polynomial strain energy potential does not account for the second invariant of the stretch tensor as shown in Equation 4.1.

Table 4.1. Values of the polynomial model parameters for the three vessel wall layers and the hypocellular plaque (Holzapfel *et al.*, 2005; Prendergast *et al.*, 2003; Gastaldi *et al.*, 2010).

Material	ρ (kg/mm^3)	C_{10}	C_{20}	C_{30}	C_{40}	C_{50}	C_{60}
Intima	1.07E-6	6.79E-3	0.54	-1.11	10.65	-7.27	1.63
Media	1.07E-6	6.52E-3	4.89E-2	9.26E-3	0.76	-0.43	0.087
Adventitia	1.07E-6	8.27E-3	1.20E-2	0.52	-5.63	21.44	-
Hypocellular Plaque	1.45E-6	2.38E-3	0.19	0.39	3.73	-2.54	0.57

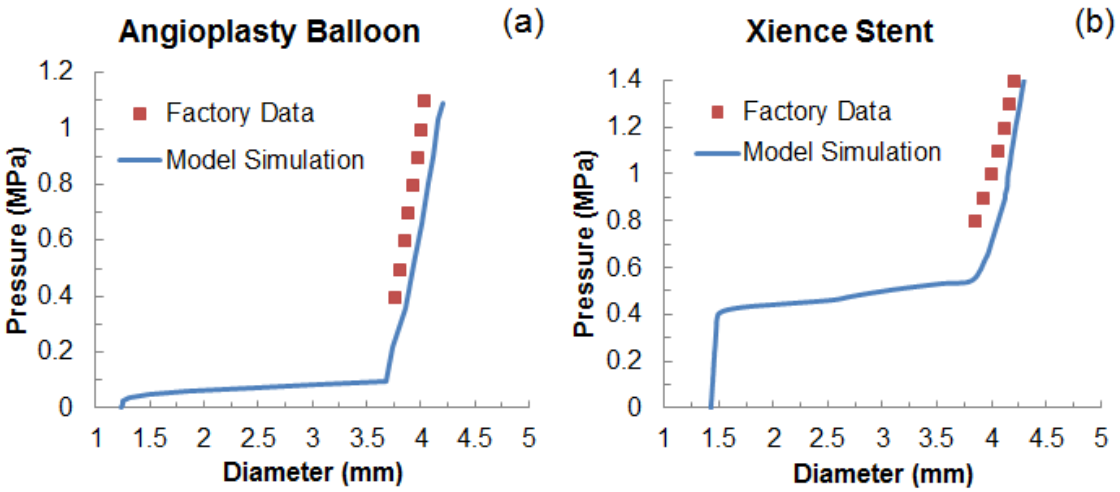

Figure 4.6. Comparison of diameter change against pressure between simulated results and factory data for free expansion of (a) the folded balloon and (b) the Xience stent.

4.3 Results and Discussion

4.3.1 Validation of the Folded Balloon Model

The folded balloon was created based on the expanding mechanism of the NC MERCURY PTCA Catheter (Abbott Laboratories, Abbott Park, Illinois, U.S.A.). In order to validate the model, factory data, in terms of diameter change against pressure, were used and compared with the simulated expansion behaviour. Results are shown in Figure 4.6a, which confirms validity of the folded geometry and material properties used in this simulation.

For further validation, the simulation of free expansion of a Xience stent was also carried out and the obtiaed expansion behaviour is compared with the manufacturer data (Abbott Vascular, 2012). As shown in Figure 4.6b, there is a very good agreement between the simulations and the factory data, confirming the validity of the folded balloon model.

4.3.2 Effects of Artery Constraints

The effect of artery constraints on the stent expansion is shown in Figure 4.7. Three types of constraints were considered, i.e., free of constraint artery, partially constrained artery and fully constrained artery. The artery free of constraint can expand in both radial and axial direction, but a middle ring of the artery was constrained in the axial direction to avoid rigid body movement. The partial artery constraint was obtained by connecting the ends of the artery to a fixed point using spring elements, with an element stiffness of 1 kN/m. The fully constrained artery was modelled by fixing the artery ends in all directions, i.e. radial, circumferential and axial directions.

As shown in Figure 4.7, the diameter at the maximum pressure was the same for all three different boundary conditions, with a value of 4.70 mm. However, the final achieved expansion was the highest if the artery was free to move. The stent-artery stabilised at a diameter of 4.12 mm, 4.03

mm and 3.73 mm for free, partially and fully constrained artery, respectively. This was mainly due to the different radial compression imposed by the different types of artery constraints. In addition, a lower recoiling effect was observed for free artery (13%) than those for partially (15%) and fully constrained artery (22%). The fully constrained artery also gave higher dogboning effect (18%) than the fully free artery (6.1%) and partially constrained artery (8.7%).

Figure 4.8 shows the von Mises stress distributions on the stenotic artery with free, partially and fully constrained artery ends. The stress contours on the artery were similar in all cases, with the maximum stresses mostly located on the plaque. The fully constrained artery exhibited less stress magnitudes (0.58 MPa) than the free one (1.05 MPa) and the partially constrained one (1.01 MPa), reflecting the reduced level of stretch and deformation of the artery if fully constrained.

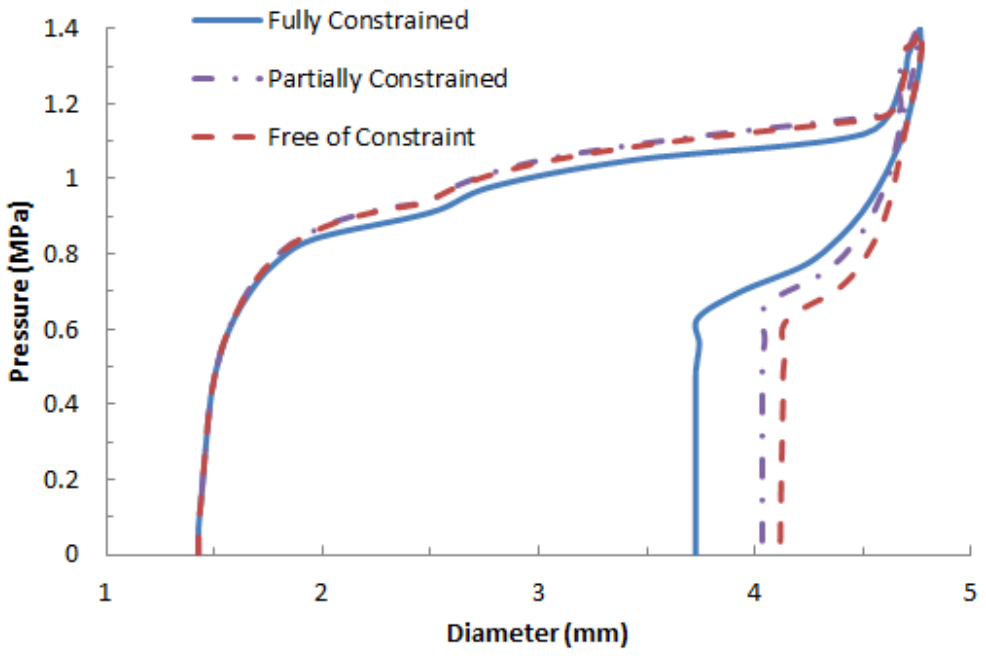

Figure 4.7 Diameter change against pressure for three different types of artery constraints.

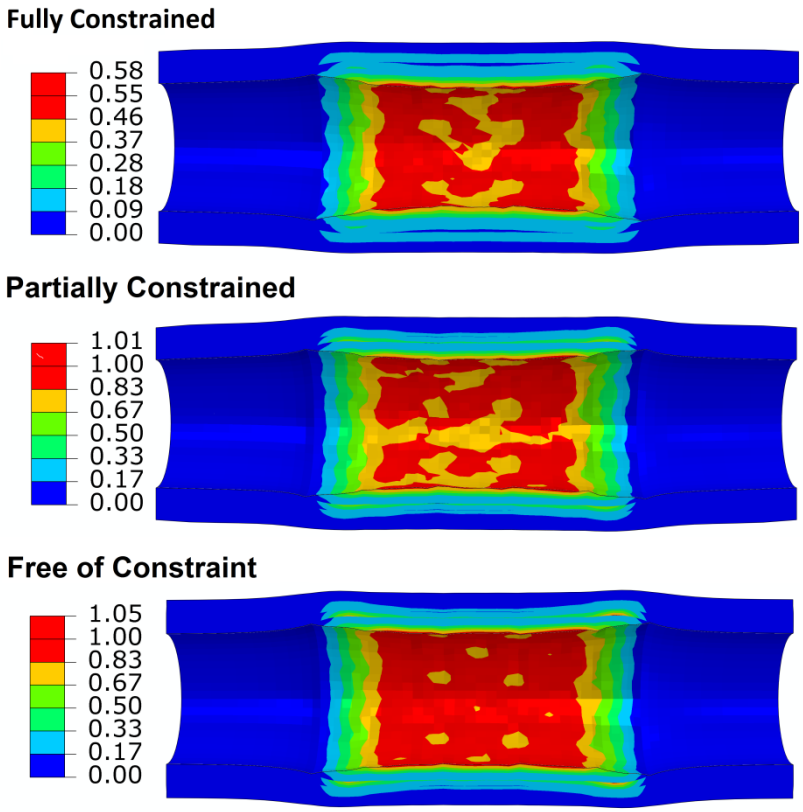

Figure 4.8. Contour plot of von Mises stress on the artery-plaque system for three different types of artery constraints.

4.3.3 Effects of Balloon Type

The comparison of the diameter change against the pressure is showed in Figure 4.9 for simulations using rubber balloon and folded balloon. In these analyses, the ends of the artery were fully constrained. The simulations using 3-folded balloon show a sustained expansion of the system at a pressure of 0.38 MPa. The sustained expansion continued at a constant rate (18.5 mm/MPa) until a pressure of 0.51 MPa is reached. Afterwards, the expansion reached a point of saturation where the system expanded at an extremely low rate to a diameter of 4.70 mm at the peak pressure of 1.4 MPa. Simulated diameter change using the polyurethane runner balloon behaved very differently from that using the folded balloons. For rubber balloon, the sustained period of

expansion started at a higher pressure (0.80 MPa) compared to that for a folded balloon, and also the expansion rate is lower than that for a folded balloon. At a pressure of 1.1 MPa, the expansion reached a saturation stage. However, the final diameters achieved at the peak pressure are similar (~4.70 mm) for both rubber and folded balloons. During deflation, the system recoiled nonlinearly until the balloons were completely separated from the stent and the artery. The diameter achieved at the end of deflation was higher for folded balloons than that for rubber balloon. Specifically, the final diameter of the stented artery is 4.04 mm for the folded balloon and 3.73 mm for the rubber balloon.

The system expanded using a rubber balloon showed higher recoiling effect (22%) compared to that using a folded balloon (12%). These results can be explained by the different volume of plastic deformation achieved in the expanded stent, which was calculated to be 29% for the case of rubber balloon and 58% for the case of folded balloons. The volume of plastic deformation is closely linked with the recoiling of the system. The stent with larger volume of plastic deformation provides stronger resistance to the elastic recovery of the deformed artery, which explains the lower recoiling effect for systems expanded using the folded balloons. However, the dogboning effect was lower for system expanded using rubber balloon (18%) than that using folded balloon (21%), which might be due to the lack of radial constraints for the folded balloons in our simulation.

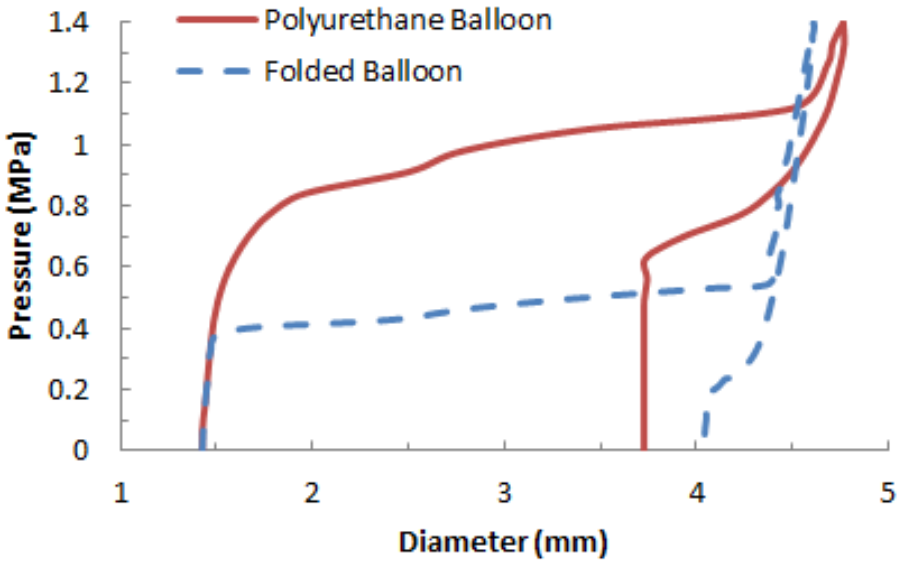

Figure 4.9. Diameter change against pressure for Xience stent expanded by polyurethane balloon and folded balloon.

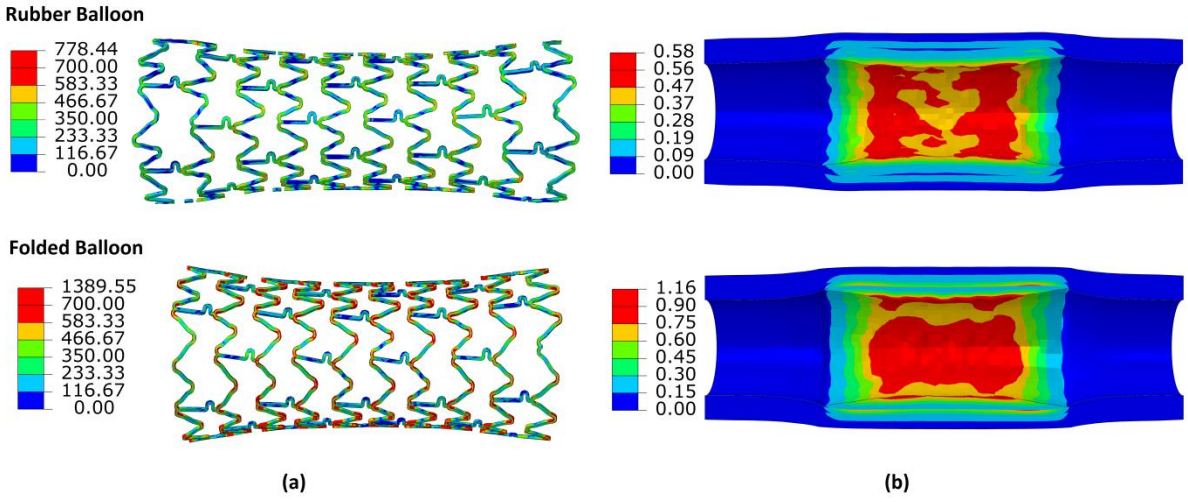

Figure 4.10. Contour plot of von Mises stress (MPa) in (a) the stent and (b) the artery-plaque system for simulations using rubber balloon and 3-folded balloon.

The von Mises stress distributions for the stent and the artery are shown in Figures 5.10a and 5.10b, respectively. On the stent, the maximum stress was significantly higher if the expansion was simulated using folded balloons, i.e. 1390 MPa for the 3-folded balloon. These values are even higher than the ultimate tensile strength of the material, which is around 1012 MPa (see Figure 2.4 in Chapter 2). This indicates a risk of failure during the stent expansion. On contrary, the simulation using rubber balloon gave a much lower maximum stress, i.e. 778 MPa, which is below the UTS of the material. On the plaque, the stress was also considerably higher for simulations using folded balloons. The maximum value was found to be 1.16 MPa for the 3-folded balloon at the end of deployment. For a rubber balloon, the stress on the plaque has a maximum value of only 0.58 MPa, about half of those for folded balloon. These results are consistent with the different levels of expansion achieved by the artery-plaque system when using rubber and folded balloons.

The results suggest that balloon type has a significant effect on stent-artery expansion and their stress distributions. Stent deployment using folded balloon led to a sustained expansion until the balloon is unfolded. After this, a saturation stage is reached and further expansion became very slow and difficult. Furthermore, the recoiling appeared to be lower for a folded balloon than that for a rubber balloon, resulting in an overall larger expansion of the artery for folded balloon. This behaviour was mainly due to the fact that the balloon remained partially in contact with the stent during the whole deflation process, preventing the artery from recoiling completely. The dogboning was also affected by the balloon folding, but this may be due to different boundary conditions used for the folded balloon and rubber balloon. The ends of folded balloon are free of constraints in radial direction, and consequently less prohibitive for the recoiling at the distal sections, resulting in the increased dogboning effect.

4.3.4 Second Stretch Invariant in Strain Energy Potential (Ogden Model vs. Polynomial Model)

Figure 4.11a shows the diameter change against the pressure during the expansion of the system simulated using Ogden model and polynomial model, where the 3-layered structure has been considered for the artery (with hypocellular plaque). For the polynomial model, the system expansion reached the point of saturation at a larger diameter (5.11 mm) due to the absence of the second stretch invariant in the strain energy function (see Eq. (5.1)). And a maximum expansion of 5.20 mm is obtained at the peak pressure of 1.2 MPa, compared to 4.70 mm for Ogden model. However, for both models, the system exhibited similar recoiling effects (22% for Ogden model and 20% for polynomial model). Consequently, the system achieved a diameter of 4.11mm for polynomial model after deflation, which is larger than that for Ogden model (3.73mm). The stress distribution on the artery for the two models is shown in Figure 4.11b, and the stress level was higher for polynomial model (0.79 MPa) due to more severe deformation.

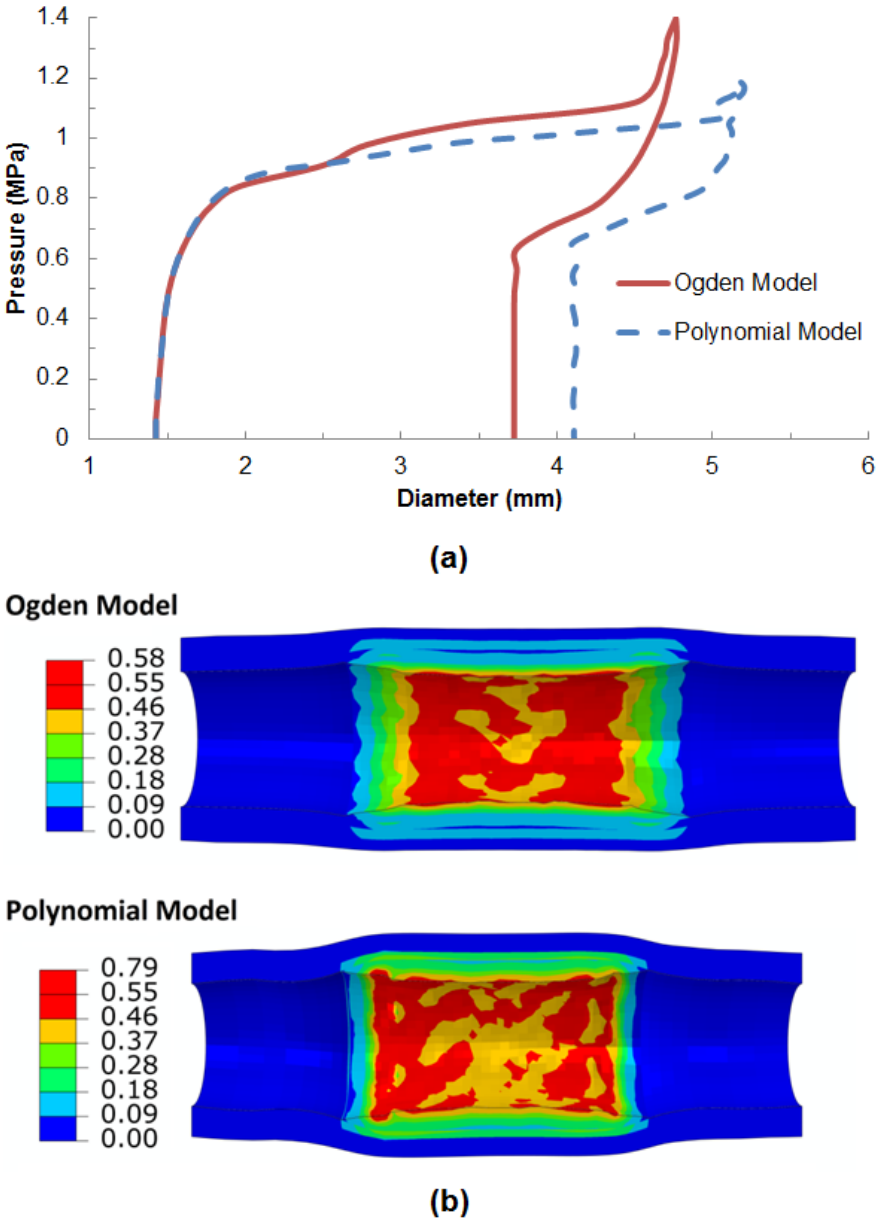

Figure 4.11. (a) Diameter change against pressure for the stent and (b) contour plot of von Mises stress in the artery-plaque system for Ogden and polynomial constitutive models.

The importance of the second stretch invariant (I_2) has been discussed in Horgan and Smayda (2012) and Khajehsaeid *et al.* (2013). It was reported that the strain-energy potential with the absence of I_2 is unable to capture some significant physical effects such as simple shear, strain

stiffening at large stretches and torsion of a circular cylinder. This work seems to be in agreement with previous results (Horgan and Smayda, 2012; Khajehsaeid *et al.*, 2013) and also confirmed the influence of I_2 in modelling stent deployment. Without considering I_2, the obtained expansion seems overestimated and could generate some misleading results.

4.3.5 Artery Wall Model (3-Layer Artery vs. Homogeneous Artery)

The blood vessel can be simulated as either 3-layer structure or homogeneous material. Using the Ogden strain energy potential, stent deployment has been modelled for both cases (with hypocellular plaque). As shown in Figure 4.12a, the expansion of the system is very similar for both models. The system reached a diameter of 4.70 mm and 4.80 mm for 3-layer model and homogeneous model, respectively, at the peak pressure of 1.4 MPa, and then recoiled to a final diameter of 3.73 mm and 3.63 mm, respectively, after balloon deflation. This suggests that using a homogeneous model or a 3-layer model for the artery wall does not influence the expansion behaviour. The stress distribution on the artery is shown in Figure 4.12b, which shows similar maximum stress magnitudes for both cases (0.57 MPa and 0.58 MPa, respectively). For layered model, the high stresses were found at the most parts of the stenotic plaque, while for homogeneous model, stress concentrations occurred at the ends of the plaque. Also, considering the layered structure of vessel wall generated the discontinuous stress distribution across the wall thickness, especially in the intima layer, a result of material heterogeneity across the vessel wall. This phenomenon can also be observed from the results obtained earlier (e.g. Figure 4.11b). We have particularly checked the stress and strain variations across the three layers. All strain components are continuous across the interfaces due to the compatibility requirement in deformation. However, all stresses are discontinuous across the interfaces due to different material properties of the three layers, which are reasonable. As the strain is continuous, the stress ought to be discontinuous due to the property mismatch across the interface.

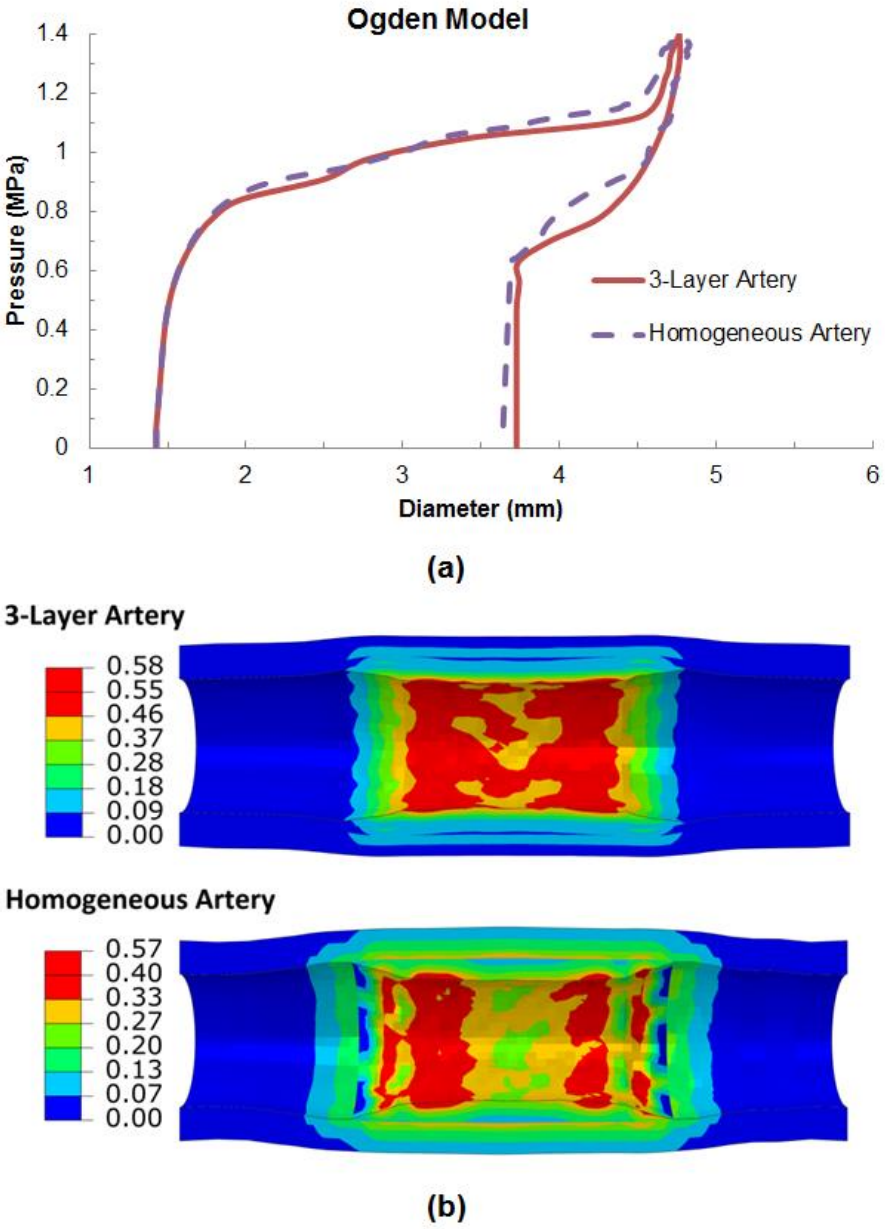

Figure 4.12. (a) Diameter change against pressure for the stent and (b) contour plot of von Mises stress in the artery-plaque system for 3-layer and homogeneous artery models.

4.6. Conclusions

The choice of balloon type and system constraints has a great influence on the simulation of stent expansion inside a stenotic artery. The type of boundary conditions used for the artery highly affects the recoiling of the system, showing that over-constraining leads to higher recoiling effect but a decrease of stress magnitude on the artery wall due to reduced stretch.

Simulations using folded and rubber balloons generate significantly different results in the stent expansion, such as sustained stent expansion behaviour, stress levels on the system and finally achieved diameter. Over constraint of the artery ends can lead to an overestimation of recoiling effect of the system. From the results of this chapter, it is more realistic to partially constrain the artery using spring elements with a proper stiffness constant. For balloon-expandable stents, folded balloon should be modelled in order to obtain a more realistic diameter-pressure response of the system.

The use of different artery-plaque constitutive models highly affects the simulated expansion behaviour of the system. Stent expansion exhibits a saturation stage for simulation using Ogden model, which has not been observed for 6-parameter polynomial models due to the negligence of the second stretch invariant in the strain energy potential. Consideration of 3-layer structure of the artery wall showed the discontinuous stress distributions across the thickness of the blood vessel which cannot be captured by the homogeneous artery constitutive model. The hyperelastic strain energy potential that includes the first two invariants of the stretch tensor should be adopted to describe the constitutive behaviour of both the artery and the plaque. The constitutive model should also take into account the layered structure of the artery.

In the following Chapter, effects of vessel factors, such as plaque thickness, asymmetric stenosis and artery curvature, on stent deployment were studied, focusing on the expansion behaviour of stent and the stresses imposed on the plaque-artery system by stenting.

Chapter 5 – The Importance of Vessel Factors in Stent Deployment

5.1. Introduction

Recent studies highlight the importance of plaque and artery geometry, particularly the shape of the atherosclerotic plaque and the tortuosity of the blood vessel, in stent deployment. Liu *et al.* (2014) identified the pathological morphology of atherosclerotic blood vessels, such as tortuosity, kinking, coiling and severity of stenosis, using Magnetic Resonance Imaging (MRI) and computed tomography (CT) scan. Among 2,218 patients, tortuosity was found to be the most common abnormality, compared with kinking and coiling. Abnormalities were more common in extracranial arteries when compared to intracranial arteries, and no case of coiling and kinking was found in intracranial vessels. Severe stenosis (70% and higher) was found in 26.5% of the patients, while 31.3% of the population exhibited intermediate level of stenosis (between 30% and 70%) and 42.2% of patients presented low level of stenosis (less than 30%). Comparison between stent expansion in curved and straight arteries was briefly studied by Wu *et al.* (2007b), showing that artery curvature tended to increase the stress levels on both the plaque and the arterial layers. Gu *et al.* (2012) studied the arterial wall mechanics during stent deployment by considering an asymmetric plaque layer with an asymmetry ratio of 2:1 and an overall stenosis of 50%. The results showed that, in addition to stent design, plaque composition and non-uniform thickness due to its asymmetry significantly affect the stresses in the artery induced by stent deployment. An increase in plaque thickness or stiffness (e.g., plaque calcification) tended to reduce the stress concentration in the arterial layers. But work in this area is very scarce according to our literature search, and there is a serious lack of understanding about the effect of arterial factors on stent deployment and the potential damage to blood vessels caused by stenting procedure. Clinical reports proved that

vessel damage is one of the main issues related to angioplasty and stenting, and high stress levels on the artery increase the chance of restenosis.

The aim of this chapter is to simulate stent deployment in atherosclerotic artery with varied plaque thickness, stenotic asymmetry and vessel curvature, focusing on expansion of stent and stresses developed in the artery-plaque system. The simulation work is divided into three parts: (1) investigating stent expansion in arteries with stenosis varied between 40% and 60%; (2) comparing the effects of plaque asymmetry, with 7:3 and 9:1 asymmetric ratios, on stent deployment; (3) understanding the role of artery curvature, with 30° and 60° bends, in stent deployment. In all cases, the expansion behaviour and the recoiling and dogboning effects of the stent were compared systematically, along with the stresses in plaque and vessel layers, to elucidate the importance of vessel factors in stent deployment.

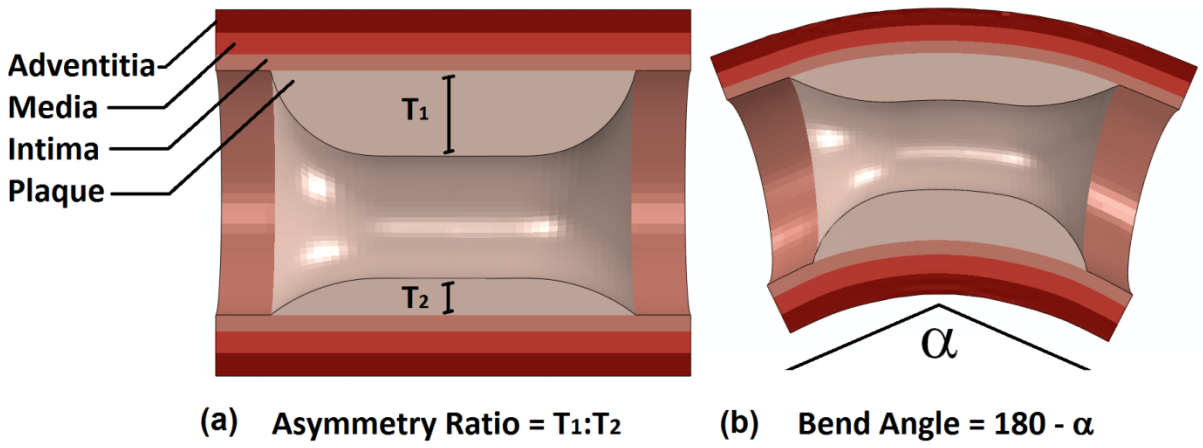

Figure 5.1. Arteries with (a) asymmetric plaque and (b) curvature, with an illustration of asymmetry ratio and bend angle.

5.2. Description of the Model

5.2.1 FE Procedure

Model of Xience stent was generated according to the methodology shown in Section 2.2 of Chapter 2. Co-Cr alloy L605 was used to describe the material properties of the stent (Section 2.2.2 in Chapter 2). The stent was meshed into 111,680 first-order incompatible brick elements (C3D8I), with four layers of elements through both the thickness and the width of the stent strut. Folded balloon was used for the expansion inside stenotic artery, with details regarding the geometry and material properties shown in Section 4.3 of Chapter 4.

Change of stent outer diameter was monitored at 5 even points in the middle ring of the stent. The overall expansion of the stent was then calculated as the mean of the values obtained at those 5 points. Diameter change at both ends of the stent was also monitored at 5 even points along the circumferential direction to calculate the dogboning effect. In the case of asymmetric plaque, the expansion of the artery and the dogboning were monitored separately at the top, middle and bottom locations of the lumen (corresponding to points A, B and C in the inset of Figure 5.6a), respectively, where the plaque has the maximum, medium and minimum thickness. The von Mises stress contours were produced at the end of deployment for all cases. Also, stress values around the middle ring of the intima, media and adventitia layers of the artery were plotted to help understand any potential damage of the arterial wall caused by stenting.

5.2.2 Artery-Plaque Model

Blood vessel was idealised as a cylinder, with an outer diameter of 6 mm and a length of 40 mm. The plaque layer is located inside the middle part of the artery, and has a length of 6 mm. The plaque thickness depends on the severity of stenosis and asymmetry as explaineded in Equation 2.5 (Section 2.3.1 of Chapter 2). Specifically, to cover the range of mild to severe vessel blockage

(Liu *et al.*, 2014), arteries with 40%, 50% and 60% stenosis were considered, corresponding to an inner diameter of 2.5 mm, 2 mm and 1.6 mm, respectively. For the asymmetric plaque, an edge ratio, which is defined as the ratio between the maximum and the minimum thickness, of 7:3 and 9:1 was considered in this work, as illustrated in Figure 5.1a. To produce a balloon-stent-artery model with curvature, Abaqus/Explicit simulations were first carried out by pushing the balloon-stent-artery system through a bended rigid guide which has the desired degree of curvature, i.e., 30° and 60° in this paper. The final geometrical model was then extracted from the output database and used for simulation of stent deployment in curved artery. Example of curved geometry for the artery-plaque system is shown in Figure 5.1b. The constitutive behaviour for both artery and plaque was described using the Ogden hyperelastic strain energy potential. The implementation details, including model parameters, were given in Section 2.2.3 of Chapter 2.

Both the artery wall and the plaque were meshed into first-order hexahedral elements with reduced integration (C3D8R), and there are four layers of elements through the thickness of each arterial layer and eight layers of elements through the thickness of the plaque, following the mesh sensitivity in Section 2.3.1 of Chapter 2. The artery and plaque systems had about 100,000 elements in total. An example of mesh is shown in Figure 5.2, including the stent, artery and balloon, for an artery with 50% stenosis and asymmetric plaque (ratio 7:3).

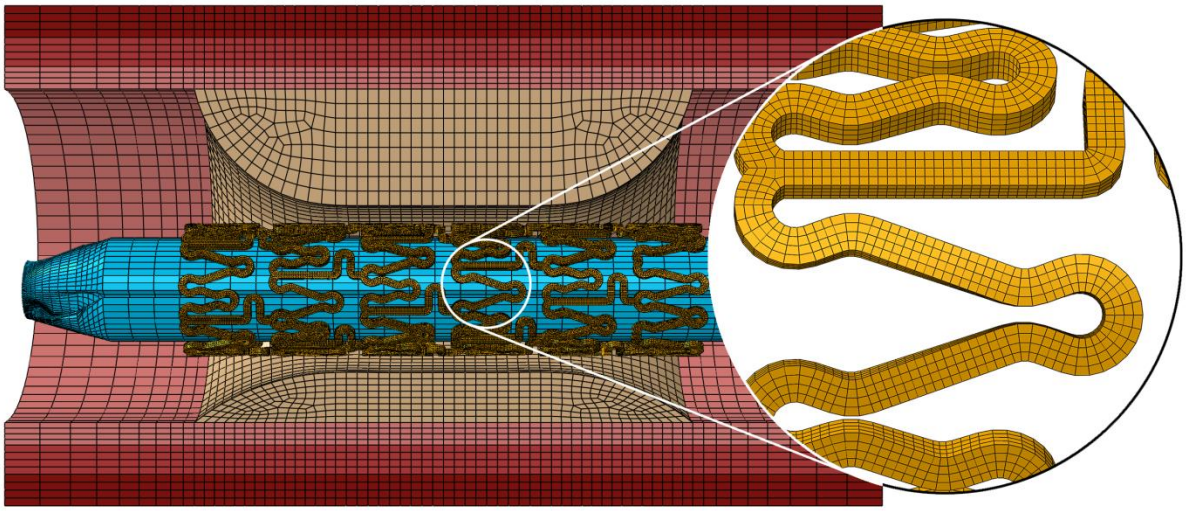

Figure 5.2. Finite element mesh for the whole balloon-stent-plaque-artery system (50% stenosis and asymmetric plaque with a ratio of 7:3).

5.3. Results and Discussion

5.3.1 Effect of Plaque Thickness

The change of stent outer diameter against the pressure is plotted in Figure 5.3a for Xience stent during the process of deployment inside a diseased artery with 40%, 50% and 60% stenosis. Overall, stent expansion at the maximum pressure (1.4 MPa) depended on the severity of stenosis, with diameter considerably reduced with the increasing plaque thickness. The artery with 40% stenosis achieved a diameter of 4.2 mm at the end of balloon inflation, and this diameter reduced to 4.1 mm for 50% stenosis and 3.7 mm for 60%. This is because the increasing plaque thickness increased the radial stiffness of the system which limited the expansion considerably at maximum pressure.

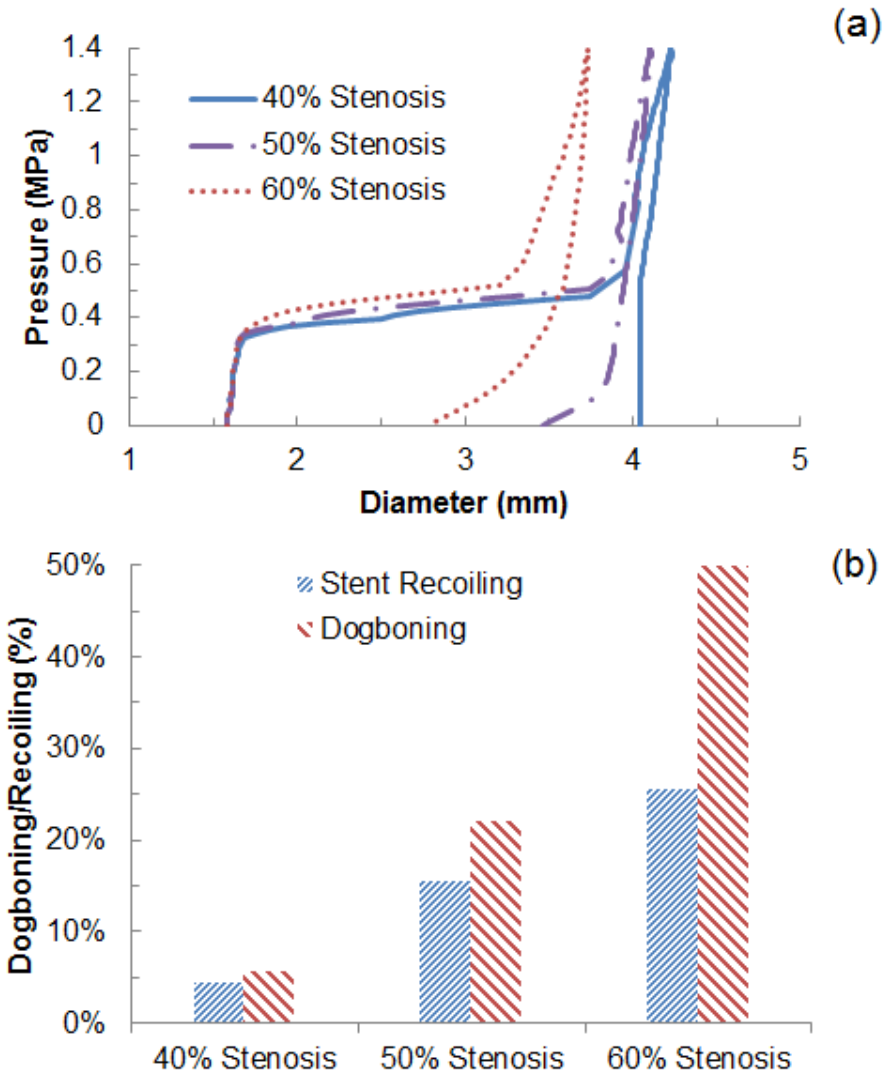

Figure 5.3. (a) Diameter change against pressure and (b) recoiling and dogboning effects for stent deployment in arteries with 40%, 50% and 60% stenosis.

During deflation, recovered elastic deformation and radial pressure from the viscoelastic artery system lead to the recoil of the stent. The diameter of the stent-artery system at the end of deflation was 4.0 mm for 40% stenosis, 3.5 mm for 50% stenosis and only 2.8 mm for 60% stenosis, indicating that the increased stenosis also increased the recoiling effect significantly. Specifically, the recoiling (Figure 5.3b) increased from a value of only 4.5% for 40% stenosis, to 15.6% for 50% stenosis and 25.7% for 60% stenosis, causing a large decrease in the diameter after the

deflation of the balloon. The dogboning effect also dramatically increased with the level of stenosis, with values of 5.6%, 22.2% and 51.2% for 40%, 50% and 60% stenosis, respectively.

The von Mises stress levels on the artery and plaque are compared in Figure 5.4 for the three different cases. The maximum stress increased markedly with the level of stenosis, showing 1.3 MPa for 40% stenosis, 2.3 MPa for 50% stenosis and 2.9 MPa for 60% stenosis. In all three cases, the maximum stresses were located on the surface of the plaque. It should be noted that the model used for arterial tissues is isotropic and unable to catch the anisotropic behaviour of the vessel. Also the material model does not include plastic behaviour for the vessel which might affect the results by predicting high levels of stent recoil and vessel stress due to the stiffer stress-strain curve developed for the vessel wall and hard plaques at later stage (~20% strain) (Holzapfel *et al.*, 2005; Zahedmanesh and Lally, 2009). Here, we particularly focused on the stresses in the artery-plaque system, and details about stress distributions on the stents are similar to the results presented in Section 3.3 of Chapter 3.

Cheng *et al.* (1993) analysed the stress distribution on 24 plaques, and showed that the circumferential stress distribution plays a primary role in plaque rupture, along with the local variation in the plaque properties. Stress analysis of the atherosclerotic plaque, subjected to internal pressure, has also been carried out by Li *et al.* (2006) through a combination of MRI imaging technique and FE analysis. Their findings showed that von Mises stress can be used to predict the location of plaque rupture. From their results, plaques which underwent rupture exhibited considerably higher stresses (0.68 MPa) compared to those not ruptured (0.23 MPa). Our results showed the importance of plaque thickness in stent deployment. For thick plaque, there is a risk of an unsuccessful treatment of the disease and also a potential of plaque rupture due to the high stress levels developed at a focalised area of the plaque. In our work, the stresses in the artery-plaque system were found to be in the range of 1~3 MPa, depending on the severity of stenosis. These values are much higher than the values reported in Li *et al.* (2006), due to the different

constitutive behaviour used for the artery and plaque. Also the simulation in Li *et al.* (2006) did not consider the stent which was believed to raise the stress level in the plaque-artery system due to its direct contact with the artery.

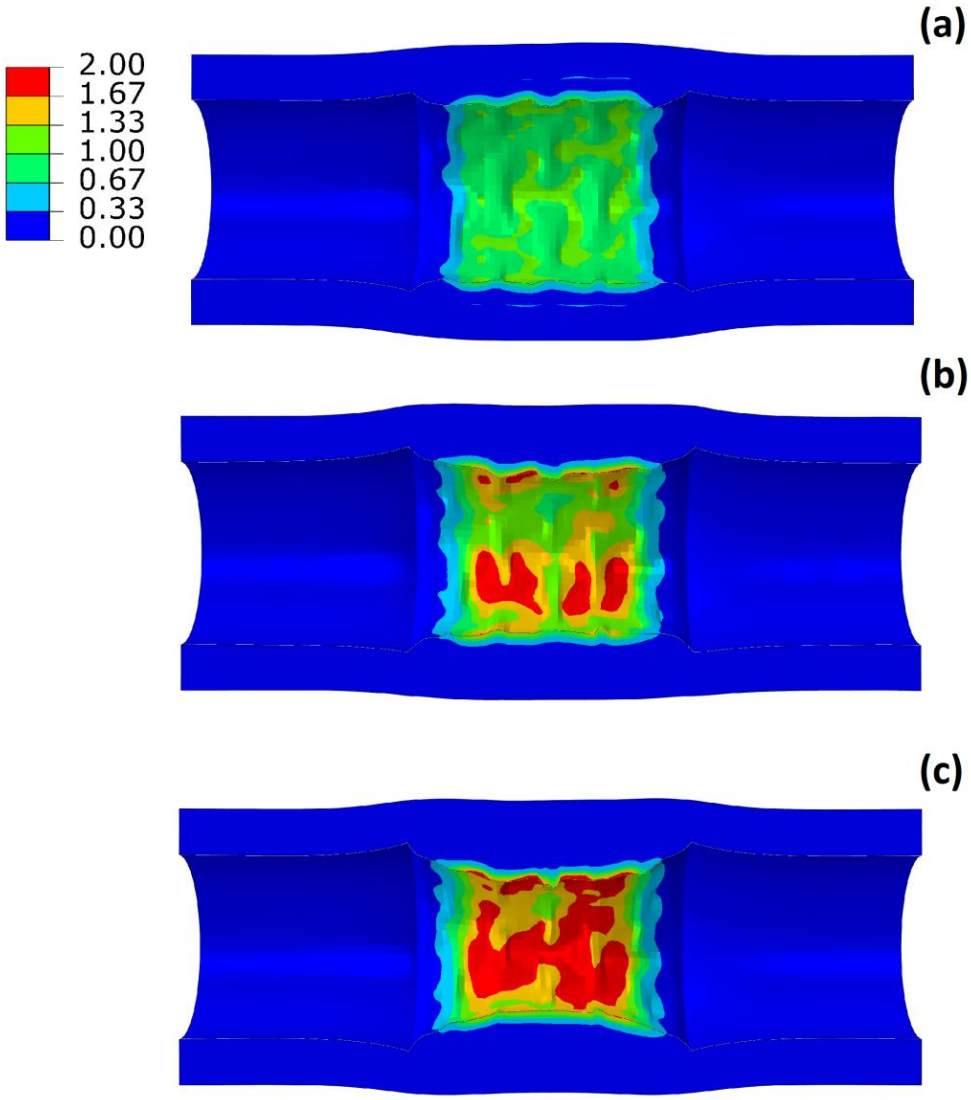

Figure 5.4. Contour plot of von Mises stress in the artery-plaque system after stent deployment in arteries with (a) 40%, (b) 50% and (c) 60% stenosis.

6.3.2 Effect of Plaque Asymmetry

Asymmetric plaque layer, with a ratio of 7:3 and 9:1, was considered to study the influence of plaque asymmetry on stent expansion inside a stenotic artery. Figure 5.5a shows the change of stent outer diameter against the pressure, in comparison with that for a symmetric plaque (ratio 1:1). The overall expansion of the stent-artery system was not affected by the asymmetry of the artery, nor the dogboning and recoiling effects. However, the expansion of the system appeared to be non-uniform due to the varied thickness of plaque. A greater expansion was obtained for the side where the plaque was the thinnest (at point C), compared to the opposite side where the plaque was the thickest (at point A). For instance, for the case with plaque asymmetry ratio of 7:3, the lumen radius expanded from 1 mm to 1.58 mm at point A and to 1.74 mm at point C (Figure 5.5a). Plaque asymmetry also led to the development of non-uniform dogboning effect, as dogboning tends to increase with the increase of plaque thickness. The dogboning effect was around 20% for all ratios when calculated at point A, but reduced dramatically when calculated at point C, i.e., only 6% for plaque asymmetry ratio 7:3 and 1% for plaque asymmetry ratio 9:1 (Figure 5.5b).

Figure 5.6 shows the distribution of von Mises stresses on the artery-plaque system. Increased stress levels were found on theplaque with the increase of asymmetric ratio. It is particularly noticed that there is a significant increase of stress levels in the intima and media layers in the healthier section of the artery, i.e., with thinner plaque. For the case with 9:1 asymmetric ratio, the stress magnitude reached a level above 1 MPa, which can be associated with the risk of arterial damage.

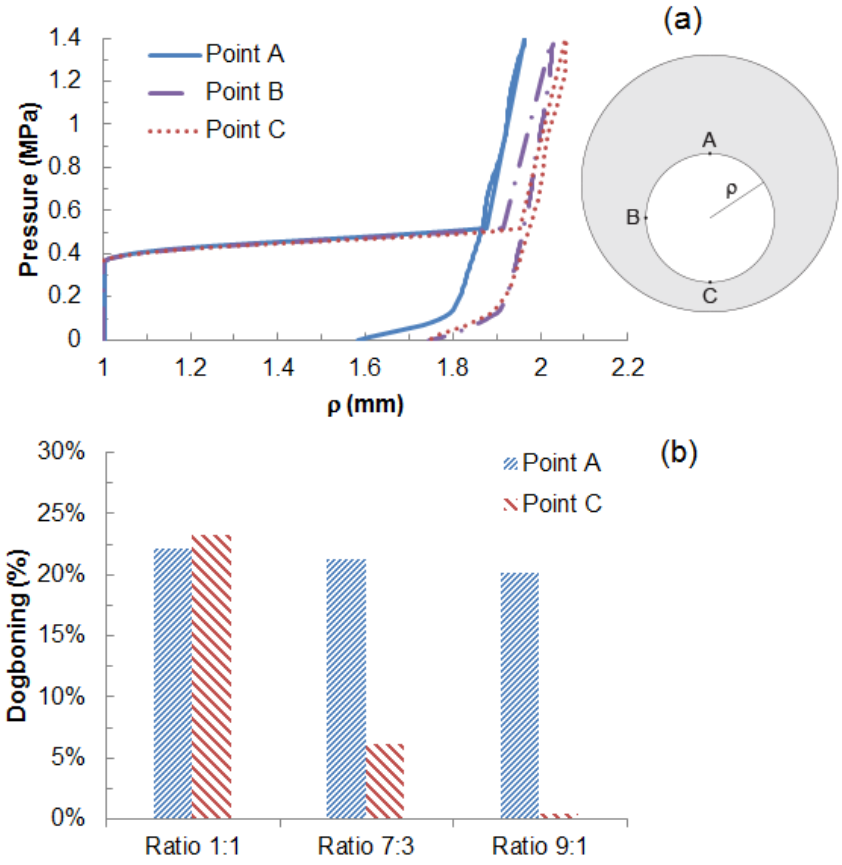

Figure 5.5. (a) Radial expansion against pressure at points A, B and C for asymmetric plaque (ratio 7:3); (b) Comparison of dogboning effects at points A and C for symmetric (1:1) and asymmetric (7:3 and 9:1) plaques.

To illustrate this more clearly, Figure 5.7 plots the stress variation around the circumferential direction for the middle section of the arterial layers. In the case of symmetric plaque, the stresses on the three layers were almost constant along the circumferential direction with a value of ~10 kPa in both the intima and media layers and ~5 kPa in the adventitia layer. In the case of asymmetric plaque, this value is slightly decreased for the section with thicker plaque ($\theta > 180°$), but significantly increased for the section with thinner plaque ($\theta < 180°$). The stress magnitude in the intima layer increased to 445 kPa for the case with plaque asymmetric ratio 7:3 and 1643 kPa

for the case with plaque asymmetric ratio 9:1, indicating an extremely high risk of arterial damage. The same effect is also noted for the media and adventitia layers, with a magnitude of 212 kPa and 378 kPa in the media and 7 kPa and 12 kPa in adventitia for asymmetric plaque ratio 7:3 and 9:1, respectively.

Clinical trials have demonstrated an association of stent angioplasty with the increase of artery perforation (Al-Mukhaini *et al.*, 2011). This can be caused by the guide wires, the angioplasty balloons or the stent itself, it is a life-threatening condition that can be classified into three types: Grade I extraluminar crater, Grade II, myocardial or pericardial blushing, and Grade III, contrast streaming or cavity spilling. A study involving 72 artery perforations in stent deployment (Javaid *et al.*, 2006) showed that Grade I perforations are mainly caused by the angioplasty catheter, whilst angioplasty balloon and stents are connected mainly to Grade II and Grade III lesions. Yıldız *et al.* (2013) investigated 7,452 patients that underwent PCI, of which 17 (0.2%) exhibited artery perforation caused by the stenting procedure. Consistently with previous reports, Grade I perforations were caused by the guide wire and Grade II and III by the balloon and stent. In total, the incidence of Grade I perforation caused by stenting was 16.7% according to Javaid *et al.* (2006) and 23.5% according to Yıldız *et al.* (2013). It was reported as 54.2% (Javaid *et al.*, 2006) and 47.1% (Yıldız *et al.*, 2013) for Grade II perforation, and 29.1% (Javaid *et al.*, 2006) and 29.4% (Yıldız *et al.*, 2013) for Grade III perforation. According to our results, the stress concentration in the intima layers of the artery can be considered as a risk factor for the perforation of the artery during stent deployment. This work suggests that the presence of the plaque reduces the stresses in the vessel walls, protecting the artery from the eventuality of perforation. When the plaque becomes too thin, the artery is more exposed to damage caused by the stent, and the doctor should be alerted when performing the surgery in patients with severe asymmetricplaques.

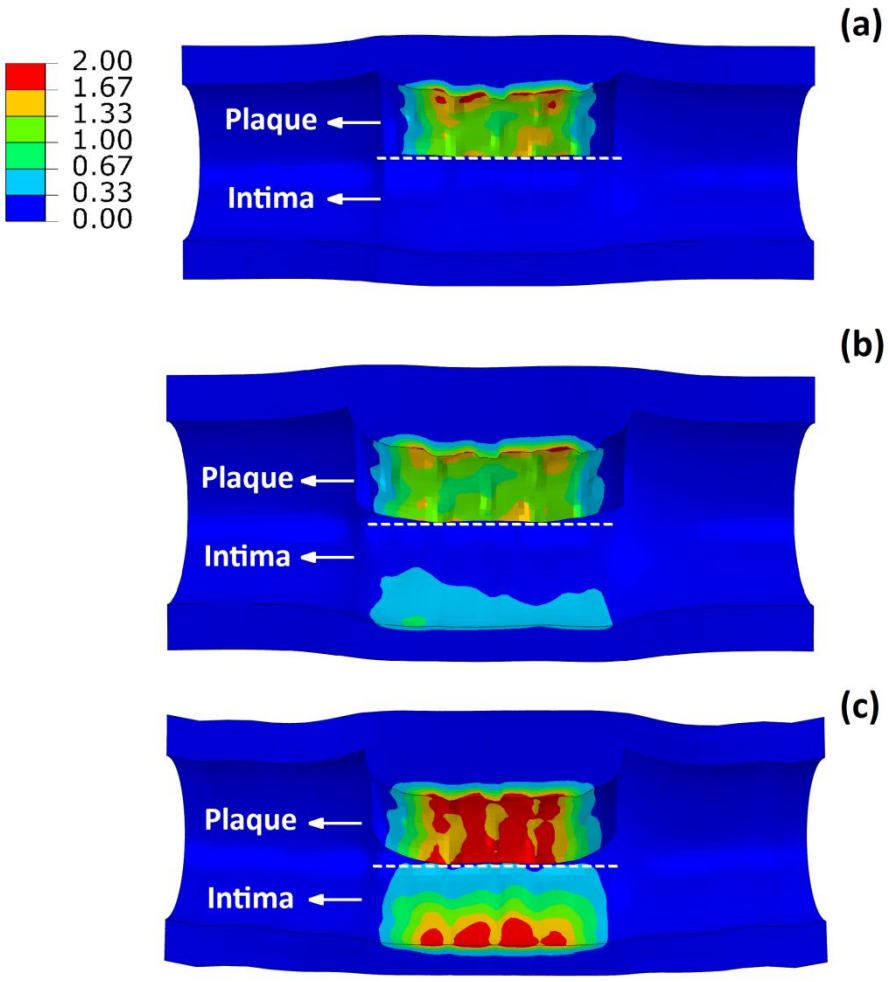

Figure 5.6. Contour plots of von Mises stress on theplaque and intima layer for (a) symmetric (ratio 1:1) and asymmetric (ratio (b) 7:3 and (c) 9:1) plaques.

The mechanisms of the arterial failure have also been studied by means of computational methods. Khamdaengyodtai *et al.* (2012) made a study analysing the effect of internal pressure on the failure of arterial layers. The work simulated the deformation of a 5-layered arterial wall under internal pressure, and their results showed that the rupture occurs in the circumferential direction, starting from the inner part of the media layer and propagating towards the outer part. Arterial dissection caused by angioplasty was also studied by Badel *et al.* (2014) using cohesive element approach on

a simplified arterial FE model. The analysis revealed several damage processes, i.e., detachment of the plaque and overt media dissection, which may lead to proliferation of restenosis. These existing studies indicated a further direction of the current work, i.e., to model and predict damage initiation and progression of artery-plaque system during stent deployment. This will require a physically-based criterion and a numerical technique to simulate the damage process properly, including a material model to describe the post-damage mechanical behaviour for the arterial layers, which will be explored in future work.

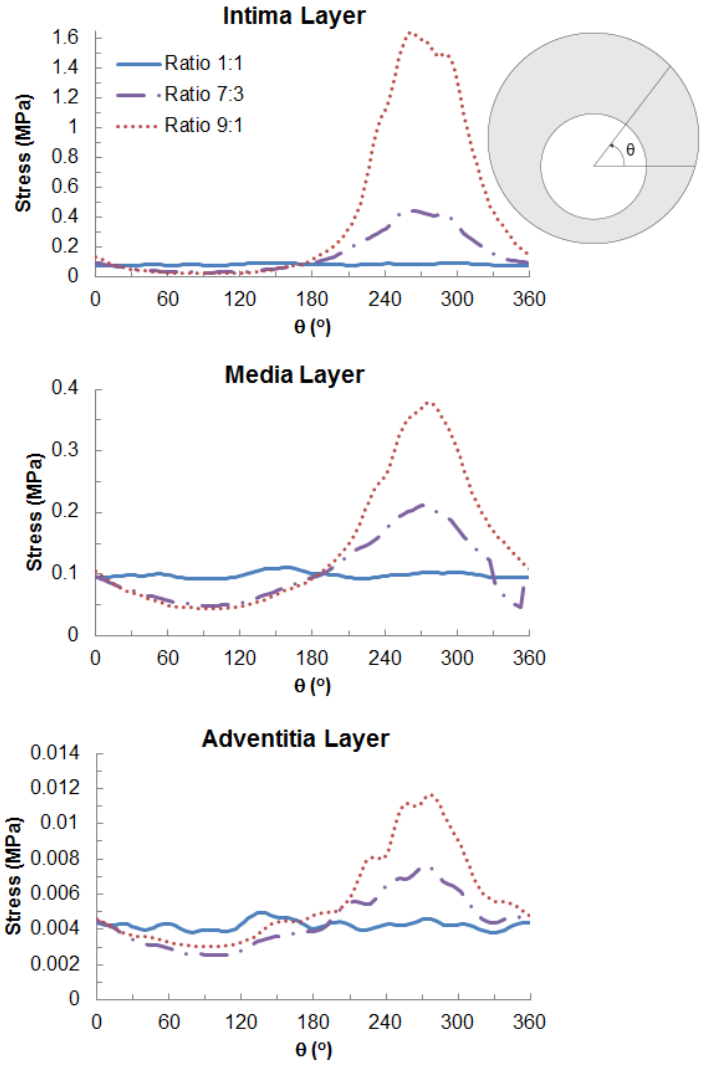

Figure 5.7. Circumferential variation of von Mises stress on the intima, media and adventitia layers for symmetric (ratio 1:1) and asymmetric (ratio 7:3 and 9:1) plaques.

5.3.3 Stent Expansion in Curved Arteries

Deployment of stent in artery, with 30° and 60° bends at the diseased location, was simulated and the results of expansion are shown in Figure 5.8, in comparison with that obtained for a straight artery. The final diameter after deflation (Figure 5.8a) was slightly reduced for a 60°-bend artery, with a value of 3.3mm, compared to 3.5mm for a straight artery. There is almost no difference for stent expansion in a 30°-bend artery when compared to that in a straight artery. The recoiling and dogboning effects are also very similar in all three cases, with recoiling around 15% and dogboning around 20%. We also noticed that the bended artery was generally straightened following stent deployment, as also reported in Auricchio *et al.* (2011). To quantify such straightening effect, Figure 5.8b compares the degree of tortuosity, calculated as the ratio between the distance of the two end points of the artery and the length of its centreline, before and after stent deployment. It is noted that, following stent deployment, arterial tortuosity reduced from 44.6% to 37.7% for 60°-bend artery and from 3.1% to 2.9% for 30°-bend artery. Figure 5.9 shows the stress contour plotted on the deformed shape of the artery for three cases. Clearly, the stress on the plaque increased with the increasing curvature of artery. The stresses on the straight artery were only 2.27 MPa, and increased to 3.22 MPa and 3.62 MPa for the 30° and 60° bend arteries, respectively. For curved artery, the maximum stresses were located at the inner and outer sides of the arterial bend.

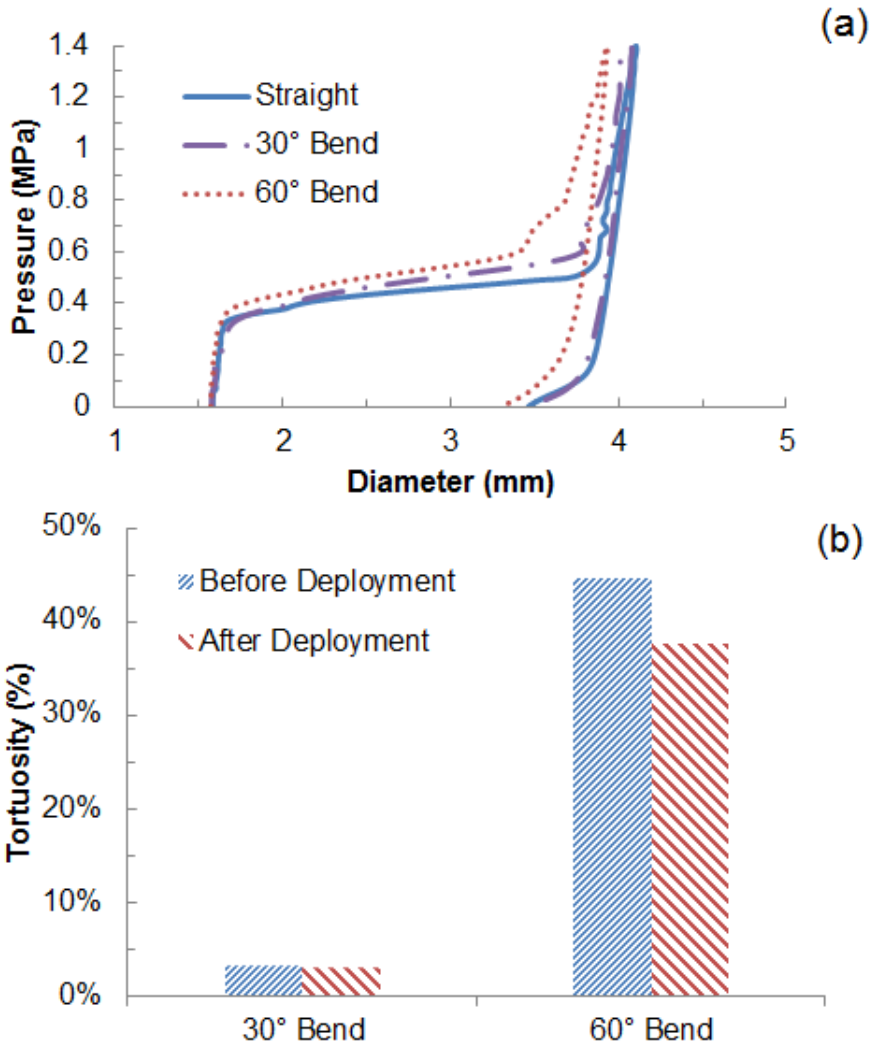

Figure 5.8. (a) Diameter change against pressure for stent deployment in straight, 30o-bend and 60o-bend arteries; (b) Degree of artery tortuosity before and after stent deployment.

The deployment of stents in tortuous or curved arteries is one of the major clinical challenges, resulting often in failure of stent placement or damage to the artery. Fernandes *et al.* (2002) reported three cases of stent angioplasty on angulated lesions, which showed that some bends can obstruct the passage of the stent and that sharp angulation of the artery is also an obstacle to stent deployment. Furthermore, Myouchin *et al.* (2013) showed that, out of 31 cases of stent deployment close to inflection points of the artery, 2 had unsuccessful treatment of the lesion. Analysis of

lesions showed that both unsuccessful cases were experiencing a vessel tortuosity of close to 90° with the stenosis located in the middle of the arterial bend. From our results, the curvature of the artery affected the stent expansion only slightly, by reducing the diameter expansion during the deployment. Also, the recoiling and dogboning effects were similar in all cases, suggesting that these effects are mainly associated with the severity of stenosis rather than the shape of the vessel.

In fact, Auricchio *et al.* (2011) carried out the simulation of deployment of six stent designs inside a patient specific artery, digitally reconstructed by computed tomography angiography (CTA). Their results showed that stent deployment significantly reduced the tortuosity of the artery, which is the case for all six designs. The stent design had no influence in vessel straightening, although it affected the stresses on the arterial wall and the lumen gain. Morlacchi *et al.* (2013) produced two models of patient specific arterial bifurcation with CTA to simulate stent deployment. The study showed that tortuosity of the artery was reduced in both cases, resulting in a straightening of the vessel. Furthermore, high stresses, on both the stents and the arteries, can be found in the areas of vessel straightening and stent overlapping, leading to potential stent and arterial failure. These phenomena were also confirmed in our simulations of stent deployment in curved arteries, where artery straightening happened mostly at the inner and outer bends, leading to the development of high stress levels and a risk of vessel rupture at those regions.

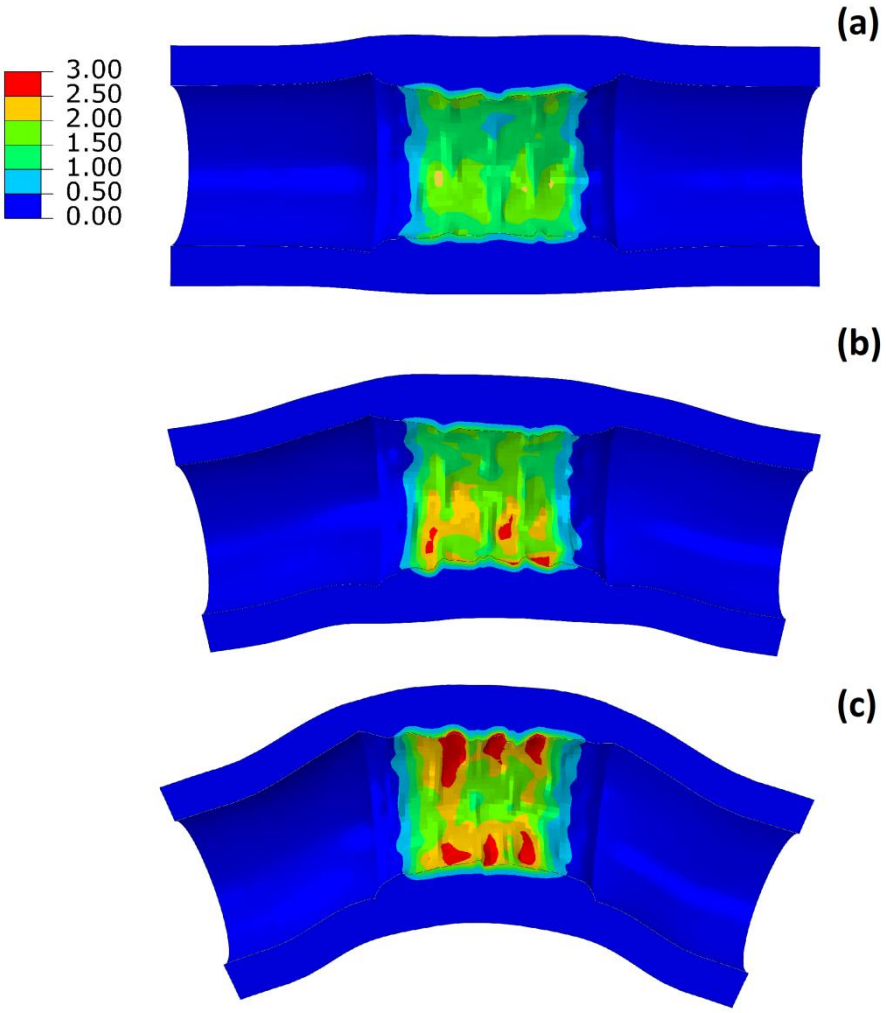

Figure 5.9. Contour plots of von Mises stress for (a) straight, (b) 30°-bend and (c) 60°-bend arteries.

5.4. Conclusions

Stent expansion and recoiling are strongly affected by the severity of stenosis. The radial stiffness of the diseased artery increased considerably with the increase of plaque thickness, which leads to reduced stent-artery expansion, high levels of stent recoiling and increased stresses on the plaque. For symmetric plaque, the stresses on the arterial walls were uniform and relatively low in magnitude due to the uniform expansion of the stent. For asymmetric plaque, the stent expansion becomes non-uniform, which is also the case for the dogboning effect. Stent expansion is very limited in the regions with thicker plaque, also accompanied by high dogboning effect. The stresses dramatically increased in the regions with thinner plaque and were mainly located in the intima and media layers of the artery. A reduction in stent expansion and an increase for the stresses on the plaque were obtained when stent deployment was simulated in bended arteries.

This work highlights different situations, associated with the geometrical character of diseased blood vessels, for which stent deployment might represent a risk for arterial damage and plaque rupture. Results suggest that severe stenosis might require stent designs such as closed cell designs that are resistant to recoiling in order to treat the disease effectively. Still, particular care should be taken when implanting stents in plaques that are not evenly distributed around the artery, as non-uniform expansion and arterial damage might occur in the areas where the plaque is particularly thin. This also includes deploying a stent in arteries with sharp curvatures due to high stresses induced at the inner and outer bends.

The following Chapter presents a study of the effect of vessel anisotropy and post-deployment stresses during stent deployment and under biomechanical forces, such as bending and radial compression.

Chapter 6 – Study of Stent Performance by Considering Vessel Anisotropy and Post-Deployment Stresses

6.1. Introduction

The state of the art in the characterization of arterial wall layers suggests that the fibre-reinforced structure of intima, media and adventitia layers, forming the vessel wall, must be taken into account when modelling the deformation of blood vessels. Holzapfel *et al.* (2000) first showed how the collagenous components of the vessel layers can be modelled by means of fibre orientation to introduce the anisotropic material properties. Their results were in good agreement with the available data for arteries under axial extension, radial inflation and torsion. The same framework has been later employed to model the layer-specific mechanical properties of human coronary arteries (Holzapfel *et al.*, 2005). The study also analysed 13 human nonstenotic left anterior descending (LAD) coronary arteries. The arterial walls were separated into three layers whose mechanical properties were tested in both longitudinal and circumferential directions. In all cases, large difference was found between the patients and also the three layers exhibited highly non-linear anisotropic behaviour between the longitudinal and circumferential directions. The computational model showed good agreement with the experimental results, confirming its capability of describing the mechanical behaviour of such materials. However, the implementation of arterial anisotropy in finite element modelling of stent biomechanics is still very limited. Existing work only adopted simplified model to model stent expansion, such as the single-layer anisotropic model used in Auricchio *et al.* (2013) and the redundant HGO anisotropic model (without the consideration of fibre family) used in Schiavone and Zhao (2015). Consequently, the results were less conclusive and further studies are required to quantitatively elucidate the effects of vessel anisotropy on stent deployment.

Body movements, tissue tethering and blood flow are key factors that induce mechanical loading on arterial branches. When the mechanical stability of the vessel is lost, buckling can occur which generates large bending deformations on the artery (Han *et al.*, 2013). As reviewed by Fortier *et al.* (2014), implanted stents may undergo a variety of repetitive deformations caused by muscular movements during daily activities such as walking, flexing, respiration and heartbeat. Smouse *et al.* (2005) studied the stented femoropopliteal arterial segment (FA) in 14 limbs of 7 human cadavers. The limbs were flexed to mimic movements such as walking, climbing stairs, sitting and standing. Bending, associated with compression, was observed for arteries behind the knee, and the presence of stents increased the axial rigidity of the vessel which can cause stent kinking or fracturing. Rosenfield *et al.* (1997) studied stented arterial branches in various vascular sites that were subjected to radial compression, such as six superficial femoral arteries and five hemodialysis conduits. Results showed that restenosis occur as a result of stent compression, and two mechanisms of compression were identified, namely, two point compressive force and complete circumferential encroachment. Despite redilation of the stents, restenosis occurred from recurrent compression in most sites. Also, radial compression of the artery can be caused by external pressures due to cardiac contraction or stenosis. Consequently, it is of importance to evaluate stent performance under biomechanical forces, especially bending and radial compression, which has not been well studied yet.

In this chapter, expansion of Xience stent inside an artery with stenosis was simulated using finite element analyses. The work compared the behaviour of stent expansion in an artery described by isotropic and anisotropic hyperelastic models, respectively. After deployment, two major biomechanical movements of the stent-artery system were considered, i.e., bending and radial compression. In particular, the effects of post-deployment stresses on stent deformation were analysed by comparing simulations that accounted for the post-deployment stress states with those that neglected post-deployment stresses. This work highlighted the importance of vessel

anisotropy and post-deployment stresses in assessing stent performance during and after deployment.

6.2 Methodology

6.2.1 Finite element model

Again, Xience stent, made of Co-Cr alloy L605, was employed for this study, with details described in Chapter 2 (Section 2.2). The stent mesh was the same as that used in Chapter 5 (Section 5.2.1). The stent was expanded using a folded balloon, with details described in Chapter 4 (Section 4.3). The 3-layer artery was modelled as perfectly symmetric with 50% stenosis and details of the finite element model are given in Chapter 5 (Section 5.2.2). The mesh of the whole system is shown in Figure 6.1.

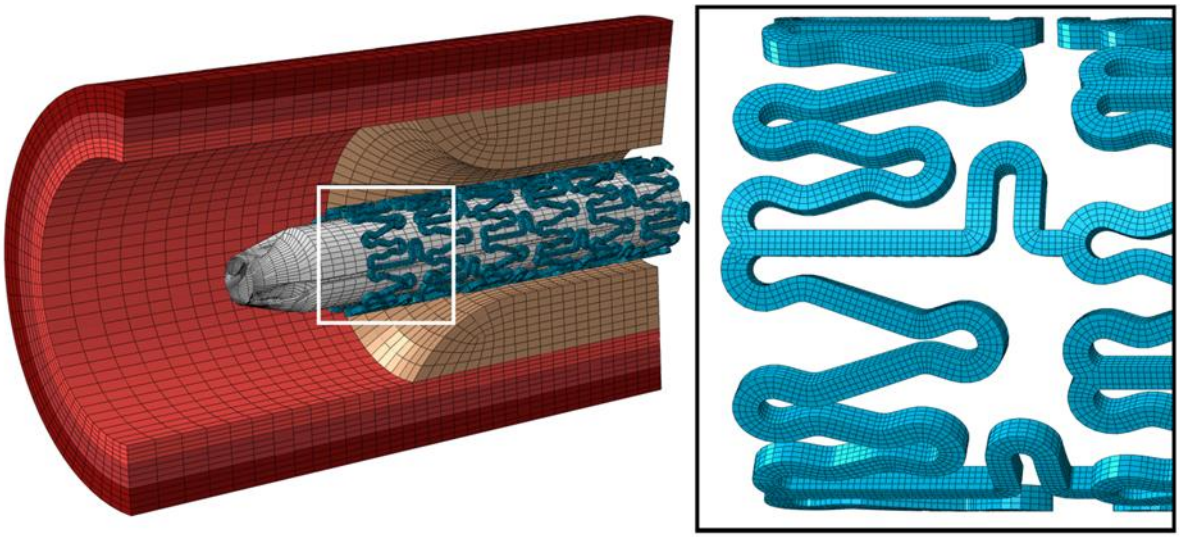

Figure 6.1. Finite element mesh of the stent-artery-balloon system.

6.2.2 Deformation under biomechanical forces

After the deployment, system deformation was modelled by considering two major biomechanical forces, i.e., bending and radial compression, generated from artery movements. For all cases, the simulations were carried out using the HGO anisotropic model for the arterial layers, with and without accounting for the post-deployment stresses in the stent-artery-plaque system induced by the stent deployment. Bending was modelled by imposing 5 mm of displacement in the Y-direction to all the nodes in the middle cross-section of the artery-plaque system, as illustrated in Figure 6.3a. Both ends of the artery were kept fully constrained, and the stresses on the stent and the artery-plaque system were monitored during the simulations. As illustrated in Figure 6.3b, radial compression was simulated by applying a linearly increasing pressure of 0.2 MPa to the outer surface of the artery, over a length of 20 mm in the middle part. In this case, the ends of the artery were fixed in all directions, similar to the bending simulations. The diameter change against pressure was monitored at the centre and the two ends of the plaque's inner surface, along with stresses in the stent-artery-plaque system.

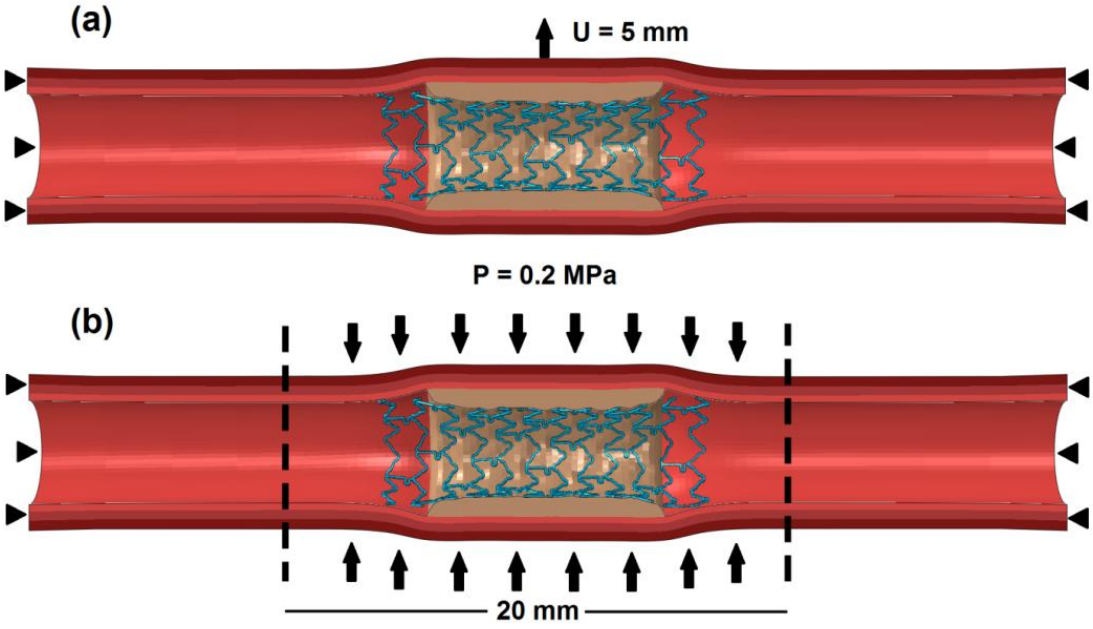

Figure 6.2. Illustration of constraints and loading conditions: (a) bending and (b) radial compression.

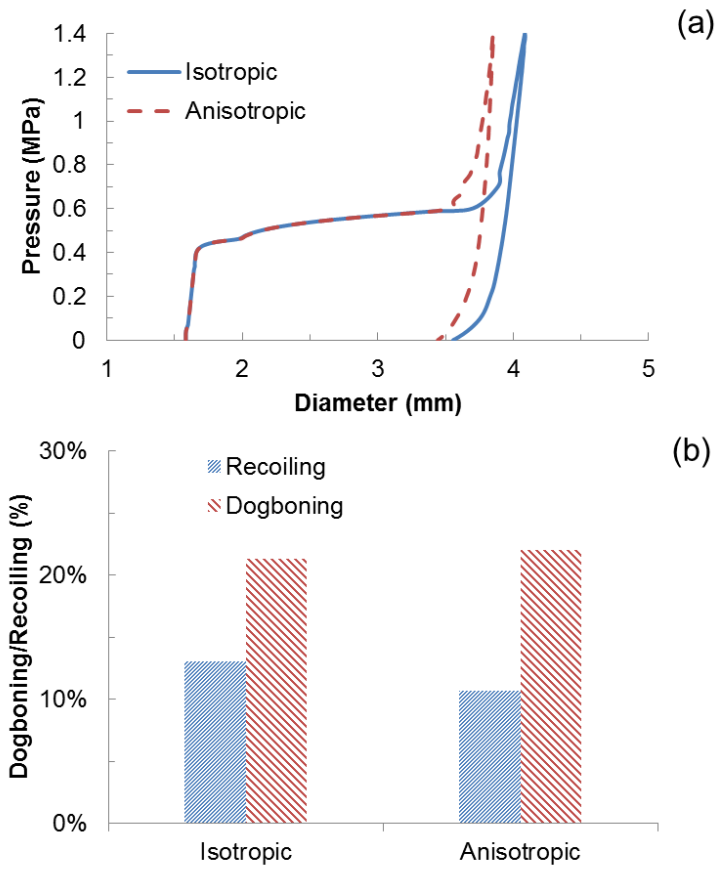

Figure 6.3. (a) Diameter change against pressure and (b) recoiling and dogboning effects for Xience stent deployed in the artery modelled with anisotropic and isotropic hyperelastic strain energy potentials.

6.3. Results

6.3.1 Effect of Vessel Anisotropy on Stent Deployment

The expansion behaviour of the stent-artery system, simulated using the isotropic and anisotropic arterial models, is compared in Figure 6.4 by plotting the change of stent outer diameter against the inflating pressure. The isotropic model of the arterial layers was described by an Ogden hyperelastic strain energy potential, with parameters given in Zahedmanesh *et al.* (2010) (Also given

in Chapter 2). The response of the isotropic model can be seen in Figure 6.2, which matches the circumferential stress-stretch response for each artery layer. Before the expansion reaches saturation, the rate of artery dilation was almost identical for both arterial models. However, for the anisotropic model, the expansion saturation started at a diameter of 3.56 mm, whilst for isotropic material behaviour, it started at a diameter of 3.90 mm. This difference was also seen at peak pressure (1.4 MPa), i.e., 3.85 mm for isotropic model versus 4.08 mm for anisotropic model. After the deflation, the recoiling (Figure 6.4b) was higher for the isotropic model than that for the anisotropic one, with a value of 13.0% and 10.6%, respectively. The final diameter achieved by the stent expansion was 3.56 mm for the isotropic model and 3.45 mm for the anisotropic model, which are comparable. Figure 6.4b also shows the dogboning effect, which was 22.1% in both cases.

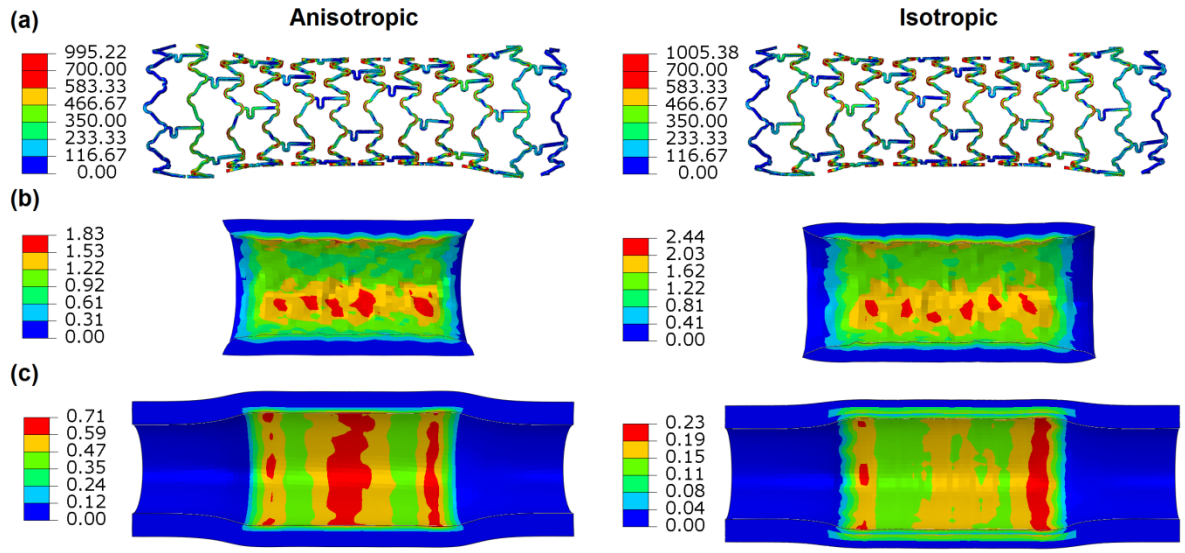

Figure 6.4. Stress contours on the (a) stent, (b) plaque and (c) artery after deployment of Xience stent, comparison between isotropic and anisotropic arterial models.

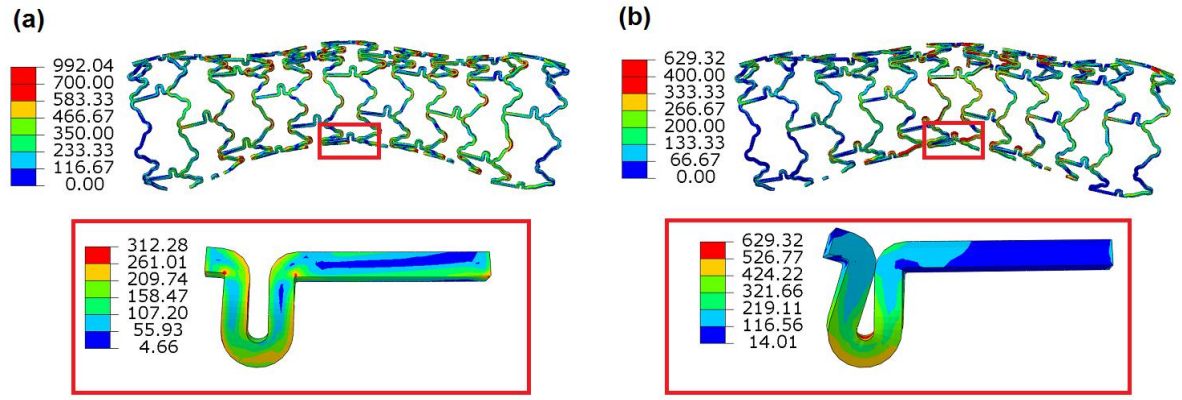

Figure 6.5. Comparison of deformation and stresses for the stent simulated (a) with and (b) without considering post-deployment stresses.

6.3.2 Post-Deployment Stresses Generated During Stent Deployment

The stress contour on the stent after deployment is compared in Figure 6.5a for anisotropic and isotropic artery models. The stress distribution was similar in both cases, with maximum stresses located at the U-bends of the stent. After deflation, the maximum von Mises stress was settled at 995 MPa and 1005 MPa for isotropic and anisotropic artery models, respectively. Figure 6.5b shows the maximum principal stresses on the plaque at the end of deployment, with a magnitude of 1.83 MPa and 2.44 MPa for anisotropic and isotropic arterial models, respectively, and similar stress distribution can be seen for both cases. The stress contour in the arterial wall is shown in Figure 6.5c. In both cases, the maximum stress was found in the intimal layer, localised to the ends of the diseased section due to the stent dogboning. The maximum principal stress in the intima layer was found to be 710 kPa for the anisotropic material behaviour and 230 kPa the isotropic one.

6.3.3 Effect of Post-Deployment Stresses on Deformation Under Bending

The post-deployment stresses on the artery and stent caused by the deployment mainly affected the vessel wall during the bending deformation of the system. On the stent (Figure 6.6a), the maximum von Mises stress was comparable before and after the bending, with a value of 995 MPa and 992 MPa, respectively. The stress level on the intima layer significantly increased during the bending process. When the post-deployment stresses were not included in the simulation, high levels of stresses (651 MPa) were found on the connector struts in the middle region of the stent (Figure 6.6b), associated with severe bending of the connector struts.

6.3.4 Effect of Post-Deployment Stresses on Deformation Under Radial Compression

Under radial compression, the diameter change against pressure was monitored at three points of the inner surface of the plaque and plotted in Figure 6.7. The diameter differed at the three points due to the circumferential variation of stent structure, with a weaker strength at Point C when compared to Points A and B. The collapse of the artery was observed in both cases at point C when the pressure reached a value of 0.2 MPa. At Point A, the final diameter was similar for the simulations with and without post-deployment stresses, with a value of 2.19 mm and 2.27 mm, respectively. There was a difference for Point B, with a value of 1.91 mm and 2.15 mm for the simulations with and without post-deployment stresses, respectively. For point C, the stent-artery system collapsed more when the post-deployment stress state was accounted for. Specifically, the lumen diameter was reduced to only 1.22 mm after the application of pressure, compared to 1.89 mm obtained from the simulation which neglected the post-deployment stress state.

Stress distributions after radial compression are shown in Figure 6.8 for the stent-artery system, with and without post-deployment stresses. For the simulation which accounted for the post-deployment stress states, an increase of stresses on the stent was found due to the compression,

i.e., increased from 995 MPa before the application of pressure to 1004 MPa after the application of pressure. This is almost equal to the ultimate tensile strength of Co-Cr L605, suggesting the risk of device failure. The stress magnitude on the plaque was reduced at the end of the compression, with a magnitude of 409 kPa compared to 1.90 MPa after stent deployment. Under compression, there was an increase of maximum principal stress levels in the intimal layer, i.e. from 632 kPa to 2.86 MPa. The maximum value was far above the maximum strength of the intima layer in the longitudinal direction, which is reported to be 944 kPa (Khamdaengyodtai *et al.*, 2012). Also, the maximum stresses were shifted towards the ends of the artery, where the tissue had more freedom to deform due to the absence of the stent. Without post-deployment stresses, the stress on the stent had a maximum level of 835 MPa which is lower than that with post-deployment stresses. On the plaque, the maximum principal stress was only 307 kPa after compression, while the stress on the artery was mainly concentrated in the intima layer, with a maximum value of 2.04 MPa. As seen in Figure 6.8, stress distribution was very similar for simulations with and without post-deployment stresses.

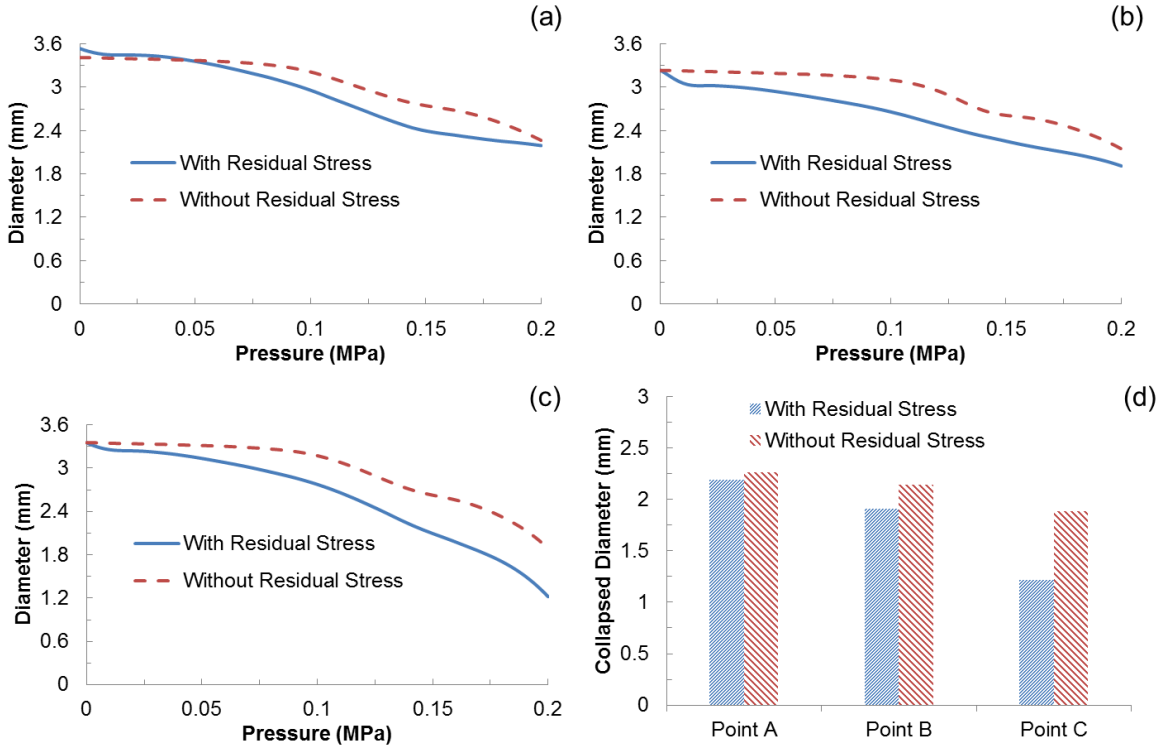

Figure 6.7. Diameter change against pressure during radial compression for (a) point A, (b) point B and (c) point C; (d) Comparison of collapsed diameters at maximum pressure (0.2MPa) for the three points.

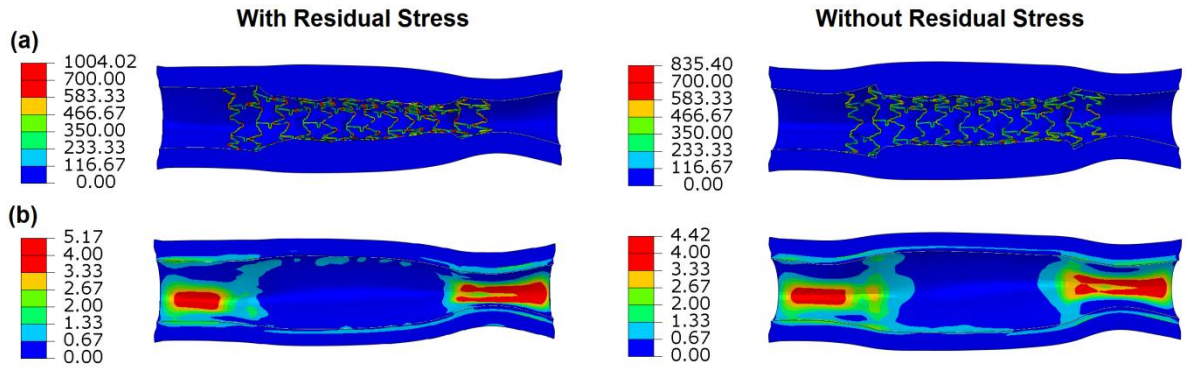

Figure 6.8. Stress contour plots for (a) the stent and (b) the arterial wall at an applied pressure of 0.2MPa obtained from simulations with and without post-deployment stresses.

6.4. Discussion

6.4.1 Vessel Anisotropy and Hyperelastic Behaviour

Results of the stent deployment highlight the importance of the anisotropic behaviour of the artery. The expansion exhibited earlier saturation state when considering the anisotropy of the artery. However, the finally achieved diameter was comparable to that for isotropic model due to the reduced recoiling. The recoiling of the plaque-artery system imposed additional compression on the stent, leading to increased levels of stresses on the stent after balloon deflation when compared to those at peak inflating pressure. Consequently, lower stress levels were found on the stent struts for anisotropic vessel model. Vessel anisotropy also affects the stress levels on the artery-plaque system. Despite the constitutive model of the plaque was identical in both simulations, the stress on the plaque was higher when neglecting the anisotropy of the arterial layers. However, the intima layer exhibited a considerable increase of stress levels when considering vessel anisotropy, which is caused by its much higher stiffness in the longitudinal direction. The results presented above were obtained based on the mean stress-stretch response of the vessel layers tested for 13 patients in Holzapfel *et al.* (2005). The data had a large scatter and showed significant variation in arterial stiffness among the patients chosen. Arterial stiffening can be associated with ageing, due to the degeneration of the elastin fibres. Other clinical factors can also affect the stiffness of the arteries, such as rapid weight gain, obesity and type II diabetes (Payne *et al.*, 2010). Furthermore, inflammation, calcification, endothelial dysfunction, vascular growth and remodelling also affect the mechanical behaviour of arterial layers. In the study of Holzapfel *et al.* (2005), specimens were gathered from thirteen different patients ranging between 54 and 80 years of age. Results showed that the stiffness of the arterial tissues was very different between the patients. To assess how arterial stiffening can affect the stent deployment, stent expansion was simulated using patient specific data, i.e. the stress-stretch response for patients VI and IX tested in Holzapfel *et al.* (2005). The two specific cases represented the stiffest and the softest arteries,

especially the intimal layer, among the 13 patients. The stress-stretch curves of the two patient specific cases, along with the mean behaviour (averaged over all the patients), are shown in Figure 6.9, where the simulations refer to HGO model whose parameters were fitted against the test data for patient VI and IX (Table 6.2).

Table 6.1. HGO model parameters for the arterial layers fitted for patients VI and IX (Holzapfel *et al.*, 2005).

	Material	ρ(kg/mm^3)	C_{10}	D	k_1	k_2	κ	γ
Patient VI	Intima	1.066E-6	0.01	8.95E-7	0.8	150	0.270	13.1°
	Media	1.066E-6	5.00E-3	5.31E-6	0.25	90	0.308	24.9°
	Adventitia	1.066E-6	4.00E-3	4.67E-6	0.5	500	0.285	75.3°
Patient IX	Intima	1.066E-6	0.023	8.95E-7	10	5000	0.308	13.1°
	Media	1.066E-6	1.40E-3	5.31E-6	0.1	100	0.313	24.9°
	Adventitia	1.066E-6	8.32E-3	4.67E-6	1.6	1800	0.310	75.3°

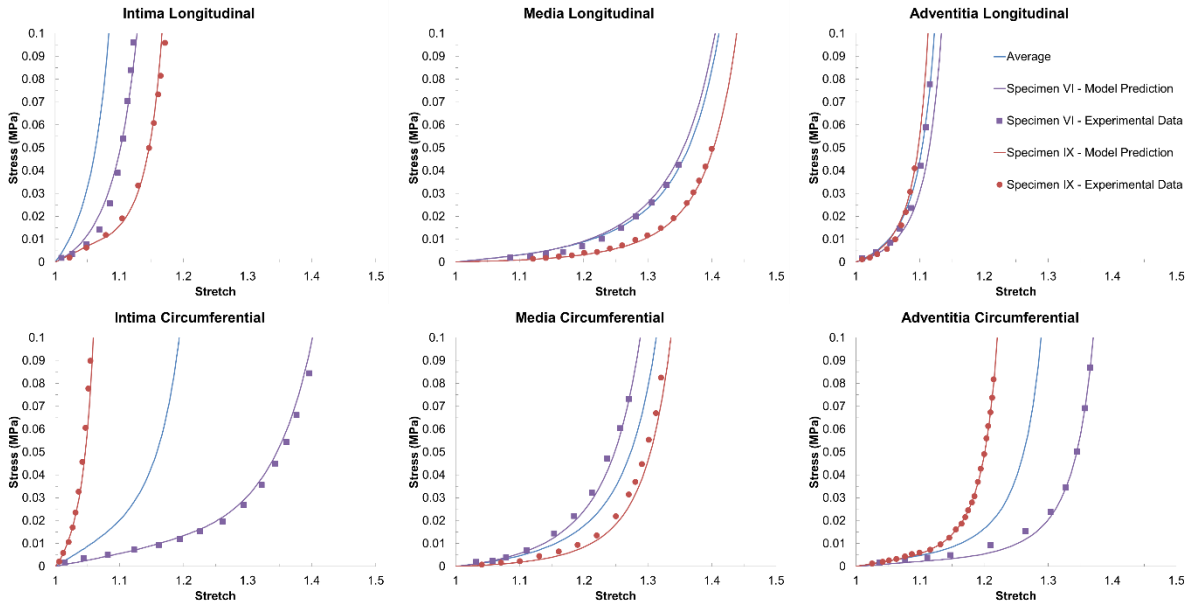

Figure 6.9. Stress-stretch response for patient VI and patient IX, according to the experimental data (Holzapfel *et al.*, 2005) and our model prediction, in comparison with the average material behaviour.

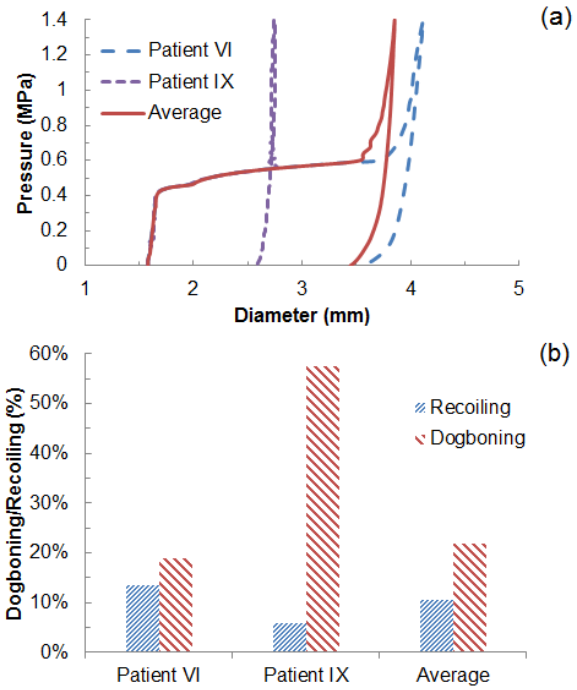

Figure 6.10. (a) Stent expansion and (b) recoiling and dogboning effects for the two specific patients, in comparison with those obtained from the mean artery behaviour.

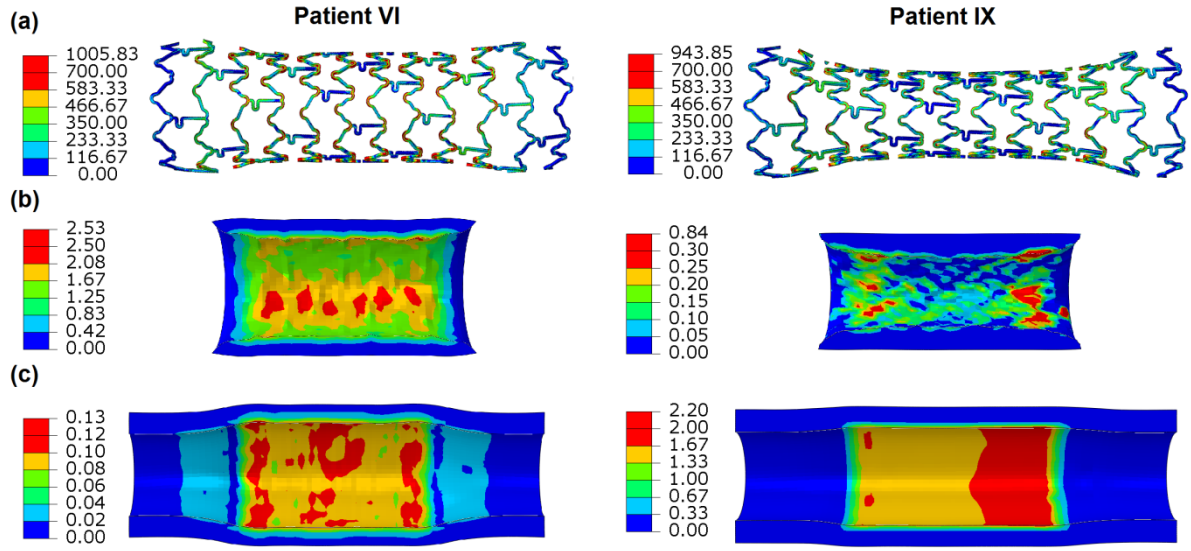

Figure 6.11. Stress contour plots for (a) stent, (b) plaque and (c) arterial layers after deployment of Xience stent in arteries with patient specific behaviour (Holzapfel *et al.*, 2005).

Figure 6.10 shows the diameter change against pressure for the two specific patients, in comparison with that obtained from the mean artery behaviour. The expansion saturation was achieved at a larger diameter for patient VI, with a maximum diameter of 4.10 mm at peak pressure and a final diameter of 3.49 mm after deflation. However, for patient IX the maximum expansion was only of 2.75 mm and the final diameter was just 2.59 mm, indicating a failure in stent expansion due to the high stiffness of the vessel. System recoiling was found increased significantly with the increasing stiffness of the arterial layers, from 5.8% for patient IX (stiff artery) to 13% for patient VI (soft artery). Dogboning was also affected by the arterial stiffness, i.e. 19% for patient VI and 58% for patient IX, compared to 10.6% obtained based on the mean behaviour.

The won Mises stress on the stent after deployment are shown in Figure 6.11a for patients VI and IX. The stress had a maximum magnitude of 1006 MPa for patient VI, compared to 944 MPa for patient IX and 995 MPa for the mean behaviour. On the plaque (Figure 6.12b, maximum principal

stress), the stress was also found increased for patient VI, with a maximum value of 2.53 MPa, compared to 0.84 MPa for patient X and 1.83 MPa for the mean behaviour. For the arterial wall (Figure 6.12c), the maximum principal stress was found higher on the intimal layer in all cases, with values of 0.13 MPa, 0.71 MPa and 2.20 MPa for patient IV, the mean artery behaviour and patient IX, respectively.

These results show that the stiffness of the arterial layers plays a major role on the stent expansion and highly affect the diameter achieved by the end of deflation. Patient IX with high arterial stiffness may represent a failure case for the stent deployment as the stenosis was only cured by 15%. The stresses on the stent and the plaque system are also strongly affected by the arterial stiffness: the stress on the artery was found considerably higher in arteries with higher stiffness (i.e. patient IX), suggesting the high risk of arterial damage and rupture.

6.4.2 Effects of Post-deployment Stresses on Deformation

This work also studied the effects of post-deployment stress on the deformation of stented artery system when subjected to biomechanical forces after deployment. For bending, post-deployment stresses affect the deformation and the final stress state of the stent-artery system significantly. When considering the post-deployment stresses, the deformation on the connector struts was not as severe as that without considering the post-deployment stress state (Figure 6.8). The high post-deployment stresses presented on the U-bend struts after deployment indicated that the stent is in the plastic deformation regime, which allows the U-bends to deform more easily when under further loading due to the lower modulus in the plastic hardening stage. On the contrary, when the post-deployment stress state is neglected, the bending of the stent is mainly carried by the connector struts. The bending appears to have little impact on the stress state in the plaque, but strongly affects the stress state in the intima layer of the artery wall. By considering the post-

deployment stresses on the artery, the stress in the intima layer caused by bending was re-distributed significantly and also had higher magnitudes, which can affect the prediction of tissue damage.

For radial compression, the anisotropy of the artery affects the system deformation considerably, since the stress-strain response of the intima and adventitia layers of the artery in the axial direction is much stiffer compared to the circumferential behaviour (Figure 6.2). For radial compression, the collapse of the stent-artery system was shown more prominently when accounting for the post-deployment stress state. Also, the stiffness of the system varied in the axial direction, with the left side of the artery being less resistant to radial compression due to its relatively higher structural strength. Stent collapse also affected the stress state on the intima layer, because it allowed the artery to be stretched uniformly in the longitudinal direction, leading to reduced stress level. The overall stress level of the system tended to increase for the simulation with post-deployment stresses, due to the collapse of the stent. For the simulation without post-deployment stress, lower stresses in the artery-plaque system were obtained due to the reduced level of deformation associated with higher stiffness of the stent in the radial direction.

6.5. Conclusions

Finite element simulation of stent deployment was carried out using an anisotropic model for the artery, consisting of three individual tissue layers, i.e., intima, media and adventitia. Each layer was modelled as a hyperelastic anisotropic material described by the Holzapfel-Gasser-Ogden (HGO) model. The results showed that, at the peak pressure, stent expansion obtained using the anisotropic model was reduced when compared to that obtained using the isotropic model. However, after deflation, the finally achieved diameter for the anisotropic model is larger than that for the isotropic model, due to the significant reduction in recoiling for the anisotropic model.

Also, the anisotropic model generated slightly higher levels of stress in the artery and the plaque than the isotropic model. Furthermore, care should be taken to treat patients with significant arterial stiffening as it can lead to failure of the arterial expansion and risk of damage. Following deployment, deformation of the system was also modelled by applying relevant biomechanical forces, such as bending and radial compression. Post-deployment stresses generated out of deployment process were found to have an influence on the deformation of the system, resulting in re-distribution of stresses and change of flexibility of the system. In summary, it is strongly recommended to take into account the vessel anisotropy and post-deployment stresses to model expansion and deformation of the stent-artery system.

In the following Chapter, the performance during deployment and the effect of post-deployment stresses generated by stent crimping are studied for a bioresorbable PLLA stent and a metallic stent. Focusing on the diameter expansion of the two stents, along with the stress distributions on stent struts and blood vessel.

Chapter 7 – Crimping and Deployment of Bioresorbable Polymeric Stents

7.1. Introduction

Metallic stents have been dominantly used for stenosis treatment since the very first development in the mid-80s, but the presence of a permanent foreign material inside the human vessels has always been a major shortcoming (Muramatsu *et al.*, 2013). The use of bioresorbable polymers such as Mg-alloys and Poly-L-Lactid Acid (PLLA) is one of the most recent developments in stent technology that aims to overcome this issue. One of the latest bioresorbable stents in the market is the Elixir DESolve stent, which demonstrated sufficient radial strength after 3 months of implantation, with bioresorption observed after one to two years. Verheye *et al.* (2014) carried out a study of the stent performance through a non-randomised trial in 15 patients. The late lumen loss and neointimal volume were measured after six months, using quantitative coronary angiography and intravascular ultrasound techniques. Results showed that successful deployment was achieved for all patients; after six months the lumen loss was found less than 0.38 mm in all cases and the neointimal volume was found between 10.75% and 3.63% only.

The interest in the mechanical behaviour of PLLA has recently increased due to the advent of PLLA stents in the market. Welch *et al.* (2014) recently studied the influence of thermal annealing on the mechanical properties of PLLA for stent applications. Their work showed that the crystallinity of the material increased within thermally annealed stent fibres when compared to the non-annealed specimens. The process of annealing resulted in a considerable increase of the strain at failure, compared to the control specimen, but with a compromise in the yield stress. Luo *et al.* (2014) developed a degradation model for PLLA cardiovascular stents. To verify the computational model, in vitro and in vivo analyses under physiological and normal conditions were

also conducted. Comparison between experimental and numerical results showed an overall good agreement with each other for the radial strength after 10 days, 20 days and 30 days of degradation. Computational analyses of PLLA stents were also carried out by Pauck and Reddy (2014) with the consideration of anisotropic elastic-plastic behaviour of the material. Material modelling of PLLA had a good agreement with the stress-strain curves from their experimental results in both circumferential and axial directions, proving the capabilities of anisotropic computational models to predict accurately the mechanical behaviour of PLLA in both circumferential and axial directions. Results showed that increasing the thickness of the struts will improve the mechanical performances while compromising the restenosis rate. However, increasing the modulus of the material to above 9 GPa will provide the suitable radial strength required (300 mmHg).

In this chapter, deployment of Elixir DESolve (Elixir Medical Corporation, CA, USA) bioresorbable stent has been simulated and compared with metallic Xience stent. In particular, the simulation accounted for the crimping process, which is a necessary step for fixing the as-manufactured stent onto the balloon catheter. A comparison of the performances of the stents has been made, based on the radial expansion of the artery-plaque system and the stresses on both the stent and the blood vessels. Furthermore, to better understand the effect of crimping, expansion has also been simulated without considering the post-crimping stresses generated out of crimping for the two stents and the results were compared with those obtained by considering the crimping-caused stresses.

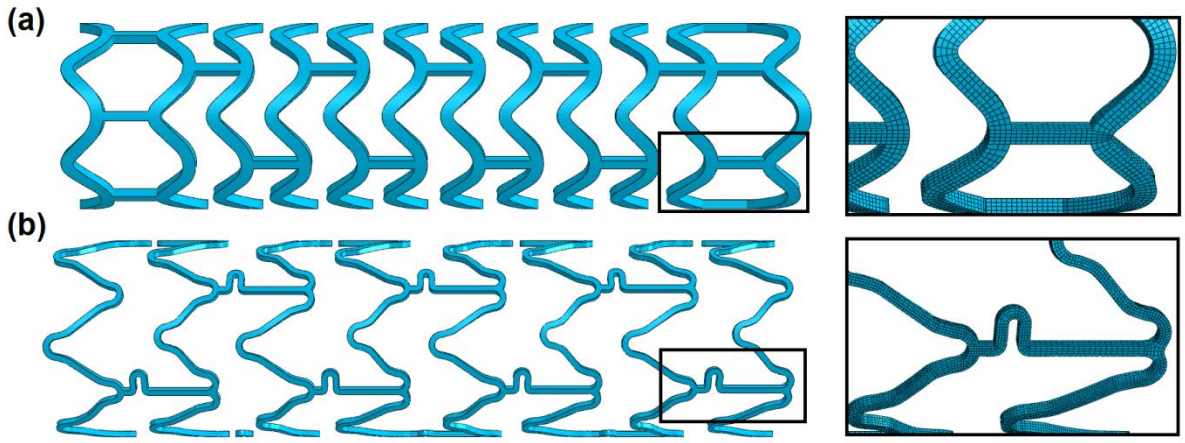

Figure 7.1. As-manufactured geometry and mesh of (a) Elixir and (b) Xience stents.

7.2. Description of the Model

7.2.1 Modelling of the stents, artery and balloon

Two stent designs were chosen for this study, the Xience stent and the bioresorbable Elixir DESolve stent. Geometries of both scaffolds were created using the same procedure described in Chapter 2 (Section 2.2.1). The stents were generated in the expanded shape with 3 mm in diameter, which corresponds to the as-manufactured geometries. The length of the stents was chosen to be 10 mm. The geometry of the Xience stent was consistent with that used in previous analyses. The Elixir stent had a strut thickness of 150 μm and the geometry was created based on dimensions reported in open resources. Both stents were meshed according to the mesh sensitivity study in Section 3.4, with four layers of elements through the width and the thickness of the stent struts. The as-manufactured geometry and mesh of the two stents are shown in Figure 7.1.

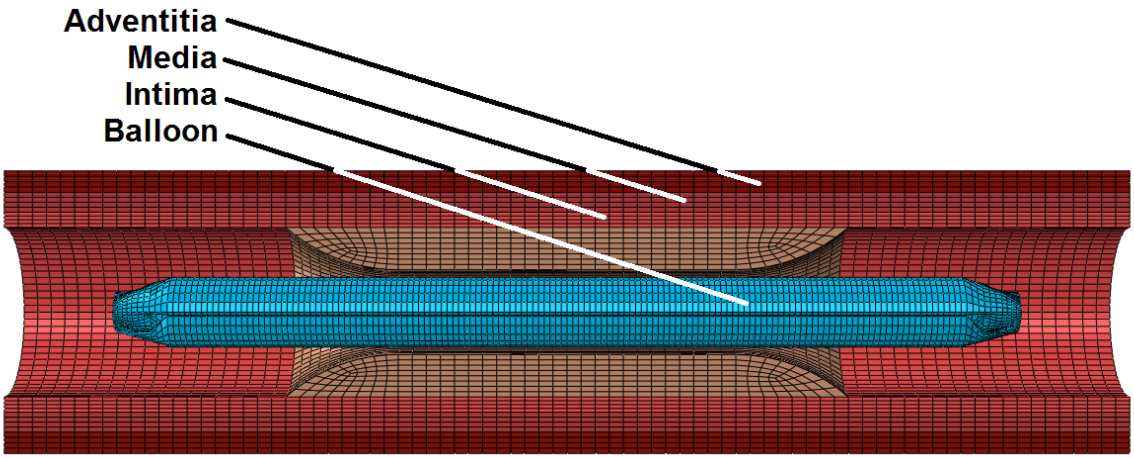

Figure 7.2. Geometry and mesh of the blood vessel with stenosis and angioplasty balloon.

A folded balloon was created and meshed according to the procedure described in Chapter 4 (Section 4.2). The length of the balloon of 14 mm and its expanded diameter was chosen to be 3 mm, which also corresponds to the target post-deployment diameter of the stents.

The arterial, with an inner diameter of 3 mm, a length of 40 mm and an overall wall thickness of 1 mm, consisted of three layers as described in Chapter 2 (Section 2.3.1). Similarly, the plaque was modelled as symmetric, with a total length of 10 mm and a stenosis of 50%. The artery and plaque were meshed with 4-layers of elements through the thickness of each arterial layer and 8-layers of elements through the thickness of the plaque, in accordance to our mesh sensitivity study (Section 3.4). Geometry and mesh of the whole system are shown in Figure 7.2.

7.2.2 Constitutive behaviour of materials

Xience stent is made of Co-Cr L605 which has the same constitutive behaviour as described in Chapter 2 (Section 2.2.2). Elixir DESolve stent is made of Poly-L-Lactid Acid (PLLA), which shows anisotropic and viscoplastic behaviour that are also affected by its biodegradation process

(Vieira *et al.*, 2013; Pauck and Reddy, 2014). For the analysis in this chapter, simplified isotropic elastic-plastic behaviour was employed, similar to that used for metallic stents (Section 2.2.2). Figure 7.3 shows the stress-strain response of PLLA (Pauck and Reddy, 2014) used for this study, which is much weaker than that of Co-Cr L605. Table 7.1 lists the properties for PLLA and Co-Cr L605 extracted from the corresponding stress-strain curves. Hardening was implemented in ABAQUS by considering the increase of yield stress with the plastic strain, which is also extracted from the stress-strain curve.

The arterial layers were modelled using the anisotropic Holzapfel-Gasser-Ogden (HGO) model as detailed in Chapter 6 (Section 6.2). Hypocellular plaque was modelled using the isotropic Ogden model as given in Chapter 2 (Section 2.2).

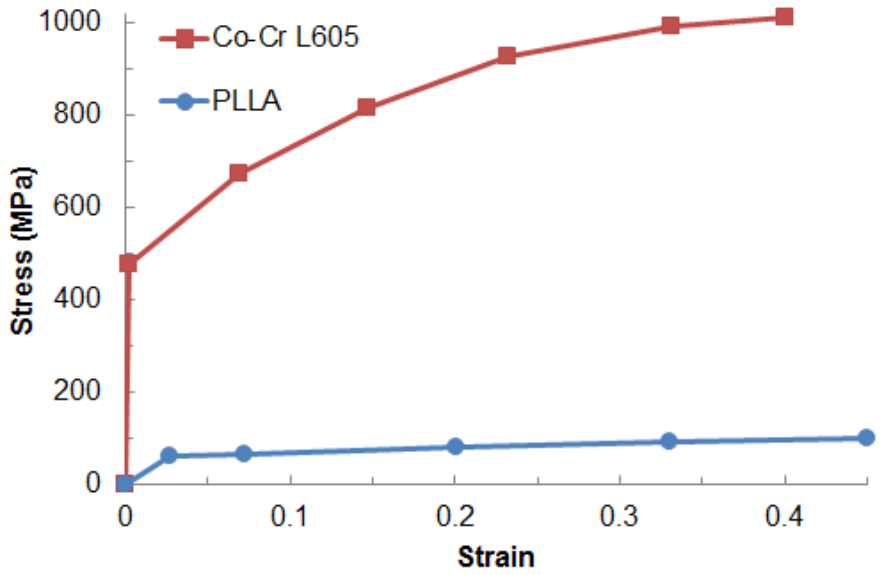

Figure 7.3. Stress-strain curves for the Co-Cr L605 alloy and PLLA (Medtronic Technical Bulletin, 2003; Pauck and Reddy, 2014).

Table 7.1. Properties for the Co-Cr L605 and PLLA stent materials (Medtronic Technical Bulletin, 2003; Pauck and Reddy, 2014).

Material	ρ (kg/mm^3)	E (GPa)	ν	σ_y (MPa)
Co-Cr L605	$9.1 \cdot 10^{-6}$	243	0.30	476
PLLA	$1.4 \cdot 10^{-6}$	2.2	0.30	60

7.2.3 Crimping procedure

To simulate the crimping of the stent, a series of 12 rigid planes were created around the scaffold in a cylindrical pattern. Each rigid plane was modelled as a shell surface with a length of 14 mm and a fixed distance of 0.1 mm from the outer surface of the stent. A displacement boundary condition was enforced to the planes in the radial direction with a magnitude linearly increasing to 1 mm. In this way, the expected stent outer diameter at the end of the crimping process would be around 1.2 mm, which is small enough to fit inside the diseased artery. Figure 7.4 shows the assembly of the crimping simulation of Elixir stent.

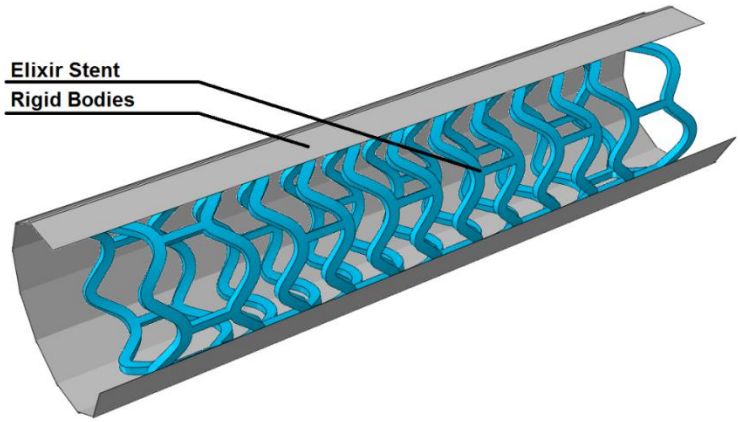

Figure 7.4. Illustration of assembly used in crimping simulation for Elixir stent.

Abaqus Dynamic/explicit solver was used for this simulation, with a step time of 0.1 s. The stent was free of constraints during the whole step, whilst the ends of the balloon were fixed in all directions. Hard contact with a friction coefficient of 0.8 was applied between the rigid planes and the outer surface of the stent and between the balloon and the inner surface of the stent, to ensure that the balloon stays within the scaffold at the end of the process. At the end of the crimping, one additional step was implemented to allow the relaxation of the stent from the fully crimped state. The step time for this relaxation process was 0.1 s, when all the contacts between the stent and the rigid bodies were removed whilst the balloon was kept in its crimped shape. In this way, the stent was able to recoil slightly without being affected by either the balloon or the rigid planes.

7.2.4 Expansion procedure

The expansion procedure was simulated according to the procedure described in Chapter 2 (Section2.3). The maximum pressure of inflation inside the balloon was chosen to be 1.2 MPa. Three cases of stent expansion were studied. In the first case, the Xience stent was expanded within the artery by accounting for the post-crimping stresses accumulated during the crimping process. The second simulation consisted of the deployment of Elixir stent within the artery, accounting for the post-crimping stress. In the third case, the fully crimped geometry of the Elixir stent was deployed without retaining any of the post-crimping stresses in the system.

These simulations were compared with each other in terms of diameter change against pressure, recoiling and dogboning effects and stress distribution in the stent-artery-plaque systems. This was used to assess the impact of the crimping procedure on the stent deployment inside a diseased artery and to compare the performances between commercially available metallic and bioresorbable polymeric stents.

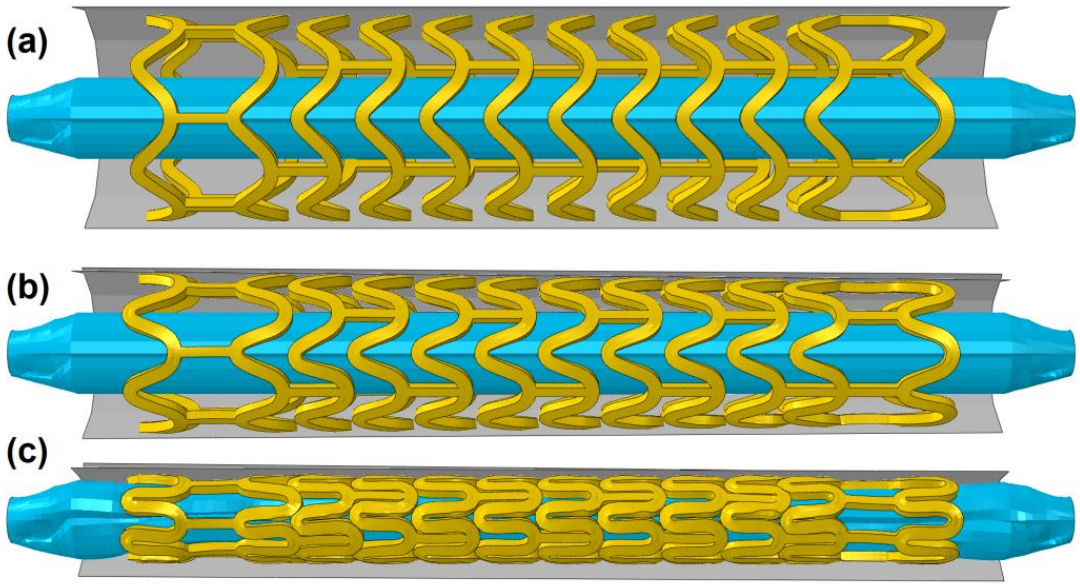

Figure 7.5. Deformation of Elixir stent and balloon (a) before, (b) during and (c) at the end of the crimping process.

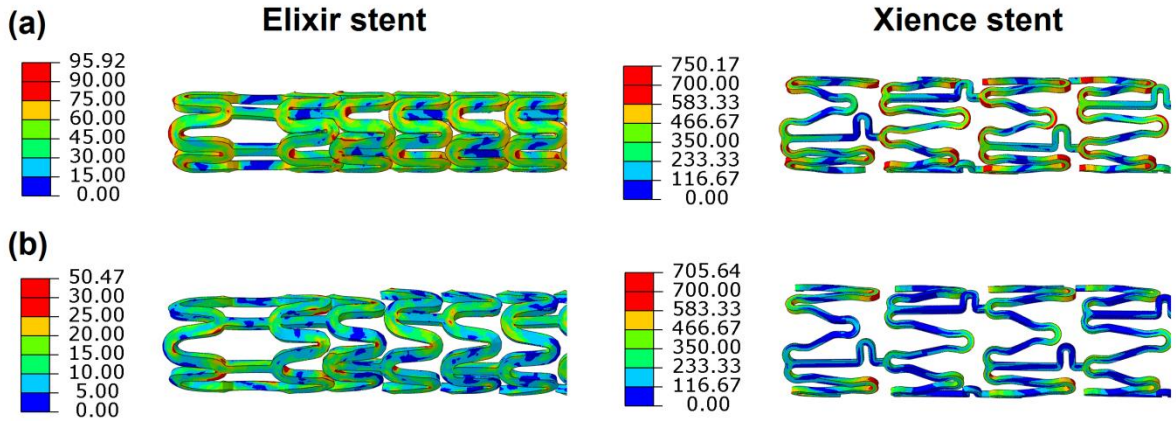

Figure 7.6. Von Mises stress contour plot for the Elixir (left) and Xience (right) stents in the (a) fully crimped configuration and (b) relaxed configuration.

7.3. Results

7.3.1 Stent crimping

The process of stent crimping for the Elixir stents is shown in Figures 8.5. Both stents were compressed to a diameter of 1.25 mm at the end of the crimping process. Maximum stresses were found at both inner and outer sides of the U-bends for both stents. The maximum von Mises stress after crimping were 755 MPa for the Xience (Figure 7.6a) stent and 96 MPa for the Elixir (Figure 7.6b). After relaxation, the post-crimping stresses were reduced to 706 MPa and 50 MPa for the Xience and Elixir stents, respectively. (Figure 7.6c and d), and the stents settled at a diameter of around 1.5 mm.

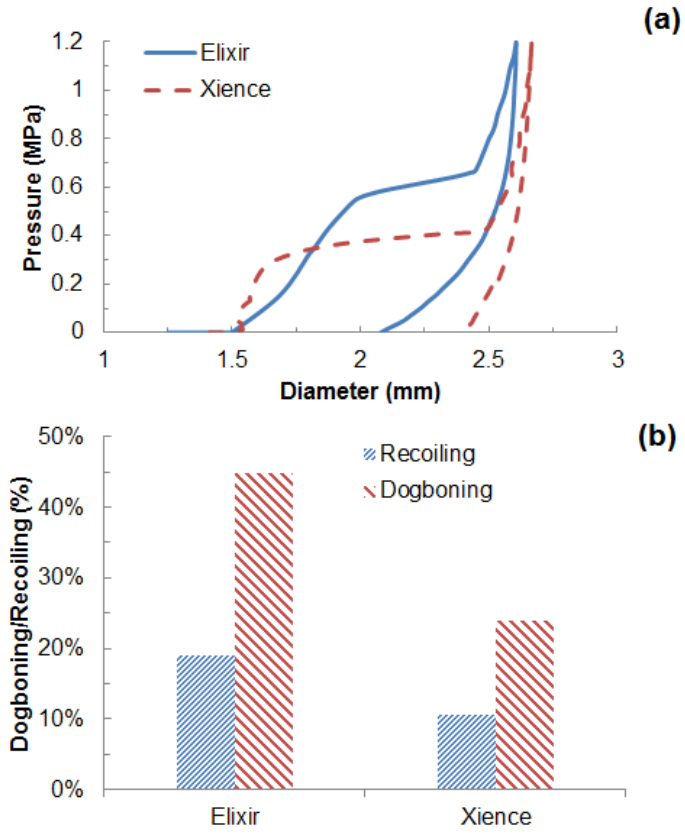

Figure 7.7. (a) Diameter change against pressure, (b) recoiling and dogboning effects during deployment of Elixir and Xience stents.

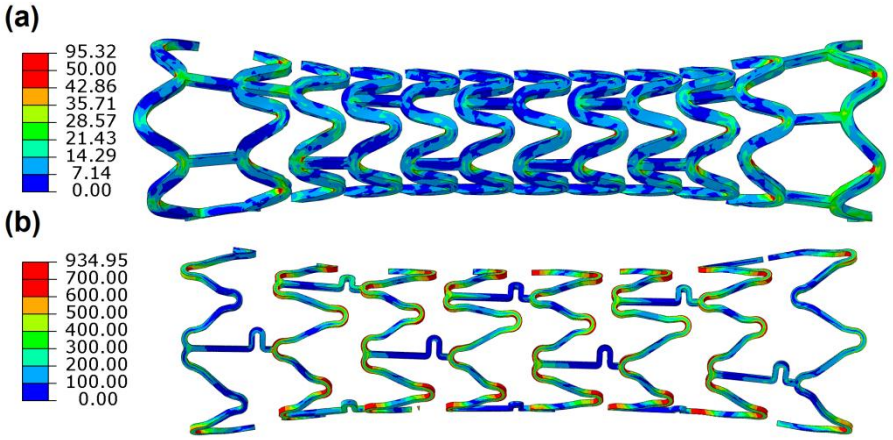

Figure 7.8. Contour plot of the von Mises stress on (a) Elixir and (b) Xience stents after deployment.

7.3.2 Comparison between Xience and Elixir stents

Expansion behaviour of Xience and Elixir stents is shown in Figure 7.7. Elixir stent expanded with a slower rate and reached saturation earlier when compared to Xience stent. As a result, the diameter at the maximum pressure was measured at 2.66 mm for the Xience stent and 2.61 mm for the Elixir stent. The recoiling (Figure 7.7b) was also significantly lower for the Xience (11%) than that for the Elixir stent (20%), which led to a final diameter of 2.40 mm for the Xience stent and only 2.10 mm for the Elixir stent. Consistent with these results, the Xience stent experienced considerably less dogboning (24%) than the Elixir stent (45%).

On the stents, the magnitude of the stress was monitored at the end of the inflation process and after the recoiling. Figure 7.8 shows the von Mises stress contour plot on both stents after deployment. The maximum stresses occurred in the inner corners of the U-bends with a magnitude of 945 MPa and 95 MPa for the Xience and Elixir stents, respectively. Figure 7.9 shows the maximum principal stress on the artery-plaque system at the end of balloon deflation. The maximum stresses were located on the inner surface of the plaque, with strong stress concentration

at both ends of the stenosis due to the dogboning effect. The maximum stress on the plaque was 1.22 MPa for the Xience stent and only 0.52 MPa for Elixir stent, which is consistent with the less arterial expansion achieved by the bioresorbable stent.

7.3.3 Effect of Post-Crimping stress

To study how the crimping process affected the stent expansion, the deployment of Elixir and Xience stents were also simulated without accounting for the post-crimping stresses generated during the compression of the stents. The diameter change against pressure in the case of expansion of Elixir stent for the two cases is shown in Figure 7.10. Stent expansion was affected by the presence of post-crimping stresses, and a larger diameter (2.75 mm) at peak pressure was achieved by the simulation without post-crimping stresses (2.61 mm when post-crimping stresses were included). After deflation the diameter was found to be 2.10 mm and 2.19 mm for simulations with and without the post-crimping stress, respectively. The recoiling effect was found similar, about 20% in both cases. However, dogboning was reduced for simulation without post-crimping stress (41%; compared to 45% for simulation with post-crimping stress).

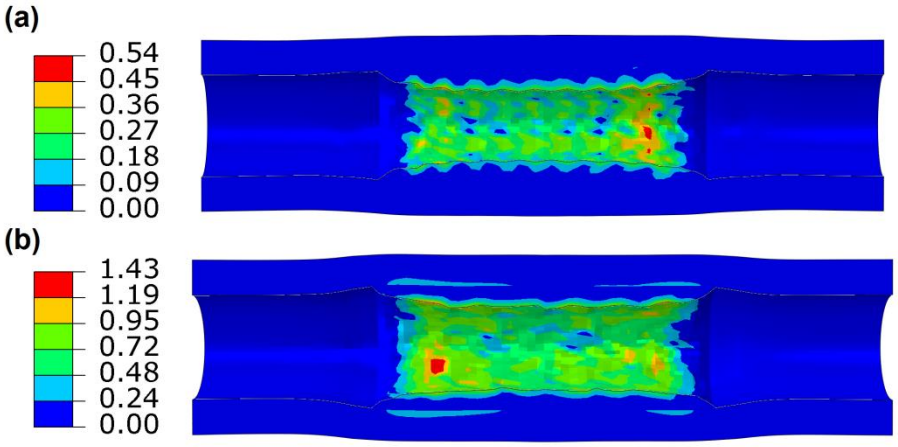

Figure 7.9. Contour plot of maximum principal stress on the stenotic plaque after stent deployment: (a) Elixir and (b) Xience stents.

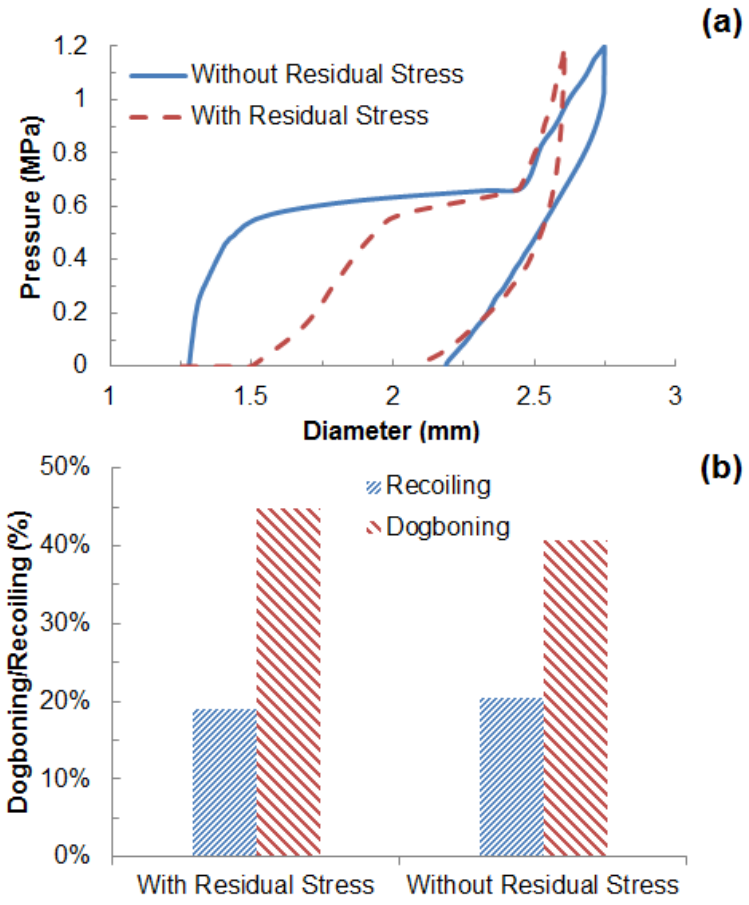

Figure 7.10. (a) Diameter change against pressure and (b) recoiling and dogboning effects obtained from simulations with and without considering crimping-caused post-crimping stresses on Elixir stent.

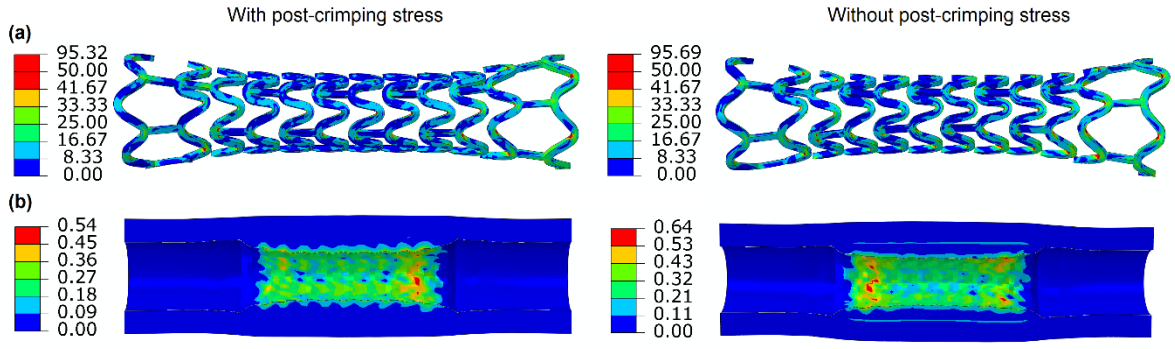

Figure 7.11. (a) von Mises stress on the Elixir stent and (b) maximum principal stress on the artery-plaque system for simulation with (left) and without (right) considering post-crimping stresses.

Figure 7.11 compares the stress contours on the Elixir stent and in the artery-plaque system for simulations with and without considering post-crimping stresses. For the stent, stress distribution had a similar pattern for the two cases, with only a small difference in the maximum stress levels. Specifically, the maximum stress on the stent was 95 MPa when the post-crimping stresses were not considered and 96 MPa when post-crimping stresses were considered. For the artery-plaque system (Figure 7.11b), stresses were concentrated at both ends of the plaque due to dogboning effect, with a magnitude of 0.54 MPa when the post-crimping stress was not considered and 0.64 MPa when the post-crimping stress was considered.

The expansion of Xience stent, on the other hand, did not exhibit any significant change when post-crimping stresses were considered. In fact, Figure 7.12 shows that both diameter change and recoiling effect are similar for the two cases (with and without post-crimping stresses). Dogboning was found increased for the simulation without the post-crimping stresses, with a value of 36% (compared to 24% for the case with post-crimping stresses). Moreover, the stresses developed on the stent and the artery were also comparable for the two cases (with and without post-crimping stresses) (Figure 7.13).

7.4 Discussion

It is clear from these results that crimping of the stent induced high levels of stress on the stent struts, which are comparable to the stresses normally achieved during expansion. For Xience stent, stresses caused by crimping were generally lower than those induced by the inflation, while for the Elixir stent, stresses caused by crimping were higher than those induced by the inflation.

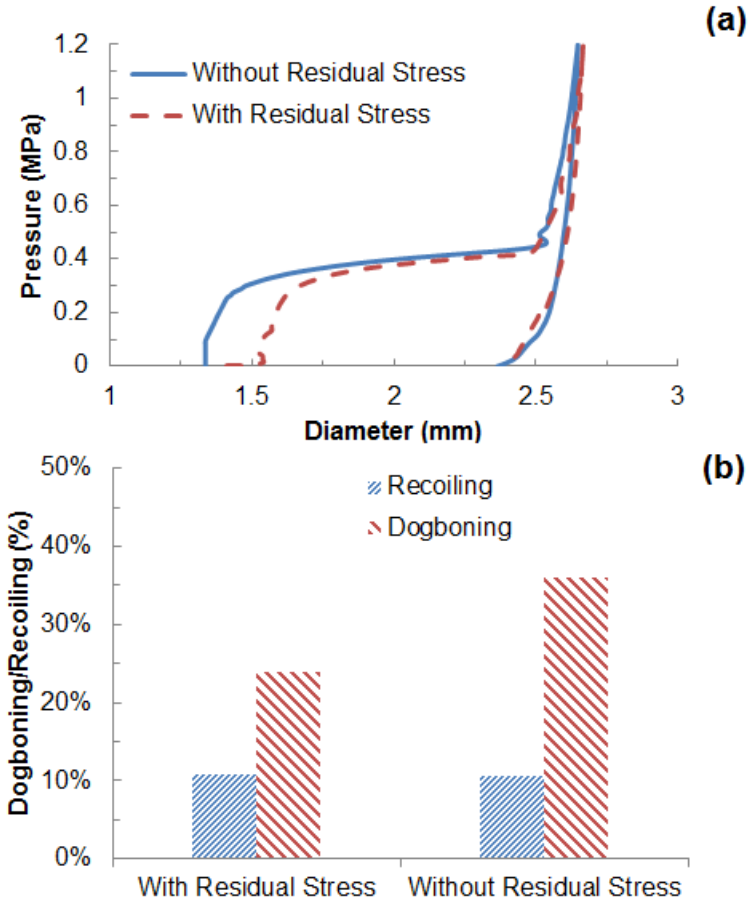

Figure 7.12. (a) Diameter change against pressure and (b) recoiling and dogboning effects obtained from simulations with and without considering crimping-caused post-crimping stresses on Xience stent.

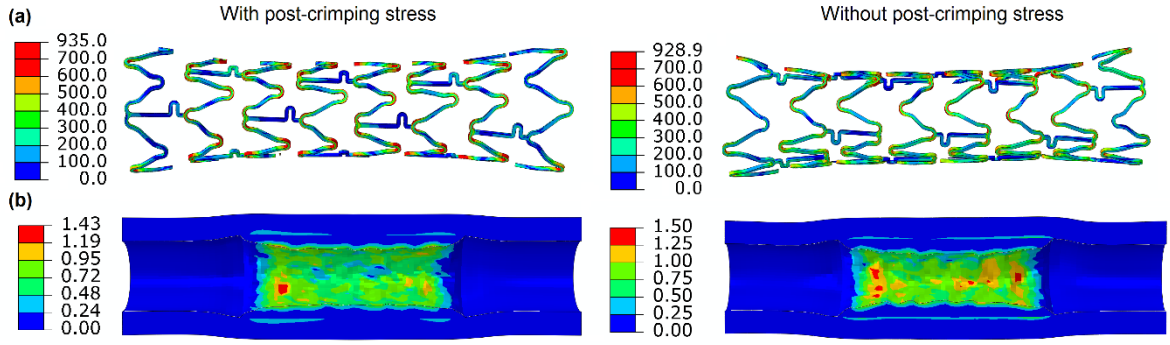

Figure 7.13. (a) von Mises stress on the Xience stent and (b) maximum principal stress on the artery-plaque system for simulation with (left) and without (right) considering post-crimping stresses.

For both stents, the target diameter of 3 mm was not achieved. This was due to the expansion saturation of the stent-artery system, which is mainly governed by the high stiffness of the intima layer that develops during the later stage of stretching. The inflation of Elixir stent was slower than that of Xience stent. Increased recoiling effect was also found for the Elixir stent due to the weaker strength of PLLA compared to that of Co-Cr alloy. This suggests that for bioresorbable PLLA stents inflation at low pressures (i.e., less than 1 MPa) is not recommended, and also the stents might not be suitable for patients with high arterial stiffness and plaque calcification. However, it is noticed that Elixir stent induced significantly lower stresses on the artery-plaque system than Xience stent. As previously discussed (Chapters 3 and 5), low arterial stresses reduce the risks of restenosis, chest pain and arterial perforation.

Möller *et al.* (2000) investigated the post-crimping stresses on the stent struts during the process of crimping and expansion. Results showed that even in as-manufactured stents, significant amount of post-crimping microstresses can be observed. Dilated stents showed an increase of post-crimping stresses due to tension. Crimped and dilated stents exhibited even more pronounced increment of post-crimping stress due to both compression (crimping) and tension (expansion). According to their conclusions, the level of post-crimping stresses caused by both crimping and expansion can significantly affect the life span of the device. From our simulations, the post-crimping stress affected the expansion of the Elixir stent and the amount of stresses developed on the plaque. The diameter gain of the artery-plaque system was lower when considering the post-crimping stresses caused by crimping, along with higher dogboning effect. In addition, reduced stress levels were found on the stenosis plaque when the post-crimping stresses were taken into account. As already discussed in Chapter 6 (Section 6.4.2), the presence of post-crimping stress on the stent struts increases flexibility of the device, inducing less stresses on the stenosis. On the other hand, the expansion of the Xience stent was not affected by the presence of the post-crimping stresses. For the Elixir stent, the maximum post-crimping stress on U-bends after

crimping was comparable to that developed during the expansion; While for the Xience stent, the post-crimping stress after crimping were 20% lower than that developed during expansion.

7.5. Conclusions

In this chapter, the process of crimping and deployment has been modelled for two commercially available stents, i.e., the bioresorbable polymeric stent, Elixir DESolve, and the Co-Cr alloy stent, Xience. The effects of post-crimping stresses caused by crimping on the system expansion were also studied in this work.

Results showed that Elixir stent has a lower expansion rate than Xience stent, with expansion saturation happening at a higher pressure. The diameters achieved at the peak pressure and after the balloon deflation were smaller for Elixir stent. Due to the difference in design and material properties, the bioresorbable stent also showed a significantly higher recoiling, which suggests that the stent is not suitable for the treatment of calcified plaques and patients with stiff or thick vessels. Post-crimping stresses on the Elixir stent generated from the crimping process reduced the expansion of the stent and increased the dogboning effect. Slightly decreased stresses were also found in the artery and plaque when the crimping-caused post-crimping stresses were considered in the simulations.

The next Chapter shows the conclusions of this Thesis. In the first part, the studies performed for this project are discussed, highlighting the main conclusions of each Chapter. The second part, presents some of the possible developments in the use of FE to improve stent surgery and in designing the future generations of stents.

Chapter 8 – Conclusions

8.1. General Discussion

Different aspects of stent expansion inside atherosclerotic arteries were studied in this thesis. The incidence of death by cardiovascular diseases (such as atherosclerosis) is shown to be one of the highest in the world and largely treated by stenting. Despite the advancements in this technology, clinical studies show the shortcomings of stent implants by exposing specific cases of post-stenting complications for the patients (restenosis, stent failure and others). Review of in vivo, ex vivo and in vitro experimental studies compared the stents' flexibility, radial stiffness and fatigue strength between different commercially available designs. However, the experimental studies are limited due to the considerable difficulties of testing the device in a realistic body environment. On the other hand, computational analyses showed a large amount of FE simulations have been carried out to study stent biomechanics. Such work showed that the arterial and plaque behaviour, as well as the vessel geometry and the methods used in modelling of balloon expansion, play a major role in the expansion process of stents. Comparison between different stent designs and vessel factors (such as arterial bifurcations, tortuosity and patient specific arterial geometries) can be successfully simulated by means of FE analyses, in order to provide an improved understanding of stent treatment. Therefore, this study aims to investigate the mechanical performance of stents during deployment inside atherosclerotic human arteries using FE analysis.

The general simulation methodology is presented in Chapter 2, along with the model validation. The model was validated using both mesh sensitivity and validation study. The mesh sensitivity showed that for the stent, four layers of elements through the thickness and two layers of elements through the width of the struts are sufficient to obtain numerical convergence. For the artery-plaque system, a mesh with two layers of elements through the thickness of each arterial tissue and four layers of elements through the thickness of the plaque was found acceptable for this study.

In addition, the model was further validated against the published work of Chua *et al.* (2003 and 2004a), in terms of stent diameter change and stress distributions on both the stent and the artery.

A study of the effects of stent designs, material choice and coating on the deployment of stent inside an artery with stenosis, exposed in Chapter 3, revealed that materials with lower yield stress and weaker strain hardening showed more severe deformations and lower post-deployment stress. The drug eluting coating only affected the recoiling and dogboning effects, with an increase of post-deployment stresses on the stent-artery system. Stents with open-cell designs expanded more easily than those with closed-cell designs, but with higher recoiling effect. On the other hand, dogboning can be significantly reduced by using more longitudinal connective struts. In addition, calcification of the plaque reduced the stent expansion considerably for all stents, but open-cell designs generated lower stress levels on the plaque, suggesting a lower risk of rupture and restenosis.

The fourth chapter shows the importance of arterial constraints, balloon folding and arterial constitutive modelling in simulations of stent deployment. In fact, over-constraining the artery resulted in an increase of recoiling effects, leading to less expansion and lower stress on the stent and the artery. Balloon folding had a significant influence in the stent expansion, exhibiting sustained expansion behaviour at lower pressure. The expansion behaviour of the stent-artery system is also highly dependent on the constitutive model used to describe the artery and the plaque. Results showed that neglecting the three layered structure of the vessel wall results in a failure of the prediction of the stress discontinuity through the thickness of the artery. Also, the constitutive model that neglected the second stretch invariant showed no saturation in its expansion behaviour.

Vessel factors are also proved to play an extensive role in the stent deployment, which is studied in Chapter 5 by considering varied stenosis, plaque asymmetry and artery curvature. The radial

stiffness of the system increased considerably with the level of stenosis, leading to lower expansion, increased recoiling effects and stress levels on the plaque. The plaque asymmetry generated non-uniform expansion in the circumferential direction and high levels of stress concentration in the vessel wall which is covered by thinner plaque. There was a reduction in stent expansion and an increase in stresses on the plaque when stent deployment was performed in a bent artery. These results confirmed the clinical complications encountered when stenting arteries with severe stenosis or arterial branches with sharp corners and non-uniform plaques.

The anisotropy of the arterial tissue and its effect on the stent expansion are presented in Chapter 6, together with the effects of post-deployment stresses on stent performance subjected to biomechanical loads (i.e. bending and compression). Results of this chapter showed that the anisotropy of the artery clearly affected the expansion of the stent inside the vessel. The saturation of stent expansion started at earlier times and the recoiling effect was reduced for simulations using the anisotropic constitutive model. Arterial stiffening, which is a common condition caused by aging, obesity and diabetes (Payne *et al.*, 2010), also affected stent deployment significantly, leading to much reduced stent expansion and increased stress levels on both the stent and the artery. Under biomechanical forces, deformation of the stent-artery system was considerably affected by the post-deployment stresses generated out of stent deployment. Specifically, stents are more prone to further deformation when the post-deployment stresses were taken into account in the simulations.

Chapter 7 presented the simulations of both crimping and deployment of two stents (i.e. Xience and Elixir) inside a diseased artery. A comparison was made between the expansion behaviour of the two stents to assess the performances of the bioresorbable PLLA Elixir stent. Results showed that the bioresorbable stent expanded slowly when compared to the Xience stent, with more recoiling after the deflation of the balloon. Also, the stress levels on the artery caused by the expansion of Elixir stent were found considerably lower than those caused by the expansion of

Xience stent. In addition, the effects of the stresses caused by crimping were also analysed, showing that the expansion of the Elixir stent and the stresses on the artery were both reduced when the post-crimping stresses were taken into account.

8.2. Limitations and Future Directions

A list of limitations was identified for this study regarding the modelling of stent deployment. These limitations need to be considered in future developments to provide more insightful results as well as confirmation of the current findings.

Most of the limitations are associated with the modelling of the arterial wall and stenosis, such as the neglectance of inelastic effects (i.e. such as plasticity and damage). As also mentioned by Maher *et al.* (2011 and 2012), the soft tissues of the blood vessel and stenosis present residual strain after being subjected to uniaxial compression. In terms of stent deployment, this is likely to translate into a reduction of the recoiling effects, due to the lower pressure exerted by the vessel during the balloon deflation.

The geometry and composition of the plaque were proved to be important factors that affected the stent deployment. In this work the plaque is modelled as a homogeneous layer of soft tissue. Better plaque modelling can be obtained with the inclusion of the two main plaque component, i.e. the lipidic pool and the fibrous cap. Furthermore, the current work should also be extended to study the effects of localised narrowing and calcification of the stenosis on stent deployment.

The geometry and tortuosity of the artery can play a critical role in the deployment of stents, as demonstrated by literature (Auricchio *et al.*, 2011; Morlacchi *et al.*, 2013). CTA can be used to produce accurate geometries of patient specific arteries, which can be employed for FE simulations of stent deployment. This technique can be included in the framework developed in this thesis to

study patient specific cases. A different technique that can be taken into consideration to model patient specific arteries is the Intravascular Ultrasound (IVUS), which is currently used to provide imaging of the cross sectional views of obstructed arteries.

In the case of stent deployment, one factor that plays a major role in the expansion process is the modelling of balloon. A realistic folded balloon model was proposed in this study, leading to more accurate prediction of the expansion behaviour. Further improvements to this model is the inclusion of dual balloon material and tapering, which modify the local stiffness of the balloon in order to obtain a more uniform expansion. The inclusion of the heterogeneous properties of the balloon is likely to affect the expansion process with a consistent reduction in the dogboning effect.

In this thesis, bending and compression of the artery were modelled after the deployment of stents. One of the most important risks after stenting of the artery is thrombosis, which is affected by the local hemodynamics. Therefore, the modelling of blood flow would make a significant improvement for post-deployment simulations, in order to identify designs with the lowest risk of thrombosis.

8.3. Clinical Implications

Results of this work showed that FE analyses can be used to provide a better understanding of the biomechanics during and after stent deployment. It has been shown in this thesis that the choice of the correct scaffolds can influence the success of the treatment. The high radial and longitudinal stiffness can cause high stress levels on the device and the artery-plaque system upon expansion. This may lead to early failure of the struts and jeopardise the long lasting purposes of the treatment. Also, high stress level on the plaque and the artery can facilitate the process of restenosis and, in extreme cases, lead to plaque rupture and arterial damage.

With constantly increasing capabilities of FE methods, it is possible to identify the influence of specific factors on the biomechanical behaviour of the system. From this work, it emerged that the biomechanics of stent deployment is governed by three main arterial factors: the stiffness of the arterial tissues, the plaque calcification and morphology. From the clinical history of the patient, it is possible to draw considerations regarding the occurrence of arterial stiffening (Payne *et al.*, 2010), whilst the amount of plaque calcification and morphology can be identified by imaging techniques (Wexler *et al.*, 1996). These can all be used as a basis to determine the best treatment for the specific patient.

On a different note, a large amount of different commercially available stents are on the market, which exhibit different behaviour when expanded inside atherosclerotic arteries. To correctly tune the treatment for the given patient, it is necessary to understand the link between the geometrical and material features of the scaffold, the radial stiffness and the stress magnitudes induced on the artery and the plaque. The radial stiffness will determine the successfulness of the treatment in terms of diameter dilation, whilst minimising the stresses on the plaque and the artery will reduce the risks of restenosis and chest pain.

In conclusion, surgeons must consider the anamnesis of the patient, the stenosis calcification and the vessel morphology in order to select a scaffold that fits the patient specific case. The choice must be made in order to provide treatment of the artery with reduced risk of further complications, in particular by avoiding excessive post-dilation (Fröbert *et al.*, 2013) or stent overlapping (Morlacchi *et al*, 2013). According to the findings of this study, open-cell designs made of Co-Cr, such as Xience and Endeavor stents, have generally better performance than stainless steel devices. Specifically, in the presence of high calcification of the plaque and arterial stiffening, the stent of choice must be flexible and possesses an open cell design and thin struts (e.g. Endeavor stent). With hypocellular plaques and absence of arterial stiffening, a stiffer design, such as Xience stent, can be taken into consideration in order to provide a larger expansion. Particular care during

the expansion must be taken when dealing with highly eccentric plaques, which are accumulated mostly on one side of the artery. In these case, expansion with high pressure and non-compliant balloons are discouraged, as damage can occur to the artery in areas where the arterial tissue is more vulnerable.

8.4. Designing Future Generations of Stents

Numerous studies suggested that patient specific simulations are key to ensure the best clinical outcomes for stenting (Zhang *et al.*, 2007; Auricchio *et al.*, 2011 and 2013; Morlacchi *et al.*, 2013). From our results, the local plaque thickness and varied composition can affect the stress distribution on the arterial layers and the expansion of the artery significantly. According to current findings, the stent could exhibit variable flexibility along the axial direction to effectively treat the arterial branches with axially varied stenosis. The connector struts of the stent may play a major role in controlling the radial stiffness of the scaffold. For instance, by changing the number of connection and their length it might be possible to tune the local stent flexibility according to the needs of the patient. The primary purpose of a patient specific design would be to uniformly distribute the pressure exerted on the arterial tissue after the expansion, in order to reduce the risk of stent fracture and avoid the induction of excessive stress at the sites of the artery which show low obstruction.

The axial flexibility must also be taken into account, particularly if the stent is implanted in proximity of joints, such as femoropopliteal arterial segments (Smouse *et al.*, 2005). Higher axial flexibility is normally achieved with shorter (preferably peak-to-peak) and less number of connective struts between the stent rings, which often results in reduced radial stiffness of the stent. Surgeons must then compromise between high flexibility and radial stiffness of the scaffold.

This compromise might also be avoided with the development of scaffolds that exhibit variable flexibility and radial stiffness according to the specific stenosis morphology.

Many technological gaps have to be filled before patient specific treatment is clinically accepted. Patient specific modelling based on imaging techniques and 3D reconstruction of the blood vessels and stenosis is helpful for the research and development of such treatment. Furthermore, the modelling techniques can be combined with the latest additive manufacturing technology, such as selective laser melting, to produce patient-specific stents, representing the future trend of healthcare.

References

Adlakha, S., M. Sheikh, S. Bruhl, E. Eltahawy, U. Pandya, W. Colyer, and C. Cooper. "Coronary Stent Fracture: A Cause of Cardiac Chest Pain?". International journal of cardiology 141, no. 2 (2010): e23-e25.

Al-Mukhaini, M., P. Panduranga, K. Sulaiman, A.A. Riyami, M. Deeb, and M.B. Riyami. "Coronary Perforation and Covered Stents: An Update and Review." Heart views 12, no. 2 (2011): 63.

Auricchio, F., M. Conti, M. De Beule, G. De Santis, and B. Verhegghe. "Carotid Artery Stenting Simulation: From Patient-Specific Images to Finite Element Analysis." Medical Engineering & Physics 33, no. 3 (2011): 281-89.

Auricchio, F., M. Conti, A. Ferrara, S. Morganti, and A. Reali. "Patient-Specific Finite Element Analysis of Carotid Artery Stenting: A Focus on Vessel Modeling." International journal for numerical methods in biomedical engineering 29, no. 6 (2013): 645-64.

Badel, P., S. Avril, M.A. Sutton, and S.M. Lessner. "Numerical Simulation of Arterial Dissection During Balloon Angioplasty of Atherosclerotic Coronary Arteries." Journal of biomechanics 47, no. 4 (2014): 878-89.

Balossino, R., F. Gervaso, F. Migliavacca, and G. Dubini. "Effects of Different Stent Designs on Local Hemodynamics in Stented Arteries." Journal of biomechanics 41, no. 5 (2008): 1053-61.

Berry, J.L., E. Manoach, C. Mekkaoui, P.H. Rolland, J. Moore Jr, and A. Rachev. "Hemodynamics and Wall Mechanics of a Compliance Matching Stent: In Vitro and in Vivo Analysis." Journal of vascular and interventional radiology 13, no. 1 (2002): 97-105.

Blouza, A., L. Dumas, and I. M'Baye. "Multiobjective Optimization of a Stent in a Fluid-Structure Context." Paper presented at the Proceedings of the 2008 GECCO conference companion on Genetic and evolutionary computation, 2008.

Bourauel, C., W. Scharold, A. Jäger, and T. Eliades. "Fatigue Failure of as-Received and Retrieved Niti Orthodontic Archwires." Dental Materials 24, no. 8 (2008): 1095-101.

Bower, A.F. "Advanced Element Formulations Incompatible Modes; Reduced Integration; and Hybrid Elements." http://solidmechanics.org/text/Chapter8_6/Chapter8_6.htm.

Bulletin, M.T. "Advantages of Cobalt Alloy for Coronary Stents." (2003).

Bünger, C.M., N. Grabow, K. Sternberg, C. Kröger, L. Ketner, K.-P. Schmitz, H.J. Kreutzer, *et al.* "Sirolimus-Eluting Biodegradable Poly-L-Lactide Stent for Peripheral Vascular Application: A Preliminary Study in Porcine Carotid Arteries." Journal of Surgical Research 139, no. 1 (2007): 77-82.

Cantón, G., D.S. Hippe, J. Sun, H.R. Underhill, W.S. Kerwin, D. Tang, and C. Yuan. "Characterization of Distensibility, Plaque Burden, and Composition of the Atherosclerotic Carotid Artery Using Magnetic Resonance Imaging." Medical physics 39, no. 10 (2012): 6247-53.

Celik, T., A. Iyisoy, M.T. Dogru, and E. Isik. "Coronary Stent Strut Fracture after Drug-Eluting Stent Implantation: A Newly Recognized Complication." International journal of cardiology 132, no. 1 (2009): 121-22.

Cheng, G.C., H.M. Loree, R.D. Kamm, M.C. Fishbein, and R.T. Lee. "Distribution of Circumferential Stress in Ruptured and Stable Atherosclerotic Lesions. A Structural Analysis with Histopathological Correlation." Circulation 87, no. 4 (1993): 1179-87.

Choe, H., G. Hur, J.H. Doh, J. Namgung, S.Y. Lee, K.T. Park, W.I. Chang, and W.R. Lee. "A Case of Very Late Stent Thrombosis Facilitated by Drug Eluting Stent Fracture: Comparative Images before and after Stent Fracture Detected by 64-Multidetector Computed Tomography." International journal of cardiology 133, no. 3 (2009): e125-e28.

Chowdhury, P.S., and R.G. Ramos. "Coronary-Stent Fracture." New England Journal of Medicine 347, no. 8 (2002): 581-81.

Chua, S.D., B. Mac Donald, and M. Hashmi. "Finite Element Simulation of Stent and Balloon Interaction." Journal of Materials Processing Technology 143 (2003): 591-97.

Chua, S.D., B. MacDonald, and M. Hashmi. "Finite Element Simulation of Slotted Tube (Stent) with the Presence of Plaque and Artery by Balloon Expansion." Journal of Materials Processing Technology 155 (2004a): 1772-79.

Chua, S.N.D., B. MacDonald, and M. Hashmi. "Effects of Varying Slotted Tube (Stent) Geometry on Its Expansion Behaviour Using Finite Element Method." Journal of Materials Processing Technology 155 (2004b): 1764-71.

Chung, I.-M., H.K. Gold, S.M. Schwartz, Y. Ikari, M.A. Reidy, and T.N. Wight. "Enhanced Extracellular Matrix Accumulation in Restenosis of Coronary Arteries after Stent Deployment." Journal of the American College of Cardiology 40, no. 12 (2002): 2072-81.

Clune, R., D. Kelliher, J.C. Robinson, and J.S. Campbell. "Nurbs Modeling and Structural Shape Optimization of Cardiovascular Stents." Structural and Multidisciplinary Optimization 50 (2014): 1-10.

Colombo, A., G. Stankovic, and J.W. Moses. "Selection of Coronary Stents." Journal of the American College of Cardiology 40, no. 6 (2002): 1021-33.

De Beule, M., P. Mortier, S.G. Carlier, B. Verhegghe, R. Van Impe, and P. Verdonck. "Realistic Finite Element-Based Stent Design: The Impact of Balloon Folding." Journal of biomechanics 41, no. 2 (2008): 383-89.

De Beule, M., S. Van Cauter, P. Mortier, D. Van Loo, R. Van Impe, P. Verdonck, and B. Verhegghe. "Virtual Optimization of Self-Expandable Braided Wire Stents." Medical engineering & physics 31, no. 4 (2009): 448-53.

Demir, A.G., B. Previtali, Q. Ge, M. Vedani, W. Wu, F. Migliavacca, L. Petrini, C.A. Biffi, and M. Bestetti. "Biodegradable Magnesium Coronary Stents: Material, Design and Fabrication." International Journal of Computer Integrated Manufacturing 27, no. 10 (2013): 936-45.

Dixon, S.A., R.G. Heikes, and R.P. Vito. "Constitutive Modeling of Porcine Coronary Arteries Using Designed Experiments." Journal of biomechanical engineering 125, no. 2 (2003): 274-79.

Etave, F., G. Finet, M. Boivin, J.-C. Boyer, G. Rioufol, and G. Thollet. "Mechanical Properties of Coronary Stents Determined by Using Finite Element Analysis." Journal of biomechanics 34, no. 8 (2001): 1065-75.

Farooq, V., B.D. Gogas, and P.W. Serruys. "Restenosis Delineating the Numerous Causes of Drug-Eluting Stent Restenosis." Circulation: Cardiovascular Interventions 4, no. 2 (2011): 195-205.

Fernandes, V., L.G. Kaluza, B. Godlewski, G. Li, and E.A. Raizner. "Novel Technique for Stent Delivery in Tortuous Coronary Arteries: Report of Three Cases." Catheterization and Cardiovascular Interventions 55 (2002): 485-90.

Ferrara, A., and A. Pandolfi. "Numerical Modelling of Fracture in Human Arteries." Computer methods in biomechanics and biomedical engineering 11, no. 5 (2008): 553-67.

Flueckiger, F., H. Sternthal, G.E. Klein, M. Aschauer, D. Szolar, and G. Kleinhappl. "Strength, Elasticity, and Plasticity of Expandable Metal Stents: In Vitro Studies with Three Types of Stress." Journal of vascular and interventional radiology 5, no. 5 (1994): 745-50.

Fortier, A., V. Gullapalli, and R.A. Mirshams. "Review of Biomechanical Studies of Arteries and Their Effect on Stent Performance." IJC Heart & Vessels 4 (2014): 12-18.

Fröbert, O., G. Sarno, S.K. James, N. Saleh, and B. Lagerqvist. "Effect of Stent Inflation Pressure and Post-Dilatation on the Outcome of Coronary Artery Intervention. A Report of More Than 90,000 Stent Implantations." PloS one 8, no. 2 (2013): e56348.

Gasser, T.C., R.W. Ogden, and G.A. Holzapfel. "Hyperelastic Modelling of Arterial Layers with Distributed Collagen Fibre Orientations." Journal of the royal society interface 3, no. 6 (2006): 15-35.

Gastaldi, D., S. Morlacchi, R. Nichetti, C. Capelli, G. Dubini, L. Petrini, and F. Migliavacca. "Modelling of the Provisional Side-Branch Stenting Approach for the Treatment of Atherosclerotic Coronary Bifurcations: Effects of Stent Positioning." Biomechanics and modeling in mechanobiology 9, no. 5 (2010): 551-61.

Gay, M., L. Zhang, and W.K. Liu. "Stent Modeling Using Immersed Finite Element Method." Computer methods in applied mechanics and engineering 195, no. 33 (2006): 4358-70.

Gervaso, F., C. Capelli, L. Petrini, S. Lattanzio, L. Di Virgilio, and F. Migliavacca. "On the Effects of Different Strategies in Modelling Balloon-Expandable Stenting by Means of Finite Element Method." Journal of biomechanics 41, no. 6 (2008): 1206-12.

Gijsen, F.J., F. Migliavacca, S. Schievano, L. Socci, L. Petrini, A. Thury, J.J. Wentzel, *et al.* "Simulation of Stent Deployment in a Realistic Human Coronary Artery." Biomedical engineering online 7, no. 1 (2008): 23.

Go, A., D. Mozaffarian, V.L. Roger, E.J. Benjamin, J.D. Berry, W.B. Borden, D.M. Bravata, *et al.* "Executive Summary: Heart Disease and Stroke Statistics--2013 Update: A Report from the American Heart Association.". Circulation 127, no. 1 (2013): 143-52.

Gorman, S.P., D.S. Jones, M.C. Bonner, M. Akay, and P.F. Keane. "Mechanical Performance of Polyurethane Ureteral Stents *in Vitro* and *Ex Vivo*." Biomaterials 18, no. 20 (1997): 1379-83.

Grewe, P.H., D. Thomas, A. Machraoui, J. Barmeyer, and K.-M. Müller. "Coronary Morphologic Findings after Stent Implantation." The American journal of cardiology 85, no. 5 (2000): 554-58.

Gu, L., S. Santra, R.A. Mericle, and A.V. Kumar. "Finite Element Analysis of Covered Microstents." Journal of biomechanics 38, no. 6 (2005): 1221-27.

Gu, L., S. Zhao, and S.R. Froemming. "Arterial Wall Mechanics and Clinical Implications after Coronary Stenting: Comparisons of Three Stent Designs." International Journal of Applied Mechanics 4, no. 02 (2012): 1250013-27.

Gu, L., S. Zhao, A.K. Muttyam, and J.M. Hammel. "The Relation between the Arterial Stress and Restenosis Rate after Coronary Stenting." Journal of Medical Devices 4, no. 3 (2010): 031005.

Haga, J.H., Y.-S.J. Li, and S. Chien. "Molecular Basis of the Effects of Mechanical Stretch on Vascular Smooth Muscle Cells." Journal of biomechanics 40, no. 5 (2007): 947-60.

Hamid, M.S., H.N. Sabbah, and P.D. Stein. "Finite Element Evaluation of Stresses on Closed Leaflets of Bioprosthetic Heart Valves with Flexible Stents." Finite Elements in Analysis and Design 1, no. 3 (1985): 213-25.

Han, H.-C., J.K. Chesnutt, J.R. Garcia, Q. Liu, and Q. Wen. "Artery Buckling: New Phenotypes, Models, and Applications." Annals of biomedical engineering 41, no. 7 (2013): 1399-410.

Hanawa, T. "Materials for Metallic Stents." Journal of Artificial Organs 12, no. 2 (2009): 73-79.

Hayes, K.R., R.J. Applegate, M.T. Sacrinty, M.A. Kutcher, S.K. Gandhi, R.M. Santos, and W.C. Little. "Target Lesion Revascularization after Bare-Metal or Drug-Eluting Stents: Clinical Presentation and Outcomes." The Journal of invasive cardiology 22, no. 6 (2010): 271-72.

Hermawan, H., A. Purnama, D. Dube, J. Couet, and D. Mantovani. "Fe–Mn Alloys for Metallic Biodegradable Stents: Degradation and Cell Viability Studies." Acta biomaterialia 6, no. 5 (2010): 1852-60.

Holzapfel, G.A., and T.C. Gasser. "Computational Stress-Deformation Analysis of Arterial Walls Including High-Pressure Response." International journal of cardiology 116, no. 1 (2007): 78-85.

Holzapfel, G.A., T.C. Gasser, and R.W. Ogden. "A New Constitutive Framework for Arterial Wall Mechanics and a Comparative Study of Material Models." Journal of elasticity and the physical science of solids 61, no. 1-3 (2000): 1-48.

Holzapfel, G.A., G. Sommer, C.T. Gasser, and P. Regitnig. "Determination of Layer-Specific Mechanical Properties of Human Coronary Arteries with Nonatherosclerotic Intimal Thickening and Related Constitutive Modeling." American Journal of Physiology-Heart and Circulatory Physiology 289, no. 5 (2005): H2048-H58.

Hopkins, C., P. McHugh, and J. McGarry. "Computational Investigation of the Delamination of Polymer Coatings During Stent Deployment." Annals of biomedical engineering 38, no. 7 (2010): 2263-73.

Horgan, C.O., and M.G. Smayda. "The Importance of the Second Strain Invariant in the Constitutive Modeling of Elastomers and Soft Biomaterials." Mechanics of Materials 51 (2012): 43-52.

Imani, S.M., A. Goudarzi, S. Ghasemi, A. Kalani, and J. Mahdinejad. "Analysis of the Stent Expansion in a Stenosed Artery Using Finite Element Method: Application to Stent Versus Stent Study." Proceedings of the Institution of Mechanical Engineers, Part H: Journal of Engineering in Medicine 228, no. 10 (2014): 996-1004.

Javaid, A., A.N. Buch, L.F. Satler, K.M. Kent, W.O. Suddath, J. Lindsay Jr, A.D. Pichard, and R. Waksman. "Management and Outcomes of Coronary Artery Perforation During Percutaneous Coronary Intervention." The American journal of cardiology 98, no. 7 (2006): 911-14.

Ju, F., Z. Xia, and K. Sasaki. "On the Finite Element Modelling of Balloon-Expandable Stents." Journal of the Mechanical Behavior of Biomedical Materials 1, no. 1 (2008): 86-95.

Kalanuria, A.A., P. Nyquist, and G. Ling. "The Prevention and Regression of Atherosclerotic Plaques: Emerging Treatments." Vascular health and risk management 8 (2012): 549.

Kamenskiy, V.A., I.I. Pipinos, A.Y. Dzenis, J. Bikhchandani, K.P. Gupta, N. Philips, S.A.J. Kazmi, and N.J. MacTaggart. "Effects of Carotid Artery Stenting on Arterial Geometry." Journal of the American College of Surgeons 217, no. 2 (2013): 251-62.

Kamura, A., T. Kawasaki, N. Koga, T. Inoue, and K. Node. "Fracture of a Sirolimus-Eluting Stent with Migration." International journal of cardiology 130, no. 2 (2008): e86-e88.

Kandzari, D.E., S.V. Rao, J.W. Moses, V. Dzavik, B.H. Strauss, M.J. Kutryk, C.A. Simonton, *et al.* "Clinical and Angiographic Outcomes with Sirolimus-Eluting Stents in Total Coronary Occlusions: The across/Tosca-4 (Approaches to Chronic Occlusions with Sirolimus-Eluting Stents/Total Occlusion Study of Coronary Arteries-4) Trial." JACC: Cardiovascular Interventions 2, no. 2 (2009): 97-106.

Kang, W.Y., W. Kim, H.G. Kim, and W. Kim. "Drug-Eluting Stent Fracture Occurred within 2 Days after Stent Implantation." International journal of cardiology 120, no. 2 (2007): 273-75.

Kathuria, Y. "Laser Microprocessing of Metallic Stent for Medical Therapy." Journal of Materials Processing Technology 170, no. 3 (2005): 545-50.

Khajehsaeid, H., J. Arghavani, and R. Naghdabadi. "A Hyperelastic Constitutive Model for Rubber-Like Materials." European Journal of Mechanics-A/Solids 38 (2013): 144-51.

Khamdaengyodtai, P., K. Vafai, P. Sakulchangsatjatai, and P. Terdtoon. "Effects of Pressure on Arterial Failure." Journal of biomechanics 45, no. 15 (2012): 2577-88.

Khan, W., S. Farah, and A.J. Domb. "Drug Eluting Stents: Developments and Current Status." Journal of controlled release 161, no. 2 (2012): 703-12.

Khosla, S. "This Map Shows Which Disease Is Most Likely to Kill You Depending on Where You Live." GlobalPost (2014).

Kim, H.-S., Y.-H. Kim, S.-W. Lee, D.-W. Park, C.W. Lee, M.-K. Hong, S.-W. Park, *et al.* "Incidence and Predictors of Drug-Eluting Stent Fractures in Long Coronary Disease." International journal of cardiology 133, no. 3 (2009): 354-58.

Kleinstreuer, C., Z. Li, C. Basciano, S. Seelecke, and M. Farber. "Computational Mechanics of Nitinol Stent Grafts." Journal of biomechanics 41, no. 11 (2008): 2370-78.

Lally, C., F. Dolan, and P. Prendergast. "Cardiovascular Stent Design and Vessel Stresses: A Finite Element Analysis." Journal of biomechanics 38, no. 8 (2005): 1574-81.

Lanzino, G., A.A. Rabinstein, and R.D. Brown. "Treatment of Carotid Artery Stenosis: Medical Therapy, Surgery, or Stenting?" Paper presented at the Mayo Clinic Proceedings, 2009.

Lee, S.-H., J.-S. Park, D.-G. Shin, Y.-J. Kim, G.-R. Hong, W. Kim, and B.-S. Shim. "Frequency of Stent Fracture as a Cause of Coronary Restenosis after Sirolimus-Eluting Stent Implantation." The American journal of cardiology 100, no. 4 (2007): 627-30.

Leong, D.P., B.K. Dundon, R. Puri, and R. Yeend. "Very Late Stent Fracture Associated with a Sirolimus-Eluting Stent." Heart, Lung and Circulation 17, no. 5 (2008): 426-28.

Li, N., and Y. Gu. "Parametric Design Analysis and Shape Optimization of Coronary Arteries Stent Structure." Paper presented at the 6th World Congress of Structural and Multidisciplinary Optimization, 2005.

Li, N., H. Zhang, and H. Ouyang. "Shape Optimization of Coronary Artery Stent Based on a Parametric Model." Finite Elements in Analysis and Design 45, no. 6 (2009): 468-75.

Li, Z., V. Taviani, T. Tang, U. Sadat, V. Young, A. Patterson, M. Graves, and J. Gillard. "The Mechanical Triggers of Plaque Rupture: Shear Stress Vs Pressure Gradient." (2014).

Li, Z.-Y., S. Howarth, and R.A. Trivedi. "Stress Analysis of Carotid Plaque Rupture Based on in Vivo High Resolution Mri." Journal of biomechanics 39, no. 14 (2006): 2611-22.

Liu, J., X.-J. Jia, Y.-J. Wang, M. Zhang, T. Zhang, and H.-D. Zhou. "Digital Subtraction Angiography Imaging Characteristics of Patients with Extra–Intracranial Atherosclerosis and Its Relationship to Stroke." Cell biochemistry and biophysics 69, no. 3 (2014): 599-604.

Loree, H.M., A.J. Grodzinsky, S.Y. Park, L.J. Gibson, and R.T. Lee. "Static Circumferential Tangential Modulus of Human Atherosclerotic Tissue." Journal of biomechanics 27, no. 2 (1994): 195-204.

Lossef, S.V., R.J. Lutz, J. Mundorf, and K.H. Barth. "Comparison of Mechanical Deformation Properties of Metallic Stents with Use of Stress-Strain Analysis." Journal of vascular and interventional radiology 5, no. 2 (1994): 341-49.

Luo, Q., X. Liu, Z. Li, C. Huang, W. Zhang, J. Meng, Z. Chang, and Z. Hua. "Degradation Model of Bioabsorbable Cardiovascular Stents." PloS one 9, no. 11 (2014): e110278.

Lusis, A.J. "Atherosclerosis." Nature 407 (2000): 233-41.

Maher, E., A. Creane, C. Lally, and D.J. Kelly. "An Anisotropic Inelastic Constitutive Model to Describe Stress Softening and Permanent Deformation in Arterial Tissue." Journal of the Mechanical Behavior of Biomedical Materials 12 (2012): 9-19.

Maher, E., A. Creane, S. Sultan, N. Hynes, C. Lally, and D.J. Kelly. "Inelasticity of Human Carotid Atherosclerotic Plaque." Annals of biomedical engineering 39, no. 9 (2011): 2445-55.

Mallika, V., B. Goswami, and M. Rajappa. "Atherosclerosis Pathophysiology and the Role of Novel Risk Factors: A Clinicobiochemical Perspective." Angiology 58, no. 5 (2007): 513-22.

Mani, G., M.D. Feldman, D. Patel, and C. Agrawal. "Coronary Stents: A Materials Perspective." Biomaterials 28, no. 9 (2007): 1689-710.

Marrey, R.V., R. Burgermeister, R.B. Grishaber, and R. Ritchie. "Fatigue and Life Prediction for Cobalt-Chromium Stents: A Fracture Mechanics Analysis." Biomaterials 27, no. 9 (2006): 1988-2000.

Martin, D., and F. Boyle. "Finite Element Analysis of Balloon-Expandable Coronary Stent Deployment: Influence of Angioplasty Balloon Configuration." International journal for numerical methods in biomedical engineering 29, no. 11 (2013): 1161-75.

McGarry, J., B. O'donnell, P. McHugh, and J. McGarry. "Analysis of the Mechanical Performance of a Cardiovascular Stent Design Based on Micromechanical Modelling." Computational Materials Science 31, no. 3 (2004): 421-38.

Migliavacca, F., L. Petrini, M. Colombo, F. Auricchio, and R. Pietrabissa. "Mechanical Behavior of Coronary Stents Investigated through the Finite Element Method." Journal of biomechanics 35, no. 6 (2002): 803-11.

Migliavacca, F., L. Petrini, V. Montanari, I. Quagliana, F. Auricchio, and G. Dubini. "A Predictive Study of the Mechanical Behaviour of Coronary Stents by Computer Modelling." Medical engineering & physics 27, no. 1 (2005): 13-18.

Möller, D., W. Reimers, A. Pyzalla, and A. Fischer. "Residual Stresses in Coronary Artery Stents." Journal of biomedical materials research 58, no. 1 (2001): 69-74.

Moore Jr, J.E., J.S. Soares, and K.R. Rajagopal. "Biodegradable Stents: Biomechanical Modeling Challenges and Opportunities." Cardiovascular Engineering and Technology 1, no. 1 (2010): 52-65.

Morlacchi, S., S.G. Colleoni, R. Cárdenes, C. Chiastra, J.L. Diez, I. Larrabide, and F. Migliavacca. "Patient-Specific Simulations of Stenting Procedures in Coronary Bifurcations: Two Clinical Cases." Medical engineering & physics 35, no. 9 (2013): 1272-81.

Morlacchi, S., G. Pennati, L. Petrini, G. Dubini, and F. Migliavacca. "Influence of Plaque Calcifications on Coronary Stent Fracture: A Numerical Fatigue Life Analysis Including Cardiac Wall Movement." Journal of Biomechanics 47, no. 4 (2014): 899-907.

Mortier, P., M. De Beule, D. Van Loo, B. Verhegghe, and P. Verdonck. "Finite Element Analysis of Side Branch Access During Bifurcation Stenting." Medical engineering & physics 31, no. 4 (2009): 434-40.

Motz, C., T. Schöberl, and R. Pippan. "Mechanical Properties of Micro-Sized Copper Bending Beams Machined by the Focused Ion Beam Technique." Acta Materialia 53, no. 15 (2005): 4269-79.

Muramatsu, T., Y. Onuma, Y.-J. Zhang, C.V. Bourantas, A. Kharlamov, R. Diletti, V. Farooq, *et al.* "Progress in Treatment by Percutaneous Coronary Intervention: The Stent of the Future." Revista Española de Cardiología (English Edition) 66, no. 6 (2013): 483-96.

Myouchin, K., K. Takayama, T. Taoka, H. Nakagawa, T. Wada, S. Masahiko, S. Iwasaki, S. Kurokawa, and K. Kichikawa. "Carotid Wallstent Placement Difficulties Encountered in Carotid Artery Stenting." SpringerPlus 2 (2013): 468-74.

Nam, N., S. Lee, J. Kim, J. Yi, and K. Lee. "Effect of Stress on the Passivation of Si-Dlc Coating as Stent Materials in Simulated Body Environment." Diamond and related materials 18, no. 9 (2009): 1145-51.

Narracott, A.J., P.V. Lawford, J.P. Gunn, and D.R. Hose. "Balloon Folding Affects the Symmetry of Stent Deployment: Experimental and Computational Evidence." Paper presented at the Engineering in Medicine and Biology Society, 2007. EMBS 2007. 29th Annual International Conference of the IEEE, 2007.

Nolan, D., A. Gower, M. Destrade, R. Ogden, and J. McGarry. "A Robust Anisotropic Hyperelastic Formulation for the Modelling of Soft Tissue." Journal of the Mechanical Behavior of Biomedical Materials 39 (2014): 48-60.

Okamura, T., T. Hiro, T. Fujii, J. Yamada, Y. Fukumoto, G. Hashimoto, T. Fujimura, K. Yasumoto, and M. Matsuzaki. "Late Giant Coronary Aneurysm Associated with a Fracture of Sirolimus Eluting Stent: A Case Report." Journal of cardiology 51, no. 1 (2008): 74-79.

ONS. "Deaths Registered in England and Wales (Series Dr), 2010." National Statistics (2011): 1-22.

Ormiston, J.A., and P.W. Serruys. "Bioabsorbable Coronary Stents." Circulation: Cardiovascular Interventions 2, no. 3 (2009): 255-60.

Park, J.-S., I.-H. Cho, and Y.-J. Kim. "Stent Fracture and Restenosis after Zotarolimus-Eluting Stent Implantation." International journal of cardiology 147, no. 2 (2011): e29-e31.

Park, J.-S., D.-G. Shin, Y.-J. Kim, G.-R. Hong, and I.-H. Cho. "Acute Myocardial Infarction as a Consequence of Stent Fracture and Plaque Rupture after Sirolimus-Eluting Stent Implantation." International journal of cardiology 134, no. 2 (2009): e79-e81.

Park, W.-P., S.-K. Cho, J.-Y. Ko, A. Kristensson, S. Al-Hassani, H.-S. Kim, and D. Lim. "Evaluation of Stent Performances Using Fea Considering a Realistic Balloon Expansion." Int J Eng Phys Sci 2, no. 2 (2008): 103-08.

Pauck, R.G., and B.D. Reddy. "Computational Analysis of the Radial Mechanical Performance of Pllacoronary Artery Stents." Medical Engineering & Physics 37, no. 1 (2014): 7-12.

Payne, R.A., I.B. Wilkinson, and D.J. Webb. "Arterial Stiffness and Hypertension Emerging Concepts." Hypertension 55, no. 1 (2010): 9-14.

Peng, L.F., D.B. McElhinney, A.W. Nugent, A.J. Powell, A.C. Marshall, E.A. Bacha, and J.E. Lock. "Endovascular Stenting of Obstructed Right Ventricle–to–Pulmonary Artery Conduits a 15-Year Experience." Circulation 113, no. 22 (2006): 2598-605.

Pericevic, I., C. Lally, D. Toner, and D.J. Kelly. "The Influence of Plaque Composition on Underlying Arterial Wall Stress During Stent Expansion: The Case for Lesion-Specific Stents." Medical engineering & physics 31, no. 4 (2009): 428-33.

Pitney, M., K. Pitney, N. Jepson, D. Friedman, T. Nguyen-Dang, J. Matthews, R. Giles, and D. Taylor. "Major Stent Deformation/Pseudofracture of 7 Crown Endeavor/Micro Driver Stent Platform: Incidence and Causative Factors." EuroIntervention: journal of EuroPCR in collaboration with the Working Group on Interventional Cardiology of the European Society of Cardiology 7, no. 2 (2011): 256-62.

Pochrząst, M., W. Walke, and M. Kaczmarek. "Biomechanical Characterization of the Balloon-Expandable Slotted Tube Stents." Journal of Achievements in Materials and Manufacturing Engineering 2, no. 37 (2009): 340-47.

Poncin, P., and J. Proft. "Stent Tubing: Understanding the Desired Attributes." Proc. of the 2003 ASM International (2003): 08-10.

Prendergast, P., C. Lally, S. Daly, A. Reid, T. Lee, D. Quinn, and F. Dolan. "Analysis of Prolapse in Cardiovascular Stents: A Constitutive Equation for Vascular Tissue and Finite-Element Modelling." Journal of biomechanical engineering 125, no. 5 (2003): 692-99.

Pujari, M.S.A., and V.R. Udupi. "Rehabilitation of Artery Revascularization through a Stent Insertion." Int. J. of Recent Trends in Engineering and Technology 1, no. 5 (2009).

Qureshi, A.M., D.B. McElhinney, J.E. Lock, M.J. Landzberg, P. Lang, and A.C. Marshall. "Acute and Intermediate Outcomes, and Evaluation of Injury to the Aortic Wall, as Based on 15 Years Experience of Implanting Stents to Treat Aortic Coarctation." Cardiology in the Young 17, no. 03 (2007): 307-18.

Reese, S., and D. Christ. "Finite Deformation Pseudo-Elasticity of Shape Memory Alloys–Constitutive Modelling and Finite Element Implementation." International Journal of Plasticity 24, no. 3 (2008): 455-82.

Richter, K., Y. Almagor, and M. Leon. "The Nir and Niroyal Coronary Stents." In Serruys P.W., Kutryk M.J.B. (Eds.), Handbook of Coronary Stents. 281-94. Martin Dunitz Ltd, London, UK, 2000.

Riley, R.F., C.W. Don, W. Powell, C. Maynard, and L.S. Dean. "Trends in Coronary Revascularization in the United States from 2001 to 2009 Recent Declines in Percutaneous Coronary Intervention Volumes." Circulation: Cardiovascular Quality and Outcomes 4, no. 2 (2011): 193-97.

Ring, G., E. Bognar, J. Dobranszky, J. Ginsztler, and L. Major. "Mechanical Behaviour of Coronary Stents." Advances in science and technology 49 (2006): 91-96.

Romagnoli, E., G.M. Sangiorgi, J. Cosgrave, E. Guillet, and A. Colombo. "Drug-Eluting Stenting: The Case for Post-Dilation." JACC: Cardiovascular Interventions 1, no. 1 (2008): 22-31.

Rosenfield, K., R. Schainfeld, A. Pieczek, L. Haley, and J.M. Isner. "Restenosis of Endovascular Stents from Stent Compression." Journal of the American College of Cardiology 29, no. 2 (1997): 328-38.

Sabaté, M., J.-Q. Pilar, J.A. Dominick, A. Fernando, H.-A. Rosana, G. Javier, B. Camino, E. Javier, M. Raúl, and C. Fernández. "Randomized Comparison of Sirolimus-Eluting Stent Versus Standard Stent for Percutaneous Coronary Revascularization in Diabetic Patients the Diabetes and Sirolimus-Eluting Stent (Diabetes) Trial." Circulation 112, no. 14 (2005): 2175-83.

Sangiorgi, G., G. Melzi, P. Agostoni, C. Cola, F. Clementi, P. Romitelli, R. Virmani, and A. Colombo. "Engineering Aspects of Stents Design and Their Translation into Clinical Practice." Annali dell'Istituto superiore di sanità 43, no. 1 (2006): 89-100.

Schmitz, K., D. Behrend, P. Behrens, and W. Schmidt. "Comparative Studies of Different Stent Designs." Progress in Biomedical Research (1999): 52-58.

Serruys, P., P. De Jaegere, M. Bertrand, G. Kober, J.F. Marquis, J. Piessens, R. Uebis, B. Valeix, and V. Wiegand. "Morphologic Change in Coronary Artery Stenosis with the Medtronic Wiktor™ Stent: Initial Results from the Core Laboratory for Quantitative Angiography." Catheterization and cardiovascular diagnosis 24, no. 4 (1991): 237-45.

Shankaran, K., and S. Karrupaswamy. "Parameterization and Optimization of Balloon Expandable Stent." SIMULIA Community Conference (2012).

Shih, C.-M., Y.-Y. Su, S.-J. Lin, and C.-C. Shih. "Failure Analysis of Explanted Sternal Wires." Biomaterials 26, no. 14 (2005): 2053-59.

Simulia. "Best Practices for Stent Analysis with Abaqus. Simulia Learning." In Answer 4516, 2010.

Smouse, H.B., A. Nikanorov, and D. LaFlash. "Biomechanical Forces in the Femoropopliteal Arterial Segment." Endovascular Today 4, no. 6 (2005): 60-66.

Solehuddin, S., M.I.Z. Ridzwan, M.N.M. Ibrahim, M.A.F.M. Ariffin, and A.B. Abdullah. "Analysis of Stress on Inflation of Balloon Catheter Using Finite Element Method." 3rd Kuala Lumpur international conference on biomedical engineering 15, no. 6 (2007): 178-81.

Stoeckel, D., A. Pelton, and T. Duerig. "Self-Expanding Nitinol Stents - Material and Design Considerations." European Radiology (2003).

Suzuki, T., A. Ei, Y. Takada, H. Uehara, T. Yamanobe, and K. Takahashi. "Modification of Physical Properties of Poly (L-Lactic Acid) by Addition of Methyl-B-Cyclodextrin." Beilstein Journal of Organic Chemistry 10, no. 1 (2014): 2997-3006.

Tambaca, J., S. Canic, M. Kosor, R.D. Fish, and D. Paniagua. "Mechanical Behavior of Fully Expanded Commercially Available Endovascular Coronary Stents." Texas Heart Institute Journal 38, no. 5 (2011): 491.

Tan, L., D. Webb, K. Kormi, and S. Al-Hassani. "A Method for Investigating the Mechanical Properties of Intracoronary Stents Using Finite Element Numerical Simulation." International journal of cardiology 78, no. 1 (2001): 51-67.

Timmins, L.H., M.W. Miller, F.J. Clubb, and J.E. Moore. "Increased Artery Wall Stress Post-Stenting Leads to Greater Intimal Thickening." Laboratory Investigation 91, no. 6 (2011): 955-67.

Tsunoda, T., H. Hara, K. Nakajima, H. Shinji, S. Ito, R. Iijima, R. Nakajima, *et al.* "Stent Deformation: An Experimental Study of Coronary Ostial Stenting." Cardiovascular Revascularization Medicine 10, no. 2 (2009): 80-87.

Umeda, H., T. Gochi, M. Iwase, H. Izawa, T. Shimizu, R. Ishiki, H. Inagaki, *et al.* "Frequency, Predictors and Outcome of Stent Fracture after Sirolimus-Eluting Stent Implantation." International journal of cardiology 133, no. 3 (2009): 321-26.

Vassilev, D., and R. Gil. "Changes in Coronary Bifurcations after Stent Placement in the Main Vessel and Balloon Opening of Stent Cells: Theory and Practical Verification on a Bench-Test Model." Journal of Geriatric Cardiology 5, no. 1 (2008): 43-49.

Valibhoy, A.R., B.P. Mwipatayi, and K. Sieunarine. "Fracture of a Carotid Stent: An Unexpected Complication." Journal of vascular surgery 45, no. 3 (2007): 603-06.

Venkatraman, S., T.L. Poh, T. Vinalia, K.H. Mak, and F. Boey. "Collapse Pressures of Biodegradable Stents." Biomaterials 24, no. 12 (2003): 2105-11.

Verheye, S., J.A. Ormiston, J. Stewart, M. Webster, E. Sanidas, R. Costa, J.R.j. Costa, *et al.* "A Next-Generation Bioresorbable Coronary Scaffold System: From Bench to First Clinical Evaluation: 6- and 12-Month Clinical and Multimodality Imaging Results." JACC Cardiovascular Intervention 7, no. 1 (2014): 89-99.

Vieira, A.F.C., R.d.I. Medeiros, R.M. Guedes, A.T. Marques, and V.I. Tita. "Visco-Elastic-Plastic Properties of Suture Fibers Made of Pla-Pcl." Materials Science Forum 730-732, no. 56-61 (2013).

Walke, W., Z. Paszenda, and J. Filipiak. "Experimental and Numerical Biomechanical Analysis of Vascular Stent." Journal of Materials Processing Technology 164 (2005): 1263-68.

Welch, T.R., R.C. Eberhart, J. Reisch, and C.-J. Chuong. "Influence of Thermal Annealing on the Mechanical Properties of Plla Coiled Stents." Cardiovascular Engineering and Technology 5, no. 3 (2014): 270-80.

Wexler, L., B. Brundage, J. Crouse, R. Detrano, V. Fuster, J. Maddahi, J. Rumberger, *et al.* "Coronary Artery Calcification: Pathophysiology, Epidemiology, Imaging Methods, and Clinical Implications a Statement for Health Professionals from the American Heart Association." Circulation 94, no. 5 (1996): 1175-92.

Whitcher, F. "Simulation of in Vivo Loading Conditions of Nitinol Vascular Stent Structures." Computers & structures 64, no. 5 (1997): 1005-11.

Wu, W., L. Petrini, D. Gastaldi, T. Villa, M. Vedani, E. Lesma, B. Previtali, and F. Migliavacca. "Finite Element Shape Optimization for Biodegradable Magnesium Alloy Stents." Annals of biomedical engineering 38, no. 9 (2010): 2829-40.

Wu, W., W.-Q. Wang, D.-Z. Yang, and M. Qui. "Stent Expansion in Curved Vessel and Their Interactions: A Finite Element Analysis." Journal of Biomechanics 40, no. 11 (2007b): 2580-85.

Wu, W., D.-Z. Yang, M. Qi, and W.-Q. Wang. "An Fea Method to Study Flexibility of Expanded Coronary Stents." Journal of Materials Processing Technology 184, no. 1 (2007a): 447-50.

Xia, Z., F. Ju, and K. Sasaki. "A General Finite Element Analysis Method for Balloon Expandable Stents Based on Repeated Unit Cell (Ruc) Model." Finite Elements in Analysis and Design 43, no. 8 (2007): 649-58.

Yıldız, A., A. Karakurt, A. Bitigen, and B. Bağırtan. "Fatal Complication, Rescue Therapy; Covered Stent for Coronary Artery Perforation." Health 5 (2013): 1-5.

Zahedmanesh, H., D. John Kelly, and C. Lally. "Simulation of a Balloon Expandable Stent in a Realistic Coronary Artery—Determination of the Optimum Modelling Strategy." Journal of biomechanics 43, no. 11 (2010): 2126-32.

Zahedmanesh, H., and C. Lally. "Determination of the Influence of Stent Strut Thickness Using the Finite Element Method: Implications for Vascular Injury and in-Stent Restenosis." Medical & biological engineering & computing 47, no. 4 (2009): 385-93.

Zhang, Y., M.L. Dunn, K.S. Hunter, C. Lanning, D.D. Ivy, L. Claussen, S.J. Chen, and R. Shandas. "Application of a Microstructural Constitutive Model of the Pulmonary Artery to Patient-Specific Studies: Validation and Effect of Orthotropy." Journal of biomechanical engineering 129, no. 2 (2007): 193-201.

Zhao, S., L. Gu, and S.R. Froemming. "Finite Element Analysis of the Implantation of a Self-Expanding Stent: Impact of Lesion Calcification." Journal of Medical Devices 6, no. 2 (2012): 021001.

Zhao, S., L. Gu, and S.R. Froemming. "On the Importance of Modeling Stent Procedure for Predicting Arterial Mechanics." Journal of biomechanical engineering 134, no. 12 (2012): 121005.

Zhou, C.-T., and H.-Y. Dong. "Stability and Dynamic Deforming Process for Structure of Coronary Artery Stents." Current Applied Physics 5, no. 5 (2005): 458-62.

Zunino, P., C. D'Angelo, L. Petrini, C. Vergara, C. Capelli, and F. Migliavacca. "Numerical Simulation of Drug Eluting Coronary Stents: Mechanics, Fluid Dynamics and Drug Release." Computer methods in applied mechanics and engineering 198, no. 45 (2009): 3633-44.